Author:
James, Michael C

Title:
Aluminium and Oxygen Termination of Diamond for Thermionic Applications

Aluminium and Oxygen Termination of Diamond for Thermionic Applications

Michael Christopher James

School of Chemistry

University of Bristol

A dissertation submitted to the University of Bristol in accordance with the requirements for award of the degree of Doctor of Philosophy in the Faculty of Science

October 2019

Word Count: 37,049

Abstract

This thesis presents a joint computational and experimental approach to developing a novel diamond surface termination with aluminium that has a negative electron affinity (NEA). There is a need for a thermally stable NEA for thermionic applications, since hydrogen termination desorbs from the diamond surface at thermionic temperatures. The choice of aluminium is based on it being a light, electropositive element that bonds strongly to different diamond surfaces.

Using density functional theory, the adsorption of Al onto bare, oxygenated and nitrogenated diamond surfaces was studied. The two key parameters considered were the adsorption energy and the electron affinity values, for different coverages and configurations of Al. NEA values of up to -1.47 eV and -1.88 eV were observed for Al addition to the (100) and (111) bare surfaces, respectively, at 1 monolayer (ML) coverage, and up to -1.36 eV and -2.17 eV for Al addition to the (100) and (111) oxygen-terminated surfaces, respectively, at 0.25 ML coverage. Al adsorbed more strongly on the ketone O-terminated surface than the ether surface. Adsorption energies for the AlO-terminations were up to -6.36 eV/atom and -8.19 eV/atom for the (100) and (111) surfaces, respectively, at 0.25 ML Al coverage, considerably larger than that of H-termination (∼-4 eV/atom).

Three different oxidation procedures were investigated experimentally. It was determined that oxidation of diamond by UV/ozone treatment results in a large ketone component on the surface, whilst also having ∼1 ML coverage. The surface structure and electronic behaviour were determined for both hydrogen and oxygen terminations.

AlO-terminations were fabricated experimentally by depositing Al onto O-terminated diamond. Three different methods were explored: (i) thick-film deposition of Al followed by an acid etch to remove excess metal, (ii) thin-film deposition of Al by atomic layer deposition, and (iii) thin-film deposition of Al by electron-beam evaporation. Low work function and NEA were observed for each method, but these values were spatially and temperature dependant. Annealing caused a change in surface structure, identified as the incorporation of O atoms into the Al layer. Tests of thermionic emission showed a small emission current density, but at a higher temperature than attainable for H-termination. Thus, AlO-terminated diamond shows promise but further optimisation is required for use in devices.

Acknowledgements

First and foremost I would like to thank my supervisors Professor Paul May and Dr Neil Fox for their kind thoughts, suggestions, encouragement and assistance throughout the PhD. My thanks extend to Professor Neil Allan for supervising my computational work, and to Drs James Smith, Zamir Othman, Mattia Cattelan and Alex Croot for their extensive assistance and training. Thanks also go to Ed Smith, Robbie Mackenzie, Gary Wan and Fabian Fogarty for their help using various pieces of equipment, which was greatly appreciated. My thanks also go to my collaborators, Professor Rui Silva and Dr Ricardo Silva at the University of Aveiro, for using their atomic layer deposition kit on my behalf, and to Dr Rob Harniman for the atomic force microscopy measurements.

I would like to offer my deepest gratitude to the Bristol Centre for Functional Nanomaterials for taking me on as a PhD student, and to the EPSRC for funding. My thanks go to my colleagues and friends in the 2015 BCFN cohort and the Bristol diamond group for your help and for all the good times over the past few years. It has been a great pleasure and I wish you all the best for the future. To all my friends and family, a giant thank you for being there to support me.

Last but not least, thank you Jenna for your inexhaustible supply of encouragement, positivity and love throughout my PhD.

Author’s Declaration

I declare that the work in this dissertation was carried out in accordance with the requirements of the University's *Regulations and Code of Practice for Research Degree Programmes* and that it has not been submitted for any other academic award. Except where indicated by specific reference in the text, the work is the candidate's own work. Work done in collaboration with, or with the assistance of, others, is indicated as such. Any views expressed in the dissertation are those of the author.

SIGNED: ..... DATE:.....

Table of Contents

ABSTRACT ..... **I**

ACKNOWLEDGEMENTS ..... **II**

AUTHOR'S DECLARATION ..... **III**

TABLE OF CONTENTS ..... **IV**

LIST OF ABBREVIATIONS ..... **VIII**

LIST OF TABLES ..... **X**

LIST OF FIGURES ..... **XII**

CHAPTER 1 – INTRODUCTION **1**

1.1 OVERVIEW OF DIAMOND 1

1.1.1 The Allotropes of Carbon *1*

1.1.2 Properties of Diamond *3*

1.1.3 Natural Diamond *4*

1.2 SYNTHETIC DIAMOND 4

1.2.1 High Pressure High Temperature *4*

1.2.2 Chemical Vapour Deposition *5*

1.2.3 Detonation Nanodiamond *6*

1.3 DIAMOND AS A WIDE BAND GAP SEMICONDUCTOR 7

1.3.1 Dopants *7*

1.3.2 Band Bending *10*

1.3.3 Negative Electron Affinity *11*

1.4 ELECTRON EMISSION 12

1.4.1 Thermionic Emission *12*

1.4.2 Thermionic Energy Converters *14*

1.4.2.1 Efficiency and Power 15

1.4.2.2 Design Considerations 17

1.4.2.3 Applications 18

1.4.3 Photon-Enhanced Thermionic Emission *19*

1.4.4 Thermionic Emission from Diamond *20*

1.5 COMPUTATIONAL CHEMISTRY 23

1.5.1 First Principles Modelling *24*

1.5.2 Density Functional Theory *24*

1.5.2.1 The Exchange-Correlation Functional 25

1.5.2.2 Basis Sets 26

1.5.2.3 Bloch's Theorem 27

1.5.2.4 Pseudopotentials 27

1.6 THESIS OUTLINE 28

REFERENCES 29

CHAPTER 2 – SURFACE FUNCTIONALISATION OF DIAMOND **34**

2.1 THE DIAMOND SURFACE 34

2.1.1 Diamond Crystal Facets *34*

2.2 NON-METAL TERMINATIONS 36

2.2.1 Hydrogen ... *36*
2.2.2 Oxygen, Hydroxyl and Carboxyl ... *39*
2.2.3 Nitrogen and Amines ... *43*
2.2.4 Sulfur and Thiol ... *44*
2.2.5 Halides ... *45*
2.2.6 Aliphatics and Aromatics ... *45*
2.3 METALLOID TERMINATIONS ... 47
2.4 METAL AND METAL-OXYGEN TERMINATIONS ... 48
2.4.1 Group I and II Metals ... *48*
2.4.2 Transition Metals ... *51*
2.4.3 Aluminium ... *52*
2.5 METAL DEPOSITION ONTO DIAMOND ... 53
2.6 OXIDE AND NITRIDE DEPOSITION ONTO DIAMOND ... 54
2.7 CHAPTER SUMMARY ... 55
REFERENCES ... 55
CHAPTER 3 – EXPERIMENTAL TECHNIQUES AND PROCEDURES ... 62
3.1 INTRODUCTION ... 62
3.2 VACUUM SYSTEMS ... 62
3.3 DIAMOND SYNTHESIS ... 63
3.3.1 Substrates ... *63*
3.3.2 Hot Filament CVD ... *64*
3.3.3 Microwave Plasma CVD ... *66*
3.3.4 Acid Cleaning ... *67*
3.3.4.1 Routine Cleaning ... 67
3.3.4.2 Al removal ... 67
3.4 TERMINATION PROCEDURES ... 68
3.4.1 Hydrogen ... *68*
3.4.2 Oxygen ... *68*
3.4.2.1 UV/Ozone ... 68
3.4.2.2 Oxygen Plasma ... 69
3.4.2.3 Acid Oxidation ... 69
3.4.2.4 ALD Oxidation ... 69
3.4.3 Aluminium ... *70*
3.4.3.1 Thermal Evaporation ... 70
3.4.3.2 Atomic Layer Deposition ... 71
3.4.3.3 Electron-Beam Evaporation ... 71
3.5 CHARACTERISATION TECHNIQUES ... 72
3.5.1 Contact Angle Measurements ... *72*
3.5.2 Fourier Transform Infrared Spectroscopy ... *73*
3.5.3 Raman Spectroscopy ... *75*
3.5.4 Scanning Electron Microscopy ... *77*
3.5.5 Energy-Filtered Photoemission Electron Microscopy ... *78*
3.5.6 Photoelectron Spectroscopy ... *79*
3.5.6.1 X-ray Photoelectron Spectroscopy ... 79
3.5.6.2 Ultraviolet Photoelectron Spectroscopy ... 81
3.5.7 Low Energy Electron Diffraction ... *83*
3.5.8 Thermionic Emission ... *84*
REFERENCES ... 86

CHAPTER 4 – COMPUTATIONAL STUDIES OF Al ON DIAMOND 88
4.1 INTRODUCTION 88
4.2 COMPUTATIONAL SETUP 89
4.2.1 CASTEP 89
4.2.1.1 Input and Output Files 90
4.2.2 BlueCrystal 90
4.2.3 Electron Affinity Calculation 91
4.2.4 Adsorption Energy Calculation 92
4.3 Al ADDITION TO THE (100) DIAMOND SURFACE 92
4.3.1 Ensuring Convergence 92
4.3.2 Geometries of the Al-Adsorbed Bare (100) Diamond Surface 95
4.3.3 Geometries of the Al-Adsorbed O-Terminated (100) Diamond Surface 99
4.3.4 Geometries of the Al-Adsorbed N-Terminated (100) Diamond Surface 102
4.3.5 Electronic Structure of the (100) Surfaces 105
4.3.6 Investigation of a Larger Supercell 108
4.4 Al ADDITION TO THE (111) DIAMOND SURFACE 110
4.4.1 Ensuring Convergence 110
4.4.2 Geometries of the Al-Adsorbed Bare (111) Diamond Surface 111
4.4.3 Geometries of the Al-Adsorbed O-Terminated (111) Diamond Surface 115
4.4.4 Geometries of the Al-Adsorbed N-Terminated (111) Diamond Surface 120
4.4.5 Electronic Structure of the (111) Surfaces 120
4.5 CONCLUSIONS 125
REFERENCES 126

CHAPTER 5 – INVESTIGATION OF THE COVERAGE, STRUCTURE AND ELECTRONIC PROPERTIES OF O- AND H-TERMINATED DIAMOND 129
5.1 INTRODUCTION 129
5.1.1 Previous O-Termination Studies 130
5.2 EXPERIMENTAL DETAILS 132
5.3 OPTIMISING OXIDATION TIME 134
5.4 CHARACTERISATION OF H- AND O-TERMINATED SURFACES 136
5.4.1 Bonding on the (100) Diamond Surface 138
5.4.2 Bonding on the (111) Diamond Surface 143
5.5 SURFACE STRUCTURE 147
5.5.1 Structure of the (100) Diamond Surface 148
5.5.2 Structure of the (111) Diamond Surface 148
5.6 ELECTRONIC BEHAVIOUR 149
5.6.1 Electronic Characteristics of the (100) Diamond Surface 149
5.6.2 Electronic Characteristics of the (111) Diamond Surface 151
5.7 CONCLUSIONS 153
REFERENCES 156

CHAPTER 6 – EXPERIMENTAL DETERMINATION OF THE WORK FUNCTION AND NEGATIVE ELECTRON AFFINITY FROM Al ON O-TERMINATED DIAMOND 158
6.1 INTRODUCTION 158
6.2 EXPERIMENTAL DETAILS 159
6.3 THICK-FILM DEPOSITION 161
6.3.1 Al Deposition on Polycrystalline Diamond 161

6.3.2 Analysis of the (100) and (111) Surfaces *163*
6.4 THIN-FILM DEPOSITION BY ALD 169
6.4.1 Effect of Oxidation Method *169*
6.4.2 Analysis of the (100) and (111) Surfaces *173*
6.5 THIN-FILM DEPOSITION BY ELECTRON-BEAM EVAPORATION 177
6.5.1 Calibration of Al Evaporation *177*
6.5.2 Analysis of the (100) and (111) Surfaces *178*
6.6 THERMIONIC EMISSION TESTS 184
6.6.1 Diamond Characterisation *184*
6.6.2 H-Termination *185*
6.6.3 AlO-Terminations *186*
6.7 CONCLUSIONS 188
REFERENCES 190
CHAPTER 7 – THESIS SUMMARY 192
7.1 SUMMARY 192
7.1.1 Computational Modelling *192*
7.1.2 Oxygenation Studies *193*
7.1.3 Experimental NEA Studies *195*
7.2 FUTURE WORK 197
APPENDIX – PUBLICATIONS AND PRESENTATIONS 199
LIST OF PUBLICATIONS 199
LIST OF ORAL PRESENTATIONS 199
LIST OF POSTER PRESENTATIONS 199

List of Abbreviations

2DHG:	Two-dimensional hole gas
ALD:	Atomic layer deposition
ATR:	Attenuated total reflectance
BDD:	Boron-doped diamond
BDE:	Bond dissociation enthalpy
CASTEP:	Cambridge serial total energy package
CBM:	Conduction band minimum
CVD:	Chemical vapour deposition
DFT:	Density functional theory
DOS:	Density of states
EA:	Electron affinity
EF-PEEM:	Energy-filtered photoemission electron microscopy
EP:	Electrostatic potential
FET:	Field effect transistor
FTIR:	Fourier transform infrared
GGA:	Generalised gradient approximation
HB:	Hexagon bridge
HF:	Hartree-Fock
HH:	Hexagon hole
HPHT:	High pressure high temperature
L:	Lower Pandey chain
LDA:	Local density approximation
LEED:	Low energy electron diffraction
MFC:	Mass flow controller
ML:	Monolayer
MOSFET:	Metal oxide-semiconductor field effect transistor
NB:	Nitrogen bridge
NDD:	Nitrogen-doped diamond
NEA:	Negative electron affinity
NP:	Nitrogen pedestal
OB:	Oxygen bridge
OP:	Oxygen pedestal
PBE:	Perdew-Burke-Ernzerhof
PDOS:	Projected density of states
PEA:	Positive electron affinity
PETE:	Photon-enhanced thermionic emission
SEM:	Scanning electron microscopy
T1:	First-tier carbon
T2:	Second-tier carbon
T3:	Third-tier carbon
T4:	Fourth-tier carbon
TEC:	Thermionic energy converter
TM:	Transition metal
U:	Upper Pandey chain
UHV:	Ultrahigh vacuum

UNCD:	Ultrananocrystalline diamond
UPS:	Ultraviolet photoelectron spectroscopy
VBM:	Valence band maximum
XPS:	X-ray photoelectron spectroscopy

List of Tables

1.1 Some of the intrinsic properties of diamond.[10–13] 3
1.2 Properties of some common emitter materials.[68,70,71] 14
1.3 Different studies of electron emission properties using an H-terminated diamond cathode. 22
2.1 Previous theoretical calculations of group I and II metal and metal-oxygen terminations. 50
2.2 Previous theoretical calculations of transition metal and metal-oxygen terminations. 52
3.1 Calibration of MFCs for BDD growth. *The B_2H_6 gas cylinder contained 5% B_2H_6 in H_2. 66
4.1 Values of the adsorption energy, E_{ads}, calculated electron affinity, χ, and bond lengths, d, for selected calculations compared with previous work on (100) diamond. d(C-C) refers to bond length of the surface dimer. (2 × 1) indicates a reconstructed surface dimer. *Per surface atom, compared with the (1 × 1) bare surface. 95
4.2 Values of electron affinity, χ, adsorption energy, E_{ads}, and relevant bond lengths, d, calculated for the minimum energy positions at different surface coverages of Al on the bare diamond (100) surface. The HH and T3 sites at 0.25 ML coverage were not energy minima and so are not included. 98
4.3 Energies and bond lengths calculated for the minimum energy positions at different surface coverages of Al on O-terminated (100) diamond. * indicates the particular (1 × 1) surface that forms this structure. (E) and (K) are ether and ketone configurations, respectively. The HB and T4 positions at 0.25 ML coverage and HB+T4 ($\sqrt{2} \times \sqrt{2}$) at 0.5 ML were not energy minima and so are not included. 101
4.4 Energies and bond lengths for Al addition to N-terminated (100) diamond. * indicates the starting configuration. [a] Both Al atoms relax into configurations just outside of NP position, in opposite directions to lengthen the Al-Al bond. [b] Same as [a] but for the NB position. 104
4.5 Energies and bond lengths calculated for the minimum energy positions at different surface coverages of Al on O-terminated (100) diamond. 109
4.6 Energies and bond lengths for selected calculations compared with previous work on (111) diamond. d(C-C) refers to the carbon-carbon bond length of surface atoms; for (2 × 1) structures these are for the upper Pandey chain. * indicates the C-C bond located beneath the oxygen atom. E_{ads} for the bare surface was calculated with respect to the relaxed (1 × 1) surface. 111
4.7 Energies and bond lengths for the minimum energy positions at different surface coverages of Al on bare (111) diamond. *only for Al coordinated with surface carbon atoms. Addition to the L sites at 0.25 and 0.5 ML coverage were not energy minima. 113
4.8 Values of χ, E_{ads}, and d, calculated for the minimum energy positions at different surface coverages of Al on O-terminated (111) diamond. (K) and (E) are ketone and ether, respectively. 118

5.1 Type of termination and O atomic percentages for different oxygen-termination methods and conditions. BDD: (polycrystalline) boron doped diamond; NCD: nanocrystalline diamond; EC: electrochemical anodic polarization; SCA: sulfochromic acid. 132
5.2 Approximate C 1s peak positions from XPS. 137
5.3 Approximate O 1s peak positions from XPS using two-component peak fitting. 137
5.4 Approximate O 1s peak positions from XPS using three-component peak fitting. 138
5.5 Stretching vibrations from FTIR from previous studies with diamond. 138
5.6 Summary of C-O/C=O peak ratio and surface coverages for different oxidation procedures on the (100) diamond surface. 142
5.7 Summary of C-O/C=O peak ratio and surface coverages for different oxidation procedures on the (111) diamond surface. 147
6.1 Approximate Al 2p peak positions from XPS.[9] 163
6.2 Atomic percentages of O and Al for AlO-terminated NDD prepared by different Al deposition methods. 187
7.1 Summary of key computational results from this thesis. 193
7.2 Summary of experimental results from different surface terminations in Chapter 5. 195
7.3 Summary of experimental results from different surface terminations in Chapter 6. *This was the initial sample that was oxidised by ALD. 197

List of Figures

1.1 The crystal structures of (a) diamond and (b) graphite..... 1
1.2 The simplified phase diagram of carbon from Steinbeck *et al.*[1]..... 2
1.3 CVD reactor designs. (a) Hot filament CVD dissociates process gases with a heated filament. (b) Linear antenna-style microwave plasma CVD uses an antenna to tune microwave radiation and form a plasma above the substrate. Adapted from May.[10] 6
1.4 Band diagram of diamond showing the relative energies of P, N and B dopants. The valence band is shown in blue and the conduction band in red. 8
1.5 Relative positions of the conduction band minimum, CBM, vacuum energy, E_{vac}, and the electron affinity, χ, for a material with positive electron affinity (PEA), 'true' negative electron affinity (NEA) and 'effective' NEA..... 12
1.6 Schematic diagram for a TEC device..... 15
1.7 Energy diagram of a TEC. E_F and E_F' are the Fermi levels of the emitter and collector, respectively. ϕ_E and ϕ_C are the work functions of the emitter and collector, respectively. Electrons in the emitter must overcome the vacuum level, E_{vac}, and an additional energy barrier from space charge to reach the collector. V_{out} is the output voltage..... 15
1.8 Different schemes for solar energy concentration. From Xiao *et al.*[70] 19
1.9 Schematic energy diagram for a PETE device. Electrons are energised into the conduction band of the cathode by photon absorption and by thermalization. From Schwede *et al.*[94]..... 20
1.10 Schematic diagram of a diamond-based PETE device. From Girolami *et al.*[113] 23
1.11 Illustration showing how the pseudopotential, V_{pseudo}, and pseudo-wavefunction, ψ_{pseudo}, approximate the potential, Z/r, and wavefunction, ψ_v, respectively, below a cut-off atomic radius, r_c. From Payne.[129]..... 28
2.1 A cubic crystal with (a) the (100) plane shown in blue and (b) the (111) plane shown in red. O is the origin, and a_1, a_2 and a_3 are the primitive lattice vectors in *x*, *y* and *z* directions, respectively. 35
2.2 Simulations of (a)–(b) the (1 × 1) (100) and (111) bare diamond surfaces, respectively, and (c)–(d) the (2 × 1) reconstructed bare diamond (100) and (111) surfaces, respectively..... 36
2.3 Simulations of the H-terminated (a) (100) and (b) (111) diamond surfaces. C and H atoms are shown in grey and white, respectively..... 37
2.4 Before and after band alignment between H-terminated diamond and surface adsorbates. Equilibration of diamond Fermi level, E_F, with adsorbate chemical potential, μ, by electron transfer leads to upwards band bending and the formation of a two-dimensional hole gas (2DHG) at the diamond surface. (H)OMO and (L)UMO are (highest) occupied molecular orbital and (lowest) unoccupied molecular orbital, respectively, for the surface acceptor species. Adapted from Ristein.[12] 38
2.5 Thermal cycling of an H-terminated diamond cathode up to 600 °C shows the peak emission current decreases and the threshold temperature for

emission increases with an increasing number of emission cycles. From Croot *et al.*[26] 39
2.6 Simulations of the (a)–(b) ether O-terminated (100) and (111) diamond surfaces, respectively, and (c)–(d) the ketone O-terminated (100) and (111) diamond surfaces, respectively. C and O atoms are shown in grey and red, respectively..... 40
2.7 Modification of hydroxyl-terminated diamond by different procedures. (a) silanisation, (b) thermal or photochemical reaction with alkene, (c) esterification and (d) zirconium and phosphorus chemistry. Adapted from Szunerits and Boukherroub.[54] 43
2.8 Amine-terminated diamond followed by HCl treatment enhances the NH_3 yield from the photoreduction of N_2 compared to H-termination. From Zhu *et al.*[58]..... 44
2.9 Functionalisation of the diamond surface with (a) photochemical grafting of alkenes and (b) reaction with aryldiazonium salt. 47
2.10 Side and plan views of (3 × 1) reconstructed (100) diamond surface with (a) Si-termination from Schenk *et al.*[91] and (b) Ge-termination from Sear *et al.*[95]..... 48
2.11 Pauling electronegativity values of different elements of the Periodic Table.[96]..... 49
2.12 Different potential interactions between a metal (M) and O-terminated diamond. (a) Covalent bonding, (b) ionic bonding and (c) dipolar interactions. Adapted from O'Donnell *et al.*[99] 50
2.13 Schematic cross-sectional diagram of a typical diamond MOSFET. Metal oxide deposition on H-terminated diamond generates a 2DHG at the diamond surface. S, G and D are source, gate and drain contacts, respectively..... 55
3.1 (a) CVD (100) and (b) HPHT (111) single crystal diamond substrates. A p-type diamond overlayer was grown on these single crystals to make the surface conductive. (c) Si and (d) Mo substrates for growth of B-doped and N-doped diamond thin films, respectively. 63
3.2 (a) Photograph of the hot filament CVD reactor. (b) Photograph of the interior setup of the reactor. 65
3.3 Photograph of the microwave plasma CVD reactor. 67
3.4 Photographs of (a) the UV ozone generator kit and (b) the oxygen plasma kit used for oxygen termination..... 69
3.5 Photograph of the bell-jar thermal evaporator used for thick-film deposition of Al. 71
3.6 Photograph of the chamber used for electron-beam evaporation of metals, in this case Al..... 72
3.7 Photograph of the drop-shape analyser used for contact-angle measurement. 73
3.8 (a) Schematic of an FTIR interferometer. (b) In FTIR-ATR infrared light in a Ge crystal reflects off the surface of a diamond sample due to the difference in refractive index. 74
3.9 Photograph of the FTIR spectrometer with ATR attachment. 75
3.10 A laser can excite electrons into 'virtual' excited states. Most of the emission has no change in energy (Rayleigh scattering) but some emission has lower energy (Stokes) or higher energy (Anti-Stokes). 76

3.11 (a) Photograph and (b) schematic of the Raman spectrometer. 76
3.12 (a) Photograph and (b) schematic of the scanning electron microscope. ... 77
3.13 (a) Photograph and (b) schematic of the NanoESCA II, which can perform EF-PEEM and UPS. 79
3.14 Example XPS survey spectrum of O-terminated diamond. The inset shows the XPS spectrum for the C 1s peak. 80
3.15 (a) Photograph and (b) schematic of the XPS setup, part of the University of Bristol NanoESCA facility. 81
3.16 (a) Model of photoemission in UPS. (1) Electrons are photoexcited from the valence to conduction band, giving information on the density of states. (2) Electron transport to the surface causes some degree of relaxation. The UPS spectrum is obtained from the emitted electrons and can be affected by whether (3) the sample has a PEA, or (4) the sample has an NEA. Adapted from Bandis and Pate.[10] (b) Example UPS spectrum from a He-I source, showing how work function, ϕ, and the difference between the Fermi level, E_F, and valence band maximum, E_{VBM}, positions are calculated. 82
3.17 Example LEED patterns that form from (a) a (1 × 1) structure, and (b) a (2 × 1) structure. 84
3.18 Photograph of the LEED setup, part of the University of Bristol NanoESCA facility. 84
3.19 (a) Photograph of the thermionic emission kit. (b) Photograph and (c) schematic of the interior of the chamber. 86
4.1 Example electrostatic potential taken perpendicular (in the *z*-direction) to the diamond slab. The smoothened potential allows more accurate determination of the average potential of the slab. 92
4.2 Variation of total enthalpy and computational time with (a) cut-off energy and (b) *k*-point size in *x* and *y* directions, using an H-terminated (100) diamond slab with 14 carbon layers. 93
4.3 Side and plan view of the bare (2 × 1) reconstructed diamond surface. The plan view shows possible high symmetry sites for surface adsorbates. HH, HB, T3 and T4 refer to the hexagon hole, hexagon bridge, third-tier carbon and fourth-tier carbon sites, respectively. 96
4.4 Minimum energy positions for (a)–(c) 0.25, 0.5 and 1 ML, respectively, of Al addition to the bare (100) diamond surface. Side and plan views are shown for each. C and Al atoms are shown in grey and yellow, respectively. 98
4.5 (a) Ether and (b) ketone arrangements of O-terminated (100) diamond. (c) Plan view showing the two high-symmetry positions for adsorption on the O-terminated surface. OP refers to the 4-coordinate oxygen pedestal sites and OB the 2-coordinate oxygen bridge sites. C and O atoms are shown in grey and red, respectively. 99
4.6 Minimum energy positions for (a)–(c) 0.25, 0.5 and 1 ML, respectively, of Al addition to the O-terminated (100) diamond surface. Side and plan views are shown for each. C, O and Al atoms are shown in grey, red and yellow, respectively. 102
4.7 (a) Half-ML N-termination is a combination of N and C-H within a (2 × 1) dimer, and (b) full-ML N-termination involves replacement of both carbon atoms with nitrogen in the surface dimer. (c) Plan views for both half- and full-ML terminations. C, N and H atoms are shown in grey, blue and white, respectively. 103

4.8 Minimum energy positions for (a)–(c) 0.25, 0.5 and 1 ML Al addition to the N-terminated (100) diamond surface. C, N and Al atoms are shown in grey, blue and yellow, respectively. 104
4.9 PDOS spectra evaluated for (a) the bare diamond surface, (b) O-terminated diamond surface with ether configuration and (c) full-monolayer N-terminated diamond surface. 105
4.10 PDOS evaluated for (a)–(c) 0.25, 0.5 and 1 ML Al coverage, respectively, on the bare (100) diamond surface. These are the lowest energy structures from Table 4.2. 106
4.11 PDOS evaluated for (a)–(c) 0.25, 0.5 and 1 ML Al coverage, respectively, on the O-terminated (100) diamond surface. These are the lowest energy structures from Table 4.3. 107
4.12 PDOS evaluated for (a)–(c) 0.25, 0.5 and 1 ML Al coverage, respectively on the N-terminated (100) diamond surface. These are the lowest energy structures from Table 4.4. 108
4.13 The (2 × 4) supercell of the ketone O-terminated diamond surface. Sites marked A–H in the plan view indicate the possible Al adsorption sites that were considered. C and O atoms are shown in grey and red, respectively. 109
4.14 (a) The (2 × 1) reconstructed (111) surface. The plan view shows the positions of the upper and lower Pandey chain. (b) The (1 × 1) (111) surface. The T1, T2 and T4 sites are located above the first, second and fourth-tier carbon atoms, respectively. 112
4.15 Lowest energy adsorption sites for Al addition to the (2 × 1) (111) bare surface. (a)–(c) represent the lowest energy structures taken from Table 4.7 for 0.25, 0.5 and 1 ML Al coverage, respectively. Side and plan views are shown for each. C and Al atoms are shown in grey and yellow, respectively. 114
4.16 Lowest energy adsorption sites for Al addition to the (1 × 1) bare (111) diamond surface. (a)–(c) represent the lowest energy structures taken from Table 4.7 for 0.25, 0.5 and 1 ML Al coverage, respectively. Side and plan views are shown for each. C and Al atoms are shown in grey and yellow, respectively. 114
4.17 Adsorption sites to the (2 × 1) O-terminated (111) diamond surfaces. (a)–(b) Side views of the half-oxidised ether and fully oxidised ketone surfaces, respectively. (c) Plan view of the ether and ketone surfaces. U and L sites are located in high-symmetry positions above the upper and lower Pandey chains, respectively. C and O atoms are shown in grey and red, respectively. 116
4.18 Side and plan view of (1 × 1) O-terminated (111) diamond surface. Sites for addition are shown in the plan view. T2 and T4 sites are located above the second and fourth-tier carbon, respectively. C and O atoms are shown in grey and red, respectively. 116
4.19 Lowest energy adsorption sites for Al addition to the (2 × 1) ketone O-terminated (111) diamond surface. (a)–(c) represent the lowest-energy structures taken from Table 4.8 for 0.25, 0.5 and 1 ML Al coverage, respectively. Side and plan views are shown for each. C, O and Al atoms are shown in grey, red and yellow, respectively. 118

4.20 Lowest-energy adsorption sites for Al addition to the (2 × 1) ether O-terminated (111) diamond surface. (a)–(b) represent the only stable structures found for 0.25 and 0.5 ML Al coverage, respectively. No stable structure was found for 1 ML coverage. Side and plan views are shown for each. C, O and Al atoms are shown in grey, red and yellow, respectively..119
4.21 Lowest-energy adsorption sites for Al addition to the (1 × 1) O-terminated (111) diamond surface. (a)–(c) represent the lowest energy structures taken from Table 4.8 for 0.25, 0.5 and 1 ML Al coverage, respectively. Side and plan views are shown for each. C, O and Al atoms are shown in grey, red and yellow, respectively.....119
4.22 Side and plan view of the clean N-terminated (111) diamond surface. C and N atoms are shown in grey and blue, respectively. 120
4.23 PDOS spectra of adsorbate-free (a) bare, (b) oxygen (ether) and (c) oxygen (ketone) (111) diamond surfaces. 121
4.24 PDOS spectra for the Al-adsorbed bare (111) diamond surface. (a)–(b), (c)–(d) and (e)–(f) are 0.25, 0.5 and 1 ML, respectively, with the left column representing lowest energy (2 × 1) structures and the right column representing lowest energy (1 × 1) structures from Table 4.7. 122
4.25 PDOS spectra for the Al-adsorbed fully O-terminated (111) diamond surface. (a)–(b), (c)–(d) and (e)–(f) are 0.25, 0.5 and 1 ML, respectively, with the left column representing lowest energy (2 × 1) structures and the right column representing lowest energy (1 × 1) structures from Table 4.8. 124
4.26 PDOS spectra for the Al-adsorbed partially O-terminated (ether) (111) diamond surface. (a) and (b) are 0.25 and 0.5 ML coverages, respectively. 125
5.1 (a) Raman spectra (514 nm) of single-crystal diamond samples with a BDD epitaxial layer. The spectrum for the (111) sample is offset for clarity. (b)–(c) SEM images of the (100) and (111) diamond surfaces, respectively. ..134
5.2 Contact angle of water on typical single crystal diamond sample with (a) H-termination, and (b) O-termination. 135
5.3 Contact angle measurements for (a) plasma, (b) UV/ozone, and (c) acid treatment show the decrease in contact angle from a previously hydrogenated diamond surface. 136
5.4 XPS spectra of the C 1s peak for (a) H-terminated (100) diamond, and (b)–(d) O-terminated (100) diamond using (b) UV/ozone, (c) plasma, and (d) acid oxidation methods. The fitted peak numbers refer to those in Table 5.2. 139
5.5 XPS spectra of the O 1s peak for O-terminated (100) diamond using (a) UV/ozone, (b) plasma and (c) acid oxidation methods. A two-component peak fitting procedure was used, with the peak labels the same as in Table 5.3. 140
5.6 XPS spectra of the O 1s peak for O-terminated (100) diamond using (a) UV/ozone, (b) plasma and (c) acid oxidation methods. A three-component peak fitting was used, as detailed in Table 5.4. 141
5.7 The C-O/C=O bond ratios of different oxidation methods from C 1s and O 1s peaks in XPS spectra. The O 1s spectra were either fitted using two or three components. 142

5.8 FTIR-ATR spectra for different O-termination methods on (100) diamond. 143
5.9 XPS spectra of the C 1s peak for (a) H-terminated (111) diamond, and (b)–(d) O-terminated (111) diamond using (b) UV/ozone, (c) plasma, and (d) acid oxidation methods. Fitted peak numbers correspond to those in Table 5.2. 144
5.10 XPS spectra of the O 1s peak for O-terminated (111) diamond using (a) UV/ozone, (b) plasma and (c) acid oxidation methods. A two-component peak fitting was used. Fitted peak numbers correspond to those in Table 5.3. 145
5.11 XPS spectra of the O 1s peak for O-terminated (111) diamond using (a) UV/ozone, (b) plasma and (c) acid oxidation methods. A three-component peak fitting was used. Fitted peak numbers correspond to those in Table 5.4. 146
5.12 The C-O/C=O bond ratios of different oxidation methods from C 1s and O 1s peaks in XPS spectra. The O 1s spectra were fitted using either two or three components. 147
5.13 LEED patterns of (a) hydrogen-terminated and (b) oxygen-terminated (100) diamond. The electron beam energy was 180 eV for both. 148
5.14 LEED patterns of (a) hydrogen-terminated and (b) oxygen-terminated (111) diamond. The electron beam energy was 190 eV for (a) and 120 eV for (b) 149
5.15 Colour-coded work function maps of (a) H- and (b) O-terminated (100) diamond. 150
5.16 UPS spectra of H- and O-terminated (100) diamond. Inset shows a magnified view of the VBM energy relative to Fermi energy. 151
5.17 Colour-coded work function maps of (a) H- and (b) O-terminated (111) diamond. 152
5.18 UPS spectra of H- and O-terminated (111) diamond. Inset shows a magnified view of the VBM energy relative to Fermi energy. 153
6.1 Two different experimental approaches have been used to fabricate aluminium-oxygen-terminated diamond. (a) The thick-film method deposits a thick metal layer onto O-terminated diamond, and excess metal (*i.e*. metal atoms that are not chemically bonded to the oxygenated surface) is selectively removed. (b) The thin-film method deposits a thin metal layer that can be 'activated' by thermal annealing. Adapted from O'Donnell *et al*.[1] 159
6.2 SEM images showing cross-sections of (a) BDD grown on Si by hot filament CVD, and (b) NDD grown on Si by microwave plasma CVD. 160
6.3 Raman spectrum (514 nm) of a BDD thin film on an Si substrate. 161
6.4 SEM images of (a) O-terminated diamond, (b) after 20 nm Al deposition, and (c) after HCl treatment. 162
6.5 XPS spectra of the Al 2p peak for polycrystalline AlO-terminated BDD prepared by the thick-film process. (a) No annealing was performed and (b) a 300 °C anneal was performed for one hour after deposition. 163
6.6 XPS spectra of (a)–(b) C 1s, (c)–(d) O 1s, and (e)–(f) Al 2p peaks at different annealing temperatures for thick-film-prepared AlO-terminated diamond. (a), (c), (e) are from the (100) surface, and (b), (d), (f) are from the (111) surface. 165

6.7 Atomic percentages of O and Al at different annealing temperatures for thick-film-prepared AlO-terminated (a) (100) and (b) (111) diamond surfaces. 166
6.8 Colour-coded work function maps of AlO-terminated diamond prepared by the thick-film procedure, after annealing at (a)–(b) 300 °C, (c)–(d) 600 °C and (e)–(f) 800 °C. (a), (c) and (e) show the (100) surface and (b), (d) and (f) show the (111) surface. 167
6.9 UPS spectra acquired after a 300 °C anneal for AlO-terminated (100) and (111) single-crystal diamond prepared by the thick-film procedure. Inset shows a magnified view of the VBM energy relative to Fermi energy. 169
6.10 XPS spectra of (a)–(b) C 1s, (c)–(d) O 1s, and (e)–(f) Al 2p peaks at different annealing temperatures for ALD-prepared AlO-terminated diamond. (a), (c), (e) are from the UV/ozone-oxidised sample, and (b), (d), (f) are from the ALD-oxidised sample. 170
6.11 Atomic percentages of O and Al at different annealing temperatures for ALD-prepared AlO-terminated (100) diamond, using (a) UV/ozone and (b) ALD oxidation methods. 172
6.12 Colour-coded work function maps acquired after a 300 °C anneal for AlO-terminated (100) diamond prepared by the ALD procedure, using (a) UV/ozone and (b) ALD oxidation methods. 172
6.13 UPS spectra acquired after a 300 °C anneal for AlO-terminated (100) single-crystal diamond prepared by the ALD procedure, using UV/ozone or ALD as the oxidation method. Inset shows a magnified view of the VBM energy relative to Fermi energy. 173
6.14 XPS spectra of (a)–(b) C 1s, (c)–(d) O 1s, and (e)–(f) Al 2p peaks at different annealing temperatures for ALD-prepared AlO-terminated diamond. (a), (c), (e) are from the (100) surface, and (b), (d), (f) are from the (111) surface. 174
6.15 Atomic percentages of O and Al at different annealing temperatures for (a) (100) and (b) (111) surfaces. 175
6.16 (a)–(c) Colour-coded work function maps of AlO-terminated (111) diamond prepared with the ALD procedure, after annealing at 300 °C, 600 °C and 800 °C, respectively. 176
6.17 UPS spectra of AlO-terminated (111) diamond prepared with the ALD procedure. Inset shows a magnified view of the VBM energy relative to Fermi energy. 177
6.18 XPS spectra of (a)–(b) C 1s, (c)–(d) O 1s, and (e)–(f) Al 2p peaks at different annealing temperatures for AlO-terminated diamond prepared by electron-beam evaporation. (a), (c), (e) are from the (100) surface, and (b), (d), (f) are from the (111) surface. 179
6.19 Atomic percentages of O and Al for AlO-terminated (a) (100) and (b) (111) diamond prepared by electron-beam evaporation. 180
6.20 Colour-coded work function maps of AlO-terminated diamond prepared by electron-beam evaporation, at annealing temperatures of (a)–(b) 300 °C, (c)–(d) 600 °C and (e)–(f) 800 °C. (a), (c) and (e) are for the (100) surface and (b), (d) and (f) are for the (111) surface. 181
6.21 UPS spectra of AlO-terminated (a) (100) and (b) (111) diamond prepared by electron-beam evaporation. Inset shows a magnified view of the VBM energy relative to Fermi energy. 183

6.22 LEED patterns for AlO-terminated (a) (100) and (b) (111) diamond. The electron beam energy was 170 eV for both. 184
6.23 Raman spectrum of an NDD thin film on a Mo substrate. 185
6.24 SEM image of an NDD thin film. 185
6.25 Change in thermionic emission current with temperature from an H-terminated NDD thin film. 186
6.26 XPS spectra of the (a) C 1s, (b) O 1s, and (c) Al 2p peaks for AlO-terminated NDD thin films prepared using thick-film, ALD and electron-beam evaporation procedures. 187
6.27 Change in thermionic emission current with temperature for AlO-terminated NDD thin films. 188

Chapter 1 – Introduction

1.1 Overview of Diamond

1.1.1 The Allotropes of Carbon

Carbon is a highly abundant element in the first row of group 14 of the periodic table. It has two core and four valence electrons with configuration $1s^2 2s^2 2p^2$. Carbon can form chemical bonds with other carbon atoms and with many other elements, ranging from metals to metalloids to non-metals, making it a particularly versatile element.

Elemental carbon can form a number of different allotropes. Figure 1.1 shows the different crystal structures of the two primary bulk carbon allotropes, diamond and graphite. In diamond, carbon atoms arrange tetrahedrally, forming the face-centred cubic crystal structure. The 2*s* and 2*p* orbitals are fully hybridised, such that each atom has four sp^3-hybridised σ-bonds. By contrast, in graphite the carbons are arranged into layers of hexagonal sheets. Each atom has a trigonal planar geometry with three sp^2-hybridised σ-bonds in a plane and one orthogonal *p*-orbital. Electrons in these *p*-orbitals delocalise to give a conjugated π-bonded system, which allows conduction along the plane. Graphite layers are held together only by van der Waals forces so can slide over each other with relative ease.

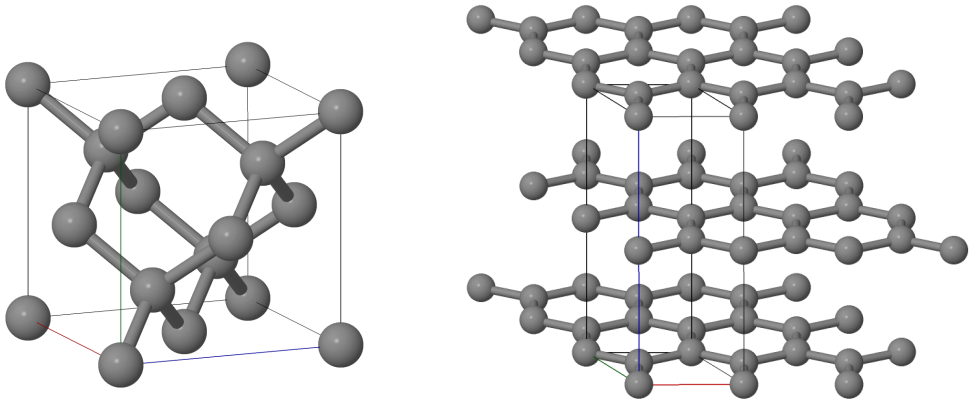

Figure 1.1: The crystal structures of (a) diamond and (b) graphite.

Under ambient conditions, graphite is the thermodynamically favoured allotrope of carbon. Diamond is, nevertheless, extremely stable as there is a significant energy barrier for conversion to graphite. The phase diagram of carbon is given in Figure 1.2. As diamond is denser than graphite, only at high pressures is the formation of diamond thermodynamically favoured.

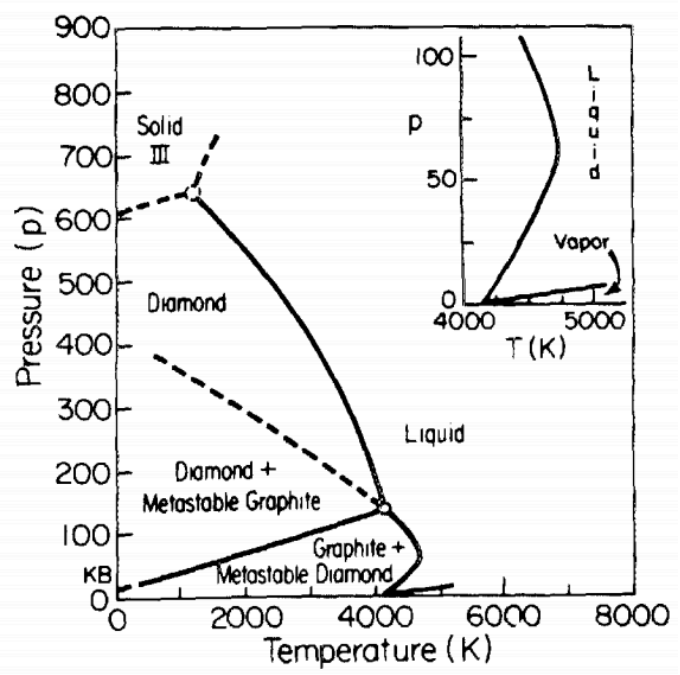

Figure 1.2: The simplified phase diagram of carbon from Steinbeck *et al*.[1]

There are other bulk carbon allotropes, for instance sp^2-hybridised glassy carbon and sp^3-hybridised lonsdaleite.[2,3] Amorphous carbon and diamond-like carbon are allotropes that contain a mixture of sp^2- and sp^3-hybridised carbon atoms, and have only short-range order.[4]

There are also numerous nanoscale allotropes of carbon. A single layer of graphite, known as graphene, has been the subject of considerable recent interest due to its unique combination of properties including strength, flexibility and electrical conductivity.[5] Other notable nanoscale allotropes include nanotubes and fullerenes, where carbon atoms form tubular or spherical structures.[6]

1.1.2 Properties of Diamond

Diamond is well known to possess many exceptional properties, some of which are listed in Table 1.1. It is one of the hardest materials, with a rating of 10 on the Mohs scale, the highest of any natural mineral. This makes diamond a desirable material for cutting and abrasion applications.

The large band gap makes diamond optically transparent to much of the electromagnetic spectrum for wavelengths longer than 227 nm. As a gemstone, diamond is traditionally colourless, but natural diamonds may show a range of colours originating from impurities such as nitrogen or boron within the crystal structure. The wide band gap makes diamond a desirable material in applications such as optics for IR windows[7] and as a deep-UV light-emitting diode.[8] As diamond is resistant to radiation damage, it is also being used in high-energy particle detectors.[9]

Table 1.1: Some of the intrinsic properties of diamond.[10–13]

Property	Value
Hardness (GPa)	90
Band Gap (eV)	5.47
Dielectric Constant	5.7
Thermal Conductivity at 300 K (W cm^{-1} K^{-1})	22
Electron mobility (cm^2 V^{-1} s^{-1})	4500
Hole mobility (cm^2 V^{-1} s^{-1})	3800
Carrier Saturation Velocity (cm s^{-1})	10^7
Breakdown Field (MV cm^{-1})	10

Diamond shows great promise as a material for next-generation electronic devices, alongside other semiconductors such as SiC, GaAs and GaN.[14] The wide band gap of diamond is advantageous, as this enables higher device temperatures, powers or frequencies to be attained before intrinsic breakdown occurs, compared to silicon-based devices. Diamond also benefits from high electron and hole mobilities. Different figures of merit, such as those of Baliga, Keyes, and Johnson, all rank diamond highest when compared to other semiconductors for future electronic device applications.[11] The high thermal

conductivity of diamond is also of interest for heat management such as in GaN power devices.[15]

In addition to the above properties, diamond is resistant to chemical degradation, including from acids and bases, and oxidises in air only above 600 °C.[16] This lack of reactivity makes diamond and nanodiamond biologically compatible, which is of interest for a variety of medicinal applications, such as drug delivery and imaging.[17]

1.1.3 Natural Diamond

Diamond forms naturally within the Earth's mantle. Conditions for diamond growth occur approximately 150 km beneath the surface, where diamonds can precipitate over millions of years from molten rock at high pressures and high temperatures. Natural diamonds can then be uplifted to the Earth's surface through volcanic activity. Diamond was first discovered in India in approximately the 4th century BC. Deposits were subsequently found in Brazil in the 1700's and, notably, in southern Africa in the 1800's. Natural diamond is now mined in many locations worldwide.[18]

Further sources of natural diamond have extra-terrestrial origin. Nanocrystalline diamond can be found in meteor craters, converted from graphite by the intense heat and pressure briefly experienced during impact.[19] Nanodiamonds are also observed to make up a small amount of interstellar matter.[20]

1.2 Synthetic Diamond

Due to the attractive qualities of diamond, and because of the scarcity and cost of high-quality natural diamond, research has been underway since the 1950's to produce it synthetically. Many companies now produce and sell synthetic diamonds, made using one of the following synthesis methods.

1.2.1 High Pressure High Temperature

The high pressure, high temperature (HPHT) synthesis involves a growth process that replicates the conditions for natural diamond formation within the Earth. Using a hydraulic press and anvil system, a high quality carbon source is

dissolved in molten metal at around 1300–1400 °C and 5–6 GPa.[21] The diamond precipitates onto a seed crystal and can be grown to several carats in weight.

The HPHT growth method can produce high quality single crystal diamond of gemstone size with several days of growth. However, the diamond may be yellow from incorporation of ambient nitrogen or otherwise coloured from impurities in the solution, so most HPHT diamonds are unsuitable for gemstones. Instead, they are used as 'industrial' diamonds for cutting and abrasion applications.[10]

1.2.2 Chemical Vapour Deposition

The chemical vapour deposition (CVD) method grows a diamond film atom-by-atom upon a substrate. Gases are flowed into a reactor kept below atmospheric pressure (10–200 Torr), dissociate into radical species, and react with the surface to grow diamond. Methane is often chosen as the carbon feedstock. Hydrogen gas is used alongside the carbon source because atomic hydrogen can cap the radical surface, and preferentially etches graphite rather than diamond.[22] Typically, ~1% carbon-containing gas in hydrogen is used to ensure high-quality diamond is grown. A small amount of oxygen may also be added, as it can enhance growth rates and improve crystallinity.[23]

The substrate is heated to high temperatures during diamond deposition (800–1000 °C). Substrates need a similar lattice constant for epitaxial growth of diamond. They also need a similar coefficient of thermal expansion to that of diamond, to prevent delamination of the diamond thin film upon cooling as a result of lattice contraction. Commonly used substrates include diamond itself, silicon, tungsten, tungsten carbide, and molybdenum.

There are a number of gas dissociation methods. One is hot filament CVD (Figure 1.3(a)), where a current is passed through a number of filament wires to heat them above 1900 °C.[24] The filament material can be a metal such as tungsten, tantalum or rhenium, as these metals have very high melting points. The choice of filament will depend on cost and durability.

Another method is microwave plasma CVD (Figure 1.3(b)). Microwave radiation (usually 2.45 GHz) is used to form a plasma from the process gases. Microwaves are tuned to give a stationary plasma localised at a node just above where the substrate is positioned. The gas pressure and microwave power affect

the plasma temperature. Microwave plasma reactors are usually run at 1–5 kW. The growth process is significantly faster than hot filament CVD, and can be in excess of 10 μm h^{-1}.[10]

Additional gas dissociation methods include arc-jet plasmas and combustion flame plasmas,[24,25] but are beyond the scope of this thesis so will not be discussed here.

CVD methods are commonly used as they allow for fine control over crystal size, and with additional input gases, dopants can be controllably introduced. Homoepitaxial CVD synthesis on a single-crystal diamond substrate will yield single-crystal diamond. The substrate dimensions can reach 2 inches through the use of mosaic wafers.[26] Heteroepitaxial CVD diamond films tend to be polycrystalline, although single-crystal diamond can also be grown onto Ir-based substrates.[26]

Unoptimised reaction conditions can result in nanocrystalline or ultrananocrystalline diamond (UNCD) films that have a larger sp^2 graphitic content. While these films do not have the properties of bulk diamond, they are sometimes desired, for example for producing more conductive films.

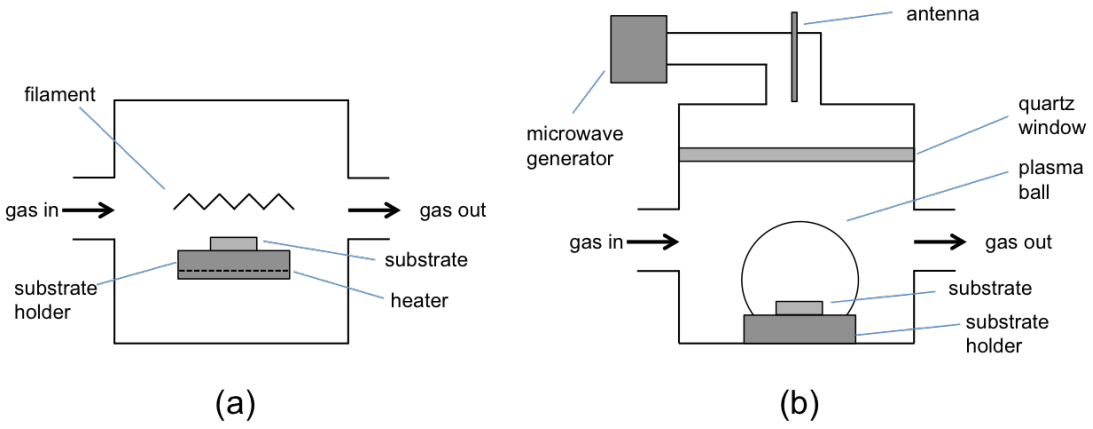

Figure 1.3: CVD reactor designs. (a) Hot filament CVD dissociates process gases with a heated filament. (b) Linear antenna-style microwave plasma CVD uses an antenna to tune microwave radiation and form a plasma above the substrate. Adapted from May.[10]

1.2.3 Detonation Nanodiamond

The synthetic production of nanodiamonds involves replication of the natural formation conditions of diamond whereby large temperatures and pressures are

briefly experienced. This can be done using the HPHT synthesis method (see Section 1.2.1), or from a controlled explosion, known as 'detonation nanodiamond'. In this case, highly explosive organic compounds such as TNT or RDX are detonated in an oxygen-deficient closed container. Nanodiamonds with a size of ~5 nm can then be isolated from other products such as soot with a high yield.[27] The nanodiamonds can be made to form stable suspensions in different liquids through changes to their surface termination making them more or less hydrophobic.

1.3 Diamond as a Wide Band Gap Semiconductor

Materials are classified as metals, semiconductors or insulators based on their band structure. Metals have an energy band that is part-filled by electrons, and so electrons are easily able to move to unoccupied sites and hence travel through the material. For semiconductors and insulators there is an energy gap between the valence band, where (at absolute zero) electrons occupy all energy states, and the conduction band, where all energy states are unoccupied. Semiconductors and insulators both exhibit temperature-dependent conductivity proportional to the number of electrons energised into the conduction band. The intentional introduction of impurities, known as dopants, into semiconductors adds additional energy states within the band gap region. Only a small amount of energy is required for electrons to migrate either to or from these states and so with doped semiconductors there is a controlled conductive regime below the temperature where electrons are thermalised from the valence to conduction band.

Diamond is usually referred to as a wide band gap semiconductor as it possesses a band gap larger than most conventional semiconductors, but it is still possible to add dopants into diamond and so introduce states at various energies within the band gap.

1.3.1 Dopants

Dopants typically displace native atoms within the crystal lattice, and may have a different number of electrons than the atoms they displace. Positive or p-type dopants have fewer valence electrons than the atom they displace, and

consequently introduce empty electron acceptor states close to the valence band. With sufficient energy, electrons may occupy these states leaving behind holes that behave as positively charged quasiparticles that migrate within the valence band. By contrast, negative or n-type dopants have an additional valence electron and so are electron donors; they introduce occupied energy states within the band gap closer to the conduction band in energy. Electrons promoted from the donor state to the conduction band may then migrate. The Fermi level in a solid, which is analogous to the chemical potential for molecules, is located halfway between the valence band maximum (VBM) and conduction band minimum (CBM) for intrinsic semiconductors, and moves closer to the valence band with p-type doping and closer to the conduction band with n-type doping.

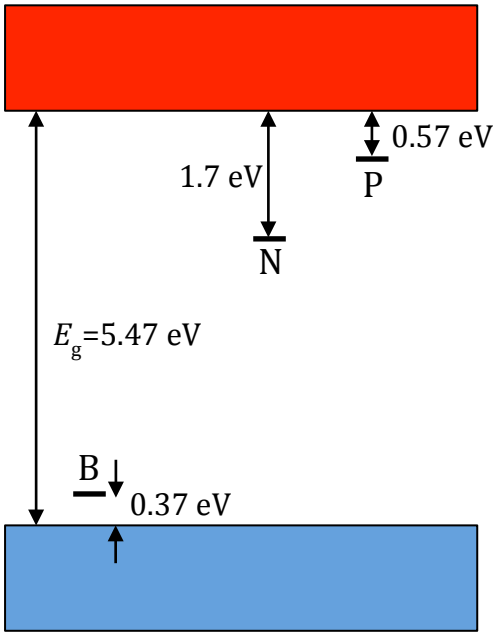

Figure 1.4: Band diagram of diamond showing the relative energies of P, N and B dopants. The valence band is shown in blue and the conduction band in red.

Figure 1.4 shows the band diagram for diamond with activation levels of common dopants. Boron is the most well-studied p-type dopant in diamond as it is a relatively shallow acceptor. It can also be incorporated easily during diamond growth, for instance by introducing a boron-containing gas in the CVD growth process. Increasing the boron concentration in the diamond above 10^{17} cm^{-3} changes the conduction regime from band conduction to nearest-

neighbour or variable-range hopping,[28] where charge carriers migrate across impurity centres due to the wavefunction overlap of adjacent centres.[29] At $\sim 10^{21}$ cm^{-3} metallic conduction dominates due to the creation of a partially-filled impurity band.[30]

In contrast to p-type dopants, shallow n-type dopants for diamond have proved hard to find due to the high energy of the conduction band. The relatively small size of the diamond lattice has restricted the number of dopants that can be incorporated. Nitrogen is an n-type dopant that incorporates into the diamond lattice quite readily, but the donor level is deep, 1.7 eV below the CBM.[31]

Phosphorus is the other well-studied n-type donor in diamond with a donor level 0.57 eV below the CBM. P-doped diamond still has poor conduction at room temperature, but mobilities significantly increase between 400–600 K.[32] Band conduction occurs at concentrations below $\sim 10^{19}$ cm^{-3} and changes to nearest-neighbour hopping at higher concentrations.[33] It has been a challenge to incorporate phosphorus into the diamond lattice as an n-type dopant, mainly due to the size of the atom, but also because phosphorus-vacancy complexes are stable but give unfavourable electronic characteristics.[34]

Other elements have been considered as potential n-type dopants with shallower donor states. Atom size prevents incorporation of the larger group 15 elements.[35] Of the group 16 elements, ion-implanted oxygen exhibits n-type conductivity with activation energy of $\sim$0.32 eV,[36] but the n-type behaviour is unstable with respect to temperature, and so annealing cannot repair lattice damage (and undesirable compensating vacancies) caused by the implantation method. Oxygen is not incorporated during CVD growth so diamond cannot be doped by this method.[37] Similarly, sulfur has been doped by ion implantation, with activation energy measured to be between 0.19 eV and 0.33 eV,[38] although the doping efficiency for sulfur is calculated to be small.[39]

Group I elements have also been considered. Computational studies have found lithium and sodium act as shallow donors in interstitial sites, with donor levels of 0.1 eV and 0.3 eV, respectively.[40] Lithium and sodium are expected to be acceptors in substitutional sites, however, resulting in charge compensation.[41] Lithium also appears to cluster in diamond, further complicating matters.[42]

Doping attempts involving Li have involved ion implantation, diffusion, addition during CVD diamond growth, and ^{10}B transmutation *via* neutron irradiation.[43,44] In ion-implanted or annealed Li-doped samples there is a low activation energy of 0.17–0.23 eV for conduction, albeit with high resistance, likely to be from variable-range hopping.[45]

Another route towards n-type diamond is the addition of two or more dopants together, known as co-doping. Eaton *et al.*[46] obtained n-type diamond with co-doped sulfur and boron at low B concentrations, later shown by Vaddiraju *et al.*[47] to have moved the Fermi level 0.8–1.9 eV above that of B-doped diamond. Theoretical co-doping studies have shown n-type behaviour in complexes such as N-B-N and H-P-H.[48] Larger combinations of dopants with low activation energies have also been proposed, including an Li + 4N complex[49] with 0.27 eV activation energy and an N + 4Si complex[50] with activation energy calculated as 0.09 eV, although this value has been disputed.[51] To form these co-doping complexes experimentally, a proposed approach is to form the donor-acceptor complex under diamond growth conditions,[52] or by in-diffusion of one dopant after growth.[49]

1.3.2 Band Bending

Band bending is the curving of energy states due to the alignment of two different Fermi levels, for example at a heterojunction between two different materials, within a material where there is a discontinuity of dopant type, or at a surface. In each case, charge migration across the interfacial region causes the Fermi levels to align. Electrons migrate to available lower-energy states, causing an upward bend of the band at the interface, while holes migrate to available higher-energy states, causing a downward band-bending effect.

At the surface, the Fermi level may differ from bulk due to surface states, which can arise from surface reconstruction or surface termination. For an intrinsic material, termination with an electropositive species relative to the bulk material will give downwards band bending at the surface, while termination with electronegative species will give upwards band bending. If the bulk material is doped, this can also affect the band-bending direction due to the change in energy of the bulk Fermi level. A material containing p-type dopants will show

downward band bending at the surface, while one with n-type dopants will show upward band bending.

1.3.3 Negative Electron Affinity

Negative electron affinity (NEA) describes the unusual situation where the CBM of a semiconductor material is higher in energy than the vacuum energy, which is defined as the energy of an isolated electron at rest an infinite distance away. For most materials, electron emission in vacuum will only occur by overcoming the work function, ϕ, defined as the difference between the Fermi level and vacuum energy. However, with NEA, it is possible for electrons located within the conduction band to migrate to the surface where there is then virtually no barrier for electron emission. An excitation process is still required to energise electrons into the conduction band.

The electron affinity (EA) of a material can be somewhat tailored by altering how the surface is terminated. Selective termination with atoms or groups of atoms that are electropositive relative to the bulk material will form an electric dipole perpendicular to the surface with positive charge outermost, raising the conduction band energy relative to the vacuum energy. If the entire CBM is above the vacuum level, this is known as 'true' NEA. Alternatively, it may be the case that large downwards band bending at the surface originating from the surface termination results in the bulk CBM being higher in energy than the vacuum energy while the surface CBM is below the vacuum energy. In this situation, electrons at the surface have a positive electron affinity (PEA) but bulk electrons with NEA can tunnel into vacuum. This is known as an 'effective' NEA, and has reduced emission compared to a 'true' NEA surface. Figure 1.5 illustrates the difference between PEA, true NEA and effective NEA.

A number of semiconductors including Si,[53] GaAs,[54] BN,[55] and AlN[56] can form an effective NEA when the highly electropositive element caesium is adsorbed to the surface. Diamond is relatively unique as a semiconductor as the conduction band lies relatively high in energy. Therefore, a number of elements that have electronegativity less than that of carbon give diamond an NEA. This includes many metals, metalloids and the hydrogen-terminated surface. Also, the NEA from diamond can be a true NEA.[57]

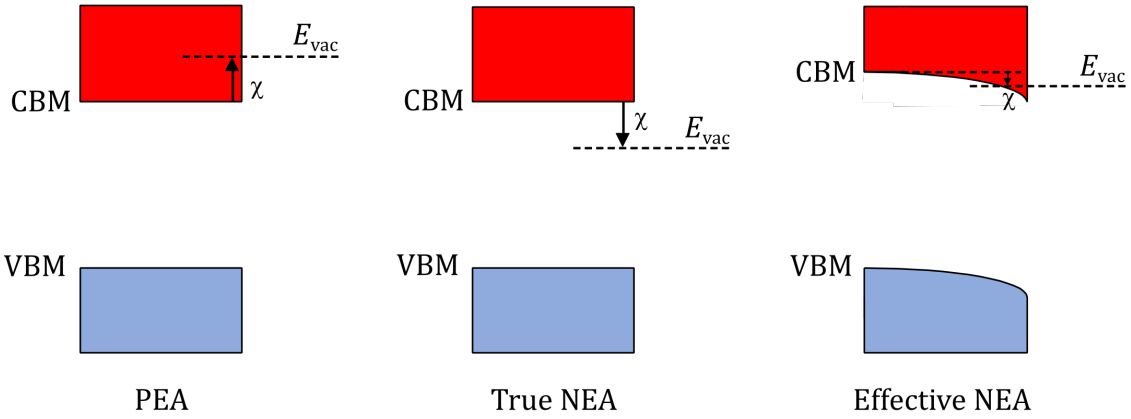

Figure 1.5: Relative positions of the conduction band minimum, CBM, vacuum energy, E_{vac}, and the electron affinity, χ, for a material with positive electron affinity (PEA), 'true' negative electron affinity (NEA) and 'effective' NEA.

1.4 Electron Emission

Electrons may be emitted from a material when subjected to particle impact, high temperatures or electric fields. Photoemission, secondary emission and thermionic emission (emission of electrons from photon absorption, electron impact and high temperatures, respectively) raise an electron to a higher energy state in order to overcome the surface energy barrier.[58] By contrast, with field emission the application of an electric field reduces the height and size of the emissive barrier, and the emission pathway involves electron tunnelling from the valence band.[58]

Good electron emitters can conduct electrons (and so replenish emitted electrons), and have a low energy barrier for emission. It is common for electron emission devices to be housed in high vacuum environments; this prevents contamination of the emissive surface and allows electrons to travel unimpeded by any gaseous species. In many applications, the cathode (emitter) and anode (collector) spacing is kept low such that the distance for the electron to travel is less than the mean free path of the electron.

1.4.1 Thermionic Emission

Thermionic emission is governed by the Richardson-Dushman equation.[59,60] Shown in Equation 1.1, the emission current density, J, depends upon cathode temperature, T, cathode work function, ϕ, the Boltzmann constant, k, and the

Richardson constant, A. The work function is assumed to be constant but in fact it increases linearly with temperature. The difference in a material's work function between room temperature and typical thermionic temperatures (1000–2000 °C) is small, less than 0.1 eV.[61]

The Richardson constant was theoretically derived for metals following Equation 1.2,[61,62] where m and e are the mass and charge of an electron, respectively, and h is the Planck constant. Experimentally determined values of the Richardson constant can significantly deviate from this value, however, particularly for non-metals. This is due to the inherent assumptions of the Richardson model,[63] for example that the work function and temperature of the cathode are uniform, and that electron energies follow a Maxwell-Boltzmann distribution, which is only valid for metals at high temperatures.[64]

Recently, a non-equilibrium Green's function model has been used to describe thermionic emission behaviour.[64,65] Musho *et al.*[64] find that this model more accurately describes emission from diamond, including better predictions of the Richardson constant, the onset temperature for emission, and the change in emission regime with an NEA surface.

$$J(T) = AT^2 \exp\left(-\frac{\phi}{kT}\right) \tag{1.1}$$

$$A = 4\pi mk^2 e \,/\, h^3 = 120 \text{ A cm}^{-2} \text{ K}^{-2} \tag{1.2}$$

Thermionic emission can be utilised in a range of vacuum-based electronics, such as high-power amplifiers and magnetrons.[66] Thermionically-generated electrons can be the electron source in electron microscopes and X-ray generators.[67,68] Thermionic energy converters (TECs) can generate electricity from heat within a solid-state device containing no moving parts, and are discussed in more detail in the next section.

A list of various different cathode materials is given in Table 1.2. The Richardson-Dushman equation can be fitted to a plot of the emission current density change with temperature, yielding values of the Richardson constant and work function. Refractory metals and rare earth hexaborides are typically used

commercially.[67,69] Electropositive elements such as Ba or Cs may be added to reduce the work function.

Table 1.2: Properties of some common emitter materials.[68,70,71]

Material	Work Function (eV)	Richardson Constant (A cm^{-2} K^{-2})	Material	Work Function (eV)	Richardson Constant (A cm^{-2} K^{-2})
W	4.54	55–104	Rh	4.7	110
Mo	4.15	39	Cs on W	1.36	3.2
LaB_6	2.86	82	BaO	1.5	0.1
CeB_6	2.39	19	C nanotube	2	110–120

1.4.2 Thermionic Energy Converters

In a TEC device, the cathode is heated and emits electrons across a small vacuum region to be collected on a cooler anode. The anode and cathode are connected externally, and the current generated thermionically can be used to drive a load. A schematic diagram for a TEC is shown in Figure 1.6. Some of the emitted electrons will not have sufficient kinetic energy to be collected at the anode and will accumulate in the vacuum gap, resulting in a negatively charged region known as space charge.

Figure 1.7 shows the energies involved in the electron emission process. For emission to occur, electrons must gain energy exceeding the work function of the emitter, ϕ_{E}. The space-charge effect will form an additional energy barrier. The collector work function, ϕ_{C}, must be lower than ϕ_{E} to ensure a forward voltage is generated.

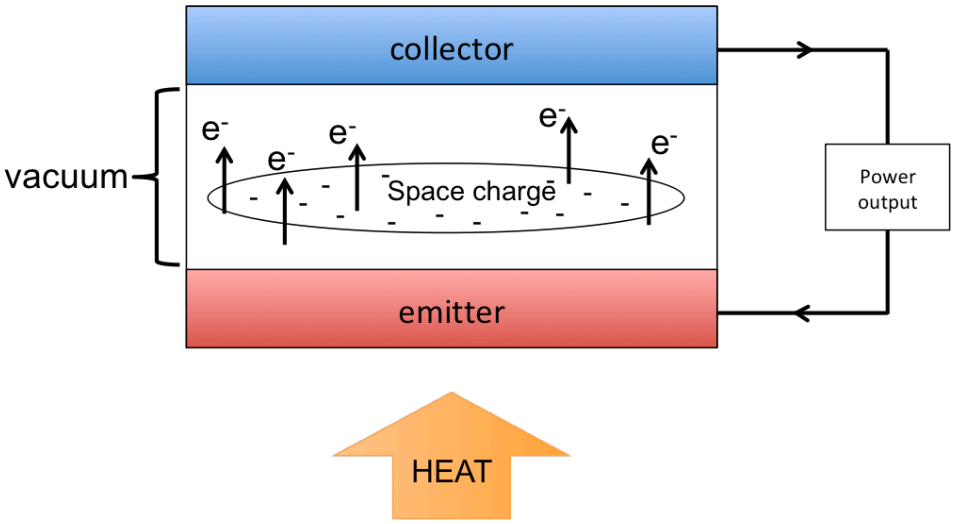

Figure 1.6: Schematic diagram for a TEC device.

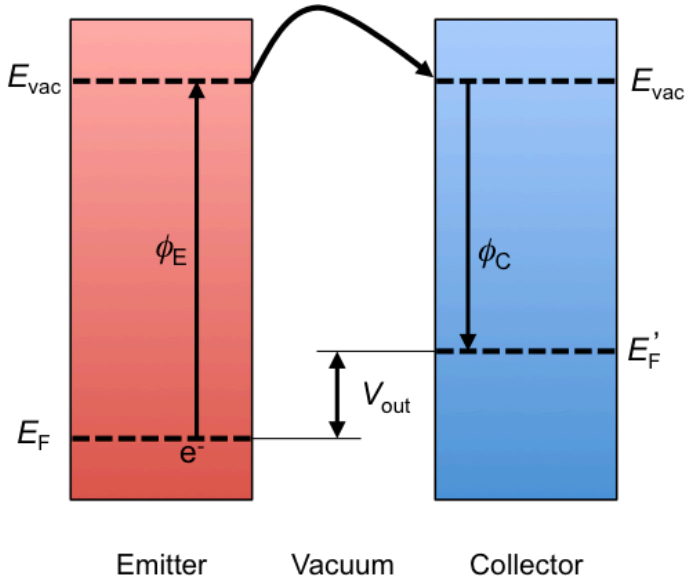

Figure 1.7: Energy diagram of a TEC. E_F and E_F' are the Fermi levels of the emitter and collector, respectively. ϕ_E and ϕ_C are the work functions of the emitter and collector, respectively. Electrons in the emitter must overcome the vacuum level, E_{vac}, and an additional energy barrier from space charge to reach the collector. V_{out} is the output voltage.

1.4.2.1 Efficiency and Power

As TECs are heat engines, the theoretical maximum efficiency is the Carnot efficiency:[72]

$$\eta = 1 - \frac{T_{cold}}{T_{hot}} \tag{1.3}$$

As one must also account for cooling losses through electron emission, the theoretical upper limit for efficiency of a TEC is 90% of the Carnot efficiency.[73] For a thermionic device with cathode at 1000 °C and anode at 25 °C the theoretical efficiency is calculated to be ~69%. This is considerably higher than the theoretical efficiency limit of a single-junction photovoltaic device (the Shockley-Queisser limit), for example, at 33.7%,[74,75] although it is possible for photovoltaic devices to surpass this limit by combining multiple different band gap materials into a multi-junction solar cell.[75]

In order to determine the maximum efficiency that can be reasonably expected for TECs, one should divide the useful output power by the total. The efficiency for a TEC has been expressed as:[73]

$$\eta = \frac{J_{\mathrm{E}}(V_{\mathrm{E}} - V_{\mathrm{C}} - V_{\mathrm{W}})}{R + H + J_{\mathrm{E}}(V_{\mathrm{E}} + 2kT_{\mathrm{E}})} \tag{1.4}$$

where J_{E} is the emission current density from the emitter, $V_{\mathrm{E}} - V_{\mathrm{C}}$ is the potential difference between the electrodes, V_{W} is the voltage loss from connection to a room-temperature load wire, R and H represent heat loss through black-body radiation and thermal conduction, respectively, k is the Boltzmann constant and T_{E} is the temperature of the emitter. This equation assumes no efficiency is lost from reverse current generation. The theoretical efficiency using an anode work function value of 1 eV can reach 30%, while a work function of 0.5 eV would allow 50% efficiency to become achievable.[61]

The power density of the device is obtained from the current density multiplied by the voltage, and can be expressed as:

$$P = AT^2 \exp\left(-\frac{\phi_{\mathrm{E}}}{kT}\right)(\phi_{\mathrm{E}} - \phi_{\mathrm{C}}) \tag{1.5}$$

The power density depends upon the difference between the emitter and collector work functions, and is maximised when $\frac{dP}{d\phi_{\mathrm{E}}} = 0$, which arises when $\phi_{\mathrm{E}} = \phi_{\mathrm{C}} + kT$.[76] As $kT \approx 0.1$ eV at thermionic temperatures, it is desirable for both emitter and collector work functions to be as small as possible. However, choosing to maximise power output will lower the efficiency; efficiencies are

greatest when the difference between emitter and collector work functions is ~0.5 eV.[61] Therefore, a compromise must be made between power output and efficiency based on energy requirements.

1.4.2.2 Design Considerations

TECs were originally designed with metal anodes and cathodes. A power density of around 1–6 W cm^{-2} could be achieved by heating the cathode to temperatures between 1000–2000 °C. The efficiency of these TEC devices was low, calculated to be up to 10–15%.[70,73,77,78] The limitation of the TEC efficiency was the work function of the emitter and collector. Metals typically have a work function of ~3–5 eV, which can be reduced to ~1.4–1.9 eV with the addition of a caesium layer.[61] Wide band gap, n-type semiconductor materials can show even lower work functions, so TECs using semiconductor electrodes have been the subject of recent research.

The space-charge barrier should also be as small as possible, so a few methods have been developed to minimise its effect. One method is simply to reduce the size of the vacuum region. The optimal distance is a few micrometres in size.[79] Below this, significant radiative heat can reach the anode, which may result in an undesirable reverse current.

Another method is to introduce a metal vapour that is easily ionised into M^+ ions into the vacuum region to neutralise the negative charge, as first shown by Langmuir.[80] Caesium vapour has often been used, and coatings of Cs on electrodes may also reduce work function.[76,81] Alternatively, the space-charge barrier can be partly bypassed by introducing a gas to act as a migration pathway for the electrons. An enhanced emission current has been shown by introducing methane or atomic hydrogen into the vacuum region as charge carriers.[82,83] The drawbacks of introducing gaseous species include higher complexity and the higher thermal conduction between the electrodes lowers the overall efficiency.[84]

Other methods that have been suggested to reduce the space-charge barrier include positioning an electron-permeable screen such as graphene between the emitter and collector to induce hole charges in the vacuum region,[85] or using a β-emitting collector material.[86]

1.4.2.3 Applications

One of the first applications of TECs was for powering spacecraft, using either solar or nuclear heat sources.[84,87] TECs with 5 kW power were developed by the Soviet Union and used for two missions in 1987, as part of the TOPAZ nuclear reactors.[84] More recently, TECs have been proposed for powering spacecraft involved in missions to the Sun or Mercury.[88]

TECs may be used in the future to scavenge waste heat in high-temperature processes. They could act as a topping cycle in fossil fuel or nuclear power plants to improve overall efficiency.[89,90] Use in automobiles and boilers has also been suggested.[84]

TECs could also offer a novel alternative means for generating renewable energy. Increasing renewable energy usage is crucial in order to satisfy increasing world energy demands, and to limit CO_2 emissions and so avoid drastic climate change.[91–93] Using TECs for renewable energy generation requires concentrating solar energy to generate enough heat for thermionic emission to occur. The principle designs for concentrating solar radiation are shown in Figure 1.8. Heliostat fields consist of an array of sunlight-tracking mirrors that concentrate solar energy on a central tower. This design has previously been used to heat water into steam and generate electricity with a turbine. Parabolic-dish reflectors are smaller in scale. The solar-tracking parabolic dish concentrates sunlight at the centre where the TEC is located. A third design is smaller in scale again, where a Fresnel lens concentrates sunlight on the TEC device. The predicted power outputs for these three designs are 5–200 MW, 1–100 kW and 1–1000 W, respectively, for predicted emitter temperatures of 500–1400 °C, 500–2000 °C and 400–1000 °C, respectively.[70] Both cost and efficiency would be important factors for determining commercial viability of these designs.

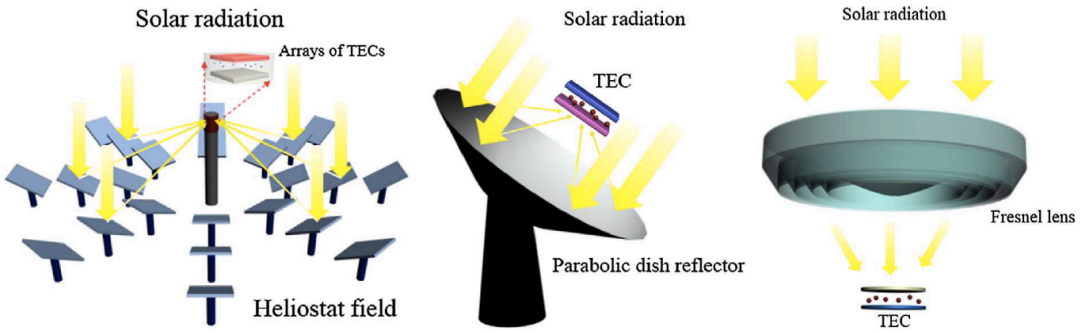

Figure 1.8: Different schemes for solar energy concentration. From Xiao *et al.*[70]

1.4.3 Photon-Enhanced Thermionic Emission

Photon-enhanced thermionic emission (PETE) is a newer concept where photon absorption and electron thermalisation are combined to increase electron emission in a device similar to a TEC. As shown in Figure 1.9, the two processes together increase the thermalised electron population within the conduction band of a p-type semiconductor. This creates an emission regime at a temperature below that of standard thermionic emission. A PETE device would be able to convert both solar heat and light into electricity from concentrated sunlight.

Schwede *et al.* first described the PETE process in 2010, and have demonstrated PETE using a caesiated GaN cathode[94] and later a caesiated GaAs/AlGaAs cathode.[95] They calculated theoretical efficiencies of 32% for 100× solar concentration, and 47% for 1000× concentration using a simple zero-dimensional model.[94] More complex models that account for additional effects such as recombination and electron transport generally predict more modest efficiencies.[96,97] The addition of a secondary thermal cycle can significantly improve PETE efficiency in all cases.[98] Segev *et al.*[99] and Xiao *et al.*[70] have both recently reviewed the progress of PETE devices.

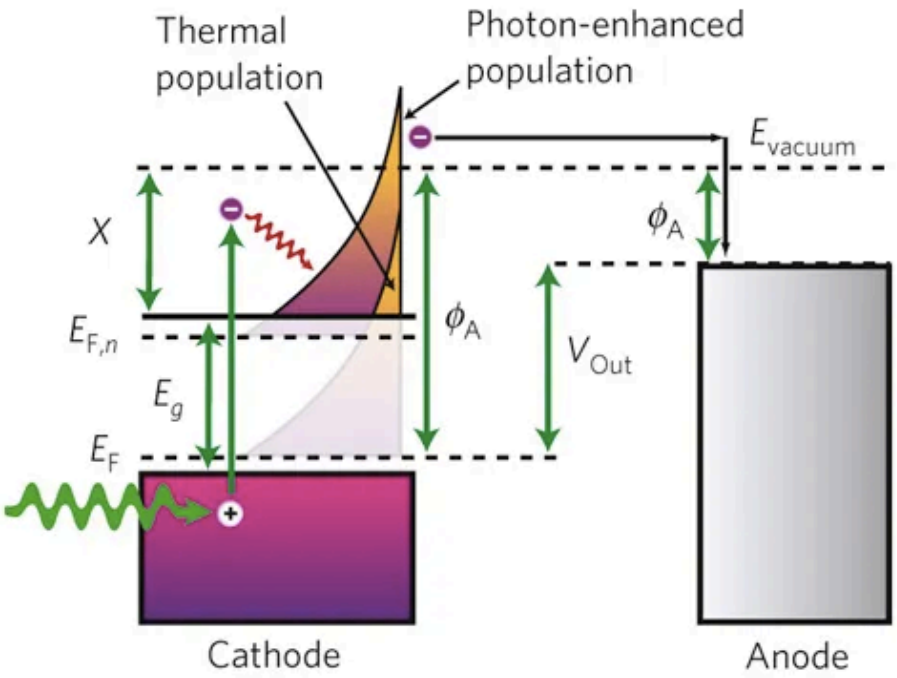

Figure 1.9: Schematic energy diagram for a PETE device. Electrons are energised into the conduction band of the cathode by photon absorption and by thermalization. From Schwede *et al*.[94]

1.4.4 Thermionic Emission from Diamond

Diamond has attracted considerable interest for use in electron emission devices. With an NEA, the population of thermalised electrons in the conduction band with energies greater than the vacuum energy is larger. Models of electron emission by Smith *et al.* find that an NEA cathode[100,101] or anode[102] outperforms an otherwise identical PEA surface. They attribute this to mitigation of space charge, and they find that NEA electrodes also have higher output power and increased device efficiency.

The work function of diamond is smallest if doped to be n-type. There will, however, be some degree of upwards band bending at the surface, creating a small additional energy barrier for emission. This barrier originates from charge transfer at the surface supressing electron emission,[103] so minimising this barrier is key to device optimisation.

Table 1.3 summarises a number of recent studies into thermionic emission from various H-terminated, N- or P-doped diamond cathodes. Large values of the Richardson constant as high as 70 A cm^{-2} K^{-2} have been obtained for N-doped diamond, but smaller values are found for P-doped diamond, with some values

many orders of magnitude smaller. This appears to correlate with the dopant concentration; a higher concentration gives a more conductive diamond film.

The work functions measured in these experiments incorporate the barrier from induced band bending. The dopant concentration correlates with the degree of band bending, but the emission current is greatest when the doping level is high. P-doped diamond shows the lowest work function, as low as 0.67 eV. This is one of the smallest values reported for any material. Considering the activation energy of the phosphorus dopant, it indicates that the upwards band bending effects are minimal.[61]

The choice of substrate also has an effect on electron emission properties. UNCD films grown on molybdenum, tungsten, and molybdenum/rhenium alloy show considerably different values for the Richardson constant.[62] The Mo/Re substrate had the highest Richardson constant, believed to be because this substrate was the only one that did not form a non-conductive carbide boundary layer between the substrate and the diamond film.

Based on the measured work function and Richardson constant values, the emission current density change with temperature can be calculated using the Richardson equation. For the most promising H-terminated diamond cathodes, the current density is predicted to be up to 30 A cm^{-2} at 1000 °C, roughly three orders of magnitude higher than the refractory metals or rare earth hexaborides listed in Table 1.2, and comparable to that of caesiated metal or carbon nanotube cathodes.

Table 1.3: Different studies of electron emission properties using an H-terminated diamond cathode.

Dopant	Crystal	Substrate	Concentration (cm^{-3})	Richardson Constant ($A\ cm^{-2}\ K^{-2}$)	Work Function (eV)	Ref.
N	UNCD	Mo	$\sim 10^{21}$	0.84	1.29	104
N	UNCD	metallic	-	1.33	1.67	83
N	UNCD	Mo	-	0.69	1.42	62
N	UNCD	W	-	1.19	1.39	62
N	UNCD	Mo/Re	-	3.67	1.40	62
N	Polycrystal	Mo	-	5.96	2.22	105
N	Polycrystal	Mo	4×10^{19}	0.1–10	1.5–1.9	106
N	Polycrystal	n-type Si	2.4×10^{20}	70	1.99	107
N	(100)	diamond	3.3×10^{19}	68	2.88	61
N	(100)	diamond	4×10^{19}	-	2.4	108
P	Polycrystal	metallic	$\sim 10^{18}$	1.0×10^{-5}	0.9	109
P	Polycrystal	Mo	5×10^{20}	15	2.3	110
P	(100)	diamond	$\sim 10^{17}$	2.3×10^{-7}	0.67	61
P	(100)	diamond	$\sim 10^{18}$	-	0.84	61
P	(111)	diamond	4.4×10^{18}	0.011	1.45	61

Diamond has also been considered for PETE devices. PETE requires photon absorption, so surface texturing can be used to make diamond optically opaque. Bellucci *et al.* have used an ultrashort pulsed laser treatment to increase light absorption to 98% of the solar spectrum.[111,112] Figure 1.10 shows a schematic for a diamond-based PETE device that has been fabricated. Solar absorption occurs at a surface-textured p-type layer while electrons are accumulated within the n-type layer. Graphitic microchannels introduced through the bulk (undoped) diamond improves conductivity between the layers, increasing the emission current density by ~4 orders of magnitude.[113]

PETE from H-terminated diamond was observed at 550 K in a polycrystalline undoped diamond sample.[114] Emission was attributed to electron activation from trap states. The Nemanich group have studied PETE using H-terminated N-doped diamond. They found enhanced emission from the diamond originating from photon absorption within a metallic or p-type Si substrate and electron

transport into the diamond film, consistent with the PETE model of emission.[115,116]

For a diamond-based TEC or PETE device, it would be optimal to use N-doped diamond as the cathode and P-doped diamond as the anode, until improvements over these n-type dopants become available. The former has shown higher emission current densities while the latter has the lower work function. A critical limiting factor in device design is currently the H-termination, as this is not stable at thermionic temperatures. The PETE regime is at lower temperatures but still enhances emission current in the thermionic regime. As will be discussed in the next chapter, a number of alternative terminations have been studied.

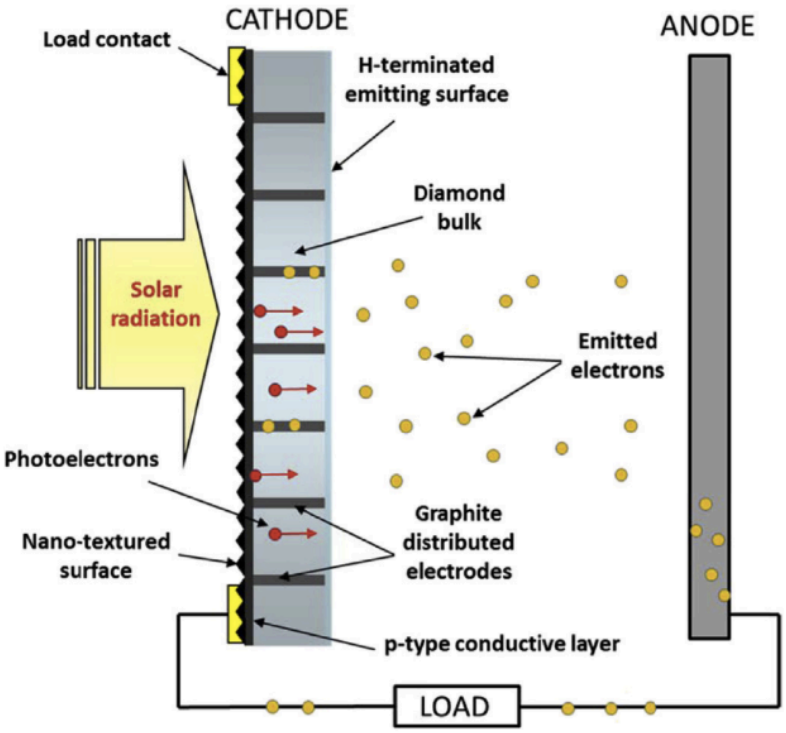

Figure 1.10: Schematic diagram of a diamond-based PETE device. From Girolami *et al.*[113]

1.5 Computational Chemistry

The rise in available computing power allows increasingly complex calculations to be performed. By modelling chemical systems, new insight can be gained into reactions or structures that may be too dangerous, costly, time-consuming or difficult to attempt experimentally. Thus, computational chemistry has proven

extremely useful to understand and predict the behaviour of materials. This section explains the underlying principles behind plane-wave density functional theory (DFT), a first principles method used in Chapter 4 of this thesis.

1.5.1 First Principles Modelling

First principles or *ab initio* methods use quantum mechanics to model chemical systems. The Schrödinger equation can determine allowed energies of an N-body system and the associated wavefunction, Ψ. Shown in Equation 1.6 is the non-relativistic time-independent Schrödinger equation; the allowed energies, E, are eigenvalues from applying the Hamiltonian operator, $\hat{H}$, to the wavefunction. The Hamiltonian, shown in Equation 1.7 in atomic units, has terms corresponding to (from left to right) the kinetic energy of the system, the electron-electron Coulombic interactions, the nuclear-electron Coulombic interactions and the nuclear-nuclear interactions. ∇^2 is the Laplacian, r and R are the positions of electrons (denoted i and j) and nuclei (denoted I and J), respectively, and Z is nuclear atomic number.

$$\hat{H}\Psi = E\Psi \tag{1.6}$$

$$\hat{H} = -\frac{1}{2}\nabla^2 + \frac{1}{2}\sum_{i\neq j}\frac{1}{|r_i - r_j|} - \sum_{i,I}\frac{Z_I}{|r_i - R_I|} + \frac{1}{2}\sum_{I\neq J}\frac{Z_I Z_J}{|R_I - R_J|} \tag{1.7}$$

Determining the ground state of a system with N electrons requires finding the minimum energy from the Schrödinger equation. With three spatial positions for each electron, there are $3N$ parameters to consider (excluding electron spin). Consequently, for systems containing many electrons, the Schrödinger equation cannot be solved directly as it becomes too computationally expensive. Computational methods therefore require approximations to be made to allow complex systems to be modelled.

1.5.2 Density Functional Theory

DFT is a widely used method for finding the ground state energy of a many-body system where the Hamiltonian is a functional of the electron density, and the electron density is a function of the three spatial coordinates. Like many other

methods, DFT first applies the Born-Oppenheimer approximation to decouple the electronic and nuclear Hamiltonians. The electrons can be treated as if they interact with stationary nuclei due to the large difference in mass between the two.

Two papers published in the 1960's were instrumental in the development of DFT. Hohenberg and Kohn[117] proved theorems that stated that: (1) the electron density is sufficient to describe the entire ground state of a system, and (2) the electron density obeys the same variational principle as a wavefunction, *i.e.* a solution to the Schrödinger equation will result in an energy equal or exceeding the true ground state energy.

Kohn and Sham[118] subsequently developed the mathematical basis for computing the expensive electron-electron interaction. A fictitious, non-interacting electron system is used, which has the same electron density as the true system. The Kohn-Sham equation resembles the electronic part of the Schrödinger equation, and can be expressed as:

$$\left(-\frac{1}{2}\nabla_i^2 + \int \frac{n(r')}{|r-r'|}dr' + v_{\text{ext}}(r) + v_{\text{xc}}(r)\right)\psi_i = \varepsilon_i\psi_i \qquad (1.8)$$

where ψ_i is a one-electron wavefunction, $n(r')$ is the electron density, $v_{\text{ext}}(r)$ is the external potential (from the nuclei), and $v_{\text{xc}}(r)$ is the exchange-correlation potential, to account for exchange and correlation effects in an interacting system. The latter term also includes kinetic energy differences between the interacting and non-interacting systems.[119] As the electron density is obtained from the sum of the square of the one-electron wavefunctions, the Kohn-Sham equation must be solved self-consistently; an assumed electron density is used to generate the one-electron wavefunctions, from which a new, improved electron density can be generated.

1.5.2.1 The Exchange-Correlation Functional

The exchange-correlation functional is unknown and must be approximated. The simplest approximation is the local density approximation (LDA) method, which can be written as:

$$E_{\mathrm{xc}}^{\mathrm{LDA}}[n] = \int n(r)\, \varepsilon_{\mathrm{xc}}(n(r))dr \tag{1.9}$$

where $\varepsilon_{\mathrm{xc}}$ is the exchange-correlation energy of a homogeneous electron gas for a particular electron density $n(r)$. The area around each calculated position is assumed to have the same density as that position, so this method is only acceptable when the density is largely uniform, only varying slowly with position.

The generalised gradient approximation (GGA) method goes one step further, by taking into account the rate of change of the electron density at each point of interest. This can be written as:

$$E_{\mathrm{xc}}^{\mathrm{GGA}}[n] = \int n(r)\varepsilon_{\mathrm{xc}}(n(r), \nabla n(r))dr \tag{1.10}$$

where $\nabla n(r)$ is the gradient of the electron density. There are a number of different GGAs, for example from Perdew and Wang (PW91), Perdew, Burke and Ernzerhof (PBE), and Wu and Cohen (WC).[120–122] Each GGA method calculates $\varepsilon_{\mathrm{xc}}$ by a slightly different approach, some using empirical data.

Hybrid functionals are a further group of exchange-correlation functionals that combine the exact exchange energy from Hartree-Fock (HF) theory with the exchange and correlation energy from DFT.[123] The HF fraction typically accounts for $\sim$25% of the exchange energy at a short range.[124] This semi-empirical combination addresses some shortcomings from DFT, such as underestimation of band gap values[125] and overestimation of electron delocalisation effects,[126] and thus hybrid functionals can, in general, predict material properties with greater accuracy. The drawback when using plane-wave DFT is that they are computationally expensive compared with the LDA and GGA functionals.

1.5.2.2 Basis Sets

Depending on the DFT code, single-electron wavefunctions will usually be expanded through plane-wave or atom-centred basis sets. The plane-wave basis set is a linear combination of plane waves:

$$\psi_k(r) = \sum_G^{|G|<G_{\max}} c_{k+G} \exp(i(k+G)\cdot r) \tag{1.11}$$

where k is a wavevector, G is a reciprocal-lattice vector perpendicular to the plane wave, r is the position and c is a coefficient. A finite number of G vectors are included, thereby giving a cut-off energy that can be written as:

$$E_{\mathrm{c}} = \frac{\hbar^2 G_{\mathrm{max}}^2}{2m_{\mathrm{e}}} \tag{1.12}$$

where E_{c} is the cut-off energy, $\hbar$ is the reduced Planck constant, and m_{e} is the electron mass.

The electron density can be represented either in real or reciprocal space by applying a Fourier transform. One of the advantages of the plane-wave basis set is that this conversion is simple, and since some potentials are computed faster in real space and some in reciprocal space this reduces computation time.

1.5.2.3 Bloch's Theorem

Crystalline materials have many thousands of atoms arranged in a periodic repeating structure. This can be simulated with a system where one or multiple unit cells of a crystal are surrounded by periodic boundaries. Bloch's theorem can be applied:

$$\psi_k(r) = \exp(ik \cdot r)\, u_k(r) \tag{1.13}$$

The electronic wavefunction is expressed as the product of the wavefunction component and a periodic component, $u_k(r)$.

1.5.2.4 Pseudopotentials

In plane-wave DFT it is too computationally expensive to model the oscillating wavefunction resulting from core electrons for each atom. Fortunately, as chemical bonding only involves valence electrons, the effect of the core electrons can be approximated. As illustrated in Figure 1.11, above a chosen cut-off atomic radius, r_{c}, the pseudopotential V_{pseudo} matches the true potential, while in the core region the pseudopotential has a smaller magnitude than the ionic potential. The true wavefunction can then be represented as a pseudo-wavefunction ψ_{pseudo}

that lacks the nodal structure. This simplification of the core region reduces the number of plane waves required to approximate it.

Prior to running the main DFT calculation, a pseudopotential can be generated for each element present in the system. Two common types are ultrasoft pseudopotentials[127] and norm-conserving pseudopotentials.[128]

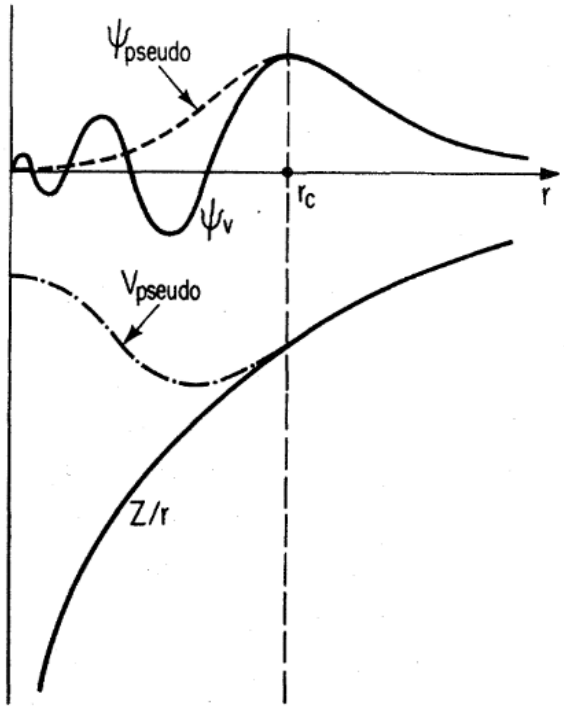

Figure 1.11: Illustration showing how the pseudopotential, V_{pseudo}, and pseudo-wavefunction, ψ_{pseudo}, approximate the potential, Z/r, and wavefunction, ψ_{v}, respectively, below a cut-off atomic radius, r_{c}. From Payne.[129]

1.6 Thesis Outline

The principle aim of this thesis is to study aluminium on diamond for the purpose of developing a material with NEA and a low work function. A thermally stable NEA would further the development of thermionic energy converters and other electron emission devices and would provide a viable alternative to H-termination. A low work function may allow the formation of a two-dimensional hole gas on the diamond surface, which can be utilised to develop novel field effect transistors and capacitors (see Chapter 2). A secondary aim is to study the oxygenated diamond surface, and attempt to better control and understand the type of oxygen termination achieved.

This thesis is split into seven chapters. Chapter 2 focuses on the diamond surface, reviewing the different surface terminations that have been studied, and how these terminations can affect properties such as surface structure, electronic structure and reactivity. Chapter 3 describes the experimental synthesis and characterisation methods used within this thesis. Chapter 4 details the computational work exploring aluminium on the bare, oxygenated and nitrogenated diamond surfaces with the intent of finding configurations that give an NEA, particularly those with large adsorption energies. Chapter 5 is an experimental chapter, exploring different oxygen termination methods on diamond. Chapter 6 is also an experimental chapter, testing the change in work function and EA with different AlO-terminations, and exploring the suitability of these surfaces for electron emission applications. Finally, results are summarised in Chapter 7, along with suggestions for future work. In the Appendix, the publications arising from this thesis are listed, as are the oral and poster presentations that were given at conferences.

References

1 J. Steinbeck, G. Braunstein, M. S. Dresselhaus, T. Venkatesan and D. C. Jacobson, *J. Appl. Phys.*, 1985, **58**, 4374–4382.
2 P. J. F. Harris, *Philos. Mag.*, 2004, **84**, 3159–3167.
3 C. Frondel and U. B. Marvin, *Nature*, 1967, **214**, 587–589.
4 R. B. Heimann, S. E. Evsyukov and Y. Koga, *Carbon*, 1997, **35**, 1654–1658.
5 Y. Zhu, S. Murali, W. Cai, X. Li, J. W. Suk, J. R. Potts and R. S. Ruoff, *Adv. Mater.*, 2010, **22**, 3906–3924.
6 A. Hirsch, *Nat. Mater.*, 2010, **9**, 868–871.
7 P. Dore, A. Nucara, D. Cannavò, G. De Marzi, P. Calvani, A. Marcelli, R. S. Sussmann, A. J. Whitehead, C. N. Dodge, A. J. Krehan and H. J. Peters, *Appl. Opt.*, 1998, **37**, 5731–5736.
8 S. Koizumi, K. Watanabe, M. Hasegawa and H. Kanda, *Science*, 2001, **292**, 1899–1901.
9 D. R. Kania, M. I. Landstrass, M. A. Plano, L. S. Pan and S. Han, *Diam. Relat. Mater.*, 1993, **2**, 1012–1019.
10 P. W. May, *Phil. Trans. R. Soc. Lond. A*, 2000, **358**, 473–495.
11 C. J. H. Wort and R. S. Balmer, *Mater. Today*, 2008, **11**, 22–28.
12 J. Liu and Y. Koide, *Sensors*, 2018, **18**, 1–17.
13 S. Szunerits, C. E. Nebel and R. J. Hamers, *MRS Bull.*, 2014, **39**, 517–524.
14 R. S. Balmer, J. R. Brandon, S. L. Clewes, H. K. Dhillon, J. M. Dodson, I. Friel, P. N. Inglis, T. D. Madgwick, M. L. Markham, T. P. Mollart, N. Perkins, G. A. Scarsbrook, D. J. Twitchen, A. J. Whitehead, J. J. Wilman and S. M. Woollard, *J. Phys. Condens. Matter*, 2009, **21**, 364221.
15 A. Wang, M. J. Tadjer and F. Calle, *Semicond. Sci. Technol.*, 2013, **28**,

055010.
16 *The Element Six CVD Diamond Handbook*, Element Six Ltd, 2015. Available at: https://e6cvd.com/media/wysiwyg/pdf/E6_CVD_Diamond_Handbook_A5_v10X.pdf. (Accessed: 24th April 2019).
17 H. B. Man and D. Ho, *Phys. Status Solidi*, 2012, **209**, 1609–1618.
18 G. E. Harlow, Ed., *The Nature of Diamonds*, Cambridge University Press, Cambridge, UK, 1998.
19 H. Ohfuji, T. Irifune, K. D. Litasov, T. Yamashita, F. Isobe, V. P. Afanasiev and N. P. Pokhilenko, *Sci. Rep.*, 2015, **5**, 1–8.
20 R. S. Lewis, T. Ming, J. F. Wacker, E. Anders and E. Steel, *Nature*, 1987, **326**, 160–162.
21 R. C. Burns, J. O. Hansen, R. A. Spits, M. Sibanda, C. M. Welbourn and D. L. Welch, *Diam. Relat. Mater.*, 1999, **8**, 1433–1437.
22 B. V. Spitsyn, L. L. Bouilov and B. V. Derjaguin, *J. Cryst. Growth*, 1981, **52**, 219–226.
23 T. Kawato and K. Kondo, *Jpn. J. Appl. Phys.*, 1987, **26**, 1429–1432.
24 R. J. Nemanich, *Annu. Rev. Mater. Sci.*, 1991, **21**, 535–558.
25 T. A. Railkar, W. P. Kang, H. Windischmann, A. P. Malshe, H. A. Naseem, J. L. Davidson and W. D. Brown, *Crit. Rev. Solid State Mater. Sci.*, 2000, **25**, 163–277.
26 S. Koizumi, H. Umezawa, J. Pernot and M. Suzuki, Eds., *Power Electronics Device Applications of Diamond Semiconductors*, Woodhead Publishing, Duxford, UK, 2018.
27 A. Krueger, *Chem. - A Eur. J.*, 2008, **14**, 1382–1390.
28 F. S. Manciu, M. Manciu, W. G. Durrer, J. G. Salazar, K. H. Lee and K. E. Bennet, *J. Mater. Sci.*, 2014, **49**, 5782–5789.
29 B. Massarani, J. C. Bourgoin and R. M. Chrenko, *Phys. Rev. B*, 1978, **17**, 1758–1769.
30 T. Tshepe, C. Kasl, J. F. Prins and M. J. R. Hoch, *Phys. Rev. B*, 2004, **70**, 245107.
31 J. Walker, *Rep. Prog. Phys.*, 1979, **42**, 1606–1659.
32 J. Chevallier, M. A. Pinault, J. Barjon, T. Kociniewski, F. Jomard, C. Saguy and R. Kalish, *2007 International Workshop on Physics of Semiconductor Devices,* 2007, 813–818.
33 T. Matsumoto, H. Kato, T. Makino and M. Ogura, *Jpn. J. Appl. Phys.*, 2014, **53**, 05FP05.
34 A. Mainwood, *J. Mater. Sci. Mater. Electron.*, 2006, **17**, 453–458.
35 P. W. May, M. Davey, K. N. Rosser and P. J. Heard, *Mater. Res. Soc. Symp. Proc.*, 2008, **1039**, 1039-P15-01.
36 J. F. Prins, *Phys. Rev. B*, 2000, **61**, 7191–7194.
37 J. F. Prins, *Semicond. Sci. Technol.*, 2003, **18**, S27–S33.
38 M. Hasegawa, D. Takeuchi, S. Yamanaka, M. Ogura, H. Watanabe, N. Kobayashi, H. Okushi and K. Kajimura, *Jpn. J. Appl. Phys.*, 1999, **38**, L1519–L1522.
39 T. Miyazaki and H. Okushi, *Diam. Relat. Mater.*, 2001, **10**, 449–452.
40 S. A. Kajihara, A. Antonelli, J. Bernholc and R. Car, *Phys. Rev. Lett.*, 1991, **66**, 2010–2013.
41 J. P. Goss and P. R. Briddon, *Phys. Rev. B*, 2007, **75**, 075202.

42 C. Uzan-Saguy, C. Cytermann, B. Fizgeer, V. Richter, R. Brener and R. Kalish, *Phys. Status Solidi Appl. Res.*, 2002, **193**, 508–516.
43 G. Popovici, A. A. Melnikov, V. S. Varichenko, S. Khasawinah, T. Sung, M. A. Prelas, A. Denisenko, N. M. Penina, V. A. Martinovich, E. N. Drozdova, A. M. Zaitsev, W. R. Fahrner, J. W. Farmer, H. White and J. Chamberlain, *Diam. Relat. Mater.*, 1996, **5**, 761–765.
44 K. Jagannadham, K. Verghese and J. E. Butler, *Appl. Phys. Lett.*, 2001, **78**, 446–447.
45 E. B. Lombardi and A. Mainwood, *Phys. B Condens. Matter*, 2007, **401–402**, 57–61.
46 S. C. Eaton, A. B. Anderson, J. C. Angus, Y. E. Evstefeeva and Y. V. Pleskov, *Electrochem. Solid-State Lett.*, 2002, **5**, G65–G68.
47 S. Vaddiraju, S. Eaton-Magana, J. A. Chaney and M. K. Sunkara, *Electrochem. Solid-State Lett.*, 2004, **7**, G331–G334.
48 R. Kalish, *Diam. Relat. Mater.*, 2001, **10**, 1749–1755.
49 J. E. Moussa, N. Marom, N. Sai and J. R. Chelikowsky, *Phys. Rev. Lett.*, 2012, **108**, 226404.
50 D. Segev and S.-H. Wei, *Phys. Rev. Lett.*, 2003, **91**, 126406.
51 J. P. Goss, P. R. Briddon and R. J. Eyre, *Phys. Rev. B - Condens. Matter Mater. Phys.*, 2006, **74**, 245217.
52 H. Katayama-Yoshida, T. Nishimatsu, T. Yamamoto and N. Orita, *J. Phys. Condens. Matter*, 2001, **13**, 8901–8914.
53 J. D. Levine, *Surf. Sci.*, 1973, **34**, 90–107.
54 D. T. Pierce, F. Meier and P. Zürcher, *Appl. Phys. Lett.*, 1975, **26**, 670–672.
55 M. J. Powers, M. C. Benjamin, L. M. Porter, R. J. Nemanich, R. F. Davis, J. J. Cuomo, G. L. Doll and S. J. Harris, *Appl. Phys. Lett.*, 1995, **67**, 3912.
56 M. C. Benjamin, C. Wang, R. F. Davis and R. J. Nemanich, *Appl. Phys. Lett.*, 1994, **64**, 3288–3290.
57 C. Bandis and B. B. Pate, *Phys. Rev. B*, 1995, **52**, 12056–12071.
58 D. M. Trucchi and N. A. Melosh, *MRS Bull.*, 2017, **42**, 488–492.
59 O. W. Richardson, *Philos. Mag.*, 1914, **28**, 633–647.
60 S. Dushman, *Phys. Rev.*, 1923, **21**, 623–636.
61 F. A. M. Koeck and R. J. Nemanich, *Front. Mech. Eng.*, 2017, **3**, 1–11.
62 F. A. M. Koeck and R. J. Nemanich, *J. Appl. Phys.*, 2012, **112**, 113707.
63 J. A. Becker, *Rev. Mod. Phys.*, 1935, **7**, 95–128.
64 T. D. Musho, W. F. Paxton, J. L. Davidson and D. G. Walker, *J. Vac. Sci. Technol. B*, 2013, **31**, 021401.
65 J. Voss, A. Vojvodic, S. H. Chou, R. T. Howe, I. Bargatin and F. Abild-Pedersen, *J. Chem. Phys.*, 2013, **138**, 204701.
66 V. L. Granatstein, R. K. Parker and C. M. Armstrong, *Proc. IEEE*, 1999, **87**, 702–716.
67 P. R. Davis, M. A. Gesley, G. A. Schwind, L. W. Swanson and J. J. Hutta, *Appl. Surf. Sci.*, 1989, **37**, 381–394.
68 K. Togawa, T. Shintake, T. Inagaki, K. Onoe, T. Tanaka, H. Baba and H. Matsumoto, *Phys. Rev. Spec. Top. - Accel. Beams*, 2007, **10**, 020703.
69 R. Forman, *Appl. Surf. Sci.*, 1979, **2**, 258–274.
70 G. Xiao, G. Zheng, M. Qiu, Q. Li, D. Li and M. Ni, *Appl. Energy*, 2017, **208**, 1318–1342.
71 C. Oshima, E. Bannai, T. Tanaka and S. Kawai, *J. Appl. Phys.*, 1977, **48**, 3925–

3927.
72 C. Stephanos, *Thermoelectronic Power Generation from Solar Radiation and Heat*, PhD Thesis, Universität Augsburg, 2012.
73 J. M. Houston, *J. Appl. Phys.*, 1959, **30**, 481–487.
74 W. Shockley and H. J. Queisser, *J. Appl. Phys.*, 1961, **32**, 510–519.
75 S. Rühle, *Sol. Energy*, 2016, **130**, 139–147.
76 P. G. Tanner, D. A. Fraser and A. D. Irving, *IEE Proc.-Sci. Meas. Technol*, 2005, **152**, 1–6.
77 G. N. Hatsopoulos and J. Kaye, *J. Appl. Phys.*, 1958, **29**, 1124–1125.
78 R. L. Bell, *Collector for Thermionic Energy Converter*, US Patent no. 4280074, 1981.
79 J. H. Lee, I. Bargatin, N. A. Melosh and R. T. Howe, *Appl. Phys. Lett.*, 2012, **100**, 173904.
80 I. Langmuir, *Proc. Inst. Radio Eng.*, 1915, **3**, 261–286.
81 V. C. Wilson, *J. Appl. Phys.*, 1959, **30**, 475–481.
82 F. A. M. Koeck, R. J. Nemanich, Y. Balasubramaniam, K. Haenen and J. Sharp, *Diam. Relat. Mater.*, 2011, **20**, 1229–1233.
83 F. A. M. Koeck, R. J. Nemanich and J. Sharp, *26th Int. Vac. Nanoelectron. Conf. IVNC 2013*, 2013, 1–3.
84 K. A. A. Khalid, T. J. Leong and K. Mohamed, *IEEE Trans. Electron Devices*, 2016, **63**, 2231–2241.
85 S. Srisonphan, M. Kim and H. K. Kim, *Sci. Rep.*, 2014, **4**, 1–6.
86 A. Croot, G. Wan, A. Rowan, H. D. Andrade, J. A. Smith and N. A. Fox, *Front. Mech. Eng.*, 2017, **3**, 1–8.
87 G. C. Szego and J. E. Taylor, Eds., *Space Power Systems Engineering*, Academic Press, New York, NY, USA, 1966.
88 A. W. Raja, P. Zilio, A. Alabastri, R. P. Zaccaria and J. Cunha, *Photon-Enhanced Thermionic Emission*, 2015. Available at: https://pdfs.semanticscholar.org/af2f/6b015de4b729d85b3e4936a00e4cbdf84023.pdf. (Accessed 21st February 2019).
89 D. V. Paramonov and M. S. El-Genk, *Energy Convers. Manag.*, 1997, **38**, 533–549.
90 A. Kribus and G. Segev, *J. Opt.*, 2016, **18**, 073001.
91 R. Eisenberg and D. G. Nocera, *Inorg. Chem.*, 2005, **44**, 6799–6801.
92 N. L. Lewis and D. G. Nocera, *PNAS*, 2006, **103**, 15729–15735.
93 *Annual Energy Outlook 2019 with projections to 2050*, US Energy Information Administration, 2019. Available at: https://www.eia.gov/outlooks/aeo/. (Accessed 19th March 2019).
94 J. W. Schwede, I. Bargatin, D. C. Riley, B. E. Hardin, S. J. Rosenthal, Y. Sun, F. Schmitt, P. Pianetta, R. T. Howe, Z. X. Shen and N. A. Melosh, *Nat. Mater.*, 2010, **9**, 762–767.
95 J. W. Schwede, T. Sarmiento, V. K. Narasimhan, S. J. Rosenthal, D. C. Riley, F. Schmitt, I. Bargatin, K. Sahasrabuddhe, R. T. Howe, J. S. Harris, N. A. Melosh and Z. X. Shen, *Nat. Commun.*, 2013, **4**, 1576.
96 A. Varpula and M. Prunnila, *J. Appl. Phys.*, 2012, **112**, 044506.
97 G. Segev, Y. Rosenwaks and A. Kribus, *J. Appl. Phys.*, 2013, **114**, 044505.
98 G. Segev, Y. Rosenwaks and A. Kribus, *Sol. Energy Mater. Sol. Cells*, 2015, **140**, 464–476.
99 A. Kribus and G. Segev, *J. Opt.*, 2016, **18**, 073001.

100 J. R. Smith, G. L. Bilbro and R. J. Nemanich, *Phys. Rev. B*, 2007, **76**, 245327.
101 J. R. Smith, G. L. Bilbro and R. J. Nemanich, *J. Vac. Sci. Technol. B*, 2009, **27**, 1132.
102 J. R. Smith, *J. Appl. Phys.*, 2013, **114**, 164514.
103 I. N. Lin, S. Koizumi, J. Yater and F. Koeck, *MRS Bull.*, 2014, **39**, 533–541.
104 F. A. M. Koeck and R. J. Nemanich, *Diam. Relat. Mater.*, 2009, **18**, 232–234.
105 W. F. Paxton, M. Howell, W. P. Kang and J. L. Davidson, *J. Vac. Sci. Technol. B*, 2012, **30**, 021202.
106 F. A. M. Koeck and R. J. Nemanich, *Diam. Relat. Mater.*, 2006, **15**, 217–220.
107 M. Suzuki, T. Ono, N. Sakuma and T. Sakai, *Diam. Relat. Mater.*, 2009, **18**, 1274–1277.
108 M. Kataoka, C. Zhu, F. A. M. Koeck and R. J. Nemanich, *Diam. Relat. Mater.*, 2010, **19**, 110–113.
109 F. A. M. Koeck, R. J. Nemanich, A. Lazea and K. Haenen, *Diam. Relat. Mater.*, 2009, **18**, 789–791.
110 H. Kato, D. Takeuchi, M. Ogura, T. Yamada, M. Kataoka, Y. Kimura, S. Sobue, C. E. Nebel and S. Yamasaki, *Diam. Relat. Mater.*, 2016, **63**, 165–168.
111 A. Bellucci, P. Calvani, M. Girolami, S. Orlando, R. Polini and D. M. Trucchi, *Appl. Surf. Sci.*, 2016, **380**, 8–11.
112 A. Bellucci, P. Calvani, M. Girolami and D. M. Trucchi, *2015 IEEE 15th Int. Conf. Environ. Electr. Eng. - Conf. Proc.*, 2015, 1616–1619.
113 M. Girolami, L. Criante, F. Di Fonzo, S. Lo Turco, A. Mezzetti, A. Notargiacomo, M. Pea, A. Bellucci, P. Calvani, V. Valentini and D. M. Trucchi, *Carbon*, 2017, **111**, 48–53.
114 S. Elfimchev, M. Chandran, R. Akhvlediani and A. Hoffman, *Phys. Status Solidi*, 2015, **212**, 2583–2588.
115 T. Sun, F. A. M. Koeck, P. B. Stepanov and R. J. Nemanich, *Diam. Relat. Mater.*, 2014, **44**, 123–128.
116 T. Sun, F. A. M. Koeck, A. Rezikyan, M. M. J. Treacy and R. J. Nemanich, *Phys. Rev. B*, 2014, **90**, 121302.
117 P. Hohenberg and W. Kohn, *Phys. Rev.*, 1964, **136**, 864–871.
118 W. Kohn and L. J. Sham, *Phys. Rev.*, 1965, **140**, 1133–1138.
119 P. Geerlings, F. De Proft and W. Langenaeker, *Chem. Rev.*, 2003, **103**, 1793–1874.
120 J. P. Perdew and Y. Wang, *Phys. Rev. B*, 1992, **45**, 244–249.
121 J. P. Perdew, K. Burke and M. Ernzerhof, *Phys. Rev. Lett.*, 1996, **77**, 3865–3868.
122 Z. Wu and R. E. Cohen, *Phys. Rev. B*, 2006, **73**, 235116.
123 A. D. Becke, *J. Chem. Phys.*, 1993, **98**, 1372–1377.
124 A. V. Krukau, O. A. Vydrov, A. F. Izmaylov and G. E. Scuseria, *J. Chem. Phys.*, 2006, **125**, 224106.
125 J. P. Perdew, *Int. J. Quantum Chem.*, 1985, **28**, 497–523.
126 V. I. Anisimov, Ed., *Strong Coulomb Correlations in Electronic Structure Calculations*, Gordon and Breach, Amsterdam, The Netherlands, 2000.
127 D. Vanderbilt, *Phys. Rev. B*, 1990, **41**, 7892–7895.
128 J. S. Lin, A. Qteish, M. C. Payne and V. Heine, *Phys. Rev. B*, 1993, **47**, 4174–4180.
129 M. C. Payne, M. P. Teter, D. C. Allan, T. A. Arias and J. D. Joannopoulos, *Rev. Mod. Phys.*, 1992, **64**, 1045–1097.

Chapter 2 – Surface Functionalisation of Diamond

2.1 The Diamond Surface

Carbon atoms at the diamond surface can no longer bond in the same way as in bulk. These surface atoms are quite reactive, considering that they possess non-bonded electrons, therefore, to minimise energy, the atoms move out of periodic sites and bond with other surface atoms and/or heteroatoms. The atomic rearrangement to form new surface geometries, known as surface reconstruction, can involve bonding between atoms across more than one surface unit cell and can affect the geometry and bonding of atoms several layers deep within the surface.

Surface carbons in diamond will commonly form bonds with heteroatoms to terminate the surface, with the lowest energy structure in many cases also involving a surface reconstruction. It is also possible to bind molecules to diamond or deposit bulk materials on diamond. Different surface terminations can affect the surface structure, electronic structure and reactivity of the diamond surface.

The diamond surface has been widely studied over the past 40 years and remains an active area of research. Since carbon can bond with most elements of the periodic table, there have been attempts to functionalise the diamond surface with many of these elements. This chapter provides a systematic and comprehensive review of the functionalisation of the diamond surface, arranged by atom group, and detailing the termination procedure, properties and applications for each of the terminations.

2.1.1 Diamond Crystal Facets

Crystal facets are described by Miller indices. A specific crystal plane is represented as (*hkl*) for cubic crystals such as diamond, where *h*, *k* and *l* are integers. The plane intersects with the reciprocal of the *x*, *y* and *z* axes at *h*, *k* and *l*, respectively. For basis lattice vectors a_1, a_2 and a_3 and corresponding reciprocal

lattice vectors b_1, b_2 and b_3, a Miller plane is orthogonal to the reciprocal lattice vector $hb_1 + kb_2 + lb_3$. To illustrate this, Figure 2.1 shows the (100) and (111) planes for a cubic crystal.

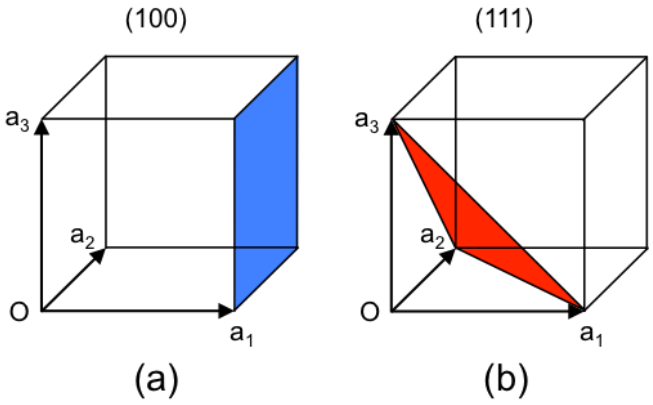

Figure 2.1: A cubic crystal with (a) the (100) plane shown in blue and (b) the (111) plane shown in red. O is the origin, and a_1, a_2 and a_3 are the primitive lattice vectors in *x*, *y* and *z* directions, respectively.

For synthetic diamond grown by chemical vapour deposition (CVD), exact growth rates of the different crystal faces vary depending on temperature and gas composition, but generally the (100) and (111) planes are the slowest growing facets.[1] Other facets such as (110) and (113) grow laterally, making (100) or (111) the predominant surface facets. The (111) facet is also the natural cleavage plane of diamond.[2]

The adsorbate-free (100) and (111) diamond surface structures are shown in Figure 2.2. The (100) surface preferentially forms a (2 × 1) reconstruction to lower surface energy, forming a C=C double bond in dimer rows perpendicular to the surface (Figure 2.2(c)). The (111) surface also forms a (2 × 1) reconstruction (Figure 2.2(d)), forming a structure where the surface carbons zig-zag along the surface, known as Pandey chains.[3] This is the lowest energy structure as the p-orbitals of the surface carbon atoms in the upper Pandey chain can form a conjugated π-bonded system. Both surfaces have a small positive electron affinity (PEA) of approximately 0.5 eV.[4]

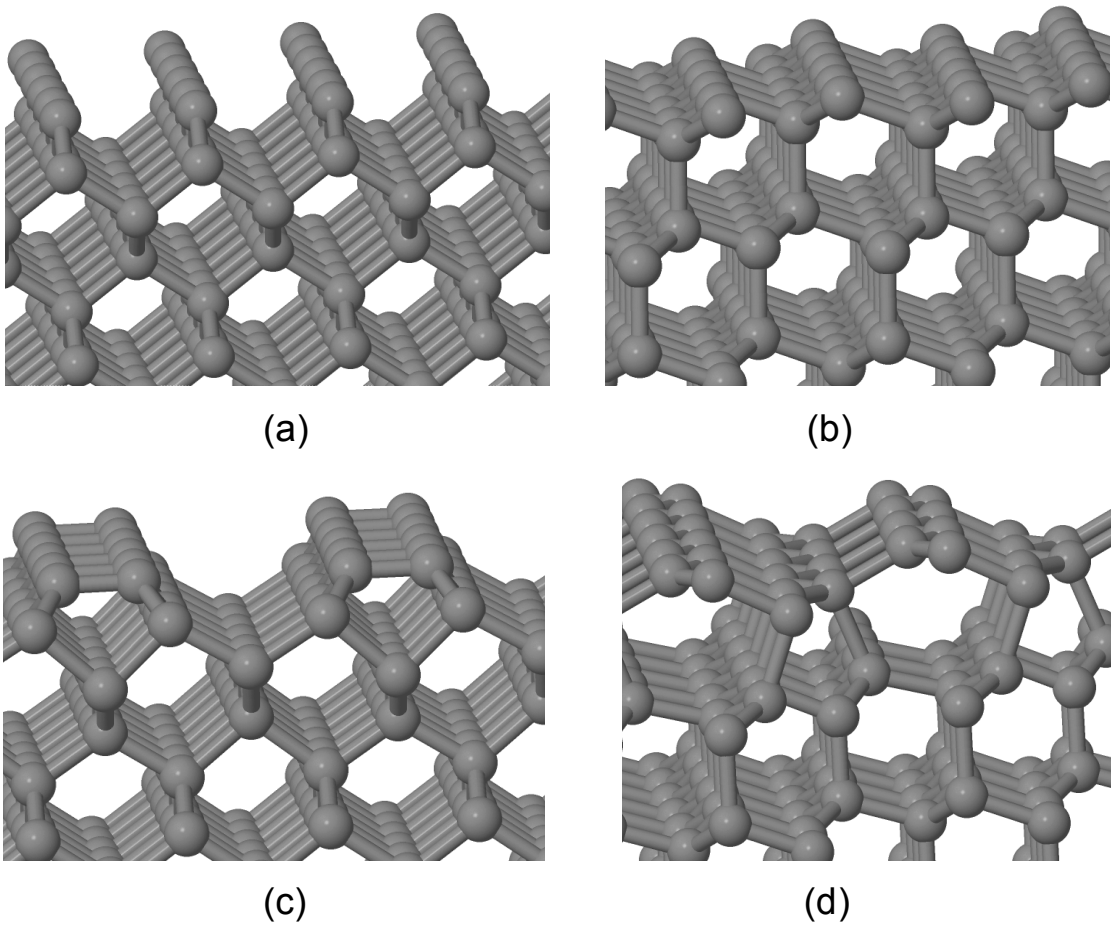

Figure 2.2: Simulations of (a)–(b) the (1 × 1) (100) and (111) bare diamond surfaces, respectively, and (c)–(d) the (2 × 1) reconstructed bare diamond (100) and (111) surfaces, respectively.

2.2 Non-Metal Terminations

2.2.1 Hydrogen

Hydrogenation of diamond can be achieved simply and reproducibly through methods including subjection to high-temperature hydrogen gas,[5] hydrogen plasma[6] and even polishing with diamond powder and olive oil.[7] Synthesis of diamond by CVD methods results in hydrogen termination due to the hydrogen-rich atmosphere used in diamond growth. Hydrogenation of the (100) surface maintains the (2 × 1) reconstruction, while for the H-terminated (111) surface it is energetically favourable to have no surface reconstruction. These surfaces are shown in Figure 2.3.

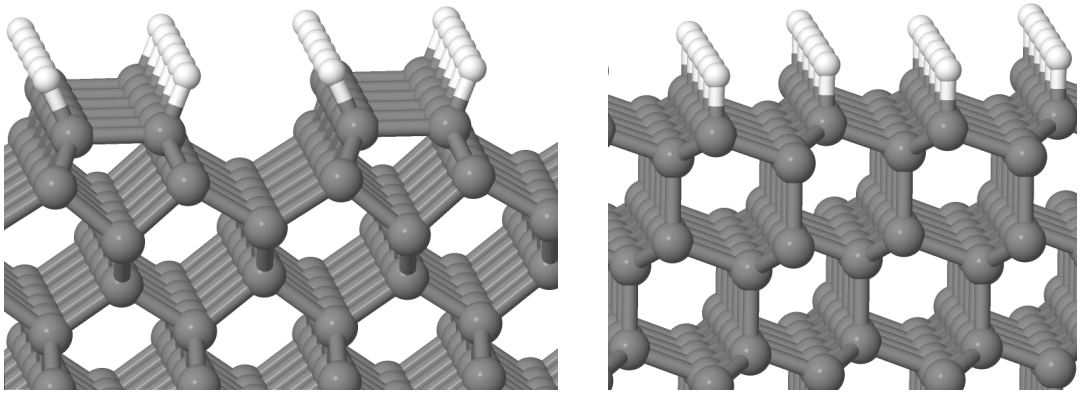

Figure 2.3: Simulations of the H-terminated (a) (100) and (b) (111) diamond surfaces. C and H atoms are shown in grey and white, respectively.

Landstrass and Ravi[8] first reported that H-termination can give diamond a significant surface conductivity, by demonstrating that hydrogenation reduces the resistivity of a single crystal by 11 orders of magnitude. It is believed that this arises from a redox reaction with moisture in the air, in a process known as surface transfer doping. The water adsorbates act as an electron sink, giving the diamond surface a conductive positive charge layer, called a two-dimensional hole gas (2DHG).[9] Figure 2.4 shows the relative energy alignment of diamond and adsorbate species that causes the formation of the 2DHG. This phenomenon has also been demonstrated with fullerenes[10] and NO_2[11] as the adsorbing species. The sheet hole carrier density of the 2DHG is in the range 10^{12}–10^{14} cm^{-2} and has a depth of a few nm. Devices incorporating the 2DHG have been developed in recent years, further details of which are given in Sections 2.5 and 2.6.

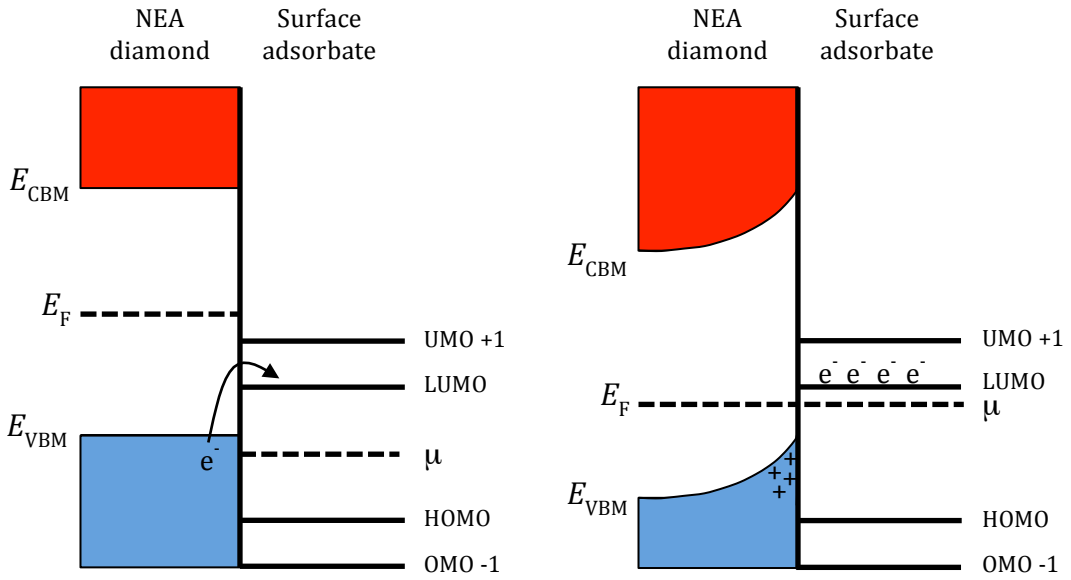

Figure 2.4: Before and after band alignment between H-terminated diamond and surface adsorbates. Equilibration of diamond Fermi level, E_F, with adsorbate chemical potential, μ, by electron transfer leads to upwards band bending and the formation of a two-dimensional hole gas (2DHG) at the diamond surface. (H)OMO and (L)UMO are (highest) occupied molecular orbital and (lowest) unoccupied molecular orbital, respectively, for the surface acceptor species. Adapted from Ristein.[12]

Hydrogen termination gives diamond an electron affinity (EA) measured experimentally to be between -0.7 eV and -1.3 eV for both the (100) and (111) surfaces.[4,13–16] A slightly more negative value of ~-2 eV has been obtained computationally from density functional theory (DFT) calculations.[17–19] This negative electron affinity (NEA) makes H-termination the subject of a number of investigations into electron emission from diamond.[20,21] The threshold temperature for emission is below 600 °C, with emission current increasing exponentially with temperature following the Richardson-Dushman relation (Chapter 1.4.1).[22] Most of the H-termination will instantly desorb from the diamond surface above a temperature of approximately 700 °C, corresponding to an adsorption energy of ~-4 eV/atom as calculated from DFT. This is the limiting factor for maximising emission current.[23–25] Figure 2.5 shows that even for an H-terminated diamond cathode operating at 600 °C there is a decrease in peak emission current with an increasing number of temperature cycles.[26] There is

also an undesirable increase in the threshold temperature for thermionic emission.

Electron emission has also been demonstrated from H-terminated diamond in water upon UV light irradiation. These electrons have high reduction potential and are capable of breaking down stable molecules, such as N_2 into NH_3 and CO_2 into CO, thus representing a promising novel route for catalysis of important industrial processes.[27,28] However, over time, oxidation of the surface removes NEA entirely, so alternative water-stable NEA surfaces are desired.

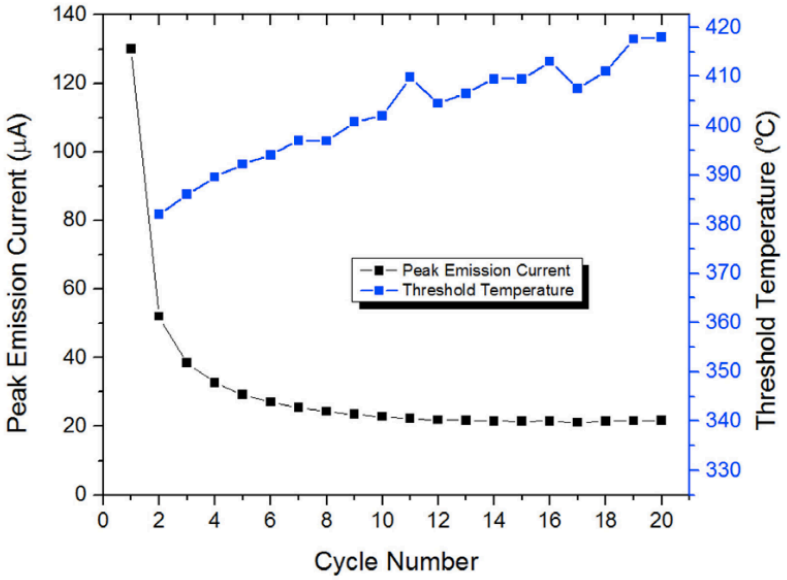

Figure 2.5: Thermal cycling of an H-terminated diamond cathode up to 600 °C shows the peak emission current decreases and the threshold temperature for emission increases with an increasing number of emission cycles. From Croot *et al.*[26]

2.2.2 Oxygen, Hydroxyl and Carboxyl

The diamond surface can be oxidised by multiple methods including treatment with oxygen plasma, with UV light and oxygen gas (producing ozone), by reaction with oxidising agents, and by electrochemical anodic polarisation. Oxygen by itself bonds with diamond in two main ways – an ether-like bonding arrangement (C-O-C), where O is bridging between two surface carbons, or a ketone-like bond (C=O), where a single surface carbon is double bonded with oxygen.[29,30] For the (100) surface, both of these types of O-termination have no surface reconstruction, but for ether and ketone bonding to the (111) surface it is energetically favourable to retain the (2 × 1) reconstruction, although the C=O

double bond formed by the ketone breaks a carbon-carbon bond of the upper Pandey chain. These surfaces are shown in Figure 2.6.

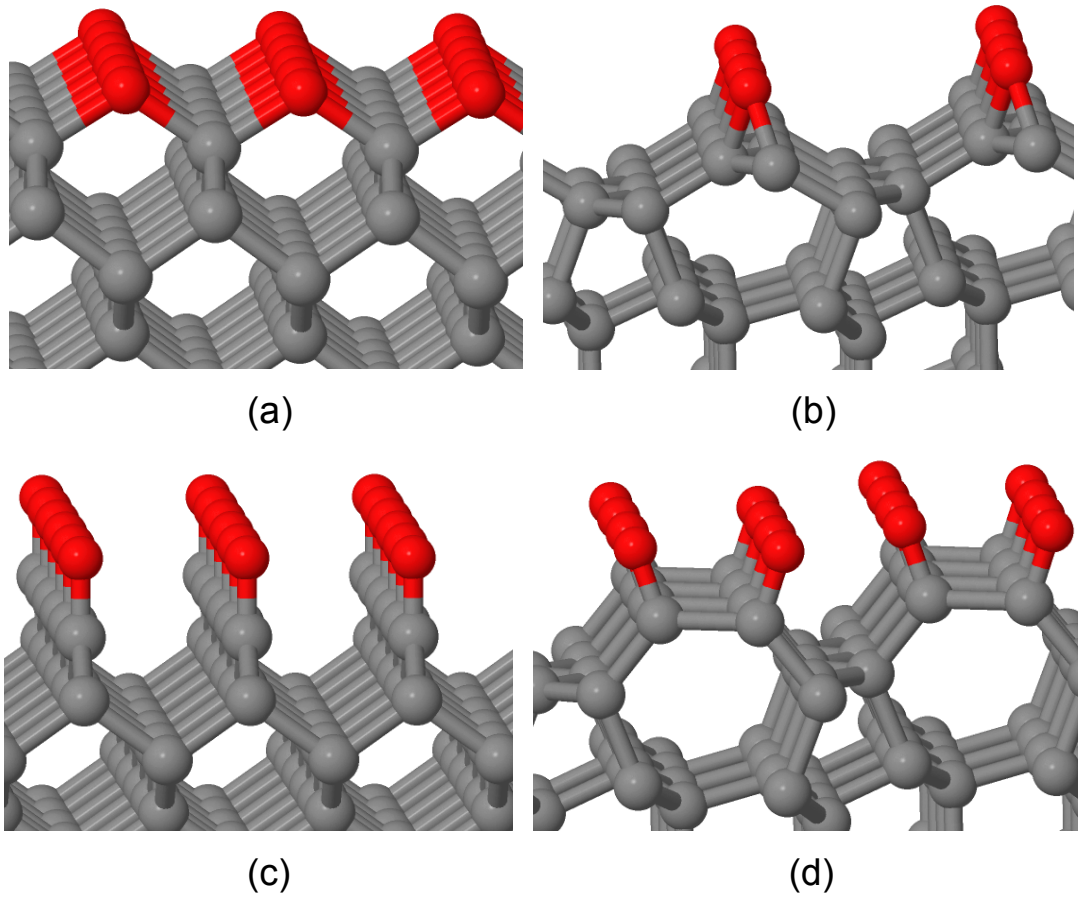

Figure 2.6: Simulations of the (a)–(b) ether O-terminated (100) and (111) diamond surfaces, respectively, and (c)–(d) the ketone O-terminated (100) and (111) diamond surfaces, respectively. C and O atoms are shown in grey and red, respectively.

Computational calculations find that formation of the ether is slightly more energetically favourable than the ketone. Even so, for both (100) and (111) diamond the ether is somewhat strained due to the carbon atom spacings in the diamond lattice. In addition, the imperfect nature of experimental surfaces will result in different structures at edges, complicating study of oxygen-terminated diamond. The maximum coverage of ether termination on (111) diamond has half as many O atoms as the ketone, so the degree of surface coverage is believed to influence the type of oxygen bonding.[31] Theoretical studies by Derry *et al.* suggest that the optimum oxygen coverage on (111) diamond is half a monolayer

(ML) due to steric repulsion at larger coverages,[32] although this result is disputed by Zheng *et al.*[29] Loh *et al.*[31] have reported that a full ML coverage can be achieved experimentally by irradiation with atomic oxygen at elevated temperatures.

A hydroxyl (C-OH) termination can also be formed from the oxidation of hydrogenated diamond. Computational studies have predicted that the hydroxyl-terminated diamond favours (2 × 1) reconstruction on the (100) surface[19] and no reconstruction on the (111) surface.[31] Loh *et al.*[31] report that the hydroxyl-termination is more thermodynamically stable than either ether or ketone on (111) diamond. Experimentally, the hydroxyl-termination has been reported on the (111) surface by heating diamond in water vapour.[33]

The oxygen termination possesses a large PEA, measured experimentally to be in the range 1.0–1.7 eV for (100) diamond.[4,34] Computationally, both ether and ketone surfaces show a larger PEA. Values of ~2.6 eV and ~3.7 eV have been reported for ether and ketone O-terminated (100) and (111) surfaces, respectively.[29,35,36] By contrast, computational studies of hydroxyl terminated diamond predict an NEA, with values ranging between -0.55 eV and -2.13 eV.[18,19,37] An NEA of -1.1 eV has been reported for a hydroxyl termination on (100) diamond obtained from a hydrogen/oxygen plasma,[16] and electrochemically oxidised (111) diamond has shown NEA,[34] which could also be attributed to a hydroxyl termination. However, no characterisation was performed to confirm the presence of a hydroxyl group in either case.

The hydroxyl termination is of interest for its potential for further functionalisation of diamond. Four different reaction pathways that have been investigated are shown in Figure 2.7. The first is functionalisation with silane groups; this has been demonstrated with perfluorodecyltrichlorosilane (from Figure 2.7(a), R=$(CH_2)_2$-$(CF_2)_7$-CF_3),[38] aminopropyltriethoxysilane (R=$(CH_2)_3$-NH_2)[39] and *N*-(3-trimethoxysilylpropyl)pyrrole (R=$(CH_2)_6$-NC_4H_4).[40] Binding amines allows the attachment of peptides for use as peptide microarrays, while attached pyrrole groups can undergo an electropolymerisation step to form a strongly adhesive polymer layer on diamond. Similarly, attachment of a polymer layer of poly(ethylene glycol) methacrylate *via* silanisation has demonstrated

antifouling properties on an ultrananocrystalline diamond/amorphous carbon nanocomposite film, with potential applications in biotechnology.[41]

Direct attachment of a polymer such as polystyrene to hydroxyl-terminated diamond has been achieved *via* a photochemical reaction with alkenes under UV light (Figure 2.7(b)).[42] A reaction with an alkene was also reported by heating diamond in a solution of 1-octadecene.[43] As shown by Figure 2.7(c), esterification reactions are another versatile way to terminate diamond. This has been demonstrated by reaction of hydroxyl groups with biotin,[44] pyrenebutyric acid ($R=(CH_2)_3\text{-}C_{16}H_9$)[45] and 3-benzoylbenzoic acid ($R=C_6H_5\text{-}CO\text{-}C_6H_5$);[46] in the latter case a further functionalisation step was used to bind oligonucleotides by photochemical reaction. Potential applications for these functionalised surfaces include novel biosensors and photocathodes. Figure 2.7(d) shows supramolecular zirconium phosphate carbonate chemistry that has been used to attach perylene- and pyrene-alkanoic acids ($R=(CH_2)_{11}\text{-}C_{20}H_{17}$ and $R=(CH_2)_x\text{-}C_{16}H_{11}$, x=0, 3, 5, 11) to boron doped diamond (BDD) for chemical sensing applications.[47] Just the initial phosphorylation step can also improve the thermal stability of nanodiamonds.[48]

Further functionalisation reactions with other oxidised diamond surfaces have also been reported. The ketone surface can selectively react with dinitrophenylhydrazine.[49] Oxidation of nanocrystalline diamond[50] or nanodiamonds[51] can give a carboxyl termination (COOH), as these diamond surfaces have exposed carbon atoms such as methyl groups. As with the hydroxyl termination it is possible to bind biomolecules to carboxyl-terminated diamond, in this case by reaction with an amine to form an amide bond.[52] Amide linkage is one of the most commonly used methods to bind biomolecules to diamond. Amide linkages may use either carboxyl or amine terminations (Section 2.2.3), or an amine or carboxyl functional group attached to an alkyl or aromatic group grafted to the diamond surface (Section 2.2.6). Binding molecules to nanodiamonds has potential for novel drug delivery, imaging and sensing.[53]

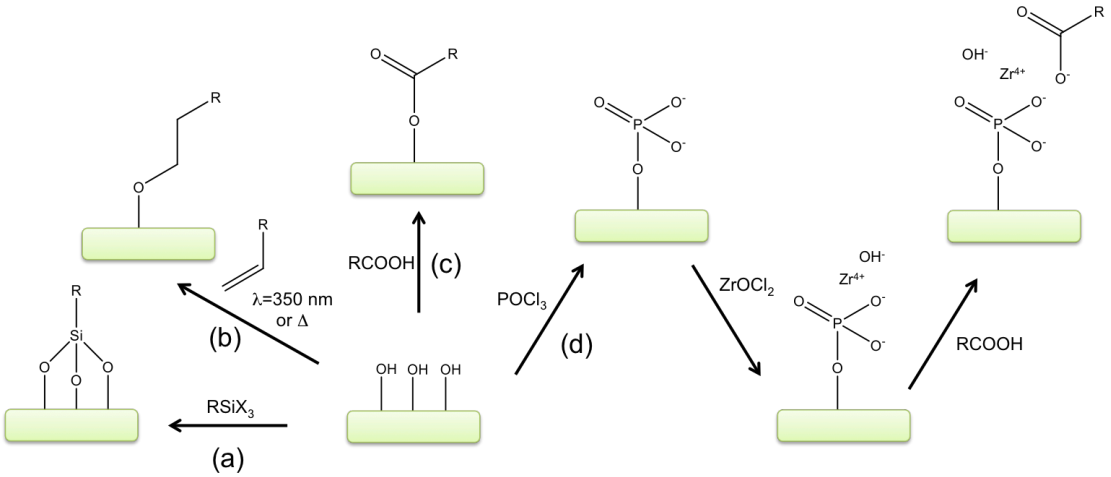

Figure 2.7: Modification of hydroxyl-terminated diamond by different procedures. (a) silanisation, (b) thermal or photochemical reaction with alkene, (c) esterification and (d) zirconium and phosphorus chemistry. Adapted from Szunerits and Boukherroub.[54]

2.2.3 Nitrogen and Amines

Nitrogen termination on (100) and (111) diamond is possible with a radio or microwave nitrogen plasma source.[55,56] As nitrogen is more electronegative than carbon, N-termination gives diamond a PEA. Nitrogen-vacancy (NV) centres in diamond, capable of single photon emission useful for quantum applications, require a PEA as surface transfer doping from NEA diamond discharges the NV^- state and quenches emission. N-termination is being considered for quantum applications as, unlike other PEA terminations, it is not electronically active, a further cause of reduced emission.[57]

Ammonia plasma treatment can give primary amine (C-NH_2) and secondary amine (C-NH-C), imine (C=NH or C=N-C) and cyanide (C≡N) terminations of diamond depending on plasma conditions.[58] Amine- and methylamine-termination can also be produced by reaction of chlorinated diamond (Section 2.2.5) with ammonia or methylamine.[59] The literature has focused on selective formation of primary amines, where 10–20% surface coverage is achievable.[60] The amine-terminated surface can be functionalised with biomolecules by amide linkage in a similar manner to carboxyl termination, as described in Section 2.2.2.

Amine-terminated diamond represents an improvement over H-termination for the catalytic breakdown of stable molecules in aqueous solution, as the

surface does not oxidise over time. Treatment of amine-termination with HCl has further been shown to form an NH_2^+ positively charged layer on the diamond surface, with a corresponding Cl^- anion in solution.[58] As shown by Figure 2.8, this positive charge layer from NH_2^+ enhances emission compared with the simple surface dipole of the amine, and for the photoreduction of N_2 roughly doubles the yield of NH_3 when compared to H-termination.

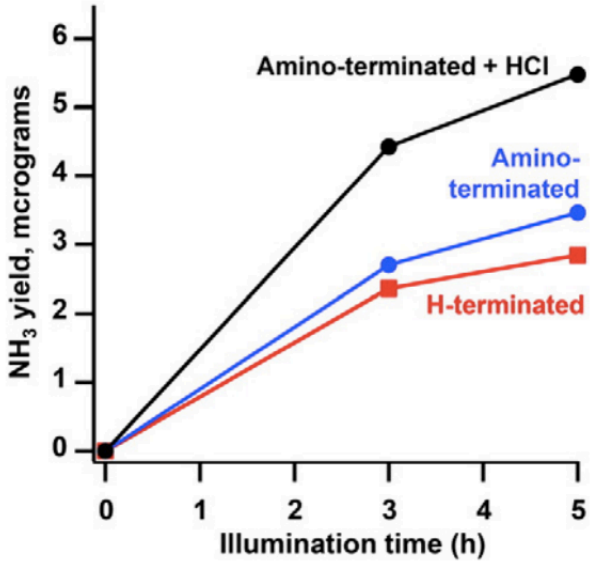

Figure 2.8: Amine-terminated diamond followed by HCl treatment enhances the NH_3 yield from the photoreduction of N_2 compared to H-termination. From Zhu *et al.*[58]

2.2.4 Sulfur and Thiol

Sulfur appears to preferentially bond as a thiol (C-SH) group with diamond. Thiol-terminated diamond has been achieved by UV irradiation under H_2S gas[59] and by reaction of hydroxyl-terminated nanodiamond with thiourea under acidic conditions.[61] A reaction between H-terminated nanodiamond powder and elemental sulfur under UV irradiation was found to have both thiol and thiocarbonyl (C=S) groups.[62] The thiocarbonyl was believed to originate from reaction of sulfur with a methyl group. Sulfur-containing groups are capable of binding diamond to gold nanoparticles and thin films.[62] These Au-diamond nanocomplexes show promise for biomedical applications.[61]

2.2.5 Halides

Halides are expected to preferentially bond with a (2 × 1) reconstruction on the (100) surface,[63] and with no reconstruction on the (111) surface.[64] Fluorination can be achieved by using fluorine-containing gases and plasmas, however in many cases surface roughening is reported. A monolayer of fluorine on (100) diamond with little surface damage has been reported by using either an SF_6 plasma[65] or by thermal-induced dissociation of XeF_2.[66] Fluorine is the most electronegative element and consequently has shown the largest PEA for diamond, measured experimentally as 2.56 eV for F-terminated BDD.[66] Fluorinated surfaces typically exhibit superhydrophobic behaviour that can be exploited for self-cleaning or low-friction materials.[67] Fluorination of diamond can extend the potential window of BDD electrodes by ~1.5 V by hindering the hydrogen evolution reaction,[68] and can prevent nonspecific binding of biomolecules in biosensors.[60] F-termination of nanodiamonds may also improve tribological properties and luminescence for bioimaging.[69,70]

Chlorination can be achieved photochemically with Cl_2 gas and UV light,[71] with lower reagent pressures and shorter irradiation times found to lead to the largest surface coverage.[59] Theoretical calculations show, however, that full ML coverage is not possible.[63,64] Bromine-terminated diamond is likewise not predicted to be stable above ~0.25 ML coverage.[72] Nevertheless, Cl- and Br-terminations have been used as an intermediate for further surface functionalisation of diamond. A photochemical reduction reaction has been demonstrated to produce amine or thiol terminations,[59,73] and a Grignard reaction has produced a range of aliphatic terminations.[74,75]

2.2.6 Aliphatics and Aromatics

A broad range of alkyl and aromatic groups can be added directly to the diamond surface. As shown in Figure 2.9(a), alkyl terminations of diamond can form from photochemical grafting of alkenes using UV light. This has been demonstrated using alkenes functionalised with fluorine, amine and carboxylic acid groups.[76] Further functionalisation has been used to covalently attach electrochemically active molecular complexes to diamond.[77–79]

The reduction of diazonium salts can be used to bond aromatic groups directly to diamond. This was first shown by Kuo *et al.*[80] with addition of nitrophenyl and trifluoromethylphenyl groups to BDD at 0.5–0.7 ML coverage (from Figure 2.9(b), R=NO_2 and R=CF_3, respectively), but this technique allows the addition of a broad range of functionalised aryl species to diamond.

The reaction mechanism for addition of both aliphatic and aromatic species proceeds *via* electron injection from diamond into solution, creating a radical anionic species. For alkenes this requires absorption of UV light by diamond and subsequent emission of high energy electrons,[81] while diazonium salts break down relatively easily with the loss of N_2 gas after a small applied bias at a BDD electrode.[82]

Functionalised alkyl and aromatic terminations can be used to make biosensors or bioelectronics. By including carboxylic acid or amine functional groups, it is possible to attach biological molecules such as DNA, RNA and proteins with an amide bond, either by direct reaction to the biomolecule or *via* a crosslinking species.[41,83–86] Suzuki coupling with aryl species containing bromine or boronic acid groups can bind additional aryl species including C_{60} fullerenes.[87] Conjugated aromatic species bonded to BDD films and foams can similarly be used to fabricate diamond-based dye-sensitized solar cells.[88]

The Diels-Alder reaction can be used to functionalise the (100) diamond surface with two covalent carbon-carbon bonds. This method first involves thermal treatment in vacuum to desorb prior termination, resulting in a clean surface containing C=C carbon dimers. The diamond surface can then undergo a [4+2] cycloaddition reaction with a diene. The addition of 1,3-butadiene can enhance secondary electron emission as it possesses a larger NEA than H-termination.[89] This reaction has also been used to graft aromatic groups to nanodiamond.[90]

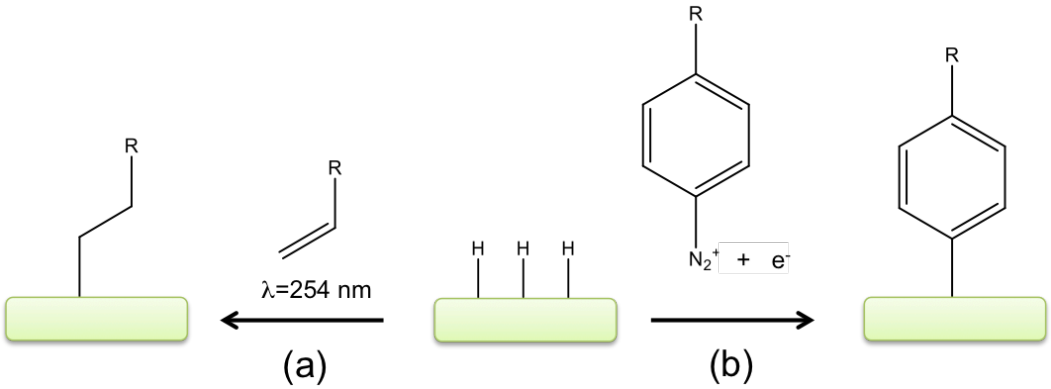

Figure 2.9: Functionalisation of the diamond surface with (a) photochemical grafting of alkenes and (b) reaction with aryldiazonium salt.

2.3 Metalloid Terminations

An ordered silicon-terminated diamond surface can be formed by the *in vacuo* deposition of Si and annealing. Figure 2.10(a) shows that addition of Si to the (100) surface creates a (3 × 1) surface reconstruction. This surface has an NEA measured as -0.86 eV.[91] The silicon termination is not air-stable, but can be oxidised without disrupting the underlying structure.[92,93] This surface was found to undergo surface transfer doping using MoO_3 as the acceptor.[94]

Germanium on (100) diamond behaves in a similar manner to silicon. Figure 2.10(b) shows the (3 × 1) surface reconstruction observed on the (100) surface.[95] In this case, saturation of the surface occurs at approximately 0.63 ML coverage, corresponding to 1.26 atoms per (3 × 1) unit cell. Ge-terminated diamond possesses an NEA measured as -0.71 eV.

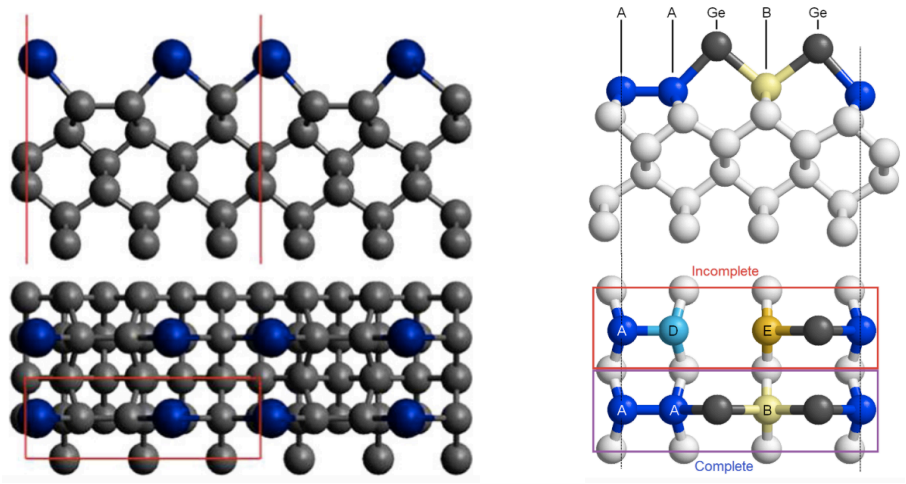

Figure 2.10: Side and plan views of (3 × 1) reconstructed (100) diamond surface with (a) Si-termination from Schenk *et al.*[91] and (b) Ge-termination from Sear *et al.*[95]

2.4 Metal and Metal-Oxygen Terminations

2.4.1 Group I and II Metals

There has been considerable interest in terminations other than hydrogen that possess an NEA for electron emission devices. Of particular interest here is that H-termination lacks stability at operational temperatures for thermionic devices, and so thermally stable alternatives are desired, but more negative electron affinities are also desirable for lower onset currents in field emission devices. Figure 2.11 shows the electronegativities of different elements in the periodic table. The group I and II elements have the smallest electronegativity values, much lower than that of hydrogen.

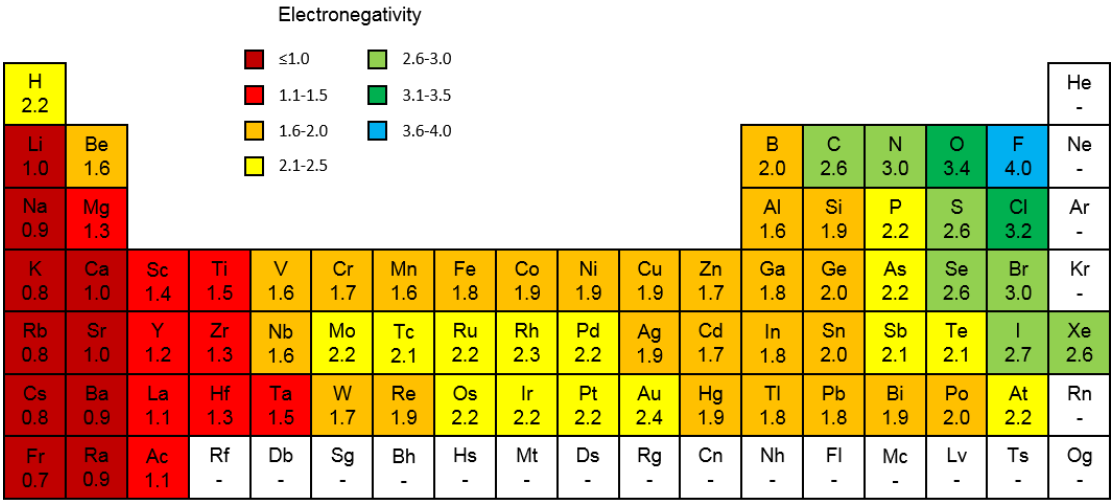

Figure 2.11: Pauling electronegativity values of different elements of the Periodic Table.[96]

The field emission behaviour of thin metal layers of Na, K, and Cs on diamond has been reported. Emission currents were found to be one order of magnitude larger than H-terminated diamond for the same applied voltage.[71] The Li, Na and K metal terminations have each been studied computationally as well.[35,97] However, the main focus of work with group I and II metals has been on metal-oxygen terminations with up to 1 ML of metal. Table 2.1 lists some of the adsorption energies and EAs that have been calculated from computational studies of terminations with the group I and II elements. The metal-oxygen terminations give larger thermal stabilities than metal terminations for up to 1 ML coverage, due to the metal-oxygen and oxygen-carbon bonds being stronger than a metal-carbon bond. The NEA is often comparable, despite the inclusion of an electronegative O atom in the metal-oxygen terminations. This is because the metal is fully ionised and so the metal-oxygen bond has a larger positive charge at the surface than the dipole from a metal-carbon bond. As the metal is ionised and (partially) oxidised, the surface is also expected to be air-stable.

Table 2.1: Previous theoretical calculations of group I and II metal and metal-oxygen terminations.

Termination	Surface	Coverage (ML)	Adsorption Energy (eV/atom)	Electron Affinity (eV)	Ref.
Li	(100)	1	-3.26	-2.70	35
Li	(111)	1	-1.50	-0.81	98
LiO	(100)	1	-3.64	-3.50	99
LiO	(111)	0.5	-4.37	-3.97	98
NaO	(100)	0.5	-2.41	-1.30	99
KO	(100)	0.25	-2.44	-2.44	99
CsO	(100)	0.25	-2.19	-2.41	99
MgO	(100)	0.5	-3.92	-2.77	99
MgO	(111)	0.25	-5.27	-3.08	100

The caesium-oxygen termination shows promising field emission characteristics, with a low onset field of 0.2 V μm^{-1}.[101] It is unsuitable for thermionic applications, however, as Cs desorbs from the surface above 400–500 °C.[102,103] While Cs is the most electropositive element available, group I metals show a trend that for the lighter, less electropositive elements the NEA is comparable to larger elements. This is likely to be because of two factors: higher coverage can be achieved due to the smaller size, and the metal-oxygen distance can be smaller, giving a larger surface dipole. Notably, the thermal stability of smaller group I elements is much larger. Figure 2.12 shows the different bonding possibilities of a metal to oxygenated diamond. Smaller group I elements form a more ionic bond, while larger elements have a weaker dipole-dipole interaction.

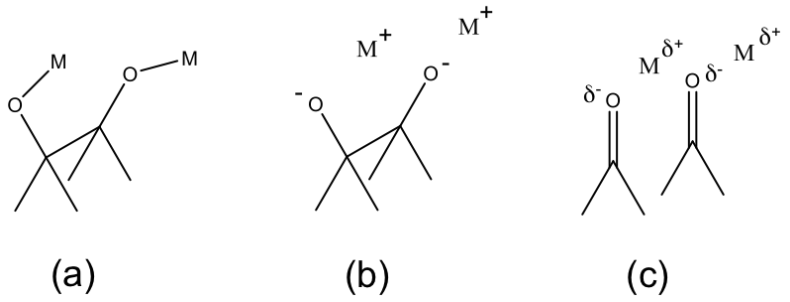

Figure 2.12: Different potential interactions between a metal (M) and O-terminated diamond. (a) Covalent bonding, (b) ionic bonding and (c) dipolar interactions. Adapted from O'Donnell *et al*.[99]

When compared to hydrogen termination, an LiO-termination with 1 ML Li has a similar predicted thermal stability, but with a larger NEA of up to -3.50 eV. Experimental work found a 200× secondary electron yield enhancement for LiO-termination compared with an O-terminated surface. The LiO-termination exhibits variable NEA values with different annealing temperatures, but an NEA is still present even after a 1200 °C anneal.[36] The LiO-termination also has shown a ~5× higher field emission current than H-termination under 3 kV bias, and a thermionic current an order of magnitude higher than for a H-terminated sample for emission at ~500 °C.[36]

Theoretical calculations of the MgO-termination show similar properties to LiO-termination but at lower coverages.[99,100] Experimentally, a 1.5 Å Mg layer deposited on O-terminated (100) diamond was found to have a large NEA of -2.0 eV, becoming more positive and reaching -0.9 eV after a 700 °C anneal. The surface was also shown to be both air and water-stable.[104]

2.4.2 Transition Metals

Similar to the group I and II metals, first-row transition metals (TMs) are more electropositive than hydrogen, and so have also been investigated for the formation of NEA surfaces.[105–110] Experimental studies of thin (<10 Å) metal layers of Ti, Co, Ni, Cu and Zr directly deposited onto the diamond surface have all shown an NEA characteristic in ultraviolet photoelectron spectroscopy (UPS).[105–108] A 3 Å Ti layer on diamond exhibits stable electron emission up to 950 °C,[20] doubling the achievable emission current density compared to a similar H-terminated sample due to the higher temperatures that can be reached. A similar result is obtained with Zr-terminated diamond.[111] The magnitude of the NEA was found to vary depending on TM and layer thickness.

A few preliminary experimental studies have been completed for metal-oxygen terminations. Co and Cu layers deposited onto O-terminated BDD have a PEA, but a Zr layer has an NEA.[112] Deposition of V onto O-terminated BDD films changed the work function from 4.7 eV to 3.8 eV with metal deposition and 650 °C anneal,[113] giving an NEA calculated to be -0.47 eV. The VO-termination on nitrogen-doped diamond did not show NEA, however.[113] A similar study using Cr

or Ti deposition changed the work function from 4.33 eV to 3.53 eV for both metals, giving an NEA of -0.37 eV for Cr and -0.54 eV for Ti.[114]

Table 2.2 lists results of computational studies of metal and metal-oxygen terminations with TMs. An NEA is predicted with Ti, V, Ni and Cu on the bare surface and Ti, Ni, Cu and Zn on the O-terminated diamond surface. Results suggest that the adsorption of carbide-forming TMs such as Ti and V onto diamond shows the largest adsorption energies and most negative EAs, likely due the stronger metal-carbon bonds formed.[109,115] The transition metals generally have much larger adsorption energies than H-termination, unlike group I and II metals, even just for metal terminations. The results show large NEAs are attainable, but they are less negative than the group I and II metals.

Table 2.2: Previous theoretical calculations of transition metal and metal-oxygen terminations.

Termination	Surface	Coverage (ML)	Adsorption Energy (eV/atom)	Electron Affinity (eV)	Ref.
Ti	(100)	0.25	-4.71	-0.90	115
V	(100)	0.5	-6.60	-0.76	115
Ni	(100)	0.25	-4.25	-0.29	115
Cu	(100)	1	-2.93	-0.55	115
TiO	(100)	0.25	-7.60	-3.10	110
NiO	(100)	0.5	-3.80	-0.16	110
CuO	(100)	0.5	-2.35	-1.28	110
ZnO	(100)	0.5	-1.13	-3.05	110

2.4.3 Aluminium

A preliminary study of Al deposition on O-terminated BDD has been completed,[114] and is the motivation behind the work completed in this thesis. After annealing at 650 °C the AlO-terminated sample had a work function of 3.61 eV and an NEA of -0.42 eV.

A computational study on AlO-terminated (100) and (111) diamond has recently reported NEAs of between -2 eV and -3 eV for an AlO_3 configuration, but found a less negative NEA or PEA at higher Al coverage.[116] The adsorption energy for the deposition of Al and O onto the bare diamond surface was

generally found to be slightly exothermic with respect to bulk Al_2O_3. This work was published after the computational results in Chapter 4 were completed.

2.5 Metal Deposition onto Diamond

For electronic devices, it is important to be able to reproducibly form metal-semiconductor contacts. These can either be Schottky contacts, where there is a barrier for electron migration, or Ohmic contacts, where there is little to no barrier. The barrier height will depend upon whether the diamond is doped. Values for many metals on diamond have been reported. Commonly, diamond devices use Al as a Schottky contact. For Ohmic contacts, metals such as Au, Ag and Pd have been used. For some metals on diamond an annealed Schottky contact can become an Ohmic contact due to the formation of a carbide layer.[117] For a high quality Ohmic contact, a layered series of metals such as Au/Ti/Pd can be used.[118]

Many metals have been deposited onto BDD electrodes electrochemically. Deposition of these metals could be used to develop novel catalysts or sensors.[119] Metals deposit in bulk onto diamond, with underpotential deposition behaviour limited to grain boundaries.[120]

The deposition of metal layers onto diamond surfaces and subsequent annealing can produce an epitaxial graphene layer through the catalytic conversion of sp^3 to sp^2 carbon.[121–126] The deposition of a thick (>20 nm) Ni layer has been shown to produce single-layer graphene on nanocrystalline diamond,[123] and multilayer graphene on single-crystal and polycrystalline diamond.[121–124] Deposition of a thin (2–3 nm) Fe layer has been shown to produce single and multilayer graphene on (111) diamond.[125,126]

Field effect transistors (FETs) have been fabricated by metal deposition onto H-terminated diamond. Surface adsorbates induce a 2DHG through surface transfer doping and are intentionally encapsulated beneath the gate contact. Gold contacts have been used to fabricate sub-100 nm FETs[127] with a large cut-off frequency of 53 GHz.[128]

2.6 Oxide and Nitride Deposition onto Diamond

Large electron affinity oxides and nitrides deposited onto diamond have been used as gate dielectrics in diamond-based capacitors and FETs.[129] When deposited onto H-terminated diamond, surface transfer doping gives a thermally stable 2DHG on the diamond surface. This type of metal oxide-semiconductor FET (MOSFET) is illustrated in Figure 2.13, and is similar to FETs described in the previous section, but without the need for surface adsorbates to induce the 2DHG. Alternatively, on PEA diamond, inversion-channel devices can be formed, where conduction occurs instead through p- and n-type layers and so diamond surface termination is tailored specifically to avoid a 2DHG. O-termination, in particular, allows a high-quality interface between diamond and the metal oxide layer.[130]

For the gate dielectric material, numerous oxides have been studied, including Al_2O_3, HfO_2, Ta_2O_5, ZrO_2, MoO_3, V_2O_5, Nb_2O_5, WO_3, Y_2O_3 and SiO_2,[131–145] as well as the nitride AlN.[146] High dielectric constant materials are desirable as these have higher charge response to small electric fields.[141] Addition of a typical metal oxide dielectric gives a hole sheet density of around 10^{12}–10^{13} cm^{-2}. Sheet density of up to 10^{14} cm^{-2} is observed with NO_2 exposure,[147] so MOSFETs with encapsulated NO_2 have also been demonstrated.[148] Recent work has also shown thin layers of ReO_3 and WO_3 can also generate sheet carrier density of 10^{14} cm^{-2}.[149] A number of bilayer structures have also been formed, which can combine the properties of two high-dielectric-constant insulators. Liu *et al*. have recently reviewed these structures.[150]

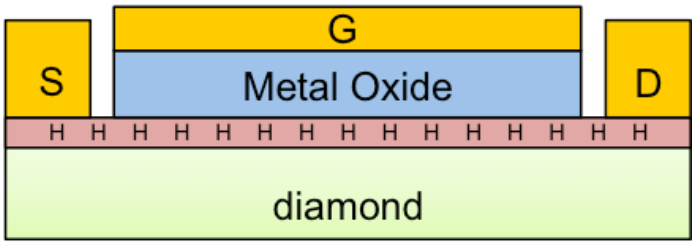

Figure 2.13: Schematic cross-sectional diagram of a typical diamond MOSFET. Metal oxide deposition on H-terminated diamond generates a 2DHG at the diamond surface. S, G and D are source, gate and drain contacts, respectively.

2.7 Chapter Summary

This chapter provides a summary of prior research on the surface functionalisation of diamond. Applications include electronic devices, quantum applications, photocatalysis, renewable energy generation and biological applications.

Of particular relevance for this thesis is the prior work on NEA and electron emission from diamond. Studies of H-terminated diamond have shown electron emission is promising, but suffers from the degradation of H-termination, removing NEA. There is a need for temperature-stable surface terminations for thermionic emission applications. A number of metal and metalloids have previously been explored. This thesis examines the potential for NEA applications using Al terminations.

References

1 L. K. Bigelow and M. P. D'Evelyn, *Surf. Sci.*, 2002, **500**, 986–1004.
2 R. H. Telling, C. J. Pickard, M. C. Payne and J. E. Field, *Phys. Rev. Lett.*, 2000, **84**, 5160–5163.
3 K. C. Pandey, *Phys. Rev. B*, 1982, **25**, 4338–4341.
4 F. Maier, J. Ristein and L. Ley, *Phys. Rev. B*, 2001, **64**, 165411.
5 T. Ando, M. Ishii, M. Kamo and Y. Sato, *J. Chem. Soc. Faraday Trans.*, 1993, **89**, 1783–1789.
6 J. Van Der Weide and R. J. Nemanich, *Appl. Phys. Lett.*, 1993, **62**, 1878–1880.
7 B. D. Thoms, M. S. Owens, J. E. Butler and C. Spiro, *Appl. Phys. Lett.*, 1994, **65**, 2957–2959.
8 M. I. Landstrass and K. V. Ravi, *Appl. Phys. Lett.*, 1989, **55**, 1391–1393.
9 F. Maier, M. Riedel, B. Mantel, J. Ristein and L. Ley, *Phys. Rev. Lett.*, 2000, **85**, 3472–3475.
10 P. Strobel, M. Riedel, J. Ristein and L. Ley, *Diam. Relat. Mater.*, 2004, **430**, 439–441.

11 M. W. Geis, T. H. Fedynyshyn, M. E. Plaut, T. C. Wade, C. H. Wuorio, S. A. Vitale, J. O. Varghese, T. A. Grotjohn, R. J. Nemanich and M. A. Hollis, *Diam. Relat. Mater.*, 2018, **84**, 86–94.
12 J. Ristein, *Surf. Sci.*, 2006, **600**, 3677–3689.
13 J. B. Cui, J. Ristein and L. Ley, *Phys. Rev. Lett.*, 1998, **81**, 429–432.
14 C. Bandis and B. B. Pate, *Phys. Rev. B*, 1995, **52**, 12056–12071.
15 C. Bandis and B. B. Pate, *Surf. Sci.*, 1996, **350**, 315–321.
16 L. Diederich, P. Aebi, O. M. Kuttel and L. Schlapbach, *Surf. Sci.*, 1999, **424**, L314–L320.
17 J. Van Der Weide, Z. Zhang, P. K. Baumann, M. G. Wensell, J. Bernholc and R. J. Nemanich, *Phys. Rev. B*, 1994, **50**, 5803–5806.
18 M. J. Rutter and J. Robertson, *Phys. Rev. B*, 1998, **57**, 9241–9245.
19 S. J. Sque, R. Jones and P. R. Briddon, *Phys. Rev. B*, 2006, **73**, 085313.
20 F. A. M. Köck, J. M. Garguilo, B. Brown and R. J. Nemanich, *Diam. Relat. Mater.*, 2002, **11**, 774–779.
21 P. Ascarelli, E. Cappelli, F. Pinzari, C. Rossi, S. Salvatori, G. Merli and A. Migliori, *J. Appl. Phys.*, 2001, **89**, 689–696.
22 M. Kataoka, C. Zhu, F. A. M. Koeck and R. J. Nemanich, *Diam. Relat. Mater.*, 2010, **19**, 110–113.
23 W. F. Paxton, M. Howell, W. P. Kang and J. L. Davidson, *J. Vac. Sci. Technol. B*, 2012, **30**, 021202.
24 F. A. M. Koeck, R. J. Nemanich, A. Lazea and K. Haenen, *Diam. Relat. Mater.*, 2009, **18**, 789–791.
25 J. Ristein, *Diam. Relat. Mater.*, 2000, **9**, 1129–1137.
26 A. Croot, G. Wan, A. Rowan, H. D. Andrade, J. A. Smith and N. A. Fox, *Front. Mech. Eng.*, 2017, **3**, 1–8.
27 D. Zhu, L. Zhang, R. E. Ruther and R. J. Hamers, *Nat. Mater.*, 2013, **12**, 836–841.
28 L. Zhang, D. Zhu, G. M. Nathanson and R. J. Hamers, *Angew. Chemie Int. Ed.*, 2014, **53**, 9746–9750.
29 X. M. Zheng and P. V. Smith, *Surf. Sci.*, 1992, **262**, 219–234.
30 T. Ando, K. Yamamoto, M. Ishii, M. Kamo and Y. Sato, *J. Chem. Soc. Faraday Trans.*, 1993, **89**, 3635–3640.
31 K. P. Loh, X. N. Xie, S. W. Yang and J. C. Zheng, *J. Phys. Chem. B*, 2002, **106**, 5230–5240.
32 T. E. Derry, N. W. Makau and C. Stampfl, *J. Phys. Condens. Matter*, 2010, **22**, 265007.
33 R. Yoshida, D. Miyata, T. Makino, S. Yamasaki, T. Matsumoto, T. Inokuma and N. Tokuda, *Appl. Surf. Sci.*, 2018, **458**, 222–225.
34 P. K. Baumann and R. J. Nemanich, *Surf. Sci.*, 1998, **409**, 320–335.
35 K. M. O'Donnell, T. L. Martin, N. A. Fox and D. Cherns, *Phys. Rev. B*, 2010, **82**, 115303.
36 T. L. Martin, *Lithium Oxygen Termination as a Negative Electron Affinity Surface on Diamond: a Computational and Photoemission Study*, PhD Thesis, University of Bristol, 2011.
37 M. Kaviani, P. Deák, B. Aradi, T. Frauenheim, J. P. Chou and A. Gali, *Nano Lett.*, 2014, **14**, 4772–4777.
38 R. Boukherroub, X. Wallart, S. Szunerits, B. Marcus, P. Bouvier and M. Mermoux, *Electrochem. commun.*, 2005, **7**, 937–940.

39 Y. Coffinier, S. Szunerits, B. Marcus, R. Desmet, O. Melnyk, L. Gengembre, E. Payen, D. Delabouglise and R. Boukherroub, *Diam. Relat. Mater.*, 2007, **16**, 892–898.
40 P. Actis, M. Manesse, C. Nunes-Kirchner, G. Wittstock, Y. Coffinier, R. Boukherroub and S. Szunerits, *Phys. Chem. Chem. Phys.*, 2006, **8**, 4924–4931.
41 W. Kulisch, C. Popov, D. Gilliland, G. Ceccone, J. P. Reithmaier and F. Rossi, *Surf. Coatings Technol.*, 2011, **206**, 667–675.
42 M. Steenackers, S. Q. Lud, M. Niedermeier, P. Bruno, D. M. Gruen, P. Feulner, M. Stutzmann, J. A. Garrido and R. Jordan, *J. Am. Chem. Soc.*, 2007, **129**, 15655–15661.
43 M. Hoeb, M. Auernhammer, S. J. Schoell, M. S. Brandt, J. A. Garrido, M. Stutzmann and I. D. Sharp, *Langmuir*, 2010, **26**, 18862–18867.
44 D. Delabouglise, B. Marcus, M. Mermoux, P. Bouvier, J. Chane-Tune, J. P. Petit, P. Mailley and T. Livache, *Chem. Commun.*, 2003, **21**, 2698–2699.
45 P. Bouvier, D. Delabouglise, A. Denoyelle, B. Marcus, M. Mermoux and J.-P. Petit, *Electrochem. Solid-State Lett.*, 2005, **8**, E57–E61.
46 S. Szunerits, N. Shirahata, P. Actis, J. Nakanishi and R. Boukherroub, *Chem. Commun.*, 2007, 2793–2795.
47 M. Mazur, P. Krysiński and G. J. Blanchard, *Langmuir*, 2005, **21**, 8802–8808.
48 C. Presti, J. G. Alauzun, D. Laurencin and P. H. Mutin, *Chem. Mater.*, 2013, **25**, 2051–2055.
49 H. Notsu, I. Yagi, T. Tatsuma, D. A. Tryk and A. Fujishima, *J. Electroanal. Chem.*, 2000, **492**, 31–37.
50 S. Torrengo, A. Miotello, L. Minati, I. Bernagozzi, M. Ferrari, M. Dipalo, E. Kohn and G. Speranza, *Diam. Relat. Mater.*, 2011, **20**, 990–994.
51 J. H. Yang, Y. Nakano, Y. Murakami, K. S. Song and H. Kawarada, *J. Nanoparticle Res.*, 2008, **10**, 69–75.
52 K. Ushizawa, Y. Sato and T. Mitsumori, *Chem. Phys. Lett.*, 2002, **351**, 105–108.
53 H. B. Man and D. Ho, *Phys. Status Solidi*, 2012, **209**, 1609–1618.
54 S. Szunerits and R. Boukherroub, *J. Solid State Electrochem.*, 2008, **12**, 1205–1218.
55 M. Chandran, M. Shasha, S. Michaelson and A. Hoffman, *Appl. Phys. Lett.*, 2015, **107**, 111602.
56 A. Stacey, K. M. O'Donnell, J. P. Chou, A. Schenk, A. Tadich, N. Dontschuk, J. Cervenka, C. Pakes, A. Gali, A. Hoffman and S. Prawer, *Adv. Mater. Interfaces*, 2015, **2**, 1500079.
57 J. P. Chou, A. Retzker and A. Gali, *Nano Lett.*, 2017, **17**, 2294–2298.
58 D. Zhu, J. A. Bandy, S. Li and R. J. Hamers, *Surf. Sci.*, 2016, **650**, 295–301.
59 J. B. Miller, *Surf. Sci.*, 1999, **439**, 21–33.
60 H. Kawarada and A. R. Ruslinda, *Phys. Status Solidi Appl. Mater. Sci.*, 2011, **208**, 2005–2016.
61 M. H. Hsu, H. Chuang, F. Y. Cheng, Y. P. Huang, C. C. Han, J. Y. Chen, S. C. Huang, J. K. Chen, D. S. Wu, H. L. Chu and C. C. Chang, *ACS Appl. Mater. Interfaces*, 2014, **6**, 7198–7203.
62 T. Nakamura, T. Ohana, Y. Hagiwara and T. Tsubota, *Phys. Chem. Chem. Phys.*, 2009, **11**, 730–734.

63 A. K. Tiwari, J. P. Goss, P. R. Briddon, N. G. Wright, A. B. Horsfall, R. Jones, H. Pinto and M. J. Rayson, *Phys. Status Solidi Appl. Mater. Sci.*, 2012, **209**, 1709–1714.
64 A. K. Tiwari, J. P. Goss, P. R. Briddon, N. G. Wright, A. B. Horsfall, R. Jones, H. Pinto and M. J. Rayson, *Phys. Rev. B*, 2011, **84**, 245305.
65 C. J. Widmann, C. Giese, M. Wolfer, S. Kono and C. E. Nebel, *Phys. Status Solidi Appl. Mater. Sci.*, 2014, **211**, 2328–2332.
66 K. J. Rietwyk, S. L. Wong, L. Cao, K. M. O'Donnell, L. Ley, A. T. S. Wee and C. I. Pakes, *Appl. Phys. Lett.*, 2013, **102**, 091604.
67 M. Karlsson, P. Forsberg and F. Nikolajeff, *Langmuir*, 2010, **26**, 889–893.
68 T. Kondo, H. Ito, K. Kusakabe, K. Ohkawa, Y. Einaga, A. Fujishima and T. Kawai, *Electrochim. Acta*, 2007, **52**, 3841–3848.
69 Y. Wang, H. Huang, J. Zang, F. Meng, L. Dong and J. Su, *Int. J. Electrochem. Sci.*, 2012, **7**, 6807–6815.
70 V. N. Mochalin, O. Shenderova, D. Ho and Y. Gogotsi, *Nat. Nanotechnol.*, 2012, **7**, 11–23.
71 P. W. May, J. C. Stone, M. N. R. Ashfold, K. R. Hallam, W. N. Wang and N. A. Fox, *Diam. Relat. Mater.*, 1998, **7**, 671–676.
72 A. K. Tiwari, *Diamond-Based Thermo-Tunnel Devices for Hostile Environments*, PhD Thesis, University of Newcastle, 2013.
73 J. B. Miller and D. W. Brown, *Langmuir*, 1996, **12**, 5809–5817.
74 M. Wang, M. R. Das, V. G. Praig, F. LeNormand, M. Li, R. Boukherroub and S. Szunerits, *Chem. Commun.*, 2008, **47**, 6294–6296.
75 M. R. Lockett and L. M. Smith, *Langmuir*, 2009, **25**, 3340–3343.
76 T. Strother, T. Knickerbocker, J. N. Russell, J. E. Butler, L. M. Smith and R. J. Hamers, *Langmuir*, 2002, **18**, 968–971.
77 R. E. Ruther, M. L. Rigsby, J. B. Gerken, S. R. Hogendoorn, E. C. Landis, S. S. Stahl and R. J. Hamers, *J. Am. Chem. Soc.*, 2011, **133**, 5692–5694.
78 I. Zegkinoglou, P. L. Cook, P. S. Johnson, W. Yang, J. Guo, D. Pickup, R. González-Moreno, C. Rogero, R. E. Ruther, M. L. Rigsby, J. E. Ortega, R. J. Hamers and F. J. Himpsel, *J. Phys. Chem. C*, 2012, **116**, 13877–13883.
79 S. A. Yao, R. E. Ruther, L. Zhang, R. A. Franking, R. J. Hamers and J. F. Berry, *J. Am. Chem. Soc.*, 2012, **134**, 15632–15635.
80 T.-C. Kuo, R. L. McCreery and G. M. Swain, *Electrochem. Solid-State Lett.*, 1999, **2**, 288–290.
81 B. M. Nichols, J. E. Butler, J. N. Russell and R. J. Hamers, *J. Phys. Chem. B*, 2005, **109**, 20938–20947.
82 S. Szunerits, C. E. Nebel and R. J. Hamers, *MRS Bull.*, 2014, **39**, 517–524.
83 T. Knickerbocker, T. Strother, M. P. Schwartz, J. N. Russell, J. Butler, L. M. Smith and R. J. Hamers, *Langmuir*, 2003, **19**, 1938–1942.
84 S. Wenmackers, P. Christiaens, M. Daenen, K. Haenen, M. Nesládek, M. Van DeVen, V. Vermeeren, L. Michiels, M. Ameloot and P. Wagner, *Phys. Status Solidi*, 2005, **202**, 2212–2216.
85 W. Yang, S. E. Baker, J. E. Butler, C. S. Lee, J. N. Russell, L. Shang, B. Sun and R. J. Hamers, *Chem. Mater.*, 2005, **17**, 938–940.
86 M. Liu, G. Zhao and Y. Qi, *Int. J. Environ. Anal. Chem.*, 2012, **92**, 534–547.
87 Y. L. Zhong, K. P. Loh, A. Midya and Z. Chen, *Chem. Mater.*, 2008, **20**, 3137–3144.
88 H. Krysova, L. Kavan, Z. V. Zivcova, W. S. Yeap, P. Verstappen, W. Maes, K.

Haenen, F. Gao and C. E. Nebel, *RSC Adv.*, 2015, **5**, 81069–81077.
89 D. Qi, L. Liu, X. Gao, T. Ouyang, S. Chen, K. P. Loh and A. T. S. Wee, *Langmuir*, 2007, **23**, 9722–9727.
90 G. Jarre, Y. Liang, P. Betz, D. Lang and A. Krueger, *Chem. Commun.*, 2011, **47**, 544–546.
91 A. K. Schenk, A. Tadich, M. J. Sear, D. Qi, A. T. S. Wee, A. Stacey and C. I. Pakes, *Nanotechnology*, 2016, **27**, 275201.
92 A. Schenk, A. Tadich, M. Sear, K. M. O'Donnell, L. Ley, A. Stacey and C. Pakes, *Appl. Phys. Lett.*, 2015, **106**, 191603.
93 A. K. Schenk, M. J. Sear, A. Tadich, A. Stacey and C. I. Pakes, *J. Phys. Condens. Matter*, 2017, **29**, 025003.
94 M. J. Sear, A. K. Schenk, A. Tadich, A. Stacey and C. I. Pakes, *Appl. Phys. Lett.*, 2017, **110**, 011605.
95 M. J. Sear, A. K. Schenk, A. Tadich, B. J. Spencer, C. A. Wright, A. Stacey and C. I. Pakes, *J. Phys. Condens. Matter*, 2017, **29**, 145002.
96 W. M. Haynes, *CRC Handbook of Chemistry and Physics*, CRC Press, Boca Raton, FL, USA, 96th edn., 2015.
97 J. L. Nie, H. Y. Xiao and X. T. Zu, *Chem. Phys.*, 2006, **326**, 308–314.
98 K. M. O'Donnell, T. L. Martin, M. T. Edmonds, A. Tadich, L. Thomsen, J. Ristein, C. I. Pakes, N. A. Fox and L. Ley, *Phys. Status Solidi*, 2014, **211**, 2209–2222.
99 K. M. O'Donnell, T. L. Martin and N. L. Allan, *Chem. Mater.*, 2015, **27**, 1306–1315.
100 M. C. James, P. W. May and N. L. Allan, *J. Phys. Condens. Matter*, 2019, **31**, 295002.
101 M. W. Geis, J. C. Twichell, J. Macaulay and K. Okano, *Appl. Phys. Lett.*, 1995, **67**, 1328–1330.
102 K. P. Loh, J. S. Foord, R. G. Egdell and R. B. Jackman, *Diam. Relat. Mater.*, 1997, **5**, 874–878.
103 K. P. Loh, X. N. Xie, S. W. Yang, J. S. Pan and P. Wu, *Diam. Relat. Mater.*, 2002, **11**, 1379–1384.
104 K. M. O'Donnell, M. T. Edmonds, A. Tadich, L. Thomsen, A. Stacey, A. Schenk, C. I. Pakes and L. Ley, *Phys. Rev. B*, 2015, **92**, 035303.
105 P. K. Baumann and R. J. Nemanich, *Appl. Surf. Sci.*, 1996, **104**–**105**, 267–273.
106 P. K. Baumann and R. J. Nemanich, *Phys. Rev. B*, 1998, **58**, 1643–1654.
107 P. K. Baumann and R. J. Nemanich, *J. Appl. Phys.*, 1998, **83**, 2072.
108 J. van der Weide and R. J. Nemanich, *J. Vac. Sci. Technol. B*, 1992, **10**, 1940–1943.
109 A. K. Tiwari, J. P. Goss, P. R. Briddon, N. G. Wright, A. B. Horsfall and M. J. Rayson, *Phys. Status Solidi*, 2012, **209**, 1697–1702.
110 A. K. Tiwari, J. P. Goss, P. R. Briddon, A. B. Horsfall, N. G. Wright, R. Jones and M. J. Rayson, *Europhys. Lett.*, 2014, **108**, 46005.
111 F. A. M. Koeck, J. M. Garguilo and R. J. Nemanich, *Diam. Relat. Mater.*, 2004, **13**, 2052–2055.
112 P. K. Baumann and R. J. Nemanich, *Diam. Relat. Mater.*, 1998, **7**, 612–619.
113 T. Sun, *Combined Photo- and Thermionic Electron Emission from Low Work Function Diamond Films*, PhD Thesis, Arizona State University, 2013.
114 M. Z. Othman, *Studies of n-type Doping and Surface Modification of CVD*

Diamond for use in Thermionic Applications, PhD Thesis, University of Bristol, 2014.
115 A. K. Tiwari, J. P. Goss, P. R. Briddon, N. G. Wright, A. B. Horsfall and M. J. Rayson, *Phys. Rev. B*, 2012, **86**, 155301.
116 J. M. A. Beattie, J. P. Goss, M. J. Rayson and P. R. Briddon, *Diam. Relat. Mater.*, 2019, **94**, 137–145.
117 M. Wade, P. Muret, F. Omnès and A. Deneuville, *Diam. Relat. Mater.*, 2006, **15**, 614–617.
118 M. Liao, J. Liu, L. Sang, D. Coathup, J. Li, M. Imura, Y. Koide and H. Ye, *Appl. Phys. Lett.*, 2015, **106**, 083506.
119 M. Awada, J. W. Strojek and G. M. Swain, *J. Electrochem. Soc.*, 1995, **142**, L42–L45.
120 F. Bouamrane, a Tadjeddine, R. Tenne, J. E. Butler, R. Kalish and C. Levy-Clement, *J. Phys. Chem. B*, 1998, **102**, 134–140.
121 J. M. García, R. He, M. P. Jiang, P. Kim, L. N. Pfeiffer and A. Pinczuk, *Carbon*, 2011, **49**, 1006–1012.
122 O. Romanyuk, M. Varga, S. Tulic, T. Izak, P. Jiricek, A. Kromka, V. Skakalova and B. Rezek, *J. Phys. Chem. C*, 2018, **122**, 6629–6636.
123 D. Berman, S. A. Deshmukh, B. Narayanan, S. K. R. S. Sankaranarayanan, Z. Yan, A. A. Balandin, A. Zinovev, D. Rosenmann and A. V. Sumant, *Nat. Commun.*, 2016, **7**, 1–8.
124 S. Tulić, T. Waitz, M. Čaplovičová, G. Habler, M. Varga, M. Kotlár, V. Vretenár, O. Romanyuk, A. Kromka, B. Rezek and V. Skákalová, *ACS Nano*, 2019, **13**, 4621–4630.
125 S. P. Cooil, F. Song, G. T. Williams, O. R. Roberts, D. P. Langstaff, B. Jørgensen, K. Høydalsvik, D. W. Breiby, E. Wahlström, D. A. Evans and J. W. Wells, *Carbon*, 2012, **50**, 5099–5105.
126 S. P. Cooil, J. W. Wells, D. Hu, Y. R. Niu, A. A. Zakharov, M. Bianchi and D. A. Evans, *Appl. Phys. Lett.*, 2015, **107**, 181603.
127 D. A. J. Moran, O. J. L. Fox, H. McLelland, S. Russell and P. W. May, *IEEE Electron Device Lett.*, 2011, 32, 599–601.
128 D. A. J. Moran, S. A. O. Russell, S. Sharabi and A. Tallaire, *IEEE Nano*, 2012, 1–5.
129 C. I. Pakes, J. A. Garrido and H. Kawarada, *MRS Bull.*, 2014, **39**, 542–548.
130 T. Matsumoto, H. Kato, K. Oyama, T. Makino, M. Ogura, D. Takeuchi, T. Inokuma, N. Tokuda and S. Yamasaki, *Sci. Rep.*, 2016, **6**, 1–6.
131 M. Kasu, H. Sato and K. Hirama, *Appl. Phys. Express*, 2012, **5**, 025701.
132 H. Kawarada, H. Tsuboi, T. Naruo, T. Yamada, D. Xu, A. Daicho, T. Saito and A. Hiraiwa, *Appl. Phys. Lett.*, 2014, **105**, 013510.
133 S. Colangeli, C. Verona, W. Ciccognani, M. Marinelli, G. Verona-Rinati, E. Limiti, M. Benetti, D. Cannatà and F. Di Pietrantonio, in *IEEE*, 2016.
134 C. Verona, F. Arciprete, M. Foffi, E. Limiti, M. Marinelli, E. Placidi, G. Prestopino and G. Verona-Rinati, *Appl. Phys. Lett.*, 2018, **112**, 181602.
135 C. Verona, W. Ciccognani, S. Colangeli, E. Limiti, M. Marinelli and G. Verona-Rinati, *J. Appl. Phys.*, 2016, **120**, 025104.
136 J. W. Liu, H. Oosato, M. Y. Liao and Y. Koide, *Appl. Phys. Lett.*, 2017, **110**, 203502.
137 T. Saito, K. H. Park, K. Hirama, H. Umezawa, M. Satoh, H. Kawarada, Z. Q. Liu, K. Mitsuishi, K. Furuya and H. Okushi, *J. Electron. Mater.*, 2011, **40**,

247–252.
138 A. Daicho, T. Saito, S. Kurihara, A. Hiraiwa and H. Kawarada, *J. Appl. Phys.*, 2014, **115**, 223711.
139 J. W. Liu, M. Y. Liao, M. Imura and Y. Koide, *Appl. Phys. Lett.*, 2012, **101**, 252108.
140 S. Cheng, L. Sang, M. Liao, J. Liu, M. Imura, H. Li and Y. Koide, *Appl. Phys. Lett.*, 2012, **101**, 232907.
141 J. Liu, M. Liao, M. Imura, A. Tanaka, H. Iwai and Y. Koide, *Sci. Rep.*, 2014, **4**, 1–5.
142 S. A. O. Russell, L. Cao, D. Qi, A. Tallaire, K. G. Crawford, A. T. S. Wee and D. A. J. Moran, *Appl. Phys. Lett.*, 2013, **103**, 202112.
143 K. G. Crawford, D. Qi, J. McGlynn, T. G. Ivanov, P. B. Shah, J. Weil, A. Tallaire, A. Y. Ganin and D. A. J. Moran, *Sci. Rep.*, 2018, **8**, 1–9.
144 C. Verona, W. Ciccognani, S. Colangeli, E. Limiti, M. Marinelli, G. Verona-Rinati, D. Cannatà, M. Benetti and F. Di Pietrantonio, 2016, **63**, 4647–4653.
145 K. G. Crawford, L. Cao, D. Qi, A. Tallaire, E. Limiti, C. Verona, A. T. S. Wee and D. A. J. Moran, *Appl. Phys. Lett.*, 2016, **108**, 042103.
146 C. Pietzka, J. Scharpf, M. Fikry, D. Heinz, K. Forghani, T. Meisch, T. Diemant, R. J. Behm, J. Bernhard, J. Biskupek, U. Kaiser, F. Scholz and E. Kohn, *J. Appl. Phys.*, 2013, **114**, 114503.
147 H. Sato and M. Kasu, *Diam. Relat. Mater.*, 2013, **31**, 47–49.
148 K. Hirama, H. Sato, Y. Harada, H. Yamamoto and M. Kasu, *Jpn. J. Appl. Phys.*, 2012, **51**, 090112.
149 M. Tordjman, K. Weinfeld and R. Kalish, *Appl. Phys. Lett.*, 2017, **111**, 111601.
150 J. W. Liu, M. Y. Liao, M. Imura, R. G. Banal and Y. Koide, *J. Appl. Phys.*, 2017, **121**, 224502.

Chapter 3 – Experimental Techniques and Procedures

3.1 Introduction

A number of different experimental techniques were used in the course of this research for synthesis, treatment and characterisation of diamond surfaces. This chapter discusses the concepts behind these different techniques and the procedures for using each technique.

3.2 Vacuum Systems

Vacuum systems were routinely used in this work for material synthesis and characterisation. All low-pressure environments required an airtight chamber constructed from materials with low outgassing rates from absorbed or adsorbed species.

Pumps were used to create and maintain a vacuum. Low vacuum is defined as atmospheric pressure down to $\sim 10^{-3}$ mbar, and was achieved by using rotary or scroll pumps. It is suitable for chemical vapour deposition (CVD) systems where air is replaced by other gases. Medium-to-high vacuum has pressures in the range $\sim 10^{-3}$–10^{-9} mbar, achievable with a secondary pump such as a diffusion or turbo pump. Ultrahigh vacuum (UHV) is considered to be at pressures below $\sim 10^{-9}$ mbar and is achievable by using a combination of pumps including cryopumps and titanium sublimation pumps. In addition, it is common for UHV systems to undergo a 'bake out' when pumping from atmospheric pressure; adsorbates are removed by heating the whole chamber and so the entire system needs to be able to withstand 100–300 °C temperatures. Characterisation and deposition methods may use medium, high or UHV vacuum systems, depending on the sensitivity of the method.

3.3 Diamond Synthesis

3.3.1 Substrates

The different substrates used for diamond growth are shown in Figure 3.1. The single-crystal diamond substrates were obtained from Element Six, Ltd. The square substrates were grown by CVD and had a polished (100) face with side length of 3 mm. A surface roughness of Ra = 3.9 nm was determined for one of these samples, as measured by atomic force microscopy over a 40 μm^2 area, where Ra is calculated from the arithmetic average of the absolute deviation of values from the mean. The triangular substrates were grown by the high pressure high temperature (HPHT) method and had a polished (111) face (with Ra = 20.1 nm), and a side length of 4 mm. The yellow colouration of the (111) single crystal is due to nitrogen impurities arising from the HPHT process. A p-type boron-doped diamond (BDD) overlayer (see Section 3.3.2) was grown homoepitaxially on these crystals with hot filament CVD to make the surface conductive and prevent surface charging effects during characterisation procedures that rely on electron emission from the sample.

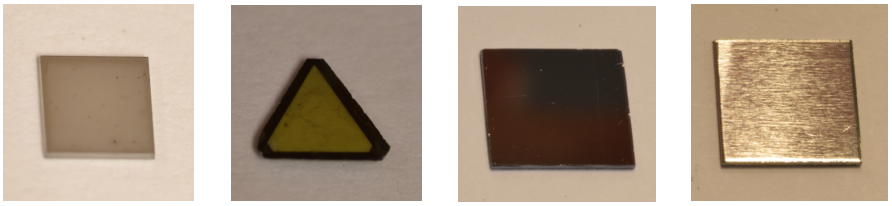

(a) (b) (c) (d)

Figure 3.1: (a) CVD (100) and (b) HPHT (111) single crystal diamond substrates. A p-type diamond overlayer was grown on these single crystals to make the surface conductive. (c) Si and (d) Mo substrates for growth of B-doped and N-doped diamond thin films, respectively.

Polycrystalline diamond was grown heteroepitaxially on larger substrates. BDD thin films were grown on polished n-type silicon (100) substrates (Si-Mat, e.K.) by hot filament CVD, while nitrogen-doped diamond (NDD) thin films were grown on molybdenum substrates (Goodfellow, Ltd) by microwave plasma CVD (Section 3.3.3). The Si substrates were typically cut into 1 cm × 1 cm or

0.5 cm × 0.5 cm squares and the Mo substrates were cut into 1 cm × 1 cm squares.

Both the Si and Mo substrates underwent a pre-treatment process before diamond growth. Nanodiamonds were electrostatically bound to the substrate to act as seed crystals, a method that can increase the nucleation density.[1] First, substrates were sonicated in acetone for 5 min, then washed with deionised water and submerged in a solution of 25% carboxyethylsilanetriol disodium salt in H_2O for 15 min. They were washed again with deionised water, then submerged in an aqueous 25 carat kg^{-1}, 18 nm nanodiamond solution (Microdiamant, GmbH) for 15 min that had been previously been ultrasonicated for 15 min to disperse the nanodiamonds. The substrates were again washed with deionised water, then dried with compressed air.

3.3.2 Hot Filament CVD

A custom-built hot filament CVD reactor was used for growing BDD thin films. Figure 3.2 shows the reactor chamber; the design is the same as shown in Section 1.2.2. The substrate was positioned on a heating stage 4 mm beneath the filament wires within the chamber. The filaments were 0.25 mm diameter tantalum wires which were spring loaded to stay taut. During diamond deposition, the Ta wires slowly react with methane and undergo a carburisation process over a period of a few hours, becoming brittle and unsuitable beyond a single use. Individual mass flow controllers (MFCs) determined gas inflows with all gases stored in gas storage containers in a separate room. The various gas flow rates were calibrated according to Table 3.1. The MFC offset at zero flow rate is included in the determination of relative flow rates.

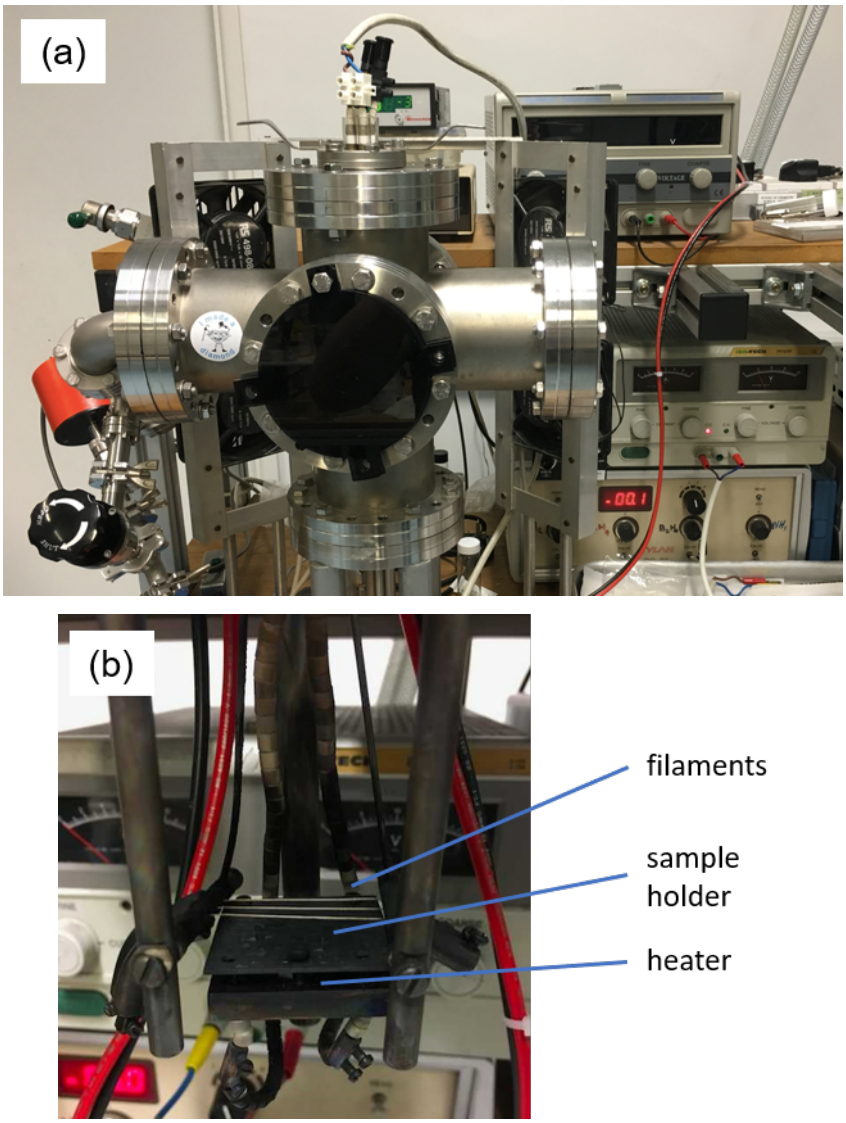

Figure 3.2: (a) Photograph of the hot filament CVD reactor. (b) Photograph of the interior setup of the reactor.

In a typical diamond growth run, the chamber was pumped to 90 mTorr, then the molybdenum sample stage was heated to ~120 °C for at least 30 min to degas adsorbates. This was achieved by passing 4 A from a separate power supply through electrical resistance wires embedded within the sample stage. This step helped to desorb oxygen-containing adsorbates that could react with and break the filaments. A gas mixture comprising H_2, CH_4 (both Air Liquide, Ltd) and B_2H_6 (BOC Group, plc) was flowed into the chamber and the pressure was adjusted to 20 Torr using a manual needle valve. The flow rates of the H_2 and CH_4 gases were 200 and 2 standard cubic centimetres per minute (sccm), respectively, *i.e.* 1% CH_4 in H_2. The boron feedstock was a gas mixture

comprising 5% B_2H_6 in H_2. The flow rate was 0.1 sccm for epitaxial B-doped layers on single crystal diamond and 0.2 sccm for polycrystalline B-doped diamond grown on n-type Si substrates. To begin diamond growth, the filaments, wired in parallel, were heated by applying a 25 A current; the voltage required to maintain this current increased slightly during the run from ~9 V to ~11 V due to the higher resistance of the carburised filament. These parameters enabled the deposition of a good quality diamond thin film at a growth rate of ~0.5 μm h^{-1}. The temperature of the filaments has been previously measured by optical pyrometry to be ~2300 K. Epitaxial layers on single-crystal diamond were grown for 1 h, while polycrystalline thin films were grown for 3 h. BDD overlayers grown in the same reactor under the same conditions has previously been shown to contain a boron concentration of up to ~10^{20} cm^{-3}, measured from a depth profile using secondary ion mass spectroscopy.[2]

Table 3.1: Calibration of MFCs for BDD growth. *The B_2H_6 gas cylinder contained 5% B_2H_6 in H_2.

Gas	Gas flow rate (sccm)	MFC offset (sccm)	Percentage relative to H_2
CH_4	2	-0.1	1.04
H_2	200	-1	-
B_2H_6*	0.1–0.2	-0.011	0.0028–0.0052

3.3.3 Microwave Plasma CVD

Polycrystalline NDD thin films were grown on molybdenum substrates by 2.45 GHz microwave plasma CVD in a 1.5 kW ASTeX-type reactor. Figure 3.3 shows the reactor chamber; the design is the same as in Section 1.2.2. Samples were positioned on a tungsten disc separated from the bottom of the chamber by a ring of 6 mInch diameter molybdenum wire to reduce thermal contact with the water-cooled baseplate. In a typical diamond growth, the chamber was pumped to 40 mTorr, then a gas mixture consisting of 300 sccm H_2 (generated by electrolysing deionised H_2O with a Noblegen H_2 generator), 12.5 sccm CH_4 and 0.125 sccm N_2 (both Air Liquide, Ltd) was introduced. The pressure and power were set to 130 Torr and 1.3 kW, respectively, corresponding to a plasma

temperature of 800–900 °C, as measured by a 2.2 μm single-colour optical pyrometer. The growth time was 15 min.

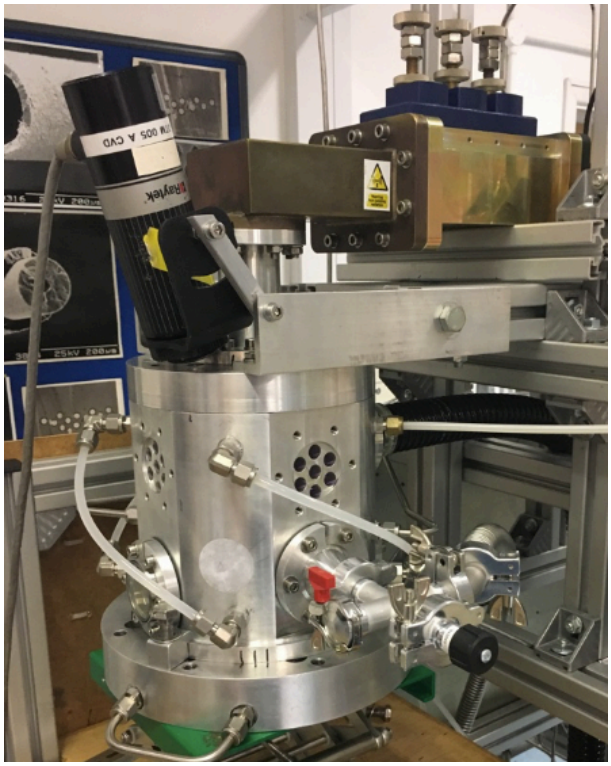

Figure 3.3: Photograph of the microwave plasma CVD reactor.

3.3.4 Acid Cleaning

3.3.4.1 Routine Cleaning

Diamond surfaces were cleaned by refluxing in a solution containing H_2SO_4 and HNO_3. The solution was created by adding 6.5 g KNO_3 to 100 mL H_2SO_4 (95%). The solution was heated in a fume cupboard to reflux temperature for 1 h for routine cleaning and 6 h for new samples. The additional time for the preliminary acid wash was because particulates were visible under an optical microscope for some purchased samples, likely originating from the polishing process. The diamond samples were then rinsed thoroughly with deionised water.

3.3.4.2 Al removal

Diamond surfaces containing Al were cleaned by refluxing in an aqua regia solution. This was prepared by addition of 2.5 mL HNO_3 (69%) to 7.5 mL HCl (37%). The solution was refluxed for 1 h in a fume cupboard. The diamond samples were then rinsed thoroughly with deionised water.

3.4 Termination Procedures

3.4.1 Hydrogen

Hydrogen termination was performed in the microwave plasma reactor, using a 9 mInch diameter Mo wire. The chamber was pumped to 40 mTorr and hydrogen gas was flowed in at 300 sccm. For single-crystal diamond, the samples were initially subjected to a hydrogen plasma at 110 Torr and 1250 W for 2 min, at a temperature of ~850 °C. This was then reduced to 45 Torr and 750–800 W for a further 2 min, equating to temperature of ~500 °C. Finally, the plasma was extinguished by reducing power to 0 W, and the chamber was maintained at the same pressure for a final 2 min in a hydrogen atmosphere. The same procedure was used for polycrystalline samples, except that to reach the same temperature, the first and second steps had pressures of 80 Torr and 40 Torr, respectively, and powers set at 1200 W and 750 W, respectively. This multi-step process first desorbed prior terminations, then allowed H atoms to bond to the diamond surface at a lower temperature.

3.4.2 Oxygen

Four different methods were used to form an oxygen termination from H-terminated diamond: UV/ozone treatment, oxygen plasma, acid wash and oxidation using an atomic layer deposition (ALD) kit. The oxidation times were chosen to maximise oxygen coverage on the surface, and are discussed in Chapter 5.3.

3.4.2.1 UV/Ozone

For UV/ozone treatment, diamond samples were positioned 1.5 inches below a mercury lamp in a Jelight UVO cleaner (Figure 3.4(a)). Air was passed over the samples, which were illuminated with UV light at room temperature and pressure, typically for 30 min. Upon irradiation, oxygen gas forms ozone and atomic oxygen, with ozone also forming further atomic oxygen, which can react with the diamond surface.

3.4.2.2 Oxygen Plasma

Atomic oxygen from an oxygen plasma can react with the diamond surface to form an O-termination. Oxygen plasma treatment was performed using an Edwards S150A sputter coater (Figure 3.4(b)), which had been modified to act as a parallel-plate AC-modulated DC plasma chamber. The sample was positioned on a lower stainless steel, earthed electrode, which was separated from the powered electrode by ~1 cm. The chamber was pumped to 20 mTorr, then oxygen gas was flowed in at 10 sccm and the pressure was adjusted to 1 Torr. An oxygen plasma was struck at 65 W, typically for 7 seconds.

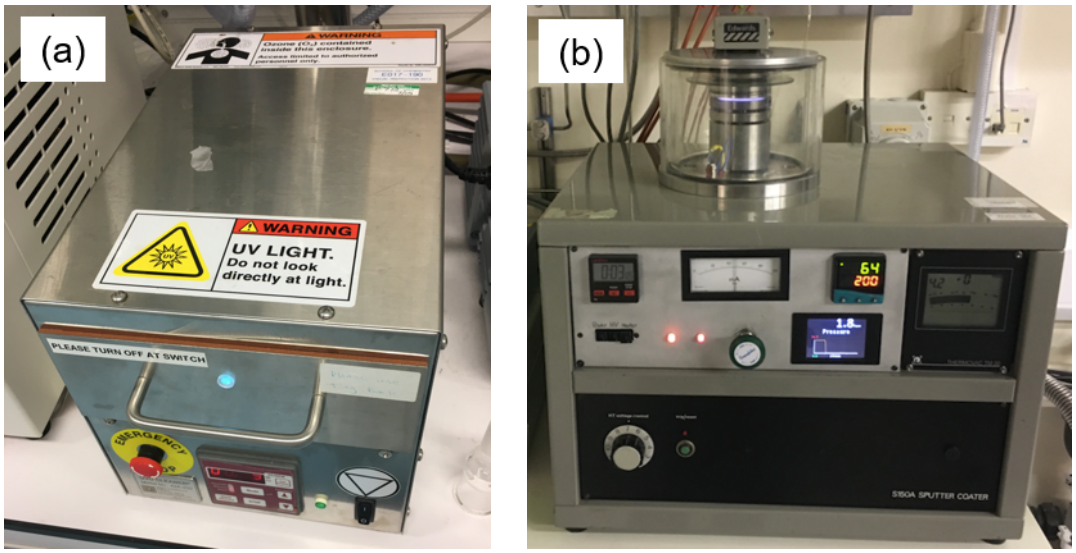

Figure 3.4: Photographs of (a) the UV ozone generator kit and (b) the oxygen plasma kit used for oxygen termination.

3.4.2.3 Acid Oxidation

Diamond can be O-terminated by treatment with oxidising agents. This procedure is the same as described in Section 3.3.4.1. Samples were refluxed in a solution containing H_2SO_4 and HNO_3, formed by adding 6.5 g KNO_3 to 100 mL H_2SO_4 (95%), for 1 h.

3.4.2.4 ALD Oxidation

ALD is a widely used technique for depositing thin films. Gaseous precursors are introduced and react with the surface of a sample in a self-limiting manner, forming up to 1 monolayer (ML) at a time. ALD is typically used to deposit

binary, tertiary and quarternary materials by stepwise introduction of different precursors.[3]

The ALD procedure was performed on samples by Dr Ricardo Silva and Professor Rui Silva at the University of Aveiro in Portugal. A schematic diagram of the ALD chamber has been published previously.[4] For the oxidation procedure, samples were heated to 200 °C at 400 mTorr, then either one or two pulses of H_2O were introduced into the chamber and then pumped out after either 1 or 5 min. H_2O is commonly used as an oxidising species in ALD, and has been shown to react with H-terminated diamond at high temperature previously.[5]

3.4.3 Aluminium

Three methods were used to deposit aluminium on diamond: thermal evaporation, ALD, and electron-beam evaporation.

3.4.3.1 Thermal Evaporation

Thermal evaporation was used to deposit thick films of Al onto O-terminated diamond, and an acid wash was subsequently used to remove excess metallic Al, leaving only an AlO-termination. Figure 3.5 shows the Edwards E306A bell-jar thermal evaporator used to deposit the thick films of Al. After pumping to $\sim 10^{-6}$ mbar, samples were heated to 120 °C for 30 min to desorb gases. Al was then deposited by slowly heating a tungsten filament wrapped in Al wire (99.999%, Fisher Scientific, Ltd). The film thickness was monitored during deposition using a quartz crystal microbalance. A coating of at least 20 nm was deposited. Some samples were thermally annealed at 300 °C for 1 h after deposition to improve the bonding of Al with the diamond surface. Excess Al was removed with an acid wash. This was done by submerging the samples in 5 mL 0.1 M HCl for >20 h.

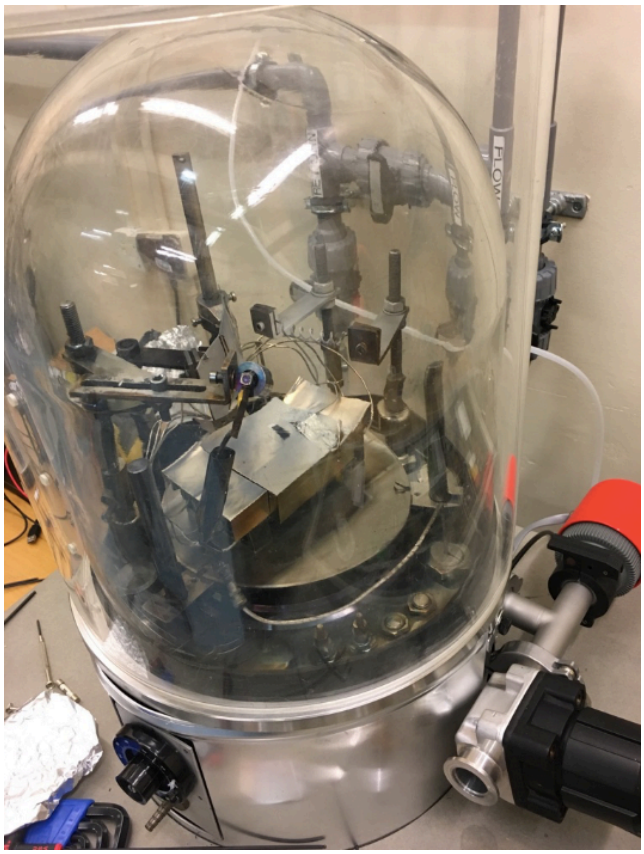

Figure 3.5: Photograph of the bell-jar thermal evaporator used for thick-film deposition of Al.

3.4.3.2 Atomic Layer Deposition

As described in Section 3.4.2.4, ALD can be used to deposit metals with ML coverage. Here, ALD was used to deposit thin layers of Al onto O-terminated diamond, again courtesy of Dr Ricardo Silva and Professor Rui Silva at the University of Aveiro in Portugal. Samples were first heated to 200 °C, then one pulse of gaseous trimethylaluminium was introduced and pumped away after 1 min. The samples were then annealed at 300 °C for 1 h after deposition in order to react the Al with the O-terminated diamond, thereby making them air-stable.

3.4.3.3 Electron-Beam Evaporation

Electron-beam evaporation can be used to deposit metals in vacuum with precise control of deposition rate. Aluminium was deposited onto room-temperature diamond at ~3×10^{-8} mbar using a Mantis Deposition Quad EV-C evaporator in a custom-built UHV chamber (Figure 3.6). Al wire (99.999%, Fisher Scientific, Ltd) was placed in a Mo crucible with an Al_2O_3 crucible liner. As the evaporator was

mounted horizontally, care was taken to prevent Al creep arising from overheating the crucible. The filament power was increased to 35 W to begin Al evaporation. After 5 min, the deposition rate became a consistent 0.34 Å min^{-1}, as measured using a quartz crystal microbalance.

Electron-beam evaporation was performed at the University of Bristol NanoESCA facility. The NanoESCA consists of a series of interconnected UHV chambers on vibration dampening legs housed on a suspended floor in order to minimise vibration effects. All samples after introduction to the UHV system were annealed at 300 °C for 1 h to remove surface adsorbates prior to treatment or analysis. Samples treated by electron-beam evaporation could be transferred to other chambers and analysed without breaking vacuum.

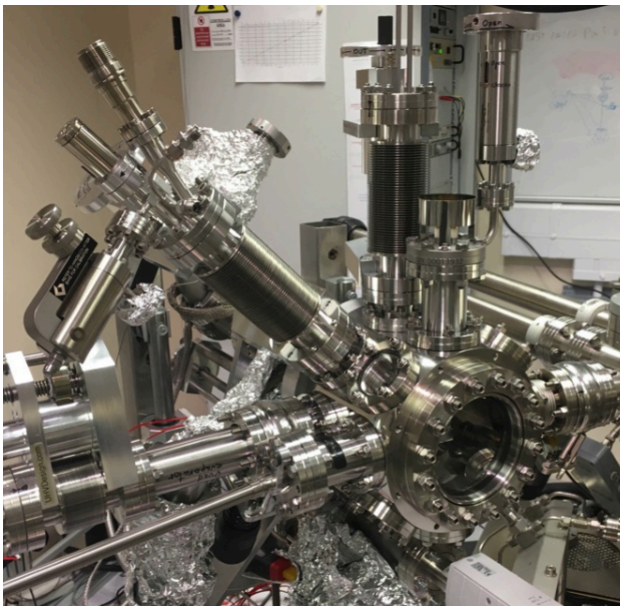

Figure 3.6: Photograph of the chamber used for electron-beam evaporation of metals, in this case Al.

3.5 Characterisation Techniques

3.5.1 Contact Angle Measurements

The wettability of a water droplet on a flat surface is affected by the hydrophilicity of the surface, and can be measured by the contact angle of the droplet at the surface. For diamond, different surface terminations can affect hydrophilicity, and so contact-angle measurements can be used to study a change in surface termination.

Contact-angle measurements were performed using a Krüss DSA100 drop shape analyser (Figure 3.7). A 0.25 μL water droplet was deposited on diamond in air and the contact angle was measured by fitting to a sessile drop.

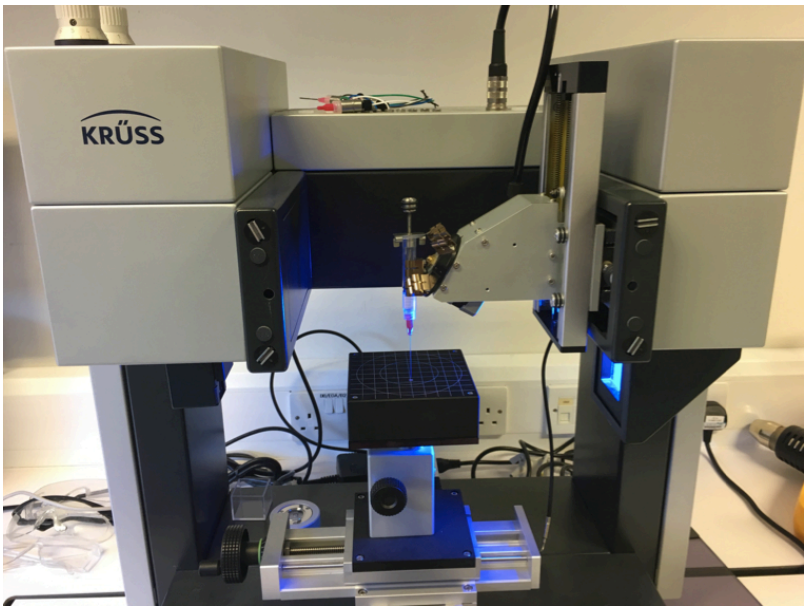

Figure 3.7: Photograph of the drop-shape analyser used for contact-angle measurement.

3.5.2 Fourier Transform Infrared Spectroscopy

Fourier transform infrared (FTIR) spectroscopy uses infrared radiation to excite vibrational modes in chemical bonds. It can provide details of the atomic bonding environments present in gaseous, liquid or solid samples. As illustrated in Figure 3.8(a), in an FTIR spectrometer, a broadband infrared light source enters a Michelson interferometer before reaching the sample, where a beam splitter and two mirrors causes wave interference effects and changes the intensity of some of the wavelengths of the light. The distance from the beam splitter to one of the mirrors is varied using a motor to change the wavelengths that experience interference effects. A Fourier transform is then performed by the software to analyse absorption from the different wavelengths, thus producing a spectrum.

FTIR with attenuated total reflectance (ATR) can be used to determine the surface termination of solid samples. As illustrated in Figure 3.8(b), in FTIR-ATR, if the sample has a different refractive index to the ATR crystal (in our case Ge),

there is total internal reflection of the infrared light. The evanescent wave penetrates up to 1 μm into the material's surface, and the glancing angle is sufficiently able to detect surface terminating species.

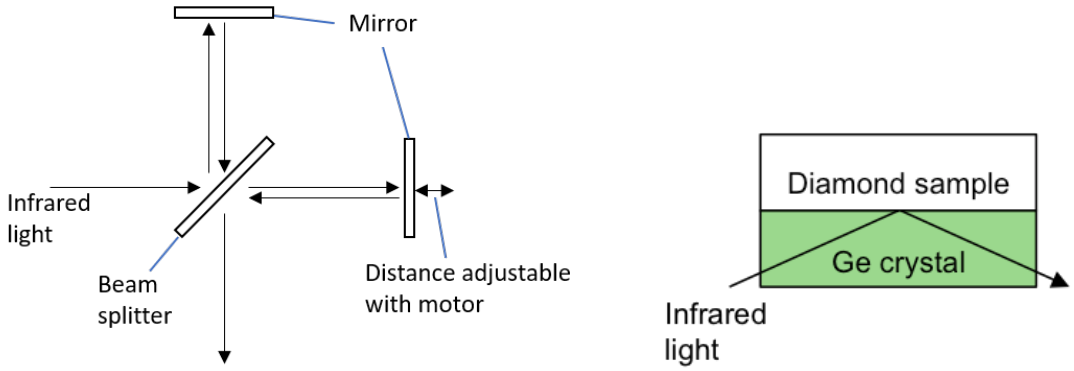

Figure 3.8: (a) Schematic of an FTIR interferometer. (b) In FTIR-ATR infrared light in a Ge crystal reflects off the surface of a diamond sample due to the difference in refractive index.

Shown in Figure 3.9 is the FTIR spectrometer with ATR attachment. FTIR-ATR was performed at room temperature using a Perkin Elmer Spectrum One spectrometer fitted with a Pike MIRacle ATR attachment. A single-reflection Ge crystal plate was equipped and the angle of incident of infrared light was on the diamond was 45°. Spectra were obtained in the range 800–4000 cm^{-1} by averaging 1000 scans with an energy resolution of 4 cm^{-1}.

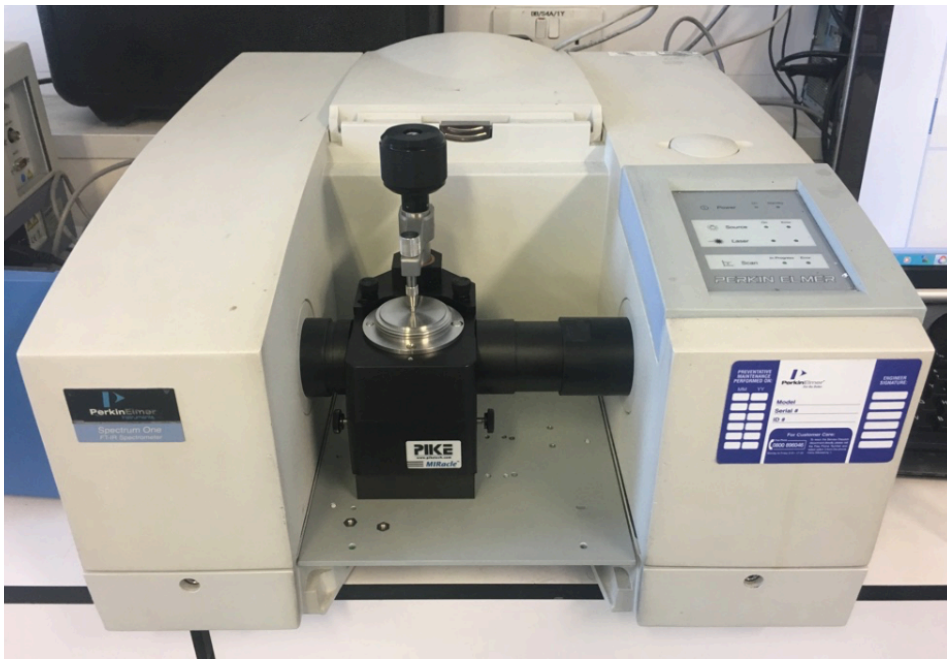

Figure 3.9: Photograph of the FTIR spectrometer with ATR attachment.

3.5.3 Raman Spectroscopy

Raman spectroscopy was also used to probe the bonding environments of diamond. In Raman spectroscopy, high intensity laser light is used to excite electrons to 'virtual' excited states. Most re-radiated light is of the same wavelength as the light source, but some wavelengths are different, depending on the electronic states involved. Longer and shorter wavelengths are termed Stokes and Anti-Stokes shifts, respectively. Figure 3.10 shows how these different wavelengths arise. In bulk materials, this is due to the interaction between laser light and phonons, and this technique can provide information about the vibrational modes present.

The intensity of Stokes or Anti-Stokes radiation can be plotted against the Raman shift. Stokes radiation has a higher intensity than Anti-Stokes so this is typically what is measured. The convention is for the Stokes shift to be a positive number, even though the wavenumber of the emitted light has decreased relative to the laser.

Raman spectroscopy can be used to distinguish between sp^3 and sp^2 carbon environments. Diamond has a singular peak at 1332 cm^{-1}, while graphite has a D-band peak at ~1350 cm^{-1} and a G-band peak and ~1580 cm^{-1}. The relative intensities of diamond and graphite peaks depend upon the laser wavelength,

with shorter wavelength light increasing sp^3 carbon intensity relative to sp^2 carbon.

Raman spectra were obtained at room temperature with a 514 nm green laser using a Renishaw 2000 Raman spectrometer attached to a microscope (Figure 3.11).

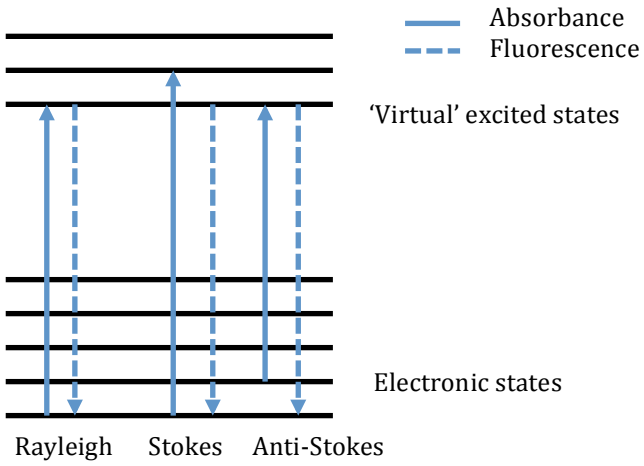

Figure 3.10: A laser can excite electrons into 'virtual' excited states. Most of the emission has no change in energy (Rayleigh scattering) but some emission has lower energy (Stokes) or higher energy (Anti-Stokes).

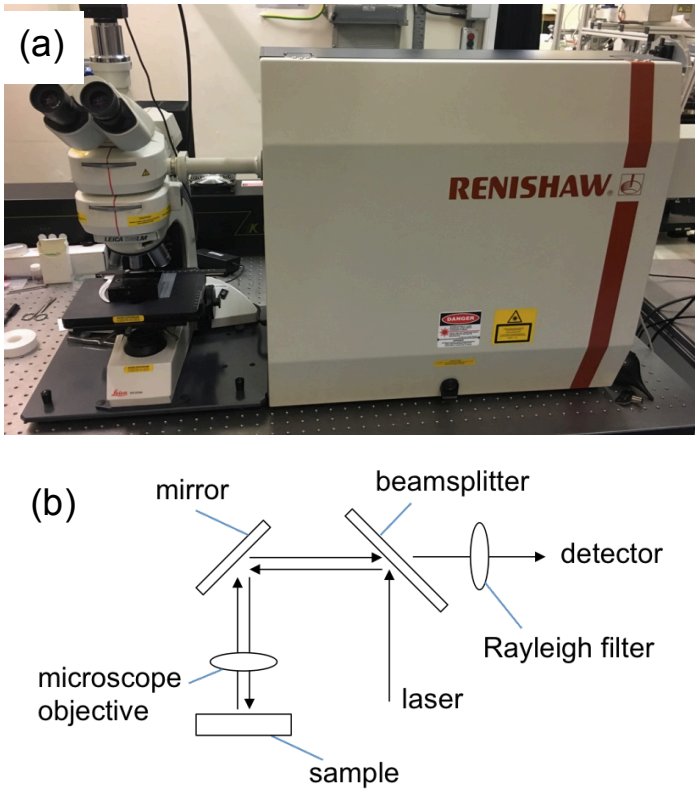

Figure 3.11: (a) Photograph and (b) schematic of the Raman spectrometer.

3.5.4 Scanning Electron Microscopy

Scanning electron microscopy (SEM) is a technique where an electron beam is used to image a sample, making imaging possible below the resolution limit for light (~200 nm). Electrons are emitted from a heated filament in high vacuum and focused into a beam with a series of lenses. When the electrons reach a sample, secondary electrons are ejected, which are then detected. An image of the material can be formed by rastering the electron beam across the sample surface, detecting the secondary electrons, and presenting the intensity as a function of beam position.

SEM images were obtained using a JEOL JSM IT-300, shown in Figure 3.12. Samples were mounted on an aluminium stub and secured with double-sided carbon tape. Boron-doped diamond samples were sufficiently conductive to prevent charging effects under the electron beam.

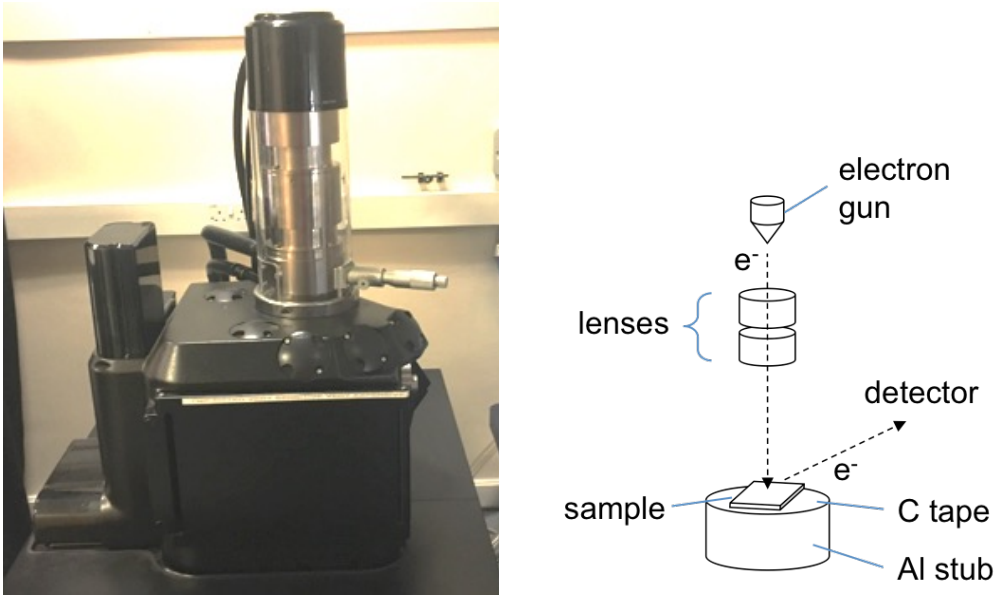

Figure 3.12: (a) Photograph and (b) schematic of the scanning electron microscope.

3.5.5 Energy-Filtered Photoemission Electron Microscopy

Photoemission electron microscopy (PEEM) is an electron microscopy technique where photon excitation emits electrons by the photoelectric effect. Energy-filtered (EF)-PEEM can filter these emitted electrons by their kinetic energies. Images are obtained for successive energies, and so a map of the work function across a material surface can be constructed. The photoemission threshold, I, is calculated for each pixel of the image by:

$$I = \frac{I_{\max}}{2} \operatorname{erfc}\left(\frac{\phi-(E-E_{\mathrm{F}})}{\sigma\sqrt{2}}\right) + I_{\mathrm{off}} \tag{3.1}$$

where E_{F} is the Fermi energy, $I_{\max}$ is the maximum pixel intensity, I_{off} is the intensity offset, σ is the standard deviation of the Gaussian distribution of energy broadening and ϕ is the local work function.[6]

Figure 3.13 shows the Scienta Omicron NanoESCA II used to perform EF-PEEM. Electron energies are filtered with an imaging double-hemisphere energy analyser. By altering the bias on the sample, the kinetic energy of the electrons changes, allowing them to be filtered with the first analyser. The second analyser then corrects for spatial aberrations. The energy resolution for this technique is 0.14 eV and the spatial resolution is 150 nm.

The UV light source was either a mercury lamp or a monochromated helium-I lamp, with energies of 5.2 eV and 21.2 eV, respectively. Electrons were extracted by applying a bias of 7–12 kV across a distance of 1.8 mm. The lower extraction voltages were sometimes required to prevent electron discharge from the sample. This increased the measured work function by up to 0.1 eV and was corrected for.

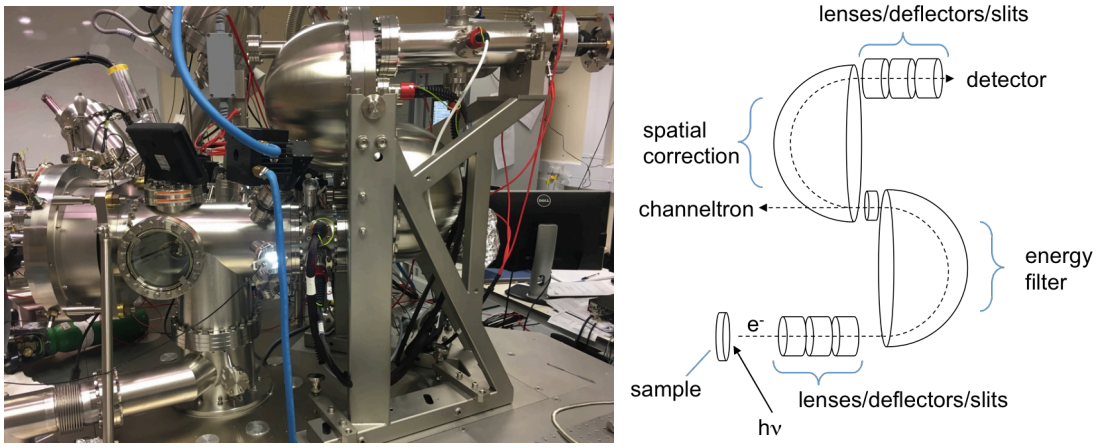

(a) (b)

Figure 3.13: (a) Photograph and (b) schematic of the NanoESCA II, which can perform EF-PEEM and UPS.

3.5.6 Photoelectron Spectroscopy

Photoelectron spectroscopy is a versatile characterisation technique, where light excites and ejects electrons from a material, and the number of electrons at different kinetic energies can be detected. The kinetic energy can be used to determine the binding energy of the electrons, from:

$$h\nu = E_{\mathrm{B}} + \phi + E_{\mathrm{K}} \tag{3.2}$$

where $h\nu$ is the photon energy, E_{B} is the binding energy relative to the Fermi level, ϕ is the work function of the sample, and E_{K} is the kinetic energy. The type of light source determines which electrons are ejected.

Photoelectron spectroscopy is conducted within a UHV environment to ensure samples are contamination-free and so that electrons reach the detector unimpeded. The detected sample depth varies depending on the wavelength of light and angle of incidence. An electric field is typically applied in order to overcome the work function of the detector.

3.5.6.1 X-ray Photoelectron Spectroscopy

X-ray photoelectron spectroscopy (XPS) uses X-rays to probe core-level electrons of atoms. The binding energy is characteristic to a certain element, so the elemental composition of the sample can be determined. It is often possible to distinguish between different bonding environments from small changes in

binding energy. The maximum sampling depth of XPS for diamond is around 9 nm,[7] but can be reduced by changing the angle of escape for the electrons.

Figure 3.14 shows an example XPS spectrum for oxygen-terminated diamond. In addition to the peaks from emission of core-level electrons, there can be peaks from emission of Auger electrons, in this case the O KLL peak. The filling of an empty K shell by an L shell electron is accompanied by emission of another L electron.

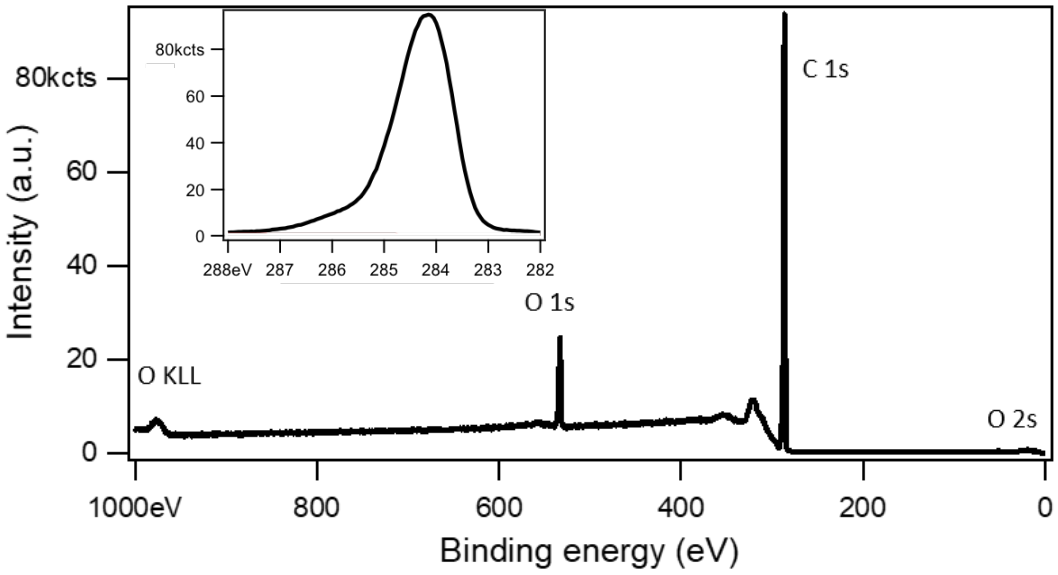

Figure 3.14: Example XPS survey spectrum of O-terminated diamond. The inset shows the XPS spectrum for the C 1s peak.

XPS can be used to obtain the stoichiometry of different elements. For example, Equation 3.3 finds the atomic percentage of oxygen relative to carbon using the O 1s and C 1s peaks. The relative amount of each element is obtained by dividing the peak area, A, by a sensitivity factor (SF) for that element. The sensitivity factors of all elements were obtained from values for cross-sectional area and asymmetry parameter.[8] The atomic percentage of an element is obtained by dividing the relative amount of that element by the total.

$$Oxygen\ \% = \frac{A(O\ 1s)/SF(O\ 1s)}{A(O\ 1s)/SF(O\ 1s)+A(C\ 1s)/SF(C\ 1s)} \times 100\% \qquad (3.3)$$

XPS characterisation was performed in the University of Bristol NanoESCA facility (Figure 3.15). A monochromated Al K_α X-ray source (1486.7 eV) oriented

at 85° to the detector was used, which had an overall energy resolution of 600 meV at a pass energy of 20 eV. The XPS signals were calibrated by aligning the Au $4f_{7/2}$ peak to 84.0 eV using a polycrystalline gold film.

XPS spectra for each sample consisted of a fast 'survey' scan between 1000 eV and 0 eV, to determine which elements were present. This was followed by more detailed scans of peaks of interest collected using a smaller step size and longer dwell time. Multiple scans were taken to improve the signal-to-noise ratio.

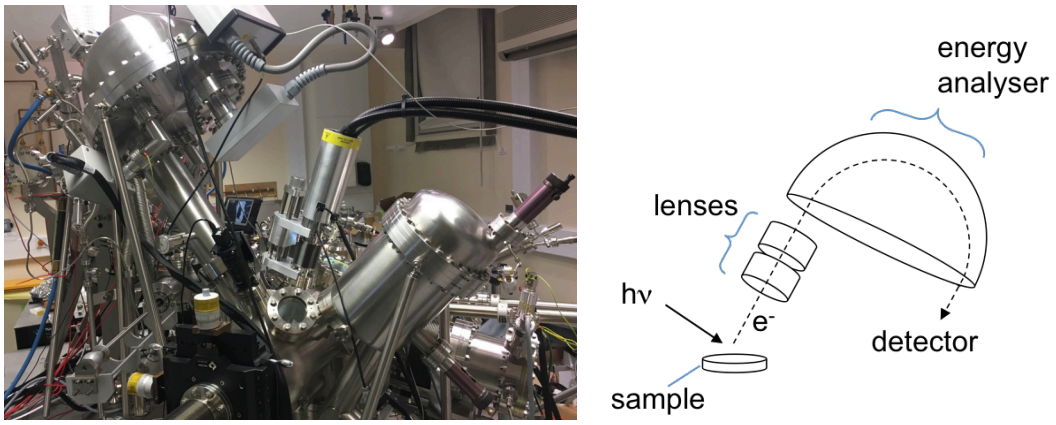

Figure 3.15: (a) Photograph and (b) schematic of the XPS setup, part of the University of Bristol NanoESCA facility.

3.5.6.2 Ultraviolet Photoelectron Spectroscopy

Ultraviolet photoelectron spectroscopy (UPS) excites electrons from the valence band of a material, from where they are ejected into vacuum and their energy analysed. The sampling depth is smaller and the energy resolution higher than those for XPS.[9] As illustrated in Figure 3.16(a), photoemission can be considered as a three-step process involving excitation, transport, and emission of electrons.[10]

A typical UPS spectrum for a semiconductor is given in Figure 3.16(b). The spectrum has a large peak at high binding energy from secondary electron emission. Other peaks give information on the electron density-of-states. NEA can be observed by the presence of an additional secondary electron emission peak component at a higher binding energy, arising from the additional secondary electron population exceeding the vacuum energy. This is possible as

real surfaces contain some mid-band gap states just below the conduction band for the electrons to occupy.

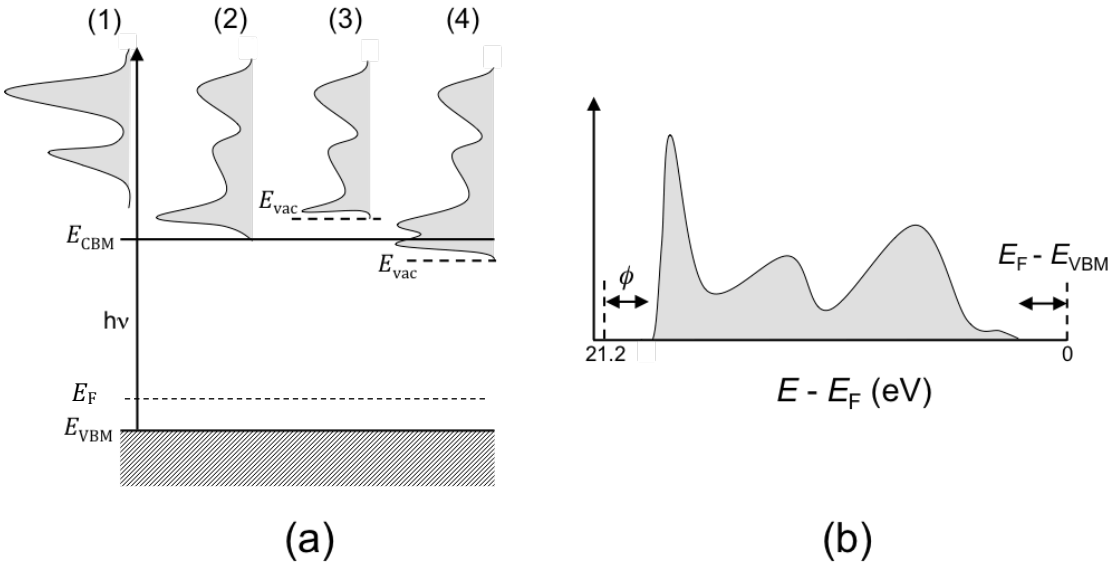

Figure 3.16: (a) Model of photoemission in UPS. (1) Electrons are photoexcited from the valence to conduction band, giving information on the density of states. (2) Electron transport to the surface causes some degree of relaxation. The UPS spectrum is obtained from the emitted electrons and can be affected by whether (3) the sample has a PEA, or (4) the sample has an NEA. Adapted from Bandis and Pate.[10] (b) Example UPS spectrum from a He-I source, showing how work function, ϕ, and the difference between the Fermi level, E_F, and valence band maximum, E_{VBM}, positions are calculated.

The work function, ϕ, can be calculated from the difference between the photon energy and the emission onset for PEA surfaces. As a result of the extra secondary electron peak, UPS cannot easily determine the work function for NEA surfaces and so other methods (such as EF-PEEM) should be used instead. UPS can also determine the difference between E_F and the energy of the valence band maximum, E_{VBM}. This allows the electron affinity, χ, to be calculated, from:

$$\chi = \phi + (E_F - E_{VBM}) - E_g \tag{3.4}$$

where E_g is the band gap of the material.

UPS was performed in the same chamber as EF-PEEM, using the monochromated He-I light source. Photoemitted electrons were filtered by kinetic energy in the first hemisphere of the imaging double-hemisphere energy analyser, and the signal was amplified using a channeltron. The energy resolution of this technique is 0.14 eV. An iris could be closed to perform UPS on a region of interest ~5–10 μm in diameter.

3.5.7 Low Energy Electron Diffraction

Low energy electron diffraction (LEED) can give information on the surface structure of a single-crystal material. In a UHV chamber, an electron beam with energy in the range 20–200 eV is directed at the sample. The electron wavelength is of the same order of magnitude as atomic bonds. The electrons are diffracted by periodic surface structure from the top few layers of the sample, and are detected using a hemispherical fluorescent phosphor screen or a channeltron.

Figure 3.17 shows an example of the relation between the surface structure and the resultant LEED pattern. The LEED pattern represents the real space lattice in reciprocal space. For a (2 × 1) arrangement of atoms there are two possible domains, which combine to give the overall LEED pattern.

LEED experiments were conducted using a channeltron detector at the University of Bristol NanoESCA facility (Figure 3.18).

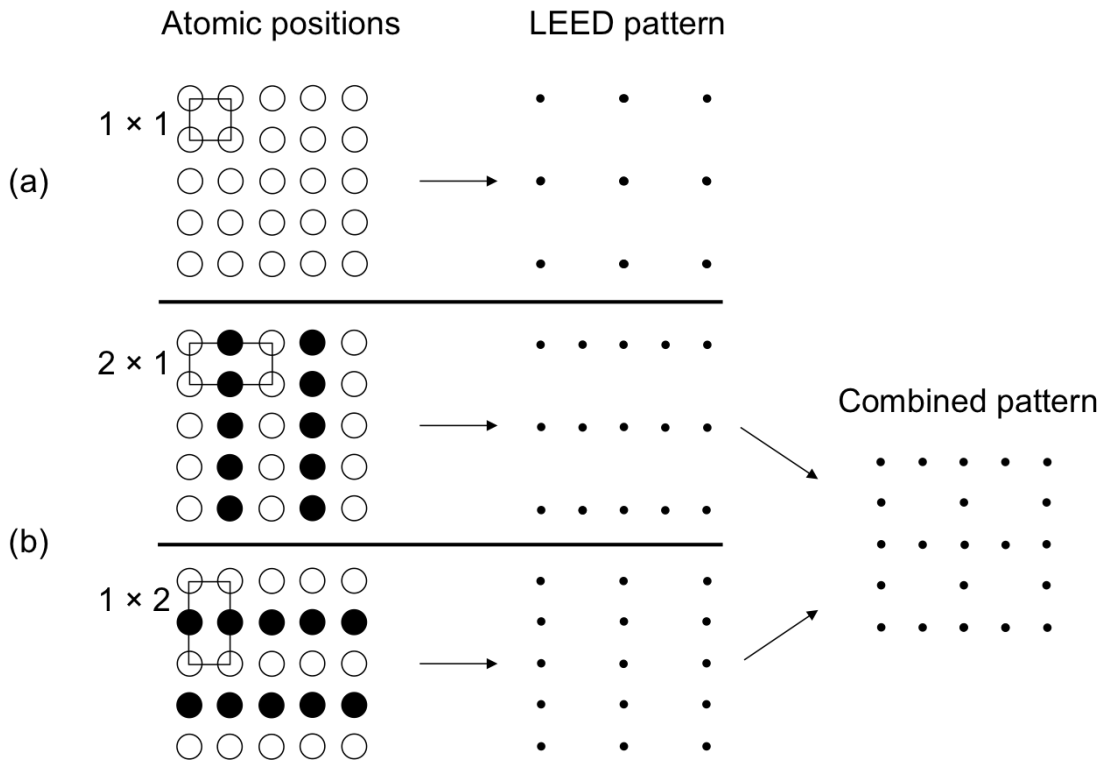

Figure 3.17: Example LEED patterns that form from (a) a (1 × 1) structure, and (b) a (2 × 1) structure.

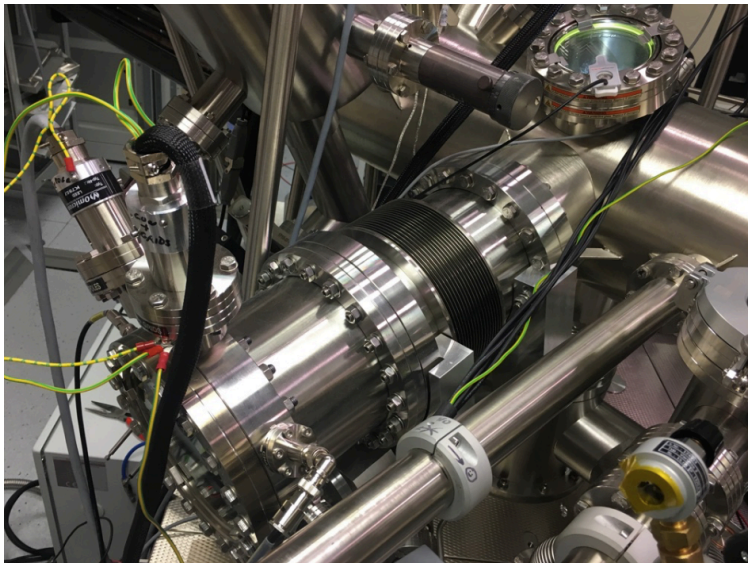

Figure 3.18: Photograph of the LEED setup, part of the University of Bristol NanoESCA facility.

3.5.8 Thermionic Emission

To measure thermionic emission, the current density, *J*, is obtained at different temperatures, *T*. By rearranging the Richardson-Dushman equation

(Equation 1.1) into the form of Equation 3.5, the work function, ϕ, and Richardson constant, A, can be obtained from a plot of $\ln(J/T^2)$ against $1/kT$.

$$\ln\left(\frac{J}{T^2}\right) = -\frac{\phi}{kT} + \ln(A) \tag{3.5}$$

Thermionic emission was performed in a custom-built chamber, details of which have been recently published.[11] The thermionic emission setup is shown in Figure 3.19. After pumping to 4×10^{-7} Torr, the vacuum gap between the sample and a molybdenum collector was set to 200 μm using a motor and a 31 V bias was applied to the collector relative to the sample.

A polarized 40 W CO_2 laser was used to heat the reverse of the sample through a hole in the sample holder. The reverse of each sample had been etched with a 10.6 μm spaced grating using a laser cutter in order to increase heat absorption from the laser. This allowed the sample to be rapidly heated in order to generate accurate emission current data at higher temperatures. The temperature was measured using a two-colour optical pyrometer operated in single-colour mode. Polycrystalline n-type diamond thin films on molybdenum substrates were used in thermionic emission experiments. Mo was preferred to Si as substrate choice to prevent melting from spot heating by the laser.

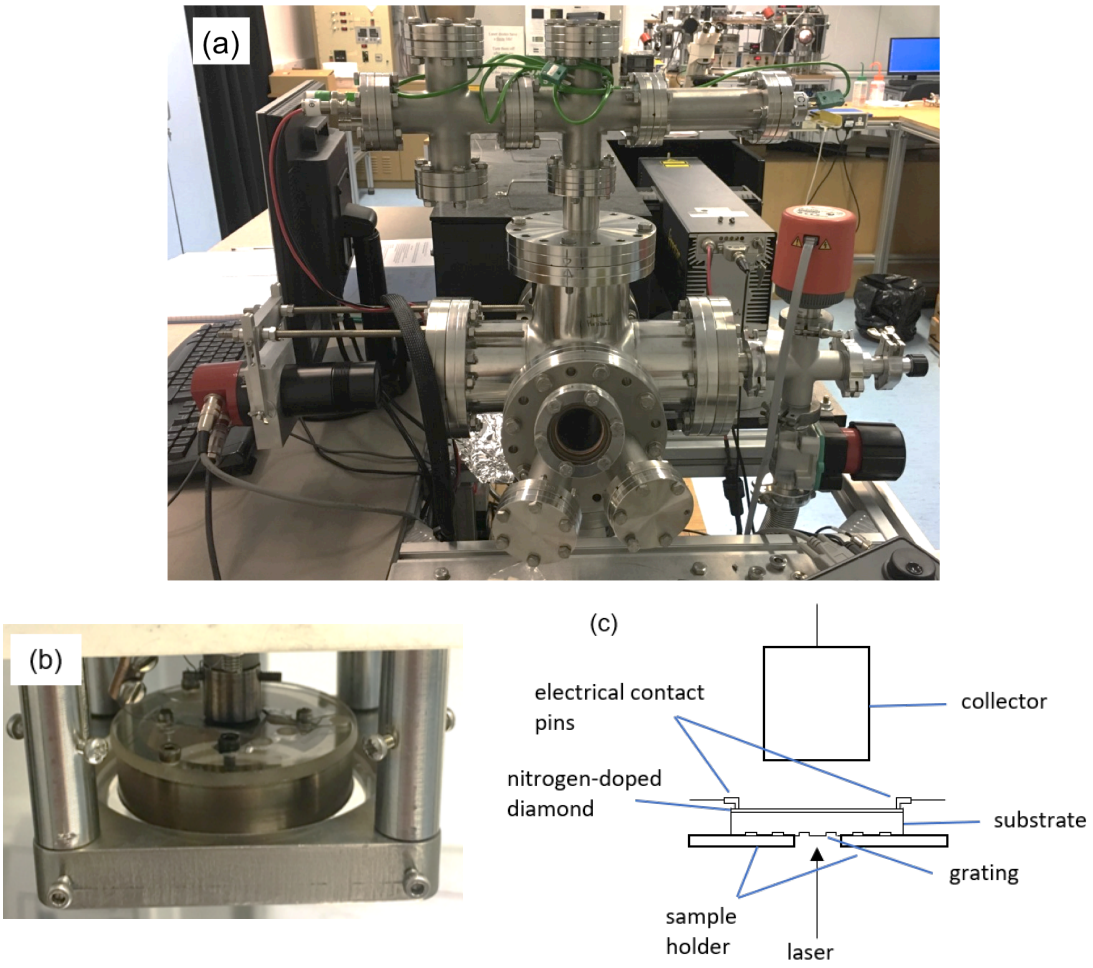

Figure 3.19: (a) Photograph of the thermionic emission kit. (b) Photograph and (c) schematic of the interior of the chamber.

References

1 W. S. Yeap, D. Bevk, X. Liu, H. Krysova, A. Pasquarelli, D. Vanderzande, L. Lutsen, L. Kavan, M. Fahlman, W. Maes and K. Haenen, *RSC Adv.*, 2014, **4**, 42044–42053.

2 X. Zhang, *Investigation of Heavily Boron Doped Diamond Thin Film for Electronic Devices*, PhD Thesis, University of Bristol, 2017.

3 H. C. M. Knoops, S. E. Potts, A. A. Bol and W. M. M. Kessels, in *Handbook of Crystal Growth: Thin Films and Epitaxy*, ed. T. F. Kuech, Elsevier, Amsterdam, The Netherlands, 2nd edn., 2015.

4 A. Jaggernauth, R. M. Silva, M. A. Neto, M. J. Hortigüela, G. Gonçalves, M. K. Singh, F. J. Oliveira, R. F. Silva and M. Vila, *J. Phys. Chem. C*, 2016, **120**, 24176–24186.

5 R. Yoshida, D. Miyata, T. Makino, S. Yamasaki, T. Matsumoto, T. Inokuma and N. Tokuda, *Appl. Surf. Sci.*, 2018, **458**, 222–225.

6 H. D. Andrade, M. Z. Othman, K. M. O'Donnell, J. H. Lay, P. W. May, N. A. Fox, J. Morin and O. Renault, *Int. J. Nanotechnol.*, 2014, **11**, 796–807.

7 F. Maier, J. Ristein and L. Ley, *Phys. Rev. B*, 2001, **64**, 165411.

8 J. J. Yeh and I. Lindau, *Atomic Calculation of Photoionization Cross-Sections and Asymmetry Parameters*, Gordon and Breach, Langhorne, PA, USA,

1993.
9 S. Hüfner, *Photoelectron Spectroscopy: Principles and Applications*, Springer, Berlin, Germany, 3rd edn., 2003.
10 C. Bandis and B. B. Pate, *Phys. Rev. B*, 1995, **52**, 12056–12071.
11 H. Dominguez-Andrade, A. Croot, G. Wan, J. A. Smith and N. A. Fox, *Rev. Sci. Instrum.*, 2019, **90**, 045110.

Chapter 4 – Computational Studies of Al on Diamond

4.1 Introduction

There is considerable interest in developing a new negative electron affinity (NEA) surface on diamond with superior properties to those of hydrogen-termination. In particular, a larger thermal stability could further the development of novel thermionic devices. NEA surfaces are also of interest for field emission and secondary electron emission applications, diamond-based field effect transistors and for photocatalysis. Chapter 2 has explored the surfaces that have been reported in the literature. For thermionic devices, the most promising terminations involve deposition of up to 1 monolayer (ML) of a metalloid or transition metal (TM) onto the bare diamond surface, or group I or II metals or TMs onto the oxygen-terminated surface. Carbide forming metals and smaller elements show the greatest thermal stability, and electropositive elements show the largest NEA. Addition of metals to the O-terminated surface can make the surface termination air- and water-stable.

Aluminium on diamond has received minimal attention for development of an NEA surface. This is somewhat surprising, since Al is a light, carbide-forming metal with electronegativity similar to first-row TMs. Aluminium bonds sufficiently well to diamond to act as a Schottky[1,2] or Ohmic[3] contact, with the latter forming after high temperature annealing. Lurie and Wilson[4] have studied Al adsorption on diamond, finding that Al gives a (2 × 2) reconstruction on the (111) surface following deposition of 10–30 Å of Al followed by annealing in vacuum. No ordering was found on (100) or (110) surfaces. Aluminium carbide was formed following a 1300 °C anneal on the (100) surface, and a 1000 °C anneal on the (111) surface.

An aluminium oxide layer on diamond is a candidate gate dielectric material in diamond-based metal oxide-semiconductor field effect transistors (MOSFETs)[5] and capacitors.[6] These films are typically thicker than what is

required to give NEA. Similarly, AlN has been used as a gate dielectric for diamond FETs,[7,8] and a diamond/AlN heterojunction diode has been fabricated.[9]

The prior studies[1–9] showing successful aluminium, aluminium oxide and aluminium nitride deposition on diamond suggest that aluminium could bond strongly with the bare, oxygenated and nitrogenated diamond surfaces. As the conversion of Al on diamond to aluminium carbide is expected to occur above 1000 °C in vacuum, there is a temperature window between ~800–1000 °C that is expected to be suitable for thermionic applications. Another factor to consider is the possibility of Al on diamond oxidising if exposed to air. Should AlO-terminated diamond be air-stable, as has been found with other metals, then oxidation in air is unlikely to occur, thus reducing the likelihood of conversion to aluminium oxide for this surface.

The relative thermal stabilities of different surface terminations can be predicted by consideration of bond dissociation enthalpies (BDEs), the enthalpy change for breaking a bond into its component atoms in the gaseous state at 298 K. Al-C, Al-O and Al-N bonds have BDEs of 267.7 kJ mol^{-1}, 501.9 kJ mol^{-1} and 368 kJ mol^{-1}, respectively.[10] These values suggest that AlO-terminations will be the most thermally stable and Al-terminations the least.

This chapter presents a systematic study of different coverages of aluminium addition to the bare, O- and N-terminated (100) and (111) diamond surfaces, with the aim of determining which surfaces and coverages are desirable for experimental NEA investigations. Much of the work in this chapter has been published in two articles, which are listed in the Appendix. I performed all calculations and analysis, and wrote the majority of each manuscript.

4.2 Computational Setup

4.2.1 CASTEP

The Cambridge Serial Total Energy Package (CASTEP) is a periodic density functional theory (DFT) code that uses a basis set of plane waves.[11] It is one of the most popular DFT codes, and for this project was installed in a Linux environment, using command line input.

4.2.1.1 Input and Output Files

CASTEP inputs are .cell and .param files. Cell files allow the user to choose the lattice parameters and atomic positions, as well as any symmetry operations, cell constraints, and specifications for number of *k*-points within the Brillouin zone. The parameter file contains details such as the type of calculation, energy cut-off, exchange-correlation functional, minimisation method and any changes to the tolerances for completing the calculation. CASTEP has a number of 'sensible' defaults that will be used in the event that a parameter is not chosen.

CASTEP will output a .castep file that contains information based on the input task. For example, a geometry optimisation will output the enthalpy, forces and bond positions for each iteration. Mulliken populations and charges,[12] adapted for use with plane-wave DFT,[13,14] are also calculated for the optimised structure. The final structure from a geometry optimisation is also available as a .geom file.

In order to generate electrostatic potentials (EPs), CASTEP's in-built one-dimensional EP function 'pot1d' can be applied to the output from a geometry optimisation. Here, the EP was calculated in the direction perpendicular to the surface. The EP represents the combination of the Hartree (Coulombic) potential and the local part of the pseudopotential.

Density-of-states (DOS) were obtained by first performing a DOS calculation in CASTEP on the optimised geometry, then OptaDOS[15] was run to obtain projected DOS (PDOS) values for each atom set. All calculations used the adaptive broadening method[16] and 0.07 eV DOS spacing to sample the Brillouin zone.

Structures were created using the DL_Visualize program,[17] which can generate crystal slabs with a chosen surface orientation. Jmol[18] was used to visualise cell and geometry files as three-dimensional structures.

4.2.2 BlueCrystal

Calculations were performed using the University of Bristol's BlueCrystal phase 3 and phase 4 supercomputers. Phase 3 of BlueCrystal has been operational since 2013, while phase 4 of BlueCrystal was first introduced in 2016. BlueCrystal runs on a Linux environment that can be accessed with a terminal or a program such as WinSCP. A supercomputer such as BlueCrystal is

well suited for running CASTEP as it has multiple nodes and cores available, and CASTEP is efficiently parallelised.

4.2.3 Electron Affinity Calculation

The ionisation energy, I, of a semiconductor can be calculated by adapting the method of Fall *et al*.[19] As shown by Equation 4.1, the ionisation energy is the difference between the vacuum energy, E_{vac}, and the valence band maximum (VBM) energy of the diamond slab, E_{VBM}. E_{VBM} can be calculated from the addition of the average potential energy of the centre of the slab, V_{slab}, to the difference between the VBM position of bulk diamond, $E_{\text{VBM, bulk}}$, and the average potential energy of bulk diamond, V_{bulk}. The difference between $E_{\text{VBM, bulk}}$ and V_{bulk} has been calculated previously as 10.52 eV.[20]

From the ionisation energy, the electron affinity (EA), χ, is calculated by subtraction of the experimental band gap, E_{g}, as shown in Equation 4.2. The experimental value of E_{g} (5.47 eV) was used because the generalised gradient approximation (GGA) method is well known to underestimate the band gap of diamond.[21]

$$I = E_{\text{vac}} - E_{\text{VBM}} = E_{\text{vac}} - (V_{\text{slab}} + E_{\text{VBM,bulk}} - V_{\text{bulk}}) \tag{4.1}$$

$$\chi = I - E_{\text{g}} \tag{4.2}$$

An example EP is shown in Figure 4.1. On the left side, within the oscillating potential, minima show areas of positive charge, *i.e.* positions of the nuclei. On the right side, the flat potential represents the vacuum energy. Since the potential energy of the slab oscillates, the average potential was determined by averaging maxima and minima in the centre of the slab. In order to determine V_{slab} more accurately, a smoothened potential was plotted with reduced peak-to-peak amplitude within the slab. This was calculated from a 13-point rolling average of EP values.

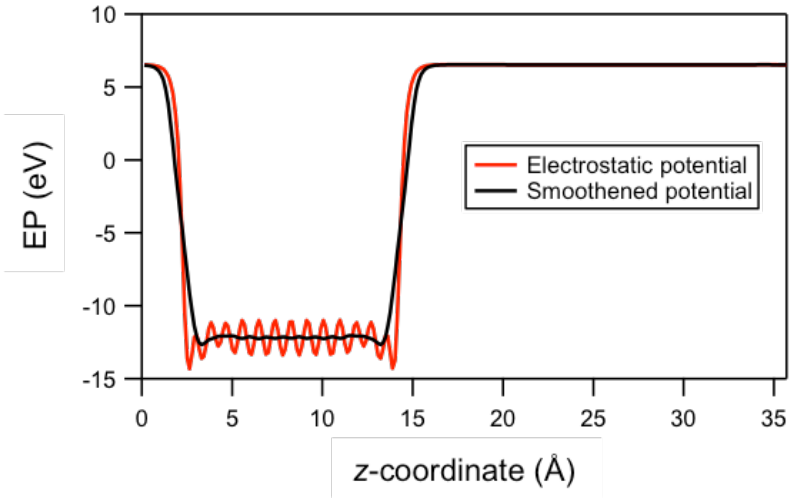

Figure 4.1: Example electrostatic potential taken perpendicular (in the *z*-direction) to the diamond slab. The smoothened potential allows more accurate determination of the average potential of the slab.

4.2.4 Adsorption Energy Calculation

As given by Equation 4.3, the energy of adsorption, E_{ads}, was calculated from the energy of the structure containing both the diamond slab and adsorbates, E_{total}, by subtraction of the diamond slab energy with no adsorbates, E_{slab}, and the energy of an isolated adsorbate atom, E_{at}, multiplied by the number of adsorbate atoms, N. This value, divided by the total number of adsorbate atoms, gives the energy per adsorbate. A negative E_{ads} indicates exothermic adsorption.

$$E_{\text{ads}} = (E_{\text{total}} - E_{\text{slab}} - N \cdot E_{\text{at}})/\, N \tag{4.3}$$

4.3 Al Addition to the (100) Diamond Surface

4.3.1 Ensuring Convergence

To ensure convergence of computational parameters, the effect of each parameter on the total enthalpy of an H-terminated diamond slab was studied. Figure 4.2 shows the change in enthalpy with energy cut-off and the number of *k*-points used for the *x* and *y* directions (parallel to the slab surface). The effect on computational time is also included and it can clearly be seen to increase rapidly in both cases. In a similar manner, the enthalpy was also measured as a function of vacuum gap size and of the number of carbon layers within the diamond slab. Different GGAs for the exchange-correlation functional were also

examined. Further tests were then conducted on 0.25 ML coverage of Al on O-terminated diamond to ensure that calculations on the surfaces of interest had also converged.

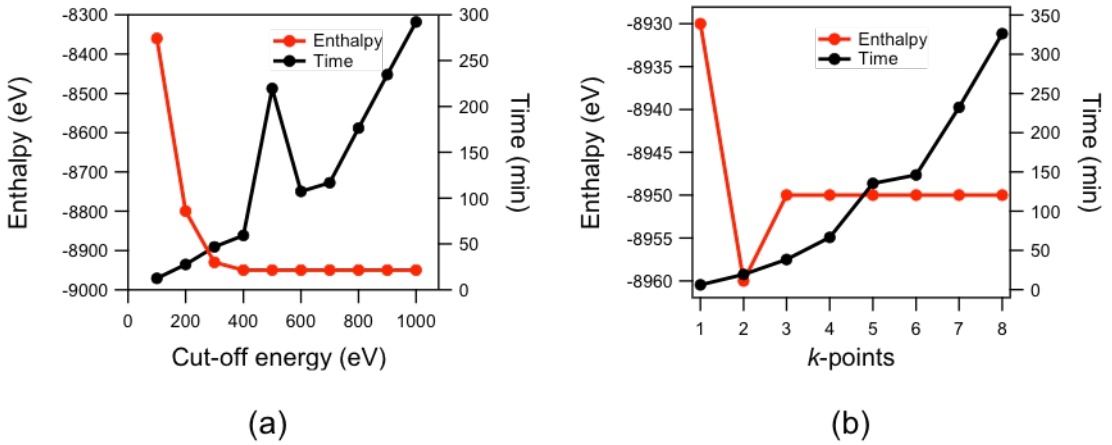

Figure 4.2: Variation of total enthalpy and computational time with (a) cut-off energy and (b) *k*-point size in *x* and *y* directions, using an H-terminated (100) diamond slab with 14 carbon layers.

For all calculations unless otherwise stated, the computational parameters were the following: an energy cut-off of 700 eV, the Perdew-Burke-Ernzerhof (PBE) GGA[22] and ultrasoft Vanderbilt pseudopotentials.[23] The Brillouin zone was sampled by a 6 × 6 × 1 Monkhorst-Pack *k*-point grid[24] for energy minimisation steps and a 12 × 12 × 1 *k*-point grid for DOS calculations. The energy of the slab was minimised with respect to all atomic positions using the Broyden-Fletcher-Goldfarb-Shanno (BFGS) optimisation method. The tolerances for convergence of ionic forces and total energy were 0.05 eV $Å^{-1}$ and 2×10^{-5} eV $atom^{-1}$, respectively.

A 14-layer diamond slab was used; the EP at the centre of the slab was not affected by changes to the surface termination so it was assumed to adequately represent bulk diamond at the centre. Fixed lattice parameters of 5.05 Å × 5.05 Å × 35.7 Å gave a continuous slab structure in the *x* and *y* directions. The top and bottom of the slab were 2 × 2 periodic supercells of the (100) surface. A vacuum gap of 20–25 Å separated repeating slabs, which was sufficient for the EP to decay fully in the vacuum region. Surface terminations were applied to both sides of the slab to prevent a non-uniform electrostatic

potential in the vacuum region arising from a charge imbalance between repeating slabs.

The first set of calculations compared results for the bare diamond surface and the H- and O-terminated surfaces with values from the literature to validate the accuracy of the calculations. As shown in Table 4.1, there is generally a good agreement of energies and bond lengths with previous computational results, although adsorption energies are slightly smaller for each of the terminations. A comparison of EAs was also made with experimental values. Maier *et al.*[25] found EAs of 0.5 eV, -1.3 eV and 1.7 eV for the bare, H- and O-terminated (100) surfaces, respectively. The O-termination is likely a combination of ether and ketone bonding. It is clear that DFT calculations are generally overestimating the magnitude of EAs compared with experimental measurements. Contributing factors for this discrepancy could be approximations in the DFT method, or the imperfect nature of experimental surfaces, such as an incomplete coverage of terminating species or a spatial variation in work function from a non-flat surface.

Table 4.1: Values of the adsorption energy, E_{ads}, calculated electron affinity, χ, and bond lengths, d, for selected calculations compared with previous work on (100) diamond. d(C-C) refers to bond length of the surface dimer. (2 × 1) indicates a reconstructed surface dimer. *Per surface atom, compared with the (1 × 1) bare surface.

Structure	Source	E_{ads} (eV/atom)	χ (eV)	d(C-C) (Å)	d(C-O) (Å)	d(C-H) (Å)
C(100)-(2 × 1)	Previous calculations	-1.46,[20] -1.512[26]	0.51–0.69,[27] 0.62,[20] 0.8,[28] 0.28[29]	1.38,[20] 1.37[30]	-	-
	Current work	-1.60*	0.53	1.38	-	-
C(100)-(2 × 1):H	Previous calculations	-5.32,[20] -4.54[30]	-1.95,[20] -2,[27] -2.2[28]	1.62,[20] 1.61[30]	-	1.1[20, 30]
	Current work	-4.14	-2.06	1.62	-	1.1
C(100)-(1 × 1):O (ether)	Previous calculations	-8.2,[20] -8.43[31]	2.61–2.7,[31] 2.63[20]	-	1.5,[20] 1.49,[31] 1.48[32]	-
	Current work	-7.47	2.54	-	1.5	-
C(100)-(1 × 1):O (ketone)	Previous calculations	-7.88,[20] -8.57[31]	3.75,[20] 3.64[31]	-	1.2,[20] 1.25,[31] 1.16[32]	-
	Current work	-7.18	3.46	-	1.2	-

4.3.2 Geometries of the Al-Adsorbed Bare (100) Diamond Surface

One atom per surface unit cell is defined here as constituting 1 ML coverage, so four atoms (on either side of the diamond slab) represents 1 ML coverage for the 2 × 2 supercell used in these calculations. This supercell size allowed sub-ML coverages of 0.25 and 0.5 ML to also be simulated by addition of only one or two atoms to each side of the slab. Al coverages above 1 ML were beyond the scope of this study, but it was expected that bulk behaviour of Al would ultimately be seen with increasing Al coverage, resulting in a Schottky barrier at the surface rather than NEA.

Energy minimisation of the bare surface gave the expected (2 × 1) reconstruction with parallel dimer rows on the surface (Figure 4.3). Four high-symmetry adsorption sites have previously been identified for the bare (2 × 1) (100) surface: hexagon hole (HH), hexagon bridge (HB), third-tier carbon (T3) and fourth-tier carbon (T4) sites.[33] At 0.25 ML coverage just one of these sites is chosen, but higher coverages require a combination of sites. For 0.5 ML

coverage, the following combinations of sites were included: identical sites, where the Al atoms are perpendicular to dimer rows; linear sites, where Al atoms are parallel to dimer rows for one half of the supercell; and a ($\sqrt{2} \times \sqrt{2}$) configuration where Al atoms are diagonal to the supercell. For 1 ML coverage, two pairs of identical sites were used.

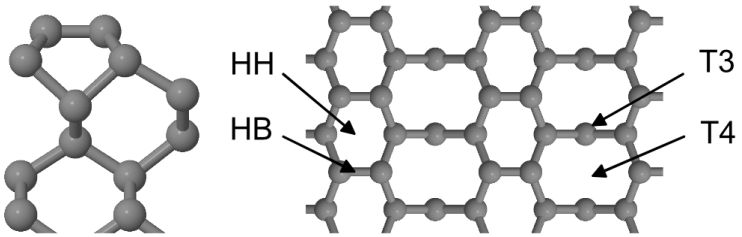

Figure 4.3: Side and plan view of the bare (2 × 1) reconstructed diamond surface. The plan view shows possible high symmetry sites for surface adsorbates. HH, HB, T3 and T4 refer to the hexagon hole, hexagon bridge, third-tier carbon and fourth-tier carbon sites, respectively.

Table 4.2 displays the results of Al adsorption to different sites on the bare diamond surface. The T4 site is lowest in energy for 0.25 and 0.5 ML Al coverages. For 1 ML the lowest energy site is a hexagonal arrangement of Al atoms, caused by relaxation of the HH+T3 positions. These lowest energy structures are shown in Figure 4.4. For the lowest energy 1 ML structure, each Al is bonded only once with a surface carbon, and Al atoms all lie on a plane. The Al-Al bond length is 2.52 Å in the *y* direction and 2.74–2.91 Å otherwise. This geometry is similar to the hexagonal (111) plane of Al metal where the Al-Al distance is 2.86 Å; the slight decrease in Al-Al bond length is from the epitaxial bonding with diamond.

The C=C double bond of the bare surface dimer changes to an extended single bond with Al addition, reflected by the bond length increase from 1.38 Å to between 1.63–1.85 Å. There is an associated reduction of Mulliken bond population of the dimer from 1.36 before Al addition to 0.52–0.78 after. Al, in general, moves further from the surface with increasing coverage, shown by the lengthening of the Al-C bonds. Adsorption energies correlate with Al-C bond populations, which lie in the range 0.02–0.67.

Analysis of Mulliken charges showed that Al atoms became positively charged and C atoms in the surface dimer became negatively charged. Al atoms were less charged at higher coverages, with charges up to 0.9*e*, 0.8*e* and 0.4*e* observed for 0.25, 0.5 and 1 ML Al coverages, respectively. Notably, Al bonded in two-coordinate HB and T4 sites had a larger Al-C_{dimer} bond population but smaller Mulliken charge than Al in four-coordinate HH and T3 sites. To explain this difference the former are defined as more 'covalent' sites and the latter as more 'ionic' sites. Al preferentially bonds to the more covalent sites as shown by the larger E_{ads} values.

Overall, the EA increased with larger Al coverage. The linear and $(\sqrt{2} \times \sqrt{2})$ HH+T3 positions at 0.5 ML coverage showed a positive EA. The most negative EA was from the hexagonal relaxation of the HH+T3 position at 1 ML, at almost -1.5 eV. Covalent sites appeared to have a more negative EA than ionic sites. When compared like-for-like with transition metals,[21,34] the EA of Al-terminated diamond was overall more negative than Cu, Ni and V with smaller variation between positions. While Ti can possess a larger NEA than Al, Ti has a positive EA when it occupies its most stable sites at 0.5 and 1 ML coverages. The adsorption energy of Al on diamond is, in general, larger than for Cu, comparable with Ni, and smaller than for V and Ti. While the minimum energy position for Al at sub-ML coverages is the covalent T4 site, for TMs it is the ionic T3 site. Based on the magnitude of adsorption energies, up to 1 ML Al on the bare surface is predicted to be slightly less thermally stable than H-termination (Table 4.1).

Table 4.2: Values of electron affinity, χ, adsorption energy, E_{ads}, and relevant bond lengths, d, calculated for the minimum energy positions at different surface coverages of Al on the bare diamond (100) surface. The HH and T3 sites at 0.25 ML coverage were not energy minima and so are not included.

Coverage (ML)	Structure	E_{ads} (eV/atom)	χ (eV)	d(C-C) (Å)	d(C-Al) (Å)
0.25	HB	-3.11	-0.04	1.40, 1.75	2.00
0.25	T4	-3.60	-0.45	1.42, 1.70	2.11
0.50	HH	-3.07	-0.23	1.71	2.19
0.50	HB	-3.56	-0.37	1.84	2.02
0.50	T3	-3.28	-0.13	1.68	2.47
0.50	T4	-3.97	-0.93	1.63	2.18
0.50	HH+T3 (linear)	-3.17	0.04	1.73	2.33, 2.32
0.50	HB+T4 (linear)	-3.73	-0.17	1.45, 1.85	2.35, 2.19
0.50	HH+T3 ($\sqrt{2} \times \sqrt{2}$)	-3.48	0.03	1.75	2.25, 2.49
0.50	HB+T4 ($\sqrt{2} \times \sqrt{2}$)	-3.56	-0.19	1.65, 1.70	2.06, 2.13
1.00	HH+T3	-4.11	-1.47	1.65	2.08, 2.08
1.00	HH+T4	-3.83	-0.93	1.74	2.27, 2.74
1.00	HB+T3	-3.78	-0.92	1.69	2.12, 2.93
1.00	HB+T4	-3.87	-0.55	1.75	2.22, 2.27

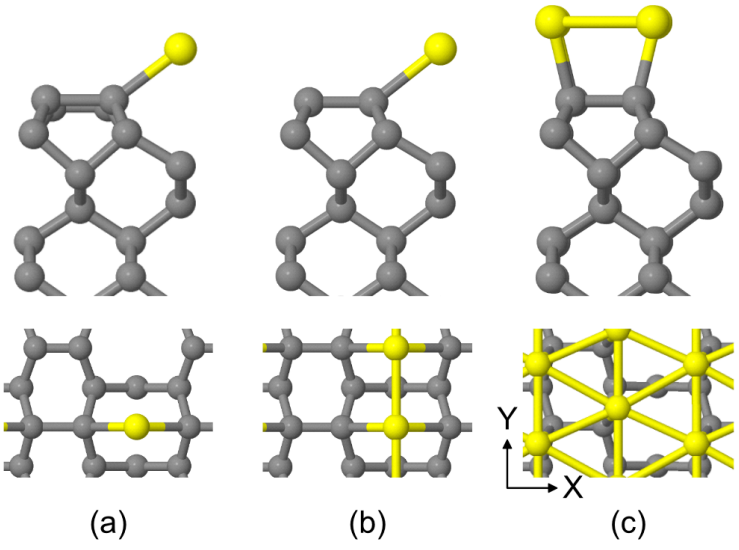

Figure 4.4: Minimum energy positions for (a)–(c) 0.25, 0.5 and 1 ML, respectively, of Al addition to the bare (100) diamond surface. Side and plan views are shown for each. C and Al atoms are shown in grey and yellow, respectively.

4.3.3 Geometries of the Al-Adsorbed O-Terminated (100) Diamond Surface

Oxygen can bond to diamond as an ether, where oxygen bridges between two carbon atoms, and as a ketone, where oxygen is double bonded to a single carbon. These structures, shown in Figure 4.5, are similar in energy, so Al addition to both the ether and ketone surface was considered. These (1 × 1) O-terminated surfaces have two high-symmetry adsorption sites: the 4-coordinate oxygen pedestal (OP) site and the 2-coordinate oxygen bridge (OB) site (Figure 4.5(c)). Al addition to high-symmetry sites for the (2 × 1) reconstructed O-terminated surface was also considered to determine the minimum energy configuration; even though the clean (2 × 1) O-terminated surface is not stable, it could be stabilised by adsorbate addition. Al addition to the (2 × 1) sites followed the procedure for the bare surface and an analogous procedure was used for addition to the (1 × 1) surface.

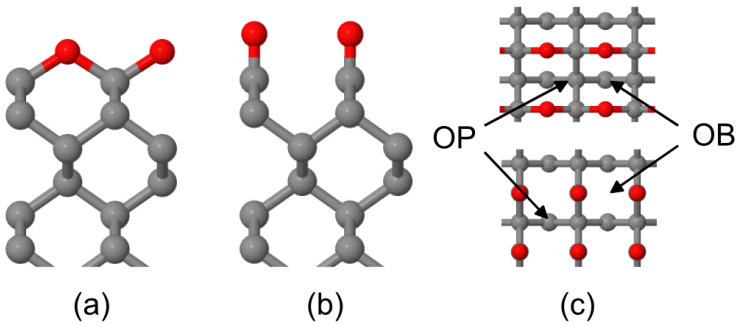

Figure 4.5: (a) Ether and (b) ketone arrangements of O-terminated (100) diamond. (c) Plan view showing the two high-symmetry positions for adsorption on the O-terminated surface. OP refers to the 4-coordinate oxygen pedestal sites and OB the 2-coordinate oxygen bridge sites. C and O atoms are shown in grey and red, respectively.

Table 4.3 displays the results for Al addition to the (2 × 1) surface and whether this configuration was obtainable from addition to either ether or ketone surfaces. Unlike for the bare surface, ionic sites were the minimum energy sites for sub-ML coverages. The T3 site was the minimum energy position for 0.25 and 0.5 ML coverages, while the HB+T3 sites were the minimum energy positions at 1 ML coverage. These are shown in Figure 4.6.

Formation of an Al-O bond requires breaking of one of the C-O bonds. With just one exception at 0.5 ML, Al addition to the ether did not break a C-O σ-bond and so no adsorption occurred. By contrast, for the ketone surface, Al addition did break the π-bond of the ketone, allowing Al-O bonding to occur. In all instances, energy minimisation caused a (2 × 1) reconstruction, although Al addition to the HB site only caused reconstruction of the atoms it lay above. At 0.25 ML coverage, Al in the OP position relaxed into the T3 site, for 0.5 ML Al in OP positions moved into the HH, HH+T3 (linear) and HH+T3 ($\sqrt{2} \times \sqrt{2}$) sites, and from OB positions to the HB and T3 sites, with final sites depending on starting configurations. At 1 ML coverage, the OP configuration changed to the HH+T4 sites with Al at different heights in the HH position, while the OB sites moved to the HB+T4 sites.

Mulliken population analysis showed bond populations for the C-O and Al-O bonds were in the range 0.57–0.73 and 0.1–0.43, respectively. The C-O bond population was closer to that of the single bond of the clean ether surface (0.57) than the double bond of the clean ketone surface (1.21). Mulliken charges of Al were more positive than for addition to the bare surface, up to 2.16*e*, 1.58*e* and 1.08*e* at 0.25, 0.5 and 1 ML coverages, respectively.

EAs were negative at 0.25 ML, calculated as -1.36 eV at the HH site and -0.37 eV at the T3 site. However, at 0.5 ML and 1 ML coverages, EAs were a mixture of positive and negative values depending on Al adsorption site. Where Al was adsorbed at covalent sites, the EA was, in general, more negative than at ionic sites.

The HH and T3 Al sites at 0.25 ML Al coverage had adsorption energies of -5.24 eV and -6.36 eV, respectively, larger than for H-terminated diamond, whilst also having NEA. Adsorption energies generally decreased with increasing Al coverage, with energies up to -5.99 eV at 0.5 ML and up to -4.58 eV at 1 ML. This trend is preferential for avoidance of island formation from metal deposition experimentally.

Overall, adsorption energies were much larger here than on the bare surface. While EAs were slightly more negative for Al-terminated diamond, here NEA was still observed, and so AlO-terminated diamond is highly promising for thermionic applications. When compared to metal-oxygen terminations using

group I and II metals, at all coverages AlO-termination had a less negative EA and significantly higher adsorption energy. For instance, metal-oxygen termination with 1 ML Li and 0.5 ML Mg have NEAs as large as -3.50 eV and -3.28 eV, with corresponding adsorption energies of -3.64 eV and -3.43 eV, respectively.[35] A comparison with transition metals shows Ti is most similar to Al as both have the largest NEA at 0.25 ML coverage and comparable adsorption energies.[36] The adsorption energy of Al at 0.25 ML coverage is larger than H-termination but the NEA is less negative.

Table 4.3: Energies and bond lengths calculated for the minimum energy positions at different surface coverages of Al on O-terminated (100) diamond. * indicates the particular (1 × 1) surface that forms this structure. (E) and (K) are ether and ketone configurations, respectively. The HB and T4 positions at 0.25 ML coverage and HB+T4 ($\sqrt{2} \times \sqrt{2}$) at 0.5 ML were not energy minima and so are not included.

Coverage (ML)	**Structure**	E_{ads} **(eV/atom)**	χ **(eV)**	d**(C-C) (Å)**	d**(C-O) (Å)**	d**(O-Al) (Å)**
0.25	HH	-5.24	-1.36	1.70	1.36	1.82
0.25	T3 *OP (K)	-6.36	-0.37	1.63	1.36	1.78
0.50	HH *OP (E, K)	-5.61	0.47	1.66	1.41	1.92
0.50	HB *OB (K)	-4.62	-0.63	1.71	1.35	1.77
0.50	T3 *OB (K)	-5.99	1.06	1.64	1.40	1.88
0.50	T4	-4.71	-0.46	1.63	1.34	1.71
0.50	HH+T3 (linear) *OP (K)	-5.85	0.72	1.64	1.40	1.85, 1.98
0.50	HB+T4 (linear)	-4.32	0.31	1.66	1.39	1.80, 1.88
0.50	HH+T3 ($\sqrt{2} \times \sqrt{2}$) *OP (K)	-5.85	1.13	1.65	1.40	1.88, 2.03
1.00	HH+T3	-4.35	-0.12	1.65	1.40	1.92, 3.11
1.00	HH+T4 *OP (K)	-4.55	-0.45	1.66	1.39	1.88, 1.88, 1.99, 2.80
1.00	HB+T3	-4.58	0.54	1.64	1.41	2.08, 2.09
1.00	HB+T4 *OB (K)	-4.35	0.00	1.64	1.39	1.84, 1.94

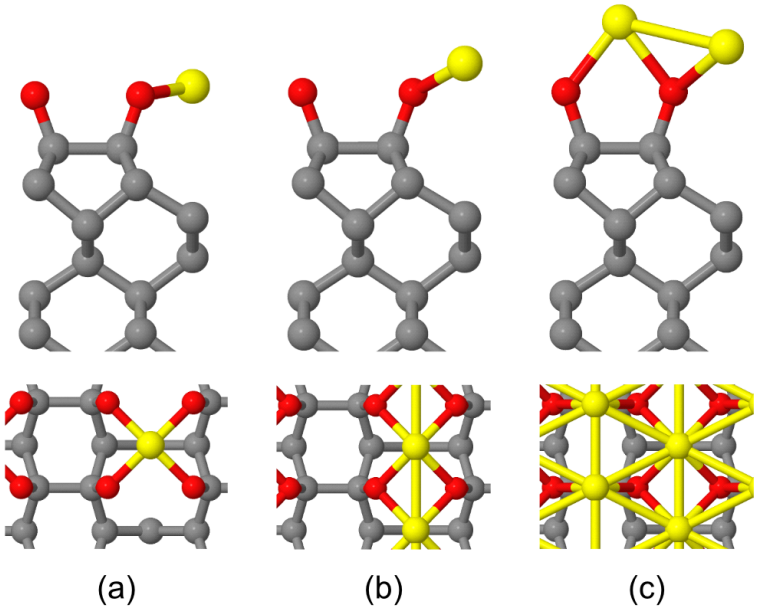

Figure 4.6: Minimum energy positions for (a)–(c) 0.25, 0.5 and 1 ML, respectively, of Al addition to the O-terminated (100) diamond surface. Side and plan views are shown for each. C, O and Al atoms are shown in grey, red and yellow, respectively.

4.3.4 Geometries of the Al-Adsorbed N-Terminated (100) Diamond Surface

The N-terminated diamond surface has received relatively little attention compared with the bare and O-terminated surfaces for NEA studies. For the (100) surface, experimental work by Chandran *et al.*[37] shows that a full ML can be achieved with a radio-frequency nitrogen plasma. The structure of nitrogen-terminated (100) diamond has been explored experimentally and computationally by Stacey *et al.*,[38] who conclude that nitrogen probably displaces a carbon atom in the dimer layer of a (2 × 1) H-terminated surface. Both a half-ML N/C-H combination and a full-ML N-termination are expected to be thermodynamically stable. These configurations are shown in Figure 4.7.

Simulation of the clean N-terminated surface with a full-ML coverage of nitrogen gives an N-N bond length of 1.61 Å and N-C bond lengths of 1.54 Å. It has a positive electron affinity (PEA) of 2.71 eV. The half-terminated surface was not considered for Al addition.

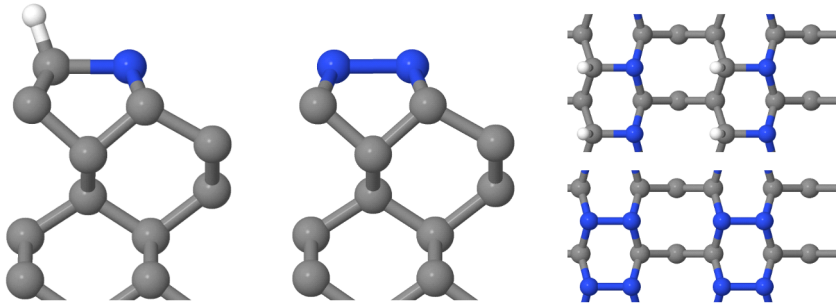

Figure 4.7: (a) Half-ML N-termination is a combination of N and C-H within a (2 × 1) dimer, and (b) full-ML N-termination involves replacement of both carbon atoms with nitrogen in the surface dimer. (c) Plan views for both half- and full-ML terminations. C, N and H atoms are shown in grey, blue and white, respectively.

Al addition to the full-monolayer N-terminated diamond surface follows the same pattern of addition to sites on the bare surface, *i.e.* HH, HB, T3 and T4 sites and combinations of these. Removal of the N-N dimer bond and reversion to the (1 × 1) surface leads to nitrogen bridge (NB) and nitrogen pedestal (NP) sites, analogous to OB and OP, for Al which is two and four co-ordinate to nitrogen, respectively.

Table 4.4 details energies, EAs and bond lengths for Al addition to nitrogenated diamond surfaces and Figure 4.8 shows the minimum energy structures. In all instances, Al addition was able to break both N-N dimer bonds, except for HB and T3 configurations where only the nearest N-N bond was broken. In most instances, Al relaxed into NP or NB sites, although in certain cases Al was located just outside of NP sites at 0.5 ML or the NB sites at 1 ML; this deformation allows the Al-Al bond to lengthen slightly.

Only at the NP site at 0.25 ML coverage was an NEA predicted. The adsorption energy at this site (-4.32 eV/atom) was the largest for that degree of coverage and comparable with hydrogen termination. However, the similarity of adsorption energies at larger coverages suggests that forming NEA from Al on N-terminated diamond is unlikely. Part of the reason for why this is so could be the lengthier Al-N bond compared with Al-O. In comparison with the O-terminated surface, Mulliken charges on Al are much lower, mostly below 1*e* for all coverages. This was expected since N is less electronegative than O.

Table 4.4: Energies and bond lengths for Al addition to N-terminated (100) diamond. * indicates the starting configuration. [a] Both Al atoms relax into configurations just outside of NP position, in opposite directions to lengthen the Al-Al bond. [b] Same as [a] but for the NB position.

Coverage (ML)	**Structure**	E_{ads} **(eV/atom)**	χ **(eV)**	d**(N-Al) (Å)**
0.25	NB *HB	-3.78	1.50	2.01
0.25	NP *HH, T3	-4.32	-0.47	1.98
0.25	NB *T4	-3.77	1.58	2.00
0.5	NB *HB, HH, T3, T4	-4.92	0.18	2.00
0.5	NP [a] *HB+T3, HH+T3 ($\sqrt{2} \times \sqrt{2}$), HH+T4	-4.24	0.55	1.96, 1.99
0.5	NB *HB+T4 ($\sqrt{2} \times \sqrt{2}$)	-4.20	1.30	1.97
0.5	NB * HB+T4 (linear)	-3.94	0.52	1.95
0.5	NP *HH+T3 (linear)	-4.23	0.73	2.10
1	NB+NP *HB+T3, HH+T4	-4.05	-0.56	1.95, 2.78
1	NB+NB *HB+T4	-4.28	-0.09	1.97
1	NB+NB [b] *HH+T3	-4.31	-0.11	1.99

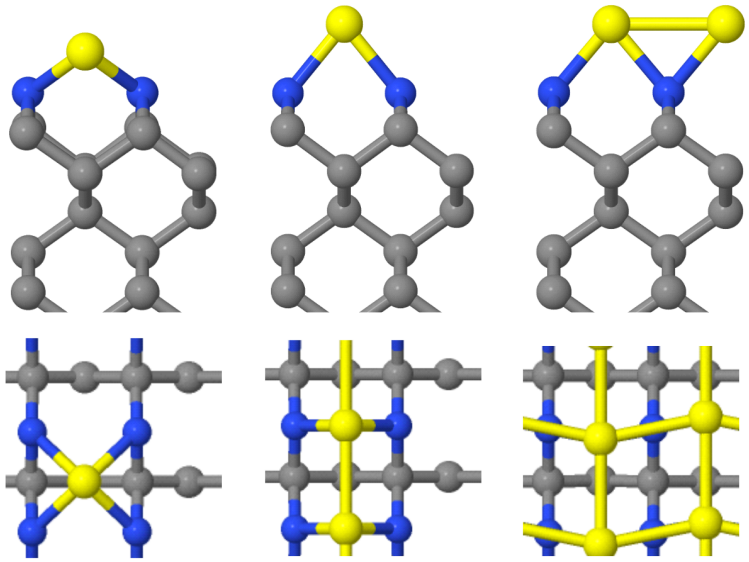

Figure 4.8: Minimum energy positions for (a)–(c) 0.25, 0.5 and 1 ML Al addition to the N-terminated (100) diamond surface. C, N and Al atoms are shown in grey, blue and yellow, respectively.

4.3.5 Electronic Structure of the (100) Surfaces

Contributions to the electronic structure from different atoms in the vicinity of the Fermi level can be determined by computing the PDOS. Figure 4.9 shows the PDOS for clean bare, oxygen (ether) and nitrogen-terminated diamond surfaces. The PDOS spectra have the VBM set to zero and the different atoms of interest are offset for clarity. The dashed vertical line represents the position of the Fermi level. Bulk carbon atoms were taken from the centre of the diamond slab and the DOS are all similar, as expected. Surface carbon atoms were from the dimer row. In each of these surfaces, there were states present within the band gap region of bulk diamond. For the bare surface, these come from surface C atoms and originate from π and π* bonds of the dimer rows.[34] Both the oxygen and nitrogen DOS have states near the valence band, originating from lone pairs.[38,39]

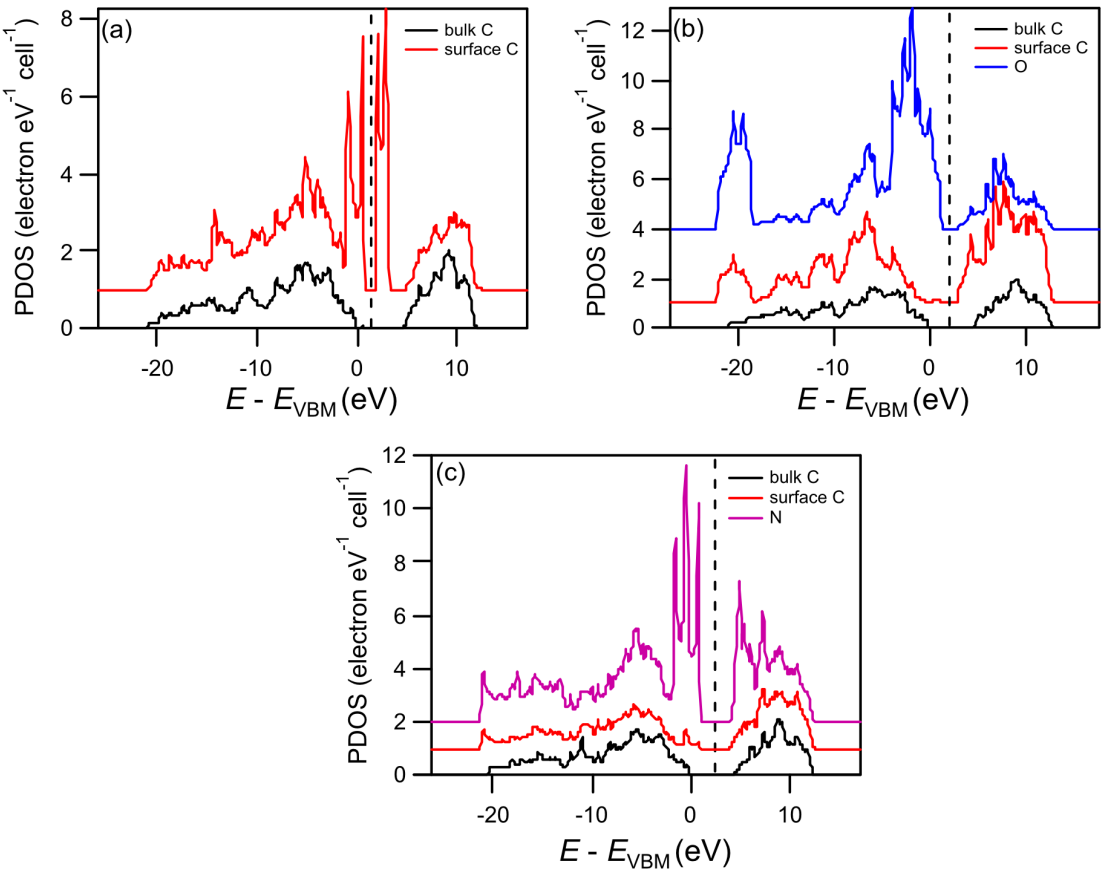

Figure 4.9: PDOS spectra evaluated for (a) the bare diamond surface, (b) O-terminated diamond surface with ether configuration and (c) full-monolayer N-terminated diamond surface.

Figure 4.10 shows the PDOS spectra for the Al-adsorbed bare diamond surface at different Al coverages. These spectra are for the minimum energy configurations from Table 4.2. The Al DOS had a high number of states spanning a wide energy range, including within the band gap of bulk diamond. Many of these peaks correspond to peaks in the surface carbon DOS, indicative of covalent bonding. Figure 4.10(a) shows the PDOS at 0.25 ML Al coverage, where Al interacts only with one of the carbon dimers, and so there are two contributions to the surface C DOS.

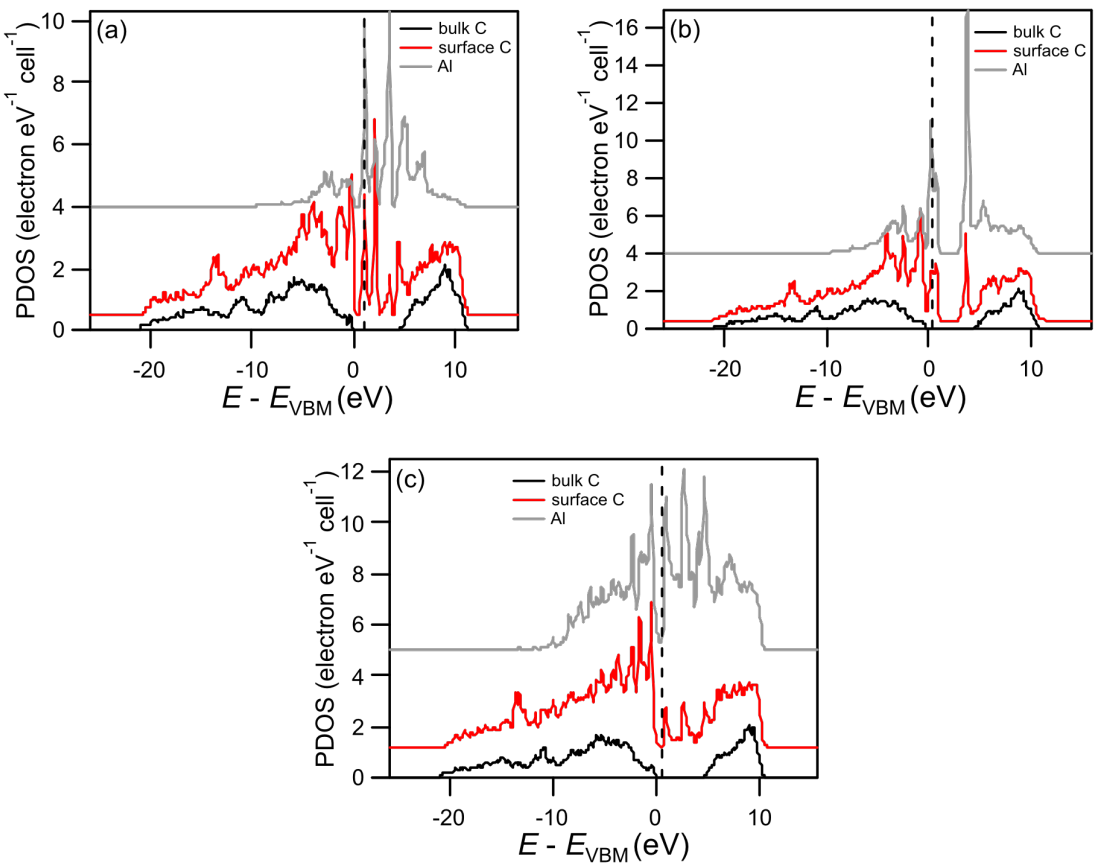

Figure 4.10: PDOS evaluated for (a)–(c) 0.25, 0.5 and 1 ML Al coverage, respectively, on the bare (100) diamond surface. These are the lowest energy structures from Table 4.2.

Figure 4.11 shows the PDOS spectra for the Al-adsorbed O-terminated surface. The Al DOS is considerably different to that of the bare surface, due to the change from covalent to ionic bonding. In particular, in Figure 4.11(a) the Al DOS at 0.25 ML coverage had just one prominent peak at 4 eV from the 3*s* and 3*p* orbitals, just below the position of the conduction band of bulk diamond. This

state lies above the Fermi level and so is unoccupied, indicating that charge transfer has occurred. In Figure 4.11(b) the Al DOS had broadened and moved down in energy such that it is now partially above and partially below the Fermi level. By 1 ML the Al DOS had multiple states spanning the entire band gap region of bulk diamond, which was attributed to metallic Al-Al bonds.

Figure 4.12 shows the PDOS spectra for the Al-adsorbed N-terminated surface. The trend here is largely similar to that for the Al-adsorbed O-terminated surface. The Al DOS again showed a singular peak at 0.25 ML, but was now located at the position of the Fermi level. This explains why the NEA is much less negative compared to that of the corresponding O-terminated surface. At 0.5 ML this peak moved down in energy and broadened, while at 1 ML coverage, metallic Al-Al bonding again caused a broad range of energy states in the Al DOS.

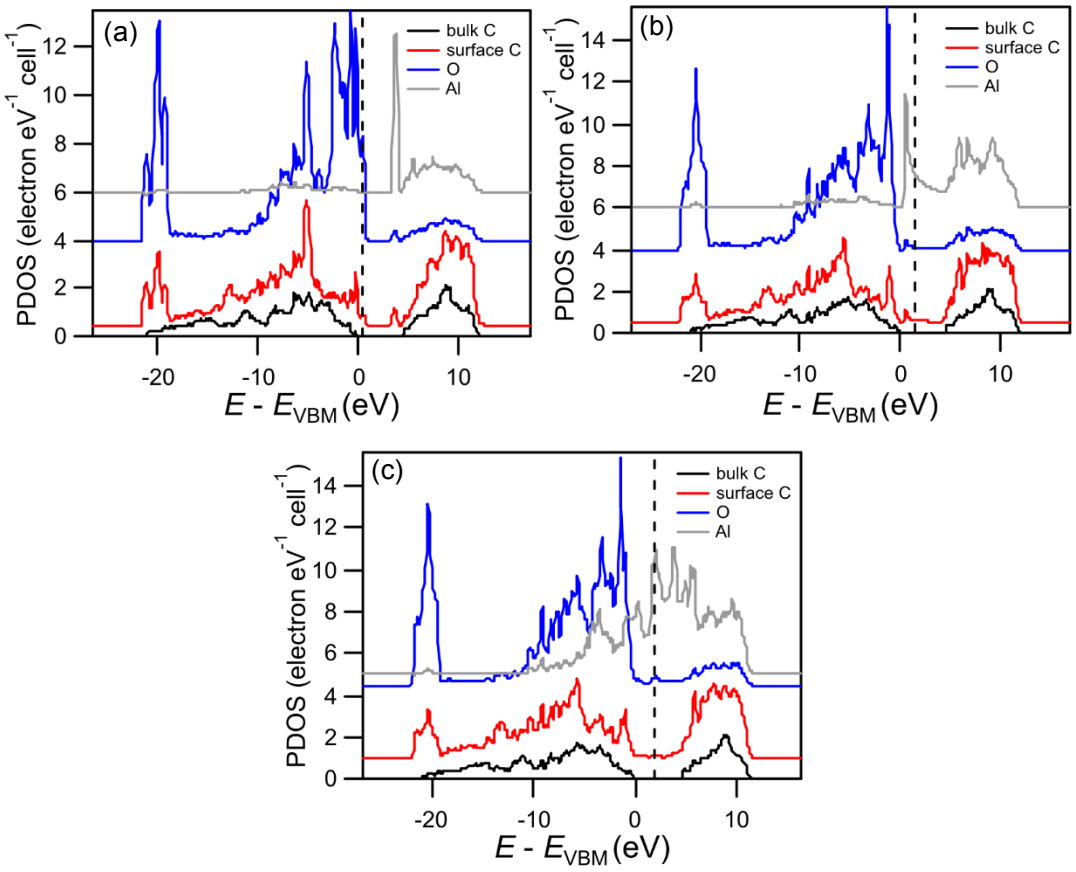

Figure 4.11: PDOS evaluated for (a)–(c) 0.25, 0.5 and 1 ML Al coverage, respectively, on the O-terminated (100) diamond surface. These are the lowest energy structures from Table 4.3.

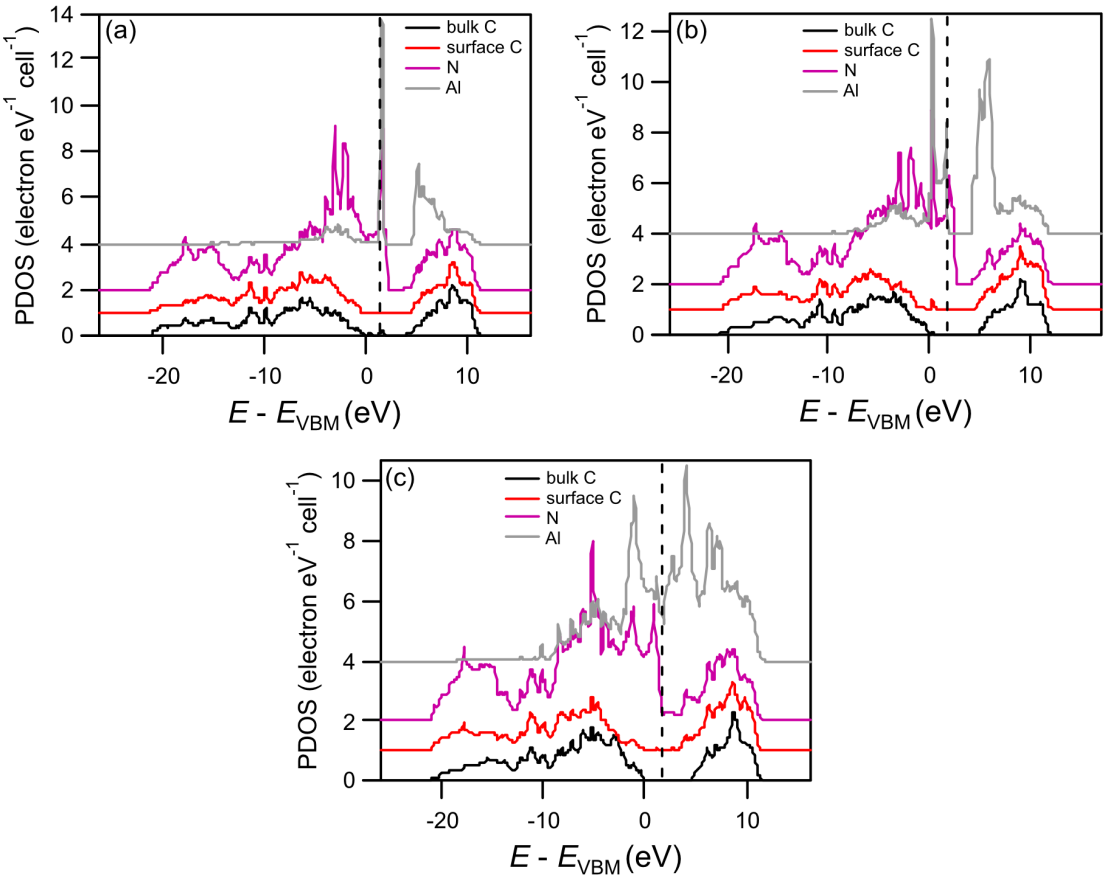

Figure 4.12: PDOS evaluated for (a)–(c) 0.25, 0.5 and 1 ML Al coverage, respectively on the N-terminated (100) diamond surface. These are the lowest energy structures from Table 4.4.

4.3.6 Investigation of a Larger Supercell

The EAs obtained from 0.25 and 0.5 ML Al coverages on the O-terminated (100) diamond surface were considerably different, with 0.25 ML Al coverage displaying NEA for all Al sites and 0.5 ML Al coverage largely having positive EA. In light of this, a further study was undertaken involving a larger supercell to consider a wider variety of adsorbate positions and additional coverages. A (2 × 4) supercell of the ketone O-terminated surface was used. The lattice parameters were accordingly adjusted to 5.05 Å × 10.1 Å × 35.7 Å. Now, one Al atom on either side of the slab represents 0.125 ML coverage and three atoms 0.375 ML coverage. As well as these new coverages, a wider variety of potential sites at 0.25 ML coverage can be studied. Figure 4.13 shows the supercell, with potential Al adsorption sites marked A–H in the plan view. In this instance only 4-coordinate OP sites were chosen.

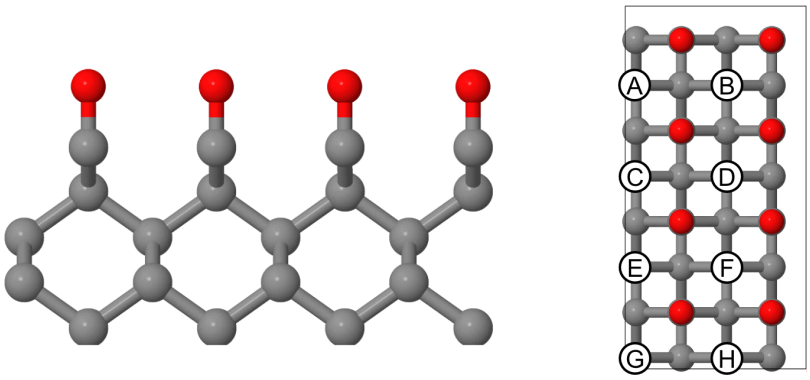

Figure 4.13: The (2 × 4) supercell of the ketone O-terminated diamond surface. Sites marked A–H in the plan view indicate the possible Al adsorption sites that were considered. C and O atoms are shown in grey and red, respectively.

Table 4.5: Energies and bond lengths calculated for the minimum energy positions at different surface coverages of Al on O-terminated (100) diamond.

Coverage	Site(s)	E_{ads} (eV/atom)	χ (eV)	d(O-Al) (Å)
0.125	A	-7.43	0.94	1.82
0.25	A+B	-6.54	1.55	1.93
0.25	A+C	-6.35	0.87	1.80, 1.86
0.25	A+D	-6.32	0.55	1.79, 1.86
0.25	A+E	-7.54	-0.35	1.78
0.25	A+F	-7.56	-0.35	1.80
0.375	A+B+D	-5.42	0.40	1.77, 1.87, 1.94
0.375	A+B+E	-6.31	-0.55	1.82, 1.90, 1.90
0.375	A+C+E	-6.52	-0.82	1.77, 1.77, 1.83
0.375	A+C+F	-6.59	-0.97	1.77, 1.79, 1.85
0.375	A+D+E	-6.59	-0.99	1.78, 1.78, 1.86

Table 4.5 displays the results for 0.125, 0.25 and 0.375 ML coverages. These represent all the possible variations of Al positioning. The 0.125 ML coverage showed a positive EA, a useful result for determining minimum coverage requirement for experimental studies. In a similar manner, at 0.25 ML coverage A+B, A+C and A+D sites all had positive EA also, which was not unexpected, as Al was not evenly distributed across the surface. A mixture of positive and negative EA components together can cancel the effects of one another across the whole surface.[40] Interestingly, these surfaces had considerably lower adsorption energies when compared with A+E and A+F, which did possess NEA. This

suggests that a method such as thermal annealing could enhance NEA by ensuring a more even distribution of Al atoms across the surface.

At 0.375 ML coverage, all sites except one showed a larger NEA than for 0.25 ML coverage. The A+B+D configuration likely showed positive EA from the larger Al-Al interactions, similar to 0.5 ML coverage described previously. Adsorption energies continued to follow the trend of decreasing energy with increasing coverage. It should be noted that adsorption energies here were calculated using the clean ketone surface, meaning they were slightly larger than those shown in Table 4.3, which uses the clean ether surface as reference instead.

4.4 Al Addition to the (111) Diamond Surface

4.4.1 Ensuring Convergence

The (111) diamond surface was also modelled using a periodic slab with a 2 × 2 supercell. The lattice vectors parallel to the slab surface were both fixed to 5.05 Å, and the angle between them was 120°. The lattice vector perpendicular to the surface was 37 Å, maintaining a vacuum gap of 20–25 Å between repeating slabs. Convergence testing was performed again on the cut-off energy, *k*-point grid size, vacuum gap and number of diamond layers due to the different slab structure. The computational parameters used in (100) calculations were deemed sufficiently accurate for the (111) calculations as well.

Computed structures of bare, H- and O-terminated (111) surfaces were first compared with existing values from the literature. Table 4.6 shows the values for adsorption energies, EAs and bond lengths. Bond lengths were all in excellent agreement. Adsorption energies showed that the (1 × 1) surface arrangement was favourable for H-termination and the (2 × 1) structure favourable for the bare and oxygenated surfaces, as expected. Adsorption energies for the oxygen terminations were slightly higher than literature values, but still reasonable. The ether surface was calculated to be more stable than the ketone, and the ketone was found to break one of the C-C bonds of the upper Pandey chain, as predicted by others. EAs were in excellent agreement with other computed values. As with the (100) surface, H-termination had a large NEA, the bare surface a small PEA

and the O-terminations large PEAs. DFT calculations again overestimate the EA values, compared with experimental values, which have been measured as 0.38 eV and -1.27 eV for the bare and H-terminated surfaces, respectively.[41] Experimental work has determined the EA of O-termination is positive,[42] but no specific values were given.

Table 4.6: Energies and bond lengths for selected calculations compared with previous work on (111) diamond. *d*(C-C) refers to the carbon-carbon bond length of surface atoms; for (2 × 1) structures these are for the upper Pandey chain. * indicates the C-C bond located beneath the oxygen atom. E_{ads} for the bare surface was calculated with respect to the relaxed (1 × 1) surface.

Structure	Source	E_{ads} (eV/atom)	χ (eV)	*d*(C-C) (Å)	*d*(C-O) (Å)	*d*(C-H) (Å)
C(111)-(2 × 1)	Previous calculations	-0.8[39]	0.35,[27] 0.35,[39] 0.26[43]	1.43,[39] 1.44[43]	-	-
	Current work	-1.05	0.31	1.44	-	-
C(111)-(1 × 1):H	Previous calculations	-4.89[44]	-2.03,[27] -1.97,[39] -1.98[43]	1.52[39]	-	1.12[39]
	Current work	-3.79	-2.2	1.54	-	1.11
C(111)-(2 × 1):½O (ether)	Previous calculations	-4.605,[45] -4.72,[43] -5.23[44]	2.09[43]	1.463* and 1.50,[45] 1.47* and 1.56,[43] 1.457* and 1.498[42]	1.44,[43] 1.434,[44] 1.434[42]	-
	Current work	-6.18	2.14	1.47* and 1.51	1.44	-
C(111)-(2 × 1):O (ketone)	Previous calculations	-4.099,[45] -4.32,[43] -4.85[44]	3.64[43]	1.71 and broken,[43] 1.703 and broken[42]	1.195,[45] 1.195[42]	-
	Current work	-5.82	3.51	1.71 and broken	1.19	-

4.4.2 Geometries of the Al-Adsorbed Bare (111) Diamond Surface

Addition of Al to the (2 × 1) reconstructed Pandey chain surface and to the (1 × 1) surface were considered. The sites for Al adsorption to the (2 × 1) surface maximise Al-C coordination with one of the Pandey chains or across two Pandey chains. These sites are designated upper (U) and lower (L), respectively, as Al is positioned above the upper and lower Pandey chains. These positions are shown in Figure 4.14(a). For addition to the (1 × 1) surface, Al was positioned either

directly above the first tier carbon (T1), or 3-coordinate to surface C atoms above the second (T2) or fourth (T4) tier carbons. These adsorption sites are shown in Figure 4.14(b).

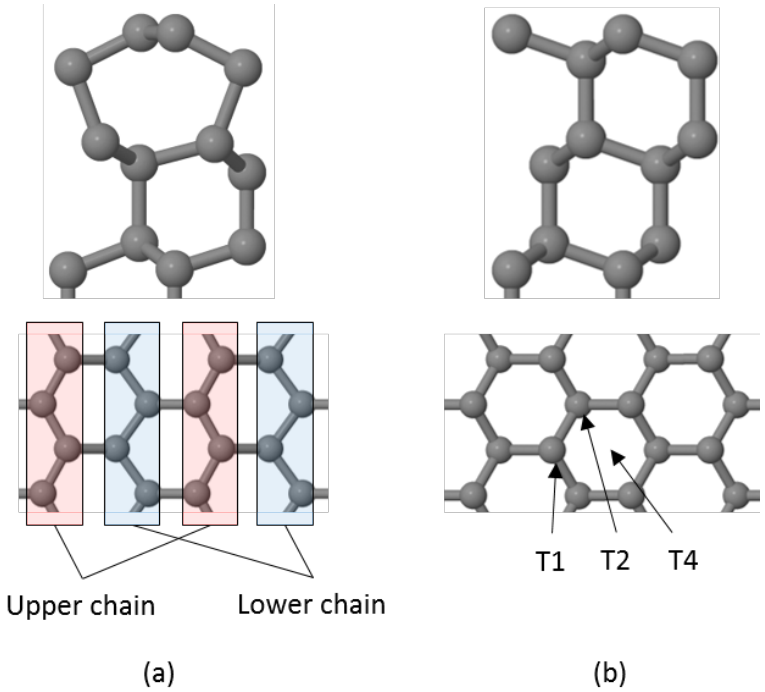

Figure 4.14: (a) The (2 × 1) reconstructed (111) surface. The plan view shows the positions of the upper and lower Pandey chain. (b) The (1 × 1) (111) surface. The T1, T2 and T4 sites are located above the first, second and fourth-tier carbon atoms, respectively.

Table 4.7 details the stable adsorption sites for up to 1 ML Al addition to both the (2 × 1) and (1 × 1) surfaces, and the most stable adsorption sites for both surfaces are shown in Figures 4.15 and 4.16, respectively. Al generally adsorbed poorly to both, with adsorption energies of up to -2.95 eV/atom at 0.25 ML coverage, and up to -3.49 eV/atom at 0.5 ML, compared with up to -3.60 eV/atom at 0.25 ML and up to -3.97 eV/atom at 0.5 ML for the (100) surface. The adsorption energy was comparable at 1 ML. For addition to the (2 × 1) surface, at 0.25 ML coverage only a 3-coordinate U site was stable. At 0.5 ML an arrangement of one atom in a 3-coordinate site and one in a 1-coordinate site was the lowest energy, and at 1 ML the most stable site only had the Al in the U site co-ordinated with the diamond surface, with the Al in the L site bonding only with Al atoms in a hexagonal arrangement. By contrast, Al bonded more strongly

with the (1 × 1) surface. The largest adsorption energies were found at the T2 site at 0.25 and 0.5 ML coverage, and the T1 site at 1 ML coverage. This suggests that the (2 × 1) surface is metastable with respect to Al addition and, with sufficient energy, the Al-adsorbed (111) surface would reorganise into the (1 × 1) structure. EAs were almost exclusively negative and generally become more negative with increasing coverage up to a value of -1.88 eV at 1 ML.

Table 4.7: Energies and bond lengths for the minimum energy positions at different surface coverages of Al on bare (111) diamond. *only for Al coordinated with surface carbon atoms. Addition to the L sites at 0.25 and 0.5 ML coverage were not energy minima.

Coverage (ML)	**Structure**	**Site**	**Al-C coordination number**	E_{ads} **(eV/atom)**	χ **(eV)**	d**(C-Al) (Å)**
0.25	2 × 1	U	3	-2.16	-0.14	2.27
0.25	1 × 1	T1	1	-1.00	0.46	1.99
0.25	1 × 1	T2	3	-2.95	-0.56	2.05
0.25	1 × 1	T4	3	-2.76	-0.59	2.05
0.5	2 × 1	U	1, 3	-3.00	-0.12	2.11, 2.40
0.5	1 × 1	T1	1	-2.98	-0.28	2.03
0.5	1 × 1	T2	3, 3	-3.49	-0.38	2.07
0.5	1 × 1	T4	3, 3	-3.42	-0.41	2.09
1	2 × 1	U+L	2 (U), 0 (L)	-3.32	-0.25	2.13*
1	2 × 1	U+L	1	-3.21	-1.88	2.12
1	1 × 1	T1	1	-3.84	-1.51	2.09
1	1 × 1	T2	3	-4.11	-0.76	2.42
1	1 × 1	T4	3	-4.19	-1.01	2.47

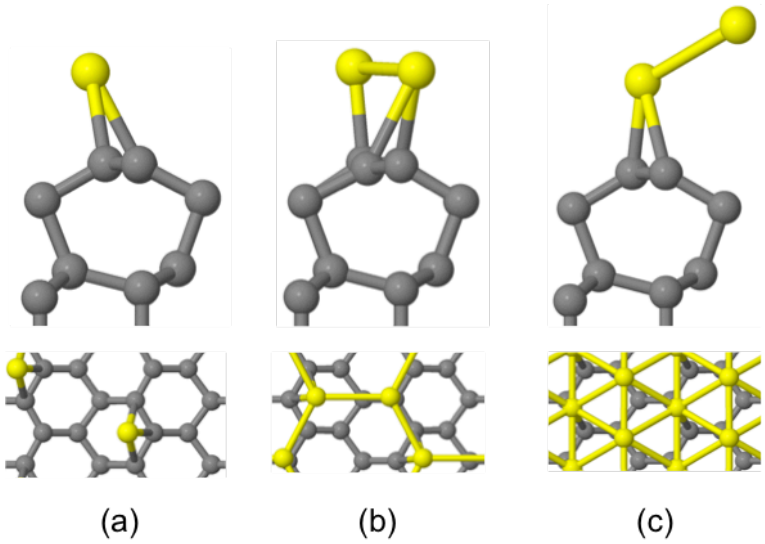

Figure 4.15: Lowest energy adsorption sites for Al addition to the (2 × 1) (111) bare surface. (a)–(c) represent the lowest energy structures taken from Table 4.7 for 0.25, 0.5 and 1 ML Al coverage, respectively. Side and plan views are shown for each. C and Al atoms are shown in grey and yellow, respectively.

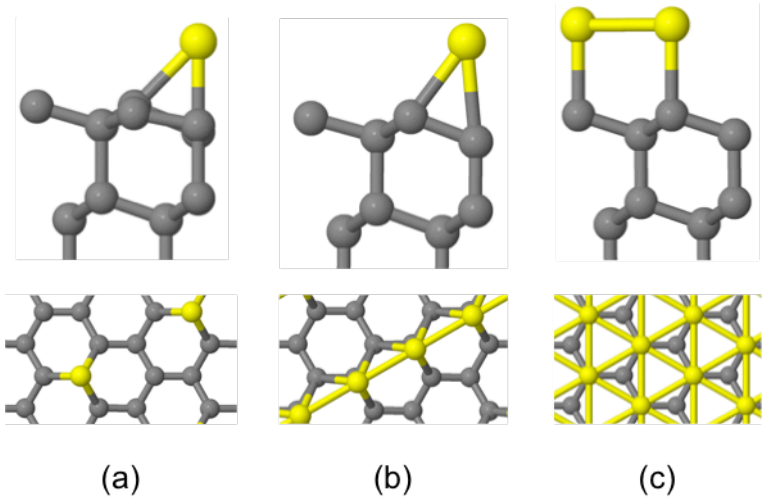

Figure 4.16: Lowest energy adsorption sites for Al addition to the (1 × 1) bare (111) diamond surface. (a)–(c) represent the lowest energy structures taken from Table 4.7 for 0.25, 0.5 and 1 ML Al coverage, respectively. Side and plan views are shown for each. C and Al atoms are shown in grey and yellow, respectively.

An analysis of Mulliken bond populations and charges can determine more clearly how Al interacts with these surfaces. Starting with the (2 × 1) surface, 0.25 ML Al coverage had no positive bond population between Al and surface C atoms, which fits with the low adsorption energy observed. At higher coverages, Al weakly bonded with one or more C atoms with a bond population of up to 0.3

observed. All coverages showed C-C bond populations within the upper Pandey chain to be >1, signifying that the Pandey chain still maintained significant double bond character. For the (1 × 1) surface, the T2 site had the largest Al-C bond population, 0.38, at 0.25 ML coverage but at higher coverages the T1 site had the largest bond population, 0.53 at 0.5 ML and 0.78 at 1 ML. For both (2 × 1) and (1 × 1) surfaces, Al-Al interactions were significant above 0.25 ML coverage, with bond population up to 1.75 observed.

Next, the Mulliken charges were considered. The Al atoms all possessed a positive charge, largest at 0.25 ML coverage and smallest at 1 ML. Al was more positively charged on the (1 × 1) surface; for instance at 0.25 ML coverage the charge on Al was up to 1.05*e* compared with 0.59*e* for the (2 × 1) surface, a further indication of the weak Al interaction with the Pandey chain. Negative charge in all instances was predominantly located on the surface C atoms.

4.4.3 Geometries of the Al-Adsorbed O-Terminated (111) Diamond Surface

The addition of Al to the ether and ketone O-terminated (2 × 1) surfaces and the addition to the (1 × 1) fully oxygenated O-terminated surface were all considered. Figure 4.17 shows the adsorption sites for addition to the (2 × 1) surfaces, and Figure 4.18 shows the adsorption sites for addition to the (1 × 1) surface. Possible adsorption sites for the (2 × 1) surfaces are again denoted ‘U’ or ‘L’ depending on whether Al was positioned above the upper or lower Pandey chains, respectively. Al sites were chosen that maximised Al-O coordination number, so that Al was 2-coordinate to O atoms of the ether termination and 3-coordinate to O atoms of the ketone. For the (1 × 1) surface Al was 3-coordinate to O atoms in either the T2 or T4 sites.

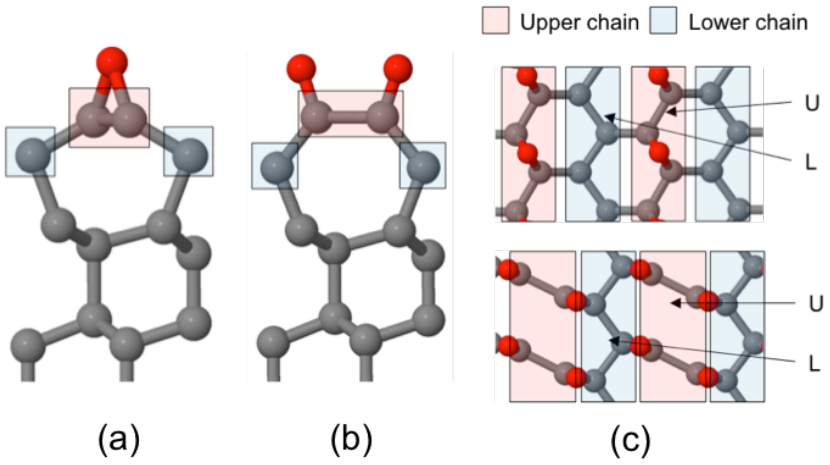

Figure 4.17: Adsorption sites to the (2 × 1) O-terminated (111) diamond surfaces. (a)–(b) Side views of the half-oxidised ether and fully oxidised ketone surfaces, respectively. (c) Plan view of the ether and ketone surfaces. U and L sites are located in high-symmetry positions above the upper and lower Pandey chains, respectively. C and O atoms are shown in grey and red, respectively.

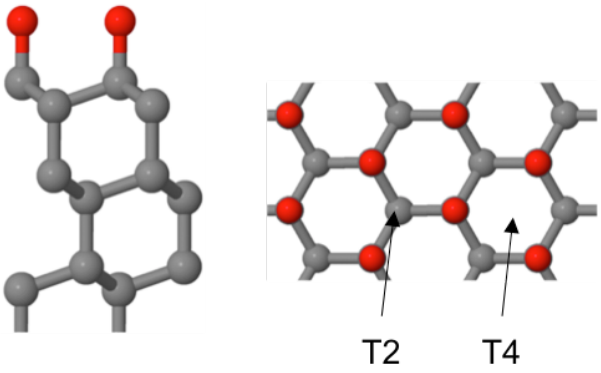

Figure 4.18: Side and plan view of (1 × 1) O-terminated (111) diamond surface. Sites for addition are shown in the plan view. T2 and T4 sites are located above the second and fourth-tier carbon, respectively. C and O atoms are shown in grey and red, respectively.

Table 4.8 displays the results of addition to these different surfaces, while Figures 4.19, 4.20 and 4.21 show the lowest energy structures for the Al-adsorbed (2 × 1) ketone, (2 × 1) ether and (1 × 1) surfaces, respectively. Starting with addition to the ketone surface, Al was lowest in energy in the L site at 0.25 and 0.5 ML coverage while at 1 ML coverage steric crowding (repulsive forces from the close spacing of Al atoms to one another) caused one Al to be pushed away from the surface. The ether surface favoured Al addition in the L site at

0.25 ML coverage and the U+L site combination at 0.5 ML coverage. No stable adsorption sites were found for 1 ML Al coverage due to Al abstracting O atoms from the surface and incorporating them into the metal layer. For the (1 × 1) surface the two adsorption sites had similar values for E_{ads} and EA. Adsorption energies were largest for addition to the (1 × 1) surface, then the ketone, then the ether, suggesting that ketone formation is preferential to the ether, but is metastable with Al adsorption and may reorganise to the (1 × 1) structure with sufficient energy. Like the (100) surface, adsorption energies decreased with increasing Al coverage.

Calculation of EAs showed Al adsorption gave all three surfaces an NEA at 0.25 ML coverage regardless of adsorption site. At larger coverages, however, the EA was mostly positive. Thus, fine control of deposition is required, but if successful should yield the desirable NEA surface. The Al adsorption energy on the ketone surface and (1 × 1) surface exceeded that of the (100) surface. In all cases Al adsorption energies were larger than that of H-termination (Table 4.6).

With Al addition, one C-O bond broke. For the ether surface, this resulted in adjacent C atoms forming C=C double bonds, as shown by an increase in Mulliken bond population from 0.82 to >1. For the ketone surface, the C=O bond population decreased with Al addition from 1.21 to ~0.7, becoming closer to a single bond, and at the same time the C-C bond of the upper Pandey chain reformed. A similar C-O bond population was observed for the Al-adsorbed (1 × 1) surface. Al-O bond populations were in the range 0.1–0.5 for all surfaces and coverages. Above 0.25 ML coverage Al-Al bonds formed, with bond population typically ~0.5. Mulliken charges showed Al was highly charged at 0.25 ML coverage, up to 1.73*e*, 2.13*e*, and 1.87*e* for the ether, ketone and (1 × 1) surfaces, respectively. In each case Al became less positively charged with increasing coverage. The majority of negative charge was located on the O atoms.

Table 4.8: Values of χ, E_{ads}, and d, calculated for the minimum energy positions at different surface coverages of Al on O-terminated (111) diamond. (K) and (E) are ketone and ether, respectively.

Coverage (ML)	Structure	Site	E_{ads} (eV/atom)	χ (eV)	d(O-Al) (Å)
0.25	2 × 1 (K)	U	-6.76	-0.53	1.77
0.25	2 × 1 (K)	L	-7.31	-2.17	1.66
0.25	2 × 1 (E)	L	-4.73	-0.68	1.74
0.25	1 × 1	T2	-8.17	-1.22	1.7
0.25	1 × 1	T4	-8.19	-1.19	1.7
0.5	2 × 1 (K)	U	-6.44	-0.01	1.8
0.5	2 × 1 (K)	L	-6.57	0.32	1.74
0.5	2 × 1 (K)	U+L	-6.52	0.10	1.72, 1.79
0.5	2 × 1 (E)	U+L	-4.41	0.78	1.84, 1.85
0.5	1 × 1	T2	-7.15	0.33	1.76
0.5	1 × 1	T4	-7.16	0.32	1.75
1	2 × 1 (K)	U+L	-5.08	-0.03	1.83, 1.94, 1.94, 2.88
1	1 × 1	T2	-5.22	0.67	1.99
1	1 × 1	T4	-5.36	0.27	2.01

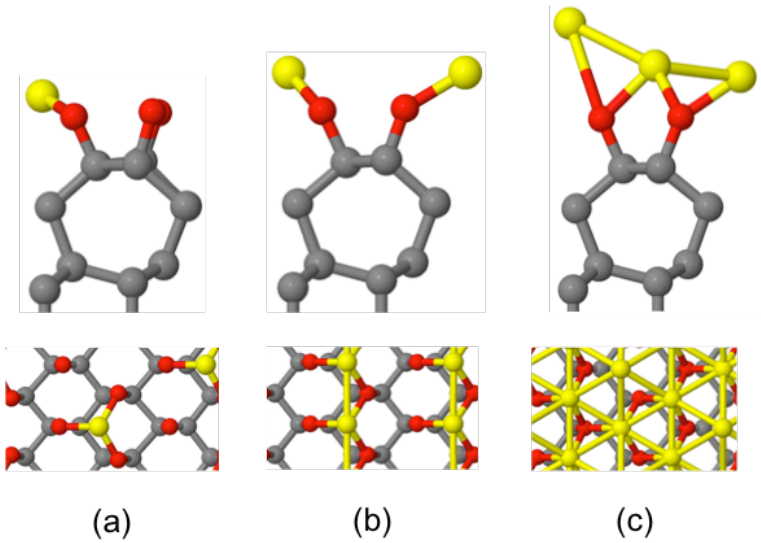

Figure 4.19: Lowest energy adsorption sites for Al addition to the (2 × 1) ketone O-terminated (111) diamond surface. (a)–(c) represent the lowest-energy structures taken from Table 4.8 for 0.25, 0.5 and 1 ML Al coverage, respectively. Side and plan views are shown for each. C, O and Al atoms are shown in grey, red and yellow, respectively.

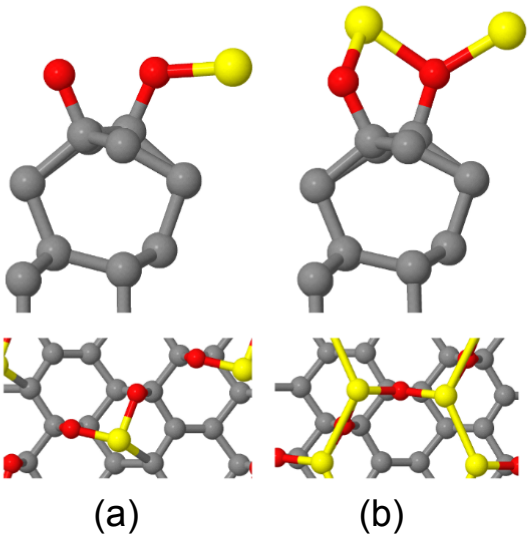

Figure 4.20: Lowest-energy adsorption sites for Al addition to the (2 × 1) ether O-terminated (111) diamond surface. (a)–(b) represent the only stable structures found for 0.25 and 0.5 ML Al coverage, respectively. No stable structure was found for 1 ML coverage. Side and plan views are shown for each. C, O and Al atoms are shown in grey, red and yellow, respectively.

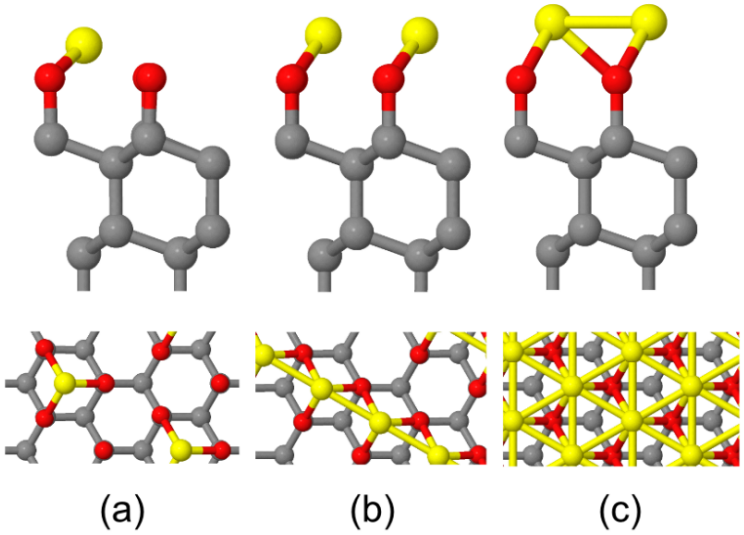

Figure 4.21: Lowest-energy adsorption sites for Al addition to the (1 × 1) O-terminated (111) diamond surface. (a)–(c) represent the lowest energy structures taken from Table 4.8 for 0.25, 0.5 and 1 ML Al coverage, respectively. Side and plan views are shown for each. C, O and Al atoms are shown in grey, red and yellow, respectively.

4.4.4 Geometries of the Al-Adsorbed N-Terminated (111) Diamond Surface

The structure of the N-terminated (111) surface, shown in Figure 4.22, has been reported to have each nitrogen atom bonding with three carbon atoms.[46] N atoms replace the surface carbon layer, similar to the N-terminated (100) surface. Simulation of the clean N-terminated surface gave N-C bond lengths of 1.54 Å and a PEA of 2.45 eV.

Al atoms were added at T1, T2 and T4 sites, similar to addition to the unreconstructed bare (111) surface. As such, each Al was either coordinated with one or three N atoms. All results, however, indicated that Al does not bond with N-terminated (111) diamond. Clearly, it is easier to break an N-N bond on the (100) surface than to break a C-N bond here. Therefore, the lack of reactivity of this surface is beneficial for quantum applications (as described in Chapter 2), but these results suggest AlN-terminations are not promising for thermionic applications.

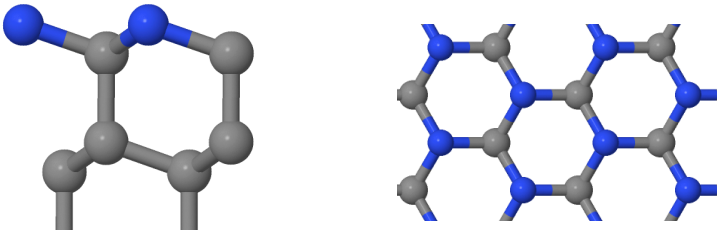

Figure 4.22: Side and plan view of the clean N-terminated (111) diamond surface. C and N atoms are shown in grey and blue, respectively.

4.4.5 Electronic Structure of the (111) Surfaces

The PDOS spectra computed for the clean bare and oxygenated (ketone and ether) (111) surfaces are shown in Figure 4.23. As with the (100) surface, the bulk diamond exhibited the same behaviour throughout, as expected. On the bare surface, the surface C atoms had two large peaks originating from π-bonding of the upper Pandey chain.[39] Both the surface C and O atoms for the ketone PDOS showed energy states within the band gap region of bulk diamond, but this was not the case for the ether. Large peaks in the O PDOS that did not align with peaks in surface C are attributed to electrons in lone pairs, similar to the (100) surface.

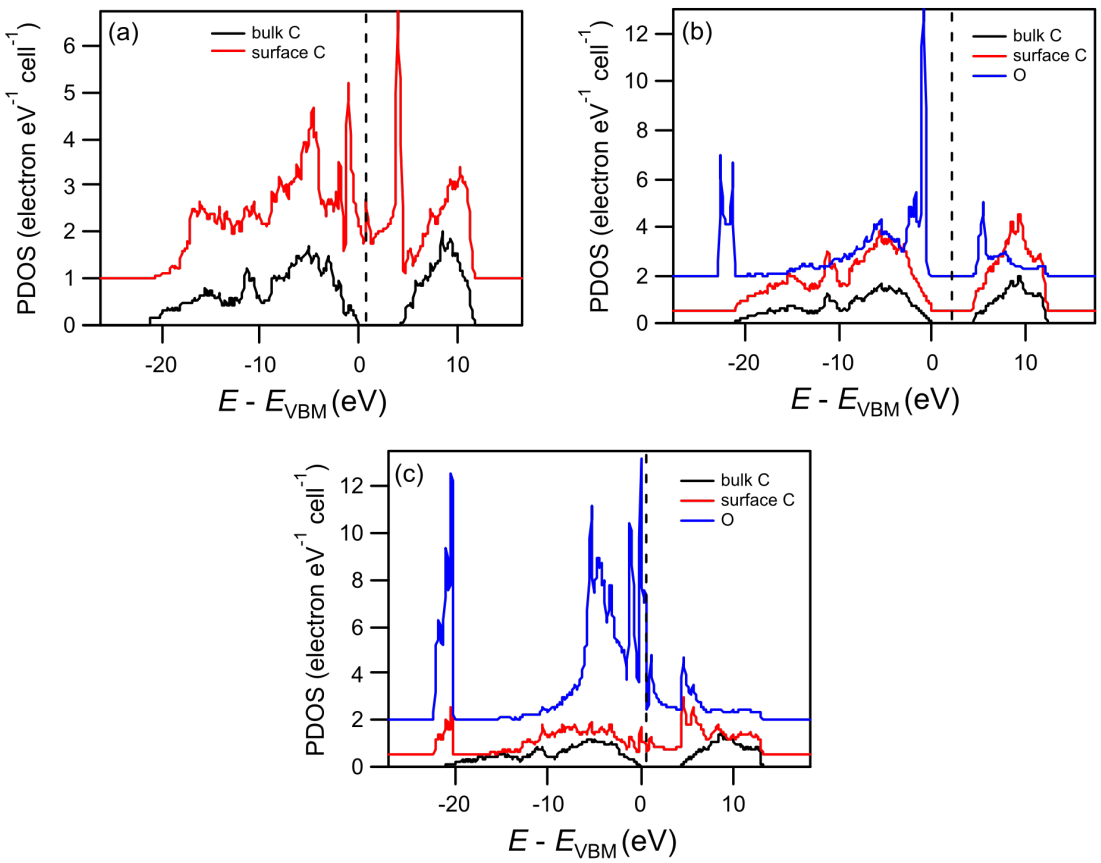

Figure 4.23: PDOS spectra of adsorbate-free (a) bare, (b) oxygen (ether) and (c) oxygen (ketone) (111) diamond surfaces.

Figure 4.24 shows the PDOS spectra for the Al-adsorbed bare (111) surfaces. The behaviour is similar to that observed for the (100) surface. The Al PDOS had more covalent behaviour, with peaks at the same positions as the surface C PDOS spanning a broad energy range. At higher coverages there were additional peaks in the Al PDOS that are attributed to metallic Al-Al bonds.

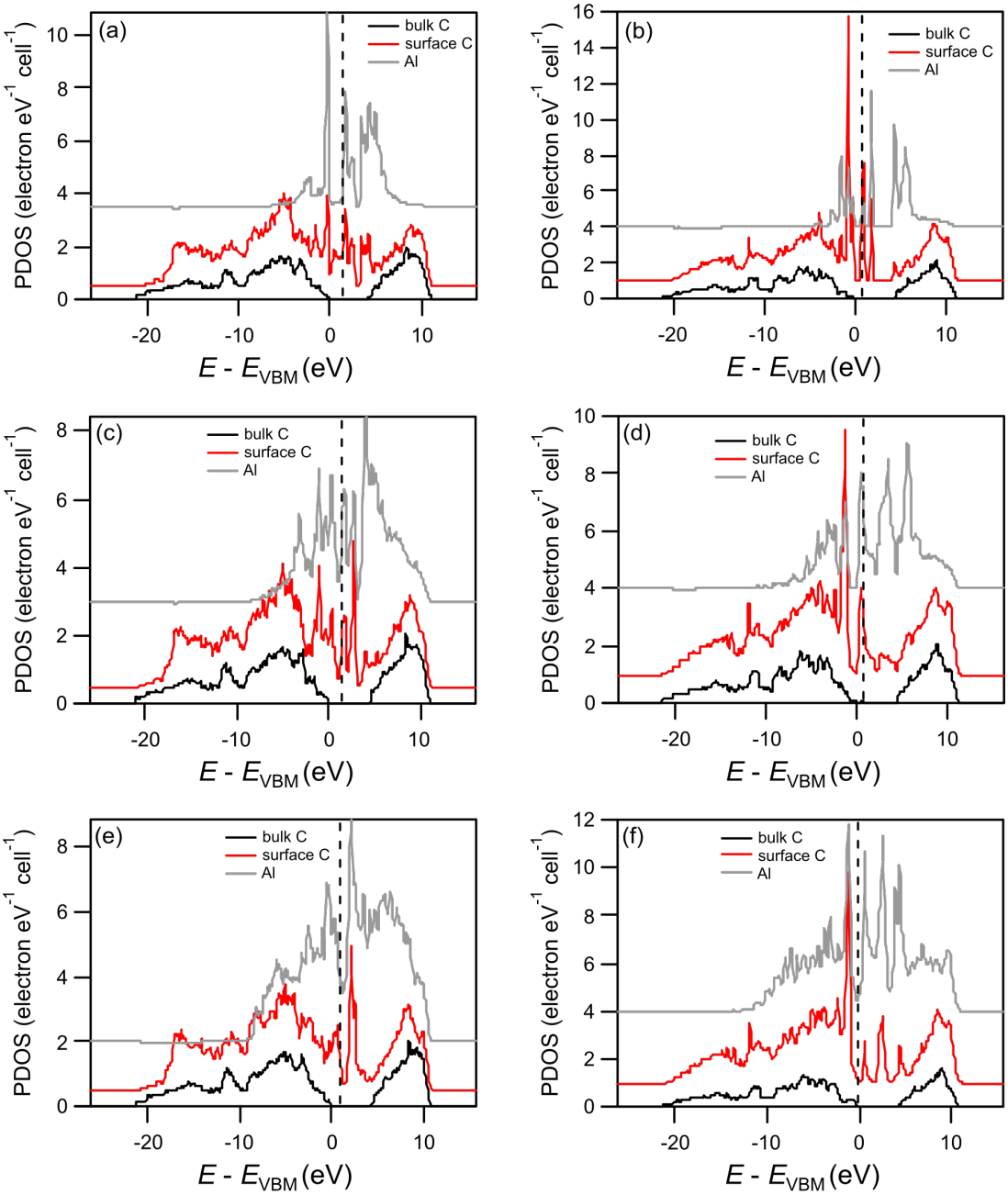

Figure 4.24: PDOS spectra for the Al-adsorbed bare (111) diamond surface. (a)–(b), (c)–(d) and (e)–(f) are 0.25, 0.5 and 1 ML, respectively, with the left column representing lowest energy (2 × 1) structures and the right column representing lowest energy (1 × 1) structures from Table 4.7.

Figure 4.25 shows PDOS spectra for the Al-adsorbed fully oxygenated (111) surfaces, *i.e.* Al addition to the (2 × 1) ketone and (1 × 1) surfaces, while Figure 4.26 shows PDOS spectra for Al addition to the half-oxygenated (2 × 1) ether surfaces. Similar to the (100) surface, 0.25 ML Al addition to the fully oxygenated surfaces showed a large singular peak in the Al PDOS located above

the position of the Fermi level. Again, this indicates that Al was largely ionically bonded to the diamond surface, and that significant charge transfer had occurred. For the 0.5 ML coverage, the peak had moved down in energy and broadened such that it was partly above and partly below the position of the Fermi level, again similar to behaviour on the (100) surface. By 1 ML coverage, there was a much broader PDOS from Al, originating from metallic Al-Al bonding. There was little difference in the PDOS between the (2 × 1) and unreconstructed fully oxygenated diamond surfaces. By contrast, the PDOS for the half-oxygenated ether surface exhibited a double peak in the Al, O and surface C PDOS at 0.25 ML, possibly due to Al bonding with both O and C atoms. At 0.5 ML the surface C DOS showed two peaks from the C=C double bond while the Al DOS was broad, possibly from metallic Al-Al bonding dominating.

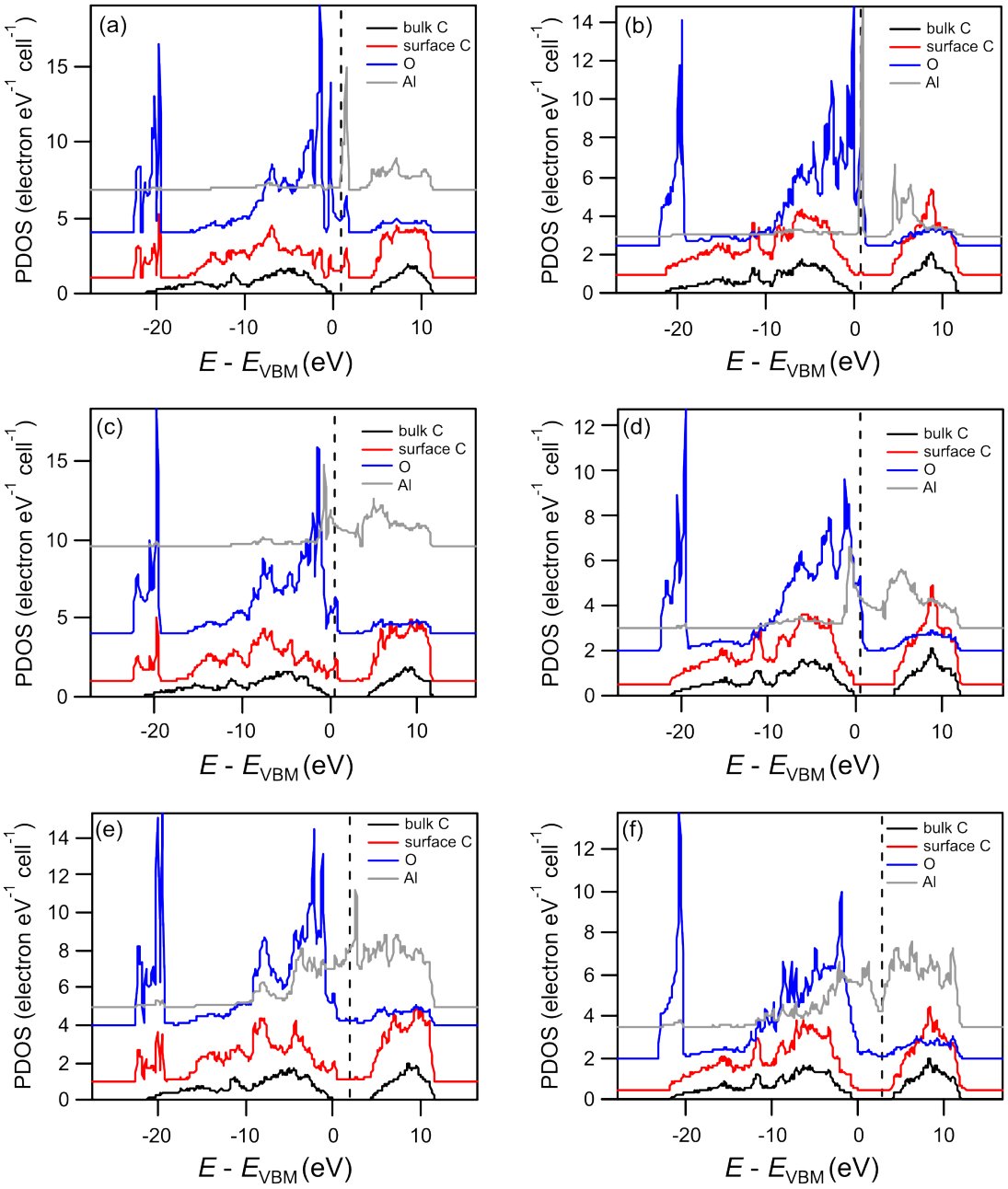

Figure 4.25: PDOS spectra for the Al-adsorbed fully O-terminated (111) diamond surface. (a)–(b), (c)–(d) and (e)–(f) are 0.25, 0.5 and 1 ML, respectively, with the left column representing lowest energy (2 × 1) structures and the right column representing lowest energy (1 × 1) structures from Table 4.8.

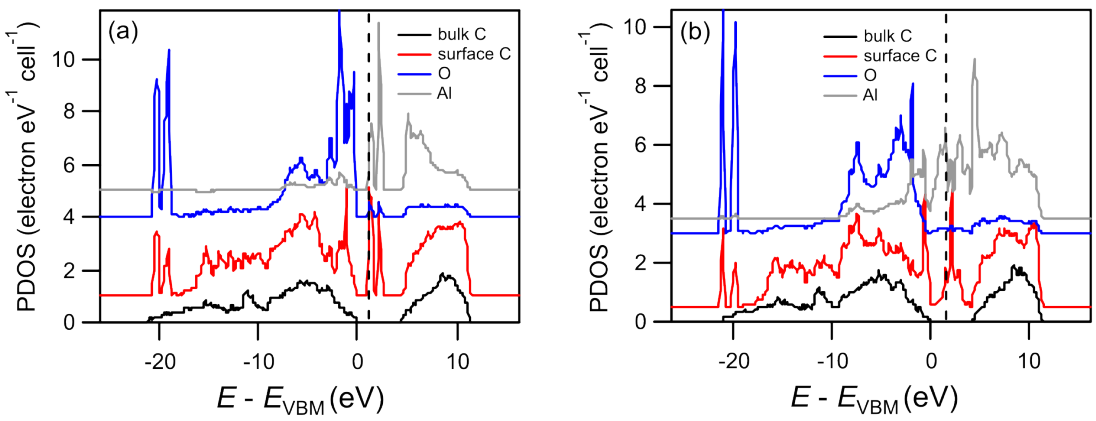

Figure 4.26: PDOS spectra for the Al-adsorbed partially O-terminated (ether) (111) diamond surface. (a) and (b) are 0.25 and 0.5 ML coverages, respectively.

4.5 Conclusions

The DFT calculations in this chapter have studied Al addition to the bare, oxygen and nitrogen-terminated (100) and (111) diamond surfaces. Al adsorbs most strongly on the O-terminated surface, as predicted from BDEs. Adsorption energies were larger than that of H-termination, suggesting higher thermal stability is possible experimentally. However, adsorption occurs far more readily on the ketone O-terminated surface than the ether on (100) diamond, and 1 ML Al on the ether (111) surface caused abstraction of O atoms into the metal layer. Al adsorption onto the bare surface showed similar adsorption energies to H-termination at 1 ML coverage. Al adsorption to N-terminated diamond showed the smallest adsorption energies, and no adsorption at all was observed on the (111) surface. Adsorption energies decreased with increasing coverage for the Al-adsorbed O-terminated surface, beneficial for preventing island formation, but increased with increasing coverage for the Al-adsorbed bare surface.

For each surface, EA values often depended upon Al coverage. For Al deposition on O-terminated diamond, 0.25 ML Al coverage appears to give the largest NEA. Expanding the supercell size showed that a large NEA is predicted as high as 0.375 ML Al coverage. By contrast, the largest NEA for Al deposition on the bare surface is predicted at 1 ML coverage. Al deposition on N-terminated (100) diamond showed only small NEAs at 1 ML coverage, whilst no stable Al configurations were observed on the N-terminated (111) surface.

The results for Al adsorption onto O-terminated diamond are consistent with the recent results published by Beattie *et al*.[47] They found slightly more negative EAs, up to -2.1 eV and -3.4 eV on the (100) and (111) surfaces, respectively, for AlO_3 coverage (corresponding to 1/3 ML of Al). They observed the same trends as here, for instance that increasing the coverage of Al caused the EA to become more positive, due to increased metallic bonding, and that the adsorption energy decreased with increasing Al coverage, although they compared the formation energy to that of Al_2O_3. They found that at 0.5 ML Al coverage and below Al and O adsorption energies were exothermic relative to Al_2O_3 formation.

Further work could use a hybrid exchange-correlation functional in order to model the band gap more accurately. In this work the PBE GGA functional was used as it is computationally inexpensive, while still able to determine DOS in the band gap region. A hybrid functional could determine exact states of ionic Al within the band gap, for instance, which would determine whether the state remains charged if the Fermi level is increased by using N-doped diamond. The change in Fermi level with N-doping could also be modelled by replacing one of the C atoms in the centre of the diamond slab with nitrogen.

In addition, further computational work could use finite-temperature real-time DFT to model electron emission from these surfaces. This has been previously shown with H- and Li-terminated diamond[48] to be able to extract Richardson constants and predict thermionic behaviour of the surface.

Considering these results, experimental work will focus solely on NEA from AlO-terminated diamond. While both ether and ketone terminations have been considered, hydroxyl terminations were not. It would be interesting to see whether it is energetically favourable for aluminium to displace the hydrogen of a hydroxyl termination and bond with oxygen in its place.

References

1 C. A. Mead and T. C. McGill, *Phys. Lett.*, 1976, **58A**, 249–251.

2 F. J. Himpsel, P. Heiman and D. E. Eastman, *Solid State Commun.*, 1980, **36**, 631–633.

3 D. A. Evans, O. R. Roberts, A. R. Vearey-Roberts, D. P. Langstaff, D. J. Twitchen and M. Schwitters, *Appl. Phys. Lett.*, 2007, **91**, 132114.

4 P. G. Lurie and J. M. Wilson, *Surf. Sci.*, 1977, **65**, 499–510.

5 T. Matsumoto, H. Kato, K. Oyama, T. Makino, M. Ogura, D. Takeuchi, T.

Inokuma, N. Tokuda and S. Yamasaki, *Sci. Rep.*, 2016, **6**, 1–6.
6 A. Maréchal, M. Aoukar, C. Vallée, C. Rivière, D. Eon, J. Pernot and E. Gheeraert, *Appl. Phys. Lett.*, 2015, **107**, 141601.
7 M. Imura, R. Hayakawa, E. Watanabe, M. Liao, Y. Koide and H. Amano, *Phys. Status Solidi - Rapid Res. Lett.*, 2011, **5**, 125–127.
8 C. Pietzka, J. Scharpf, M. Fikry, D. Heinz, K. Forghani, T. Meisch, T. Diemant, R. J. Behm, J. Bernhard, J. Biskupek, U. Kaiser, F. Scholz and E. Kohn, *J. Appl. Phys.*, 2013, **114**, 114503.
9 C. R. Miskys, J. A. Garrido, C. E. Nebel, M. Hermann, O. Ambacher, M. Eickhoff and M. Stutzmann, *Appl. Phys. Lett.*, 2003, **82**, 290–292.
10 Y.-R. Luo and J.-P. Cheng, in *CRC Handbook of Chemistry and Physics*, eds. J. R. Rumble Jr, D. R. Lide and T. J. Bruno, CRC Press, Boca Raton, FL, USA, 98th edn., 2017.
11 S. J. Clark, M. D. Segall, C. J. Pickard, P. J. Hasnip, M. I. J. Probert, K. Refson and M. C. Payne, *Zeitschrift fuer Krist.*, 2005, **220**, 567–570.
12 R. S. Mulliken, *J. Chem. Phys.*, 1955, **23**, 1833–1840.
13 M. D. Segall, C. J. Pickard, R. Shah and M. C. Payne, *Mol. Phys.*, 1996, **89**, 571–577.
14 M. D. Segall, R. Shah, C. J. Pickard and M. C. Payne, *Phys. Rev. B*, 1996, **54**, 16317–16320.
15 A. J. Morris, R. J. Nicholls, C. J. Pickard and J. R. Yates, *Comput. Phys. Commun.*, 2014, **185**, 1477–1485.
16 J. R. Yates, X. Wang, D. Vanderbilt and I. Souza, *Phys. Rev. B*, 2007, **75**, 195121.
17 B. G. Searle, *Comput. Phys. Commun.*, 2001, **137**, 25–32.
18 *Jmol: an open-source Java viewer for chemical structures in 3D.* Available at: http://www.jmol.org/
19 C. J. Fall, N. Binggeli and A. Baldereschi, *J. Phys. Condens. Matter*, 1999, **11**, 2689–2696.
20 K. M. O'Donnell, T. L. Martin, N. A. Fox and D. Cherns, *Phys. Rev. B*, 2010, **82**, 115303.
21 A. K. Tiwari, J. P. Goss, P. R. Briddon, N. G. Wright, A. B. Horsfall and M. J. Rayson, *Phys. Status Solidi*, 2012, **209**, 1697–1702.
22 J. P. Perdew, K. Burke and M. Ernzerhof, *Phys. Rev. Lett.*, 1996, **77**, 3865–3868.
23 D. Vanderbilt, *Phys. Rev. B*, 1990, **41**, 7892–7895.
24 H. J. Monkhorst and J. D. Pack, *Phys. Rev. B*, 1976, **13**, 5188–5192.
25 F. Maier, J. Ristein and L. Ley, *Phys. Rev. B*, 2001, **64**, 165411.
26 J. Furthmüller, J. Hafner and G. Kresse, *Europhys. Lett.*, 1994, **28**, 659.
27 M. J. Rutter and J. Robertson, *Phys. Rev. B*, 1998, **57**, 9241–9245.
28 J. Van Der Weide, Z. Zhang, P. K. Baumann, M. G. Wensell, J. Bernholc and R. J. Nemanich, *Phys. Rev. B*, 1994, **50**, 5803–5806.
29 D. Qi, L. Liu, X. Gao, T. Ouyang, S. Chen, K. P. Loh and A. T. S. Wee, *Langmuir*, 2007, **23**, 9722–9727.
30 J. Furthmüller, J. Hafner and G. Kresse, *Phys. Rev. B*, 1996, **53**, 7334–7351.
31 X. M. Zheng and P. V. Smith, *Surf. Sci.*, 1992, **262**, 219–234.
32 H. Tamura, H. Zhou, K. Sugisako, Y. Yokoi, S. Takami, M. Kubo, K. Teraishi, A. Miyamoto, A. Imamura, M. N.-Gamo and T. Ando, *Phys. Rev. B*, 2000, **61**, 11025–11033.

33 J. L. Nie, H. Y. Xiao and X. T. Zu, *Chem. Phys.*, 2006, **326**, 308–314.
34 A. K. Tiwari, J. P. Goss, P. R. Briddon, N. G. Wright, A. B. Horsfall and M. J. Rayson, *Phys. Rev. B*, 2012, **86**, 155301.
35 K. M. O'Donnell, T. L. Martin and N. L. Allan, *Chem. Mater.*, 2015, **27**, 1306–1315.
36 A. K. Tiwari, J. P. Goss, P. R. Briddon, A. B. Horsfall, N. G. Wright, R. Jones and M. J. Rayson, *Europhys. Lett.*, 2014, **108**, 46005.
37 M. Chandran, M. Shasha, S. Michaelson and A. Hoffman, *Appl. Phys. Lett.*, 2015, **107**, 111602.
38 A. Stacey, K. M. O'Donnell, J. P. Chou, A. Schenk, A. Tadich, N. Dontschuk, J. Cervenka, C. Pakes, A. Gali, A. Hoffman and S. Prawer, *Adv. Mater. Interfaces*, 2015, **2**, 1500079.
39 S. J. Sque, R. Jones and P. R. Briddon, *Phys. Rev. B*, 2006, **73**, 085313.
40 J. B. Cui, J. Ristein and L. Ley, *Phys. Rev. B*, 1999, **60**, 16135–16142.
41 J. B. Cui, J. Ristein and L. Ley, *Phys. Rev. Lett.*, 1998, **81**, 429–432.
42 K. P. Loh, X. N. Xie, S. W. Yang, J. S. Pan and P. Wu, *Diam. Relat. Mater.*, 2002, **11**, 1379–1384.
43 T. L. Martin, *Lithium Oxygen Termination as a Negative Electron Affinity Surface on Diamond: a Computational and Photoemission Study*, PhD Thesis, University of Bristol, 2011.
44 K. P. Loh, X. N. Xie, S. W. Yang and J. C. Zheng, *J. Phys. Chem. B*, 2002, **106**, 5230–5240.
45 T. E. Derry, N. W. Makau and C. Stampfl, *J. Phys. Condens. Matter*, 2010, **22**, 265007.
46 J. P. Chou, A. Retzker and A. Gali, *Nano Lett.*, 2017, **17**, 2294–2298.
47 J. M. A. Beattie, J. P. Goss, M. J. Rayson and P. R. Briddon, *Diam. Relat. Mater.*, 2019, **94**, 137–145.
48 T. Shinozaki, S. Hagiwara, N. Morioka, Y. Kimura and K. Watanabe, *Appl. Phys. Express*, 2018, **11**, 064301.

Chapter 5 – Investigation of the Coverage, Structure and Electronic Properties of O- and H-Terminated Diamond

5.1 Introduction

From the previous chapter, it was established that one promising route towards a thermally stable negative electron affinity (NEA) diamond surface was from aluminium addition to oxygen-terminated diamond. However, one caveat that must be considered for experimental studies is the type of oxygen termination. For the (100) surface, adsorption of Al was dependent upon the underlying oxygen being double-bonded to surface carbon (*i.e.* C=O or 'ketone' bonding), since aluminium addition could break the π-bond of the ketone with greater ease than the σ-bond of a C-O-C 'ether' termination. The (111) surface also benefits from ketone formation as this gives a higher surface coverage of oxygen – up to 1 monolayer (ML) for the ketone compared to a maximum of 0.5 ML for the ether – although Al addition was found to be able to bond with either ether or ketone oxygen atoms. Hydroxyl terminations were not considered in this study.

The results of this chapter are divided into two parts. The first part (Sections 5.3 and 5.4) characterises three different oxidation methods. Initially the optimal oxidation time was determined. Since ether, ketone and hydroxyl terminations are all stable, the relative amount of each were determined separately for (100) and (111) diamond. The primary aim of this investigation was to maximise the ketone component of oxygen, but the potential benefits of fine control of oxygen termination extend beyond metal-oxygen terminations for NEA surfaces. As discussed in Chapter 2, many applications make use of the oxygen termination. O-terminated diamond is used as the basis of deep-depletion and inversion-channel field effect transistors (FETs). A more controlled O-termination would allow for fewer surface states, which are considered a primary reason for the low carrier mobility in inversion-channel FETs.[1] The surface states arising from harsh oxygenation methods, and from ether termination, interfere with nitrogen-vacancy centres, hindering the development of quantum applications.[2]

Formation of a fully hydroxyl-terminated surface would also be desirable for further functionalisation of the diamond surface.[3]

The second part of this chapter (Sections 5.5 and 5.6) studies the surface and electronic structure of both hydrogen and oxygen terminations on (100) and (111) diamond surfaces, using the oxidation method that was used for experimental NEA studies in Chapter 6. The electronic properties of the H-terminated surfaces are of interest as it is the most widespread method used to form NEA diamond, and so a comparison can be made with the AlO-terminations in Chapter 6.

5.1.1 Previous O-Termination Studies

Table 5.1 summarises the oxygen terminations and coverages that have been obtained from different oxidation methods from a number of studies over the past 20 years. Oxidation has been achieved from plasma, chemical, photochemical, electrochemical and thermal treatments. The oxygen coverage is typically quantified using the relative atomic percentages of oxygen and carbon in X-ray photoelectron spectroscopy (XPS). So, while a comparison between studies is not useful, it is nonetheless helpful for comparing the effectiveness of the different oxygenation methods for each study. One of the biggest challenges has been determination of the relative proportions of ether, ketone and hydroxyl bonding. In the literature, it is common to use the C 1s peak to distinguish the ketone C=O bond from ether and hydroxyl C-O bonds, and C-O/C=O ratios are often reported. There is disagreement about the assignment of O 1s spectra, which is discussed later.

One method that can be used to differentiate between the different oxygen components is to add linkers to specific binding sites. Notsu *et al.*[4,5] used dinitrophenylhydrazine for the detection of carbonyl groups, and 3-aminopropyltrioxysilane for the detection of hydroxyl groups, both on polycrystalline boron-doped diamond (BDD), finding each to be less than half of the total oxygen content. Wang *et al.*[3] similarly have used trifluoroacetic acid for identification of hydroxyl groups on BDD, finding that an electrochemical oxidation procedure enhances the amount of hydroxyl groups present compared to UV/ozone oxidation.

Klauser *et al*.[6] systematically investigated the oxygen composition from four different oxidation methods at different oxidation times on single-crystal and nanocrystalline diamond. The (100) and (111) single crystals had similar surface coverages of oxygen, and approximately half the coverage compared with nanocrystalline diamond due to smaller surface area. Only a small selection of their results are shown in Table 5.1 for simplicity; oxidation times that are listed are the minimum time the authors found gave saturation of the surface. Their results suggest a slight increase in ketone content with oxidation time for each method.

Ghodbane *et al.*[7] also studied multiple different oxidation methods. They found that the majority of methods preferentially formed C-O bonds rather than C=O, except in the case of electrochemical oxidation. They suggested that the unexpectedly high oxygen coverage and number of C=O groups for electrochemical oxidation may have resulted from increased surface roughness and formation of highly oxidised functional groups in addition to the ketone bonding.

Yoshida *et al*.[8] found that heating H-terminated diamond in water vapour formed a hydroxyl termination above 500 °C on the (111) surface. This was determined through Fourier transform infrared (FTIR) spectroscopy, using attenuated total reflectance (ATR), and so could distinguish between hydroxyl and ether groups.

A comparison of these studies finds that most oxidation methods result in primarily ether or hydroxyl termination. This is not surprising because ether bonding is slightly thermodynamically favourable compared to the ketone. A comparison of oxygen coverage for different methods did not show any particular method as being preferable for full ML coverage, although sub-ML coverage occurs if an insufficient oxidation time is used.

Table 5.1: Type of termination and O atomic percentages for different oxygen-termination methods and conditions. BDD: (polycrystalline) boron doped diamond; NCD: nanocrystalline diamond; EC: electrochemical anodic polarization; SCA: sulfochromic acid.

Authors	Surface	Method	Conditions	Termination	O %
Notsu *et al.*[9]	BDD	O_2 plasma	100 W, 120 s	Mostly C-O	-
		EC (in KOH)	0.1 M, 2.4 V *vs* Ag|AgCl, 1 h	Mostly C=O	-
Notsu *et al.*[4]	BDD	O_2 plasma	70 W, 60 s	C=O/O: <0.5	-
		EC (in H_2SO_4)	0.1 M, 2.4 V *vs* Ag|AgCl, 1 h	C=O/O: <0.5	-
Notsu *et al.*[5]	BDD	O_2 plasma	70 W, 60 s	OH/O: <0.5	-
		EC (in H_2SO_4)	0.1 M, 2.4 V *vs* Ag|AgCl, 1 h	OH/O: <0.5	-
Girard *et al.*[10]	BDD	EC (in H_2SO_4)	0.5 M, 0.1 mA cm^{-2}, 10 s	C-O/C=O: 1.5	20
		EC (in H_2SO_4)	0.5 M, 100 mA cm^{-2}, 10 s	C-O/C=O: 2.3	10
Wang *et al.*[11]	BDD	O_2 plasma	100 W, 40 s	C-O/C=O: 1.2	12
		UV/ozone	55 min	C-O/C=O: 5.8, C-O mostly ether	23
		EC (in H_2SO_4)	0.5 M, 0.1 mA cm^{-2}, 40 min	C-O/C=O: 2.8, C-O mostly OH	18
Klauser *et al.* [6]	NCD	O_2 plasma	150 W, 10 min	C-O/C=O: 3.0	14
		SCA	250 °C, 10 min	C-O/C=O: 25.0	14
		UV/ozone	55 min	C-O/C=O: 1.7	11
		Heat in air	600 °C, 10 min	C-O/C=O: 4.5	11
Wang *et al.*[3]	BDD	UV/ozone	10 min	C-O/C=O: 3.0, ~0% OH	10
		EC (in H_2SO_4)	0.5 M, 0.1 mA cm^{-2}, 17 min	C-O/C=O: 2.8, ~18% OH	11
Ghodbane *et al.*[7]	NCD	O_2 plasma	150 W, 10 min	C-O/C=O: 26.3	10
		Heat in air	600 °C, 10 min	C-O/C=O: 2.3	11
		UV/ozone	55 min	C-O/C=O: 1.6	11
		SCA (70% in H_2O)	250 °C, 30 min	C-O/C=O: 1.4	12
		EC (in H_2SO_4)	0.5 M, 0.1 mA cm^{-2}, 40 min	C-O/C=O: 0.7	19
Torrengo *et al.*[12]	NCD	O_2 Plasma	50 W, 10 s	Mainly C-O	7
		UV/ozone	2 bar O_2, 4 h	Mainly C-O	4
		H_2SO_4:H_2O_2 3:1	110 °C, 4 h	Mainly C-O	8
Navas *et al.*[13]	Single crystal	UV/ozone	80 °C, 20 min	Mainly C-O	7
		UV/ozone	500 mbar, 2 h	Mainly C-O	6
		H_2SO_4:HNO_3 3:1	200 °C, 2 h	Mainly C-O	10
Yoshida *et al.*[8]	(111)	Heat in H_2O vapour	>500 °C	OH	-

5.2 Experimental Details

Full details of materials and techniques can be found in Chapter 3. In this chapter, single-crystal diamond substrates were used for the oxidation experiments. The (100) and (111) surfaces were both studied to determine the

behaviour of each facet. The samples had been polished, to reduce the effect of surface roughness on electronic behaviour.

Newly-purchased samples were first acid cleaned, then an epitaxial BDD layer was grown for 1 h (a ~500 nm layer) to prevent charging effects during characterisation. This also moves the Fermi level towards the valence band, increasing values obtained for the work function. Figure 5.1 shows typical Raman spectra and scanning electron microscopy (SEM) images for the boron-doped epitaxial single-crystal layer. The Raman spectra each have a single peak at 1332 cm^{-1}, from the sp^3-hybridised carbon-carbon bonding. Lack of the D or G bands show that growth of the epitaxial BDD layer has not caused any detectable graphitic content to be present in the BDD layer. The SEM images show that the polished surfaces remain smooth, with only a very small number of nucleation sites observed. These samples did not show any charging effects under the electron beam. A two-point probe showed a resistivity of ~100 kΩ after deposition of the BDD layer, consistent with the expected semiconducting nature of the BDD layer for a B concentration of ~10^{20} cm^{-3}. As mentioned in Chapter 1.3.1, BDD with B concentrations of >10^{21} cm^{-3} can become metallic in nature.

The BDD-coated single-crystal diamond samples were then hydrogen-terminated using a hydrogen plasma, which also cleaned the surface of any contaminants. This was shortly followed by the oxidation procedure of interest. The samples could be reused by acid cleaning and then repeating each of the preparation steps.

The oxidation methods studied were UV/ozone, oxygen plasma, and acid treatment with H_2SO_4 and HNO_3. The details of these procedures are given in Chapter 3.3.2. Samples were also prepared by oxidation using atomic layer deposition (ALD) (Chapters 3.4.2.4 and 6.4). It was intended for the ALD-oxidised samples to be studied here also, however a large tantalum impurity was present in the XPS survey scan, accompanied by a larger-than-expected oxygen peak, suggesting that Ta_2O_5 was present on the sample. This may have originated from the ALD system or from the filaments of the chemical vapour deposition reactor. For this reason, results from the ALD samples have been omitted.

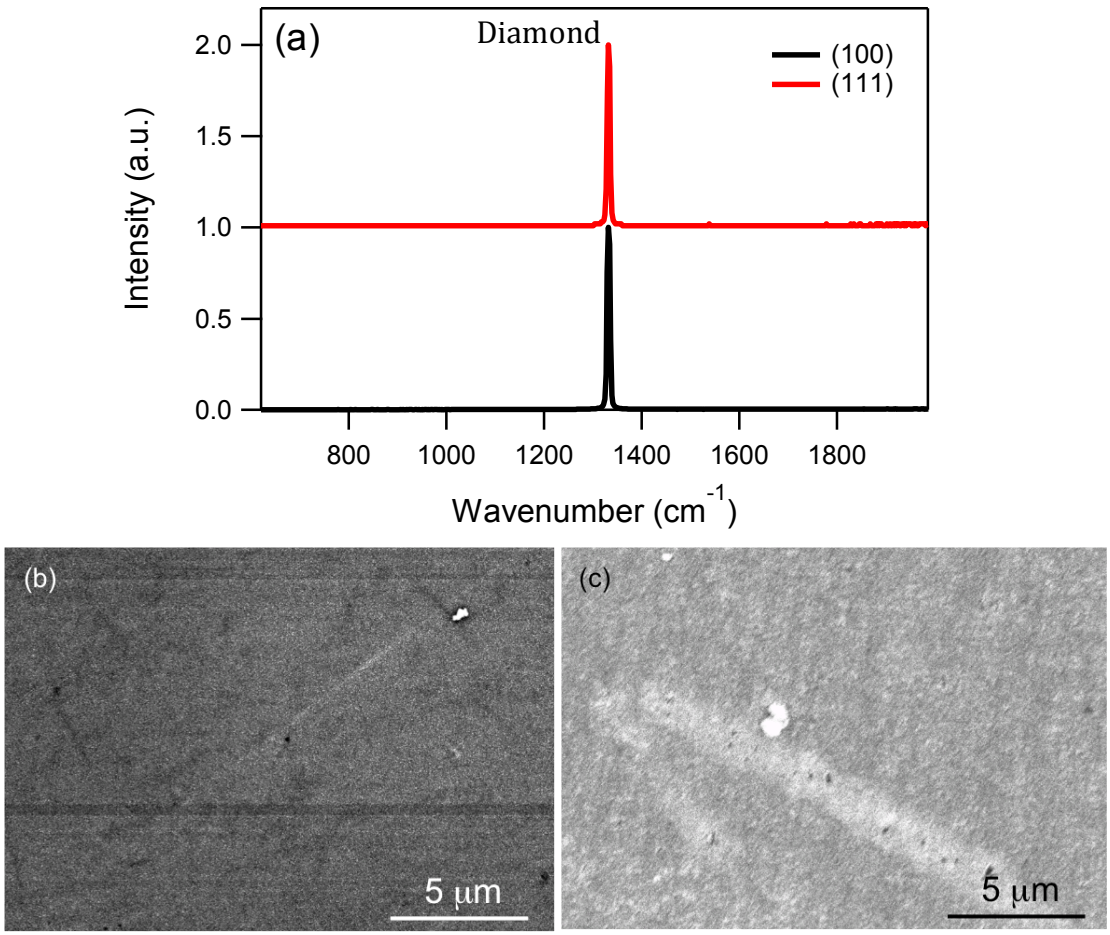

Figure 5.1: (a) Raman spectra (514 nm) of single-crystal diamond samples with a BDD epitaxial layer. The spectrum for the (111) sample is offset for clarity. (b)–(c) SEM images of the (100) and (111) diamond surfaces, respectively.

5.3 Optimising Oxidation Time

To ensure that a complete ML coverage of oxygen was formed for each oxidation procedure, the contact angle of a water droplet on the surface was measured as a function of oxidation time, using the method described in Chapter 3.5.1. As shown by Figure 5.2, the H-termination is hydrophobic, while O-terminations are hydrophilic, so the wettability of the surface increases with increasing oxidation.

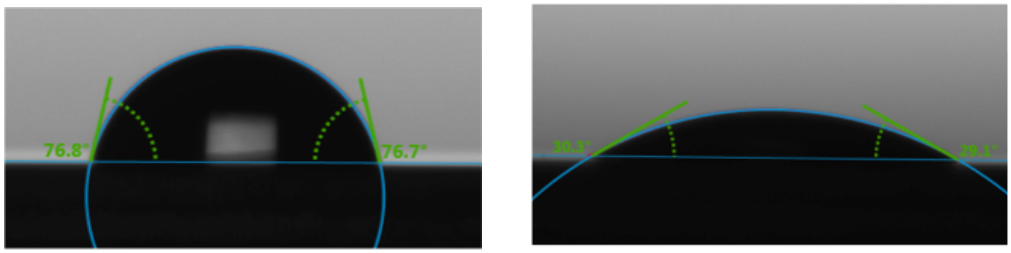

Figure 5.2: Contact angle of water on typical single crystal diamond sample with (a) H-termination, and (b) O-termination.

Figure 5.3 shows the contact angle values for both (100) and (111) single crystals for each oxidation treatment at increasing oxidation times. The average of the two contact angles is plotted, with the range given by the error bars. There is an immediate decrease in the contact angle for oxidised samples by >20° with respect to the angle of the H-terminated samples, even at the shortest oxidation times. With longer oxidation times, the contact angle remains relatively constant, between 30–50°, and it does not appear that a longer oxidation time decreases contact angle further for any of the methods. Based on these results, it was assumed that a full ML coverage has been achieved by 7 s for the oxygen plasma procedure, by 30 minutes for the UV/ozone procedure, and 1 h for the acid-wash procedure. The plasma treatment time is shorter than most used in the literature as this procedure has been noted to significantly graphitise the surface after only 40 s exposure.[11]

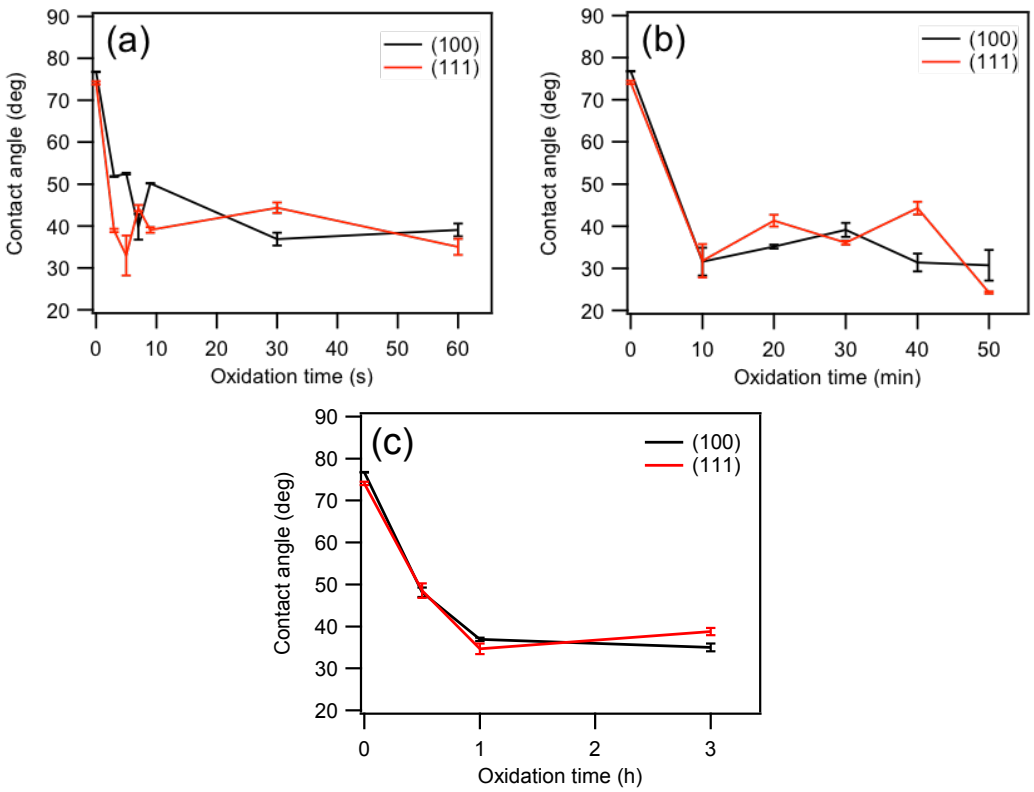

Figure 5.3: Contact angle measurements for (a) plasma, (b) UV/ozone, and (c) acid treatment show the decrease in contact angle from a previously hydrogenated diamond surface.

5.4 Characterisation of H- and O-terminated Surfaces

XPS and FTIR-ATR were used to determine how different oxidation procedures affected the way in which oxygen bonds to diamond. For XPS spectra, peak fitting was completed with the XPSPEAK41 program. A Shirley[14] background was taken and component peaks were given a line shape comprising 80% Gaussian and 20% Lorentzian, which our group and others[15] have found suitable for fitting diamond peaks.

For diamond, the deconvoluted C 1s peak has been widely used in the literature in order to determine the type of surface bonding. Table 5.2 summarises the different peak components of the C 1s peak, which were in excellent agreement with literature values.[16,17] There were two peaks that could always be fitted to the spectrum, regardless of surface termination, with binding energies of ~284.3 eV and ~285.0 eV, corresponding to the bulk sp^3 and surface sp^3-hybridised C atoms, respectively. The surface sp^3 C peak is believed to arise from structural relaxation of sub-surface carbon layers.[18] There is also evidence that increased B doping contributes to the relative area of this peak.[17] Any sp^2-

hybridised carbon on the diamond surface manifested as a lower energy binding peak at ~283.6 eV. Oxygen-terminated diamond typically had two additional peaks at higher binding energies, with a component at ~286.0 eV corresponding to C-O bonds from ether and hydroxyl groups, and a component at ~287.2 eV corresponding to C=O bonds of a ketone group.

Table 5.2: Approximate C 1s peak positions from XPS.

Peak	Binding Energy (eV)	Assignment
C1	284.3	Bulk sp^3 C-C
C2	285.0	Surface sp^3 C-C
C3	286.0	C-O
C4	287.2	C=O
C5	283.6	sp^2 C-C

The O 1s peak has been previously deconvoluted into two component peaks, with approximate binding energies listed in Table 5.3. Yagi *et al.*[19] suggest the two components are from C-O and C=O bonds, while Navas *et al.*[13] and Gaisinskaya *et al.*[20] attribute the two components to hydroxyl and ether C-O bonds. Huang *et al.*,[21] meanwhile, have used three components – corresponding to ether, ketone and hydroxyl bonds – to fit the O 1s peak in O-terminated ultrananocrystalline diamond. The peak positions for the three-component peak fit is given in Table 5.4. Most commonly, however, no assignment is provided for the O 1s peak. The O 1s peak was therefore investigated alongside the C 1s peak to determine whether the peak components can be attributed to particular bonding environments.

Table 5.3: Approximate O 1s peak positions from XPS using two-component peak fitting.

Peak	Binding Energy (eV)	Assignment
O1	531.5	C-O or C=O
O2	533.0	C-O

Table 5.4: Approximate O 1s peak positions from XPS using three-component peak fitting.

Peak	Binding Energy (eV)	Assignment
O3	531.0	C-O (hydroxyl)
O4	532.1	C=O
O5	532.9	C-O (ether)

FTIR has been widely used for the characterisation of functionalised diamond surfaces. Transmission and diffuse reflection modes have been used to characterise diamond powders,[22–27] while reflection mode has been used to characterise polycrystalline diamond.[28,29] ATR mode has been used to characterise single-crystal diamond.[8,30,31] Table 5.5 summarises the main peak positions that have been observed for the different types of bonding in H- and O-terminated diamond samples.

Table 5.5: Stretching vibrations from FTIR from previous studies with diamond.

Bond	Wavenumber (cm^{-1})	Ref.
C-H	2800–2970	[22]
C-O-C	1106, 1264	[22]
C=O	1650–1850	[22]
O-H (hydroxyl)	850–1125, 1633, 3200–3700	[8,23,32]
O-H (carboxyl)	1384	[23]

5.4.1 Bonding on the (100) Diamond Surface

XPS spectra of the C 1s peak for the hydrogenated and oxidised diamond surfaces are shown in Figure 5.4. The H-terminated sample can be fitted with two component peaks, one from the bulk and one from surface sp^3 C-C bonding. For the O-terminated samples, two additional peaks from C-O and C=O bonds could be fitted. There was a large sp^2 carbon component for the acid-oxidised sample (Figure 5.4(d)) and a small sp^2 carbon component for the UV/ozone-oxidised sample (Figure 5.4(b)).

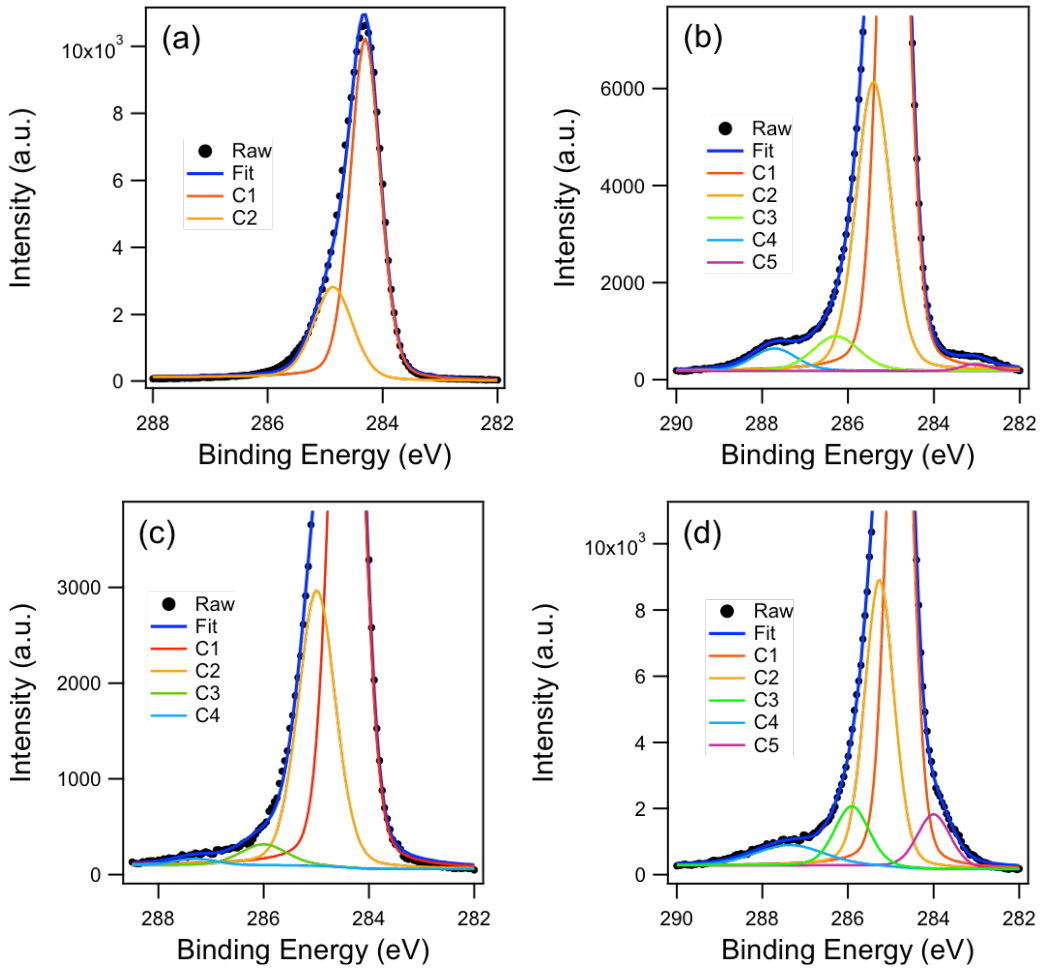

Key: C1: bulk sp^3 C-C; C2: surface sp^3 C-C; C3: C-O; C4: C=O; C5: sp^2 C-C

Figure 5.4: XPS spectra of the C 1s peak for (a) H-terminated (100) diamond, and (b)–(d) O-terminated (100) diamond using (b) UV/ozone, (c) plasma, and (d) acid oxidation methods. The fitted peak numbers refer to those in Table 5.2.

XPS spectra for the O 1s peaks fit by two components are shown in Figure 5.5. For each peak it was assumed that the lower binding energy component of the O 1s peak was from a ketone bond, since the presence of a C=O bond was identified from the C 1s peak. In this case, results suggest that the UV/ozone-oxidised surface is primarily formed of ether bonds, the plasma-oxidised surface is primarily formed of ketone bonds, and acid oxidation slightly favours ketone bonding.

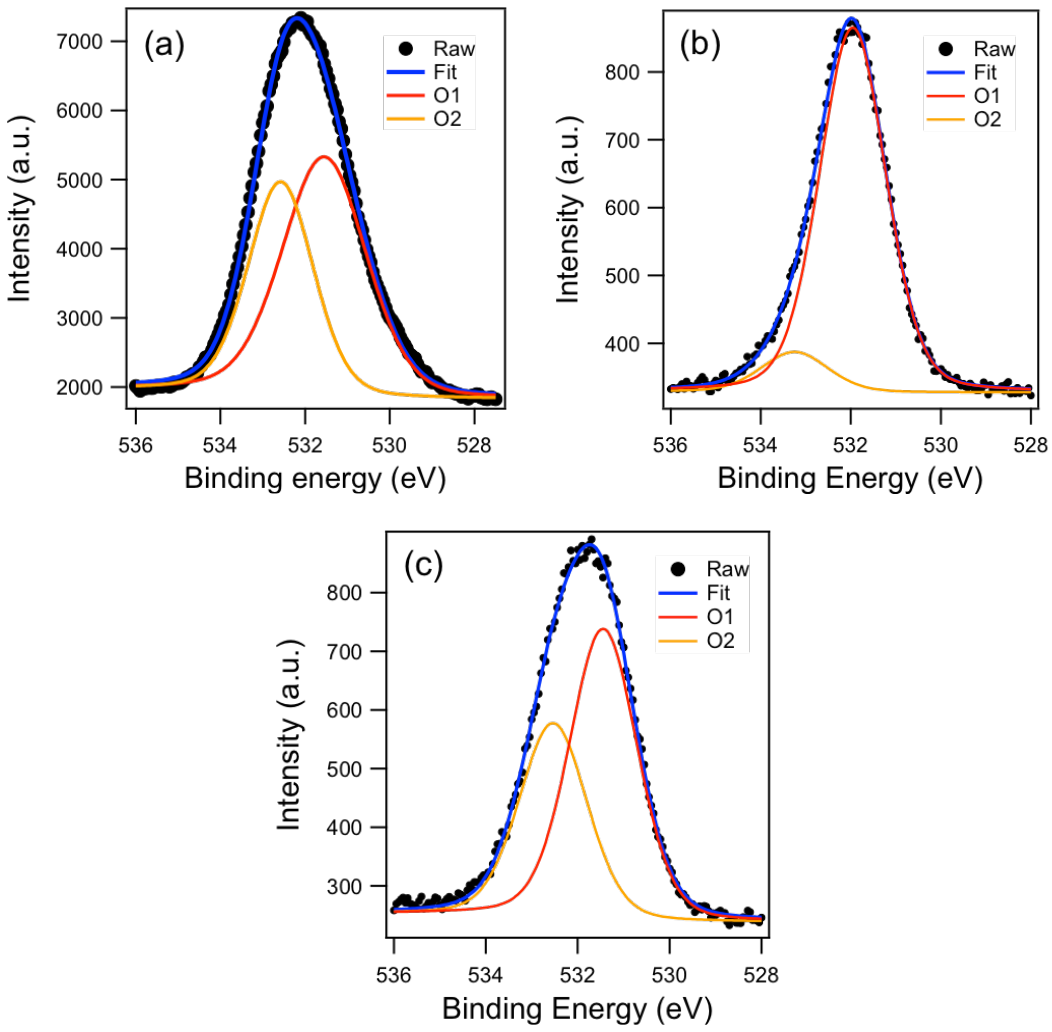

Key: O1: C=O; O2: C-O

Figure 5.5: XPS spectra of the O 1s peak for O-terminated (100) diamond using (a) UV/ozone, (b) plasma and (c) acid oxidation methods. A two-component peak fitting procedure was used, with the peak labels the same as in Table 5.3.

Shown in Figure 5.6 are XPS spectra for the O 1s peaks fit using three components. Based on this fitting, the C-O component for UV/ozone oxidation primarily consists of ether bonds, in agreement with the literature (Table 5.1). For plasma oxidation C-O bonds are primarily from hydroxyl groups, and for acid oxidation the peak areas for the ether and hydroxyl components are similar.

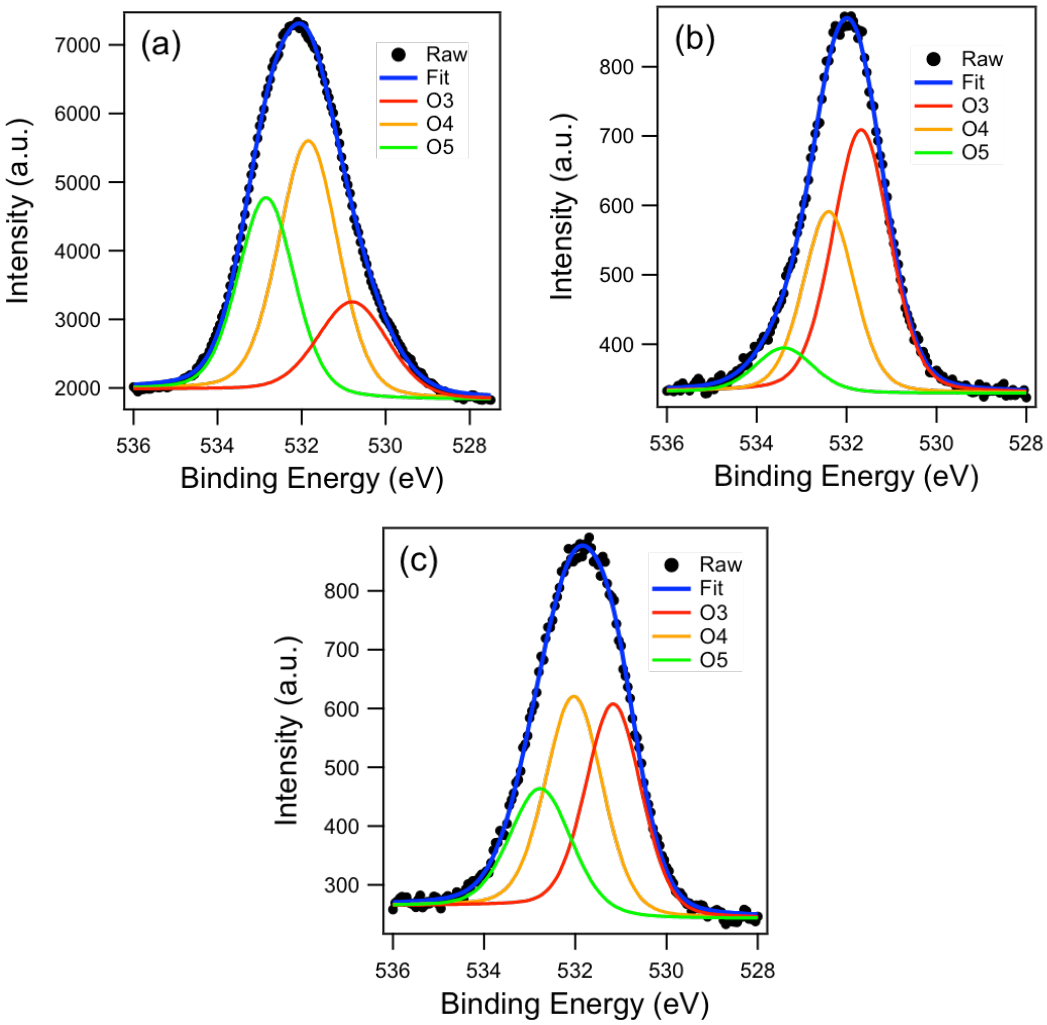

Key: O3: C-O (hydroxyl); O4: C=O; O5: C-O (ether)

Figure 5.6: XPS spectra of the O 1s peak for O-terminated (100) diamond using (a) UV/ozone, (b) plasma and (c) acid oxidation methods. A three-component peak fitting was used, as detailed in Table 5.4.

Table 5.6 summarises the C-O/C=O ratios observed for the C 1s and O 1s peaks from XPS, and the relative atomic percentages of oxygen for each oxidation method, calculated using Equation 3.3 in Chapter 3. The C-O/C=O ratios from the C 1s and O 1s peaks are also plotted in Figure 5.7. The UV/ozone and acid-oxidation methods appear to have the smallest C-O/C=O ratios, corresponding to the largest amount of ketone bonding. Using three-component fitting gives a much stronger correlation between C-O/C=O calculated from the C 1s and O 1s peaks. This suggests that the O 1s peak is reliable for identifying oxygen components on the (100) surface, and (unlike the C 1s peak) can distinguish between ether and hydroxyl bonding environments.

The acid oxidation showed the highest atomic percentage of oxygen, followed by UV/ozone oxidation, with plasma oxidation the smallest. The low coverage for plasma oxidation is attributed to the short oxidation time.

Table 5.6: Summary of C-O/C=O peak ratio and surface coverages for different oxidation procedures on the (100) diamond surface.

Termination Method	C 1s C-O/C=O	O 1s C-O/C=O (2 components)	O 1s C-O/C=O (3 components)	O at. %
UV/ozone	1.9	0.7	1.8	5.2
Oxygen Plasma	2.7	0.2	1.9	3.0
Acid	1.5	0.7	1.6	6.9

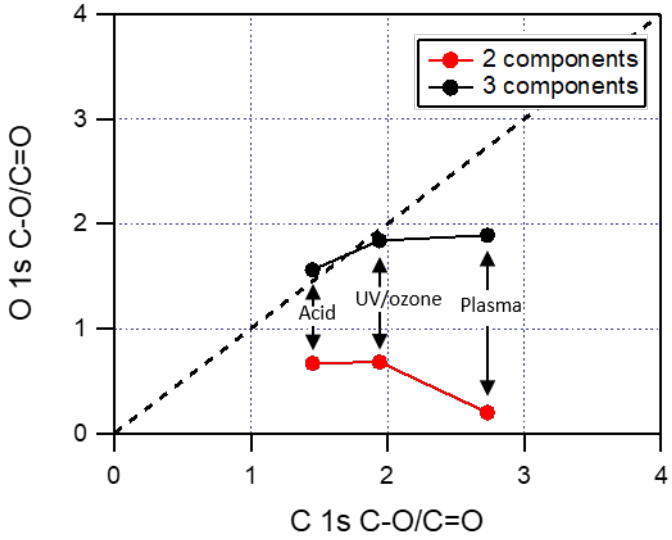

Figure 5.7: The C-O/C=O bond ratios of different oxidation methods from C 1s and O 1s peaks in XPS spectra. The O 1s spectra were either fitted using two or three components.

FTIR spectra acquired for the differently terminated samples are shown in Figure 5.8. The background absorbance was subtracted from each spectrum to give the same baseline and the peak positions associated with ether, hydroxyl and ketone groups are indicated. Each oxidation method showed peaks for the three oxygen bonding environments, which alone justifies the use of three-peak fitting in XPS. The UV/ozone method showed the lowest absorbance for the hydroxyl peak, and the highest absorbance for the ether peak, as would be expected from XPS results. The acid and plasma-oxidised samples were similar

for both peaks. In this case, the UV/ozone and plasma-oxidised samples showed a larger absorbance for the ketone peak than the acid-oxidised sample. The plasma-oxidised sample showed additional absorbance at ~1500 cm^{-1}, which was attributed to sp^2 carbon.[33] Thus, there was a qualitative agreement with results from XPS where a 3-component fit was used for the O 1s peak.

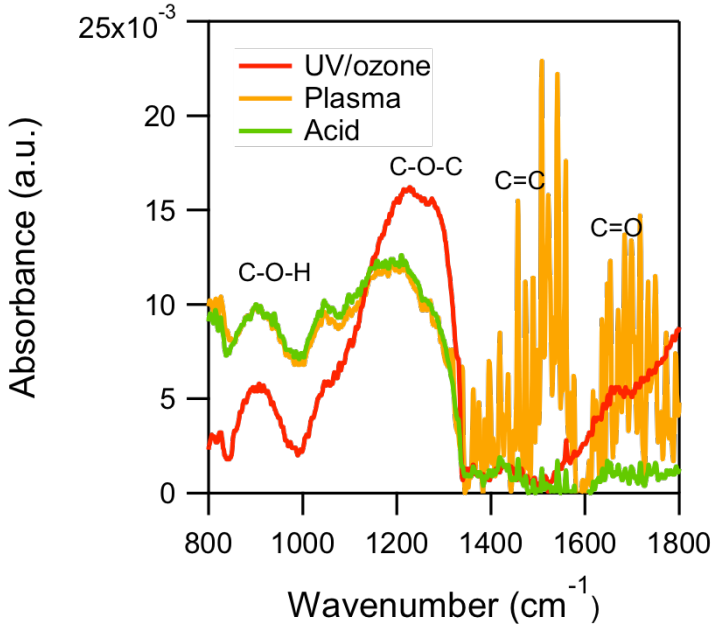

Figure 5.8: FTIR-ATR spectra for different O-termination methods on (100) diamond.

5.4.2 Bonding on the (111) Diamond Surface

The C 1s spectra for the H- and O-terminated (111) diamond samples are given in Figure 5.9. Again, only two components were fitted for the H-terminated sample, while two additional components from C-O and C=O bonds were fitted to each of the O-terminated samples. A small sp^2 carbon component was observed for the acid oxidation method.

Figures 5.10 and 5.11 show XPS spectra for the O 1s peak using 2- and 3-component peak fitting, respectively. The 2-component peak fit suggested that the UV/ozone-oxidised sample was predominantly ether bonded, while the plasma and acid oxidation methods had slightly higher ketone component. By contrast, the 3-component peak fit showed very similar fits of the 3 components for each oxidation method, with ketone largest, then ether, then hydroxyl.

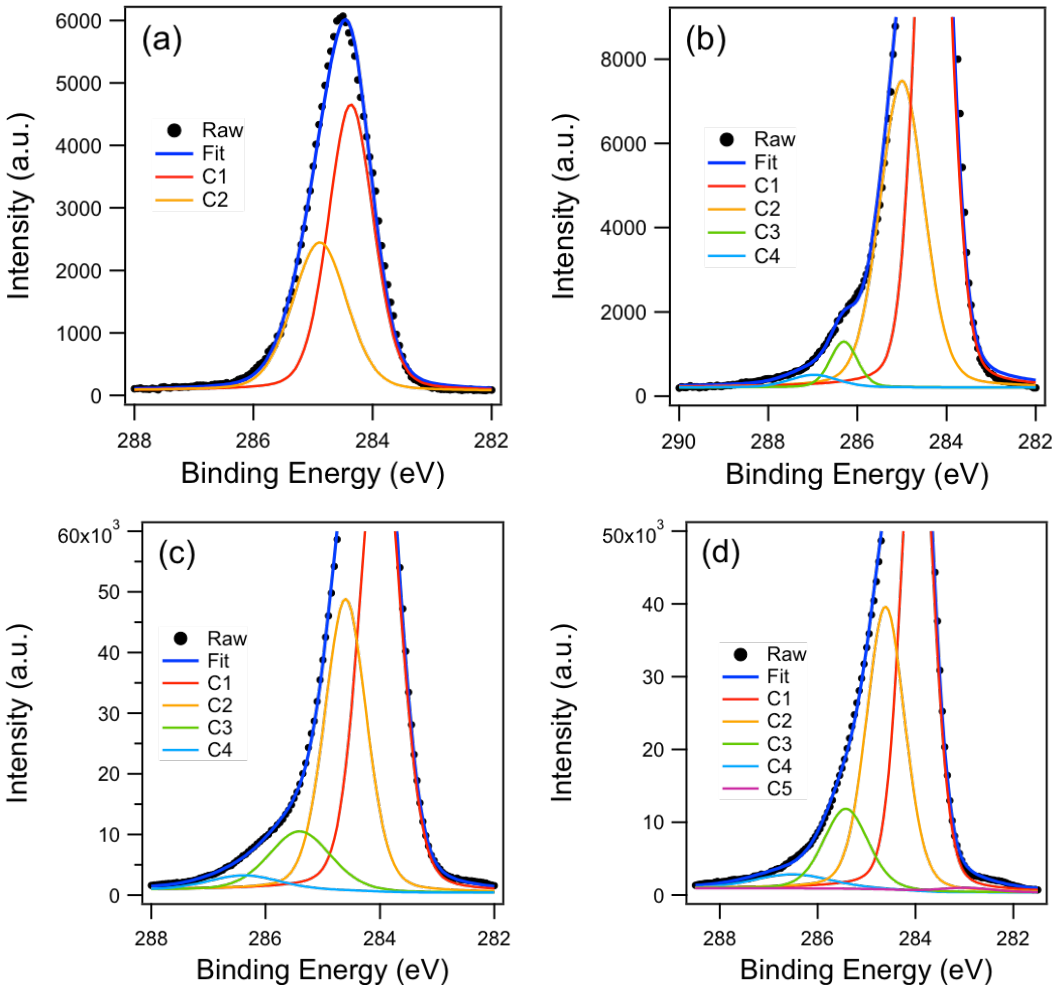

Key: C1: bulk sp^3 C-C; C2: surface sp^3 C-C; C3: C-O; C4: C=O; C5: sp^2 C-C

Figure 5.9: XPS spectra of the C 1s peak for (a) H-terminated (111) diamond, and (b)–(d) O-terminated (111) diamond using (b) UV/ozone, (c) plasma, and (d) acid oxidation methods. Fitted peak numbers correspond to those in Table 5.2.

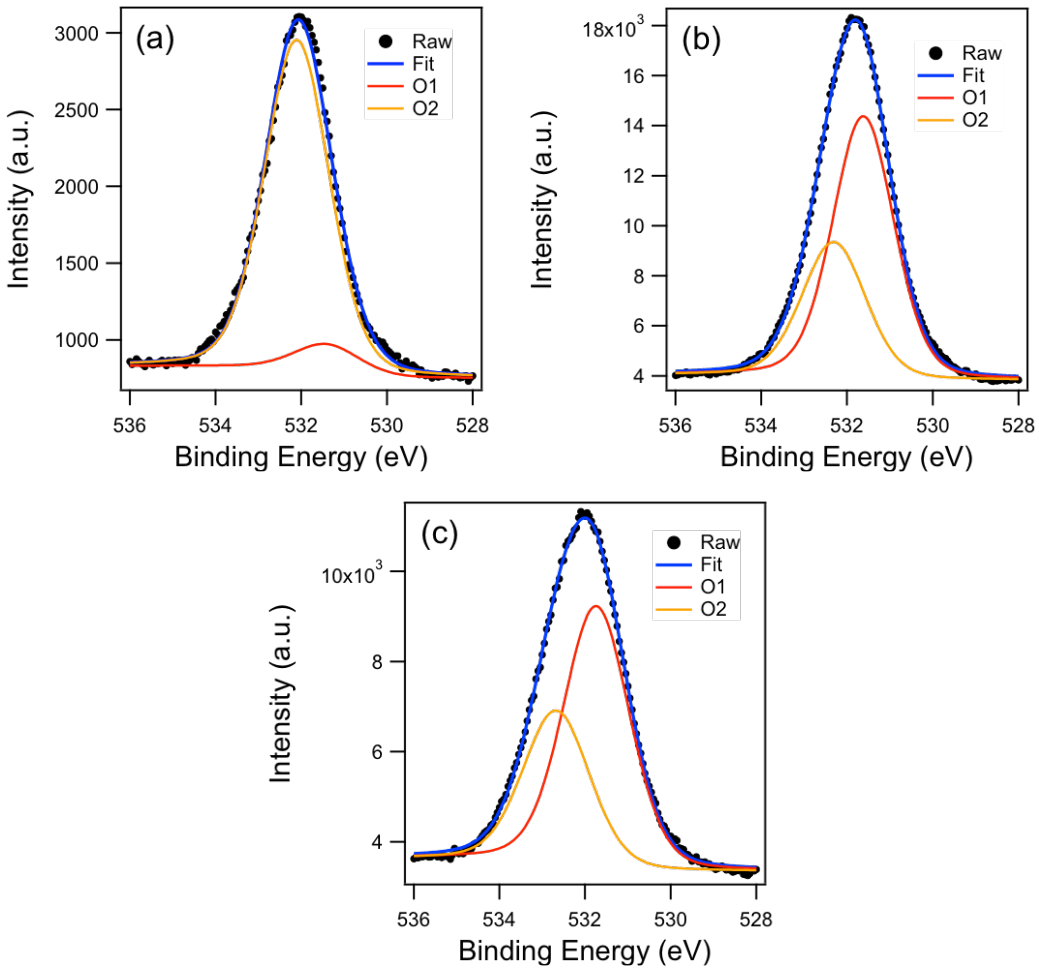

Key: O1: C=O; O2: C-O

Figure 5.10: XPS spectra of the O 1s peak for O-terminated (111) diamond using (a) UV/ozone, (b) plasma and (c) acid oxidation methods. A two-component peak fitting was used. Fitted peak numbers correspond to those in Table 5.3.

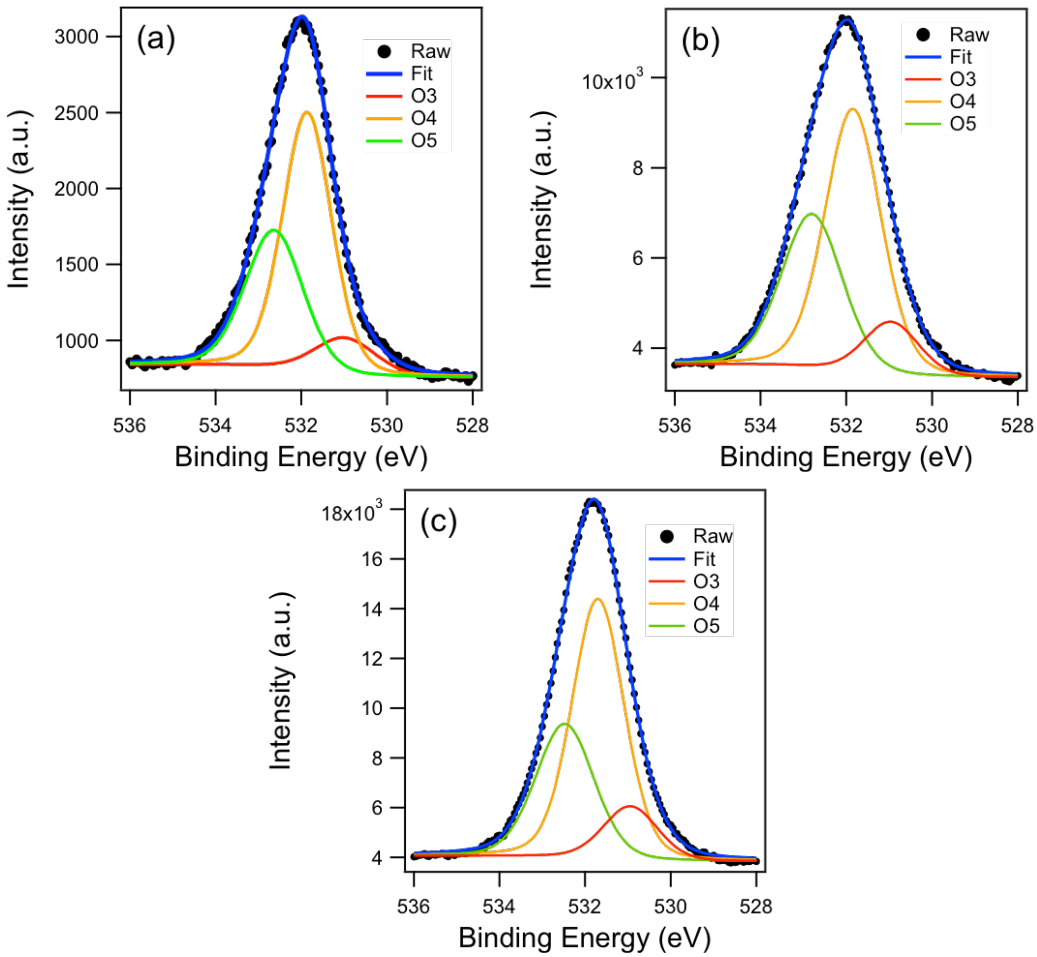

Key: O3: C-O (hydroxyl); O4: C=O; O5: C-O (ether)

Figure 5.11: XPS spectra of the O 1s peak for O-terminated (111) diamond using (a) UV/ozone, (b) plasma and (c) acid oxidation methods. A three-component peak fitting was used. Fitted peak numbers correspond to those in Table 5.4.

Table 5.7 shows the C-O/C=O ratios obtained from XPS and the atomic percentages of oxygen. The O atomic percentage was largest for plasma oxidation in this case, then UV/ozone oxidation, then acid oxidation. The results here and for the (100) surface suggest that ~6–7% of O is equivalent to 1 ML coverage.

The C-O/C=O ratios are plotted in Figure 5.12. Neither 2- or 3-component fits of the O 1s peak show a correlation between C 1s and O 1s C-O/C=O ratios. One possible explanation for this is that the larger roughness of the (111) surface has caused other bonding environments. This is supported by the larger full-width half-maximum value of the surface C-C component of the C 1s peak for H-terminated (111) diamond compared to that from the H-terminated (100)

surface (Figures 5.9(a) and 5.4(a), respectively). This would also mean that the O 1s peak is more reliable for identifying the different bonding arrangements that are present.

Table 5.7: Summary of C-O/C=O peak ratio and surface coverages for different oxidation procedures on the (111) diamond surface.

Termination Method	C 1s C-O/C=O	O 1s C-O/C=O (2 components)	O 1s C-O/C=O (3 components)	O at. %
UV/ozone	2.1	11.1	0.8	5.4
Oxygen Plasma	3.5	0.5	0.8	6.8
Acid	3.3	0.6	0.8	4.8

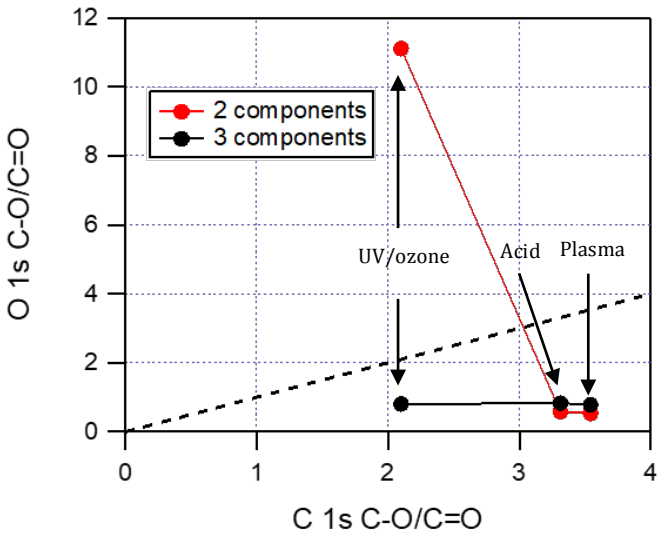

Figure 5.12: The C-O/C=O bond ratios of different oxidation methods from C 1s and O 1s peaks in XPS spectra. The O 1s spectra were fitted using either two or three components.

FTIR spectra were acquired for the H- and O-terminated (111) samples, however there was a much higher background absorbance from the sample and thus no peaks were identifiable for this surface. This is attributed to scattering of infrared light due to the higher surface roughness of the (111) single crystals.

5.5 Surface Structure

Low energy electron diffraction (LEED) was used to observe the surface structure of H- and O-terminated (100) and (111) diamond, in order to examine

the change in surface structure upon oxidation, and to assist with interpreting LEED patterns from aluminium-oxygen terminations (Chapter 6). The UV/ozone oxidation method was chosen to create the O-terminated diamond, as the previous section established that this method gave a high surface coverage on (100) and (111) diamond, with a high ketone component and low hydroxyl component.

5.5.1 Structure of the (100) Diamond Surface

LEED patterns for the H- and O-terminated (100) surfaces are shown in Figure 5.13. H-termination gives a (2 × 1) pattern and O-termination gives a (1 × 1) pattern. These are the same as reported in the literature.[34,35]

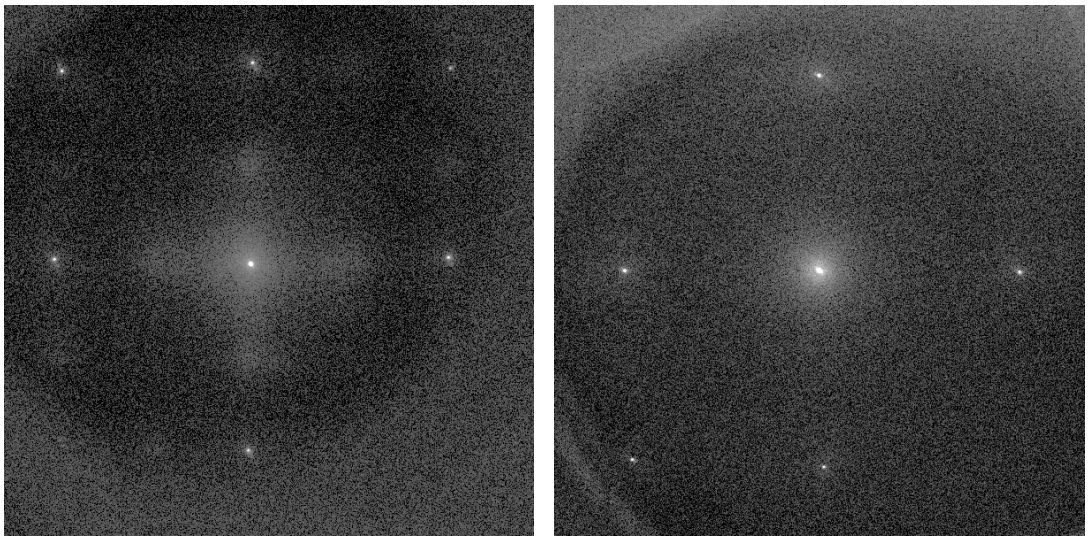

Figure 5.13: LEED patterns of (a) hydrogen-terminated and (b) oxygen-terminated (100) diamond. The electron beam energy was 180 eV for both.

5.5.2 Structure of the (111) Diamond Surface

LEED patterns for H- and O-terminated (111) diamond are shown in Figure 5.14. The H-termination gives a (1 × 1) pattern, in agreement with the literature.[36,37] The O-termination was also found to have a (1 × 1) pattern. Klauser *et al.*[36] have previously reported that saturation coverage of oxygen on (111) diamond gives a (2 × 1) LEED pattern, while Loh *et al.*[38] find a (1 × 1) pattern from addition of atomic oxygen at high-temperatures to (111) diamond, using reflection high energy electron diffraction (RHEED). This difference can be explained by the

degree of coverage on the reconstructed surface (the O-terminated unreconstructed surface is not predicted to be stable). Saturation coverage of oxygen results in a half-oxidised ether-bonded surface with the (2 × 1) reconstruction pattern, but with sufficient energy the surface can become fully oxidised, giving a (1 × 1) diffraction pattern. The (2 × 1) diffraction pattern is lost as the C=O bond of the ketone breaks one of the C-C bonds in the upper Pandey chain. As no reconstruction is observed here, it is assumed the surface is well-oxidised.

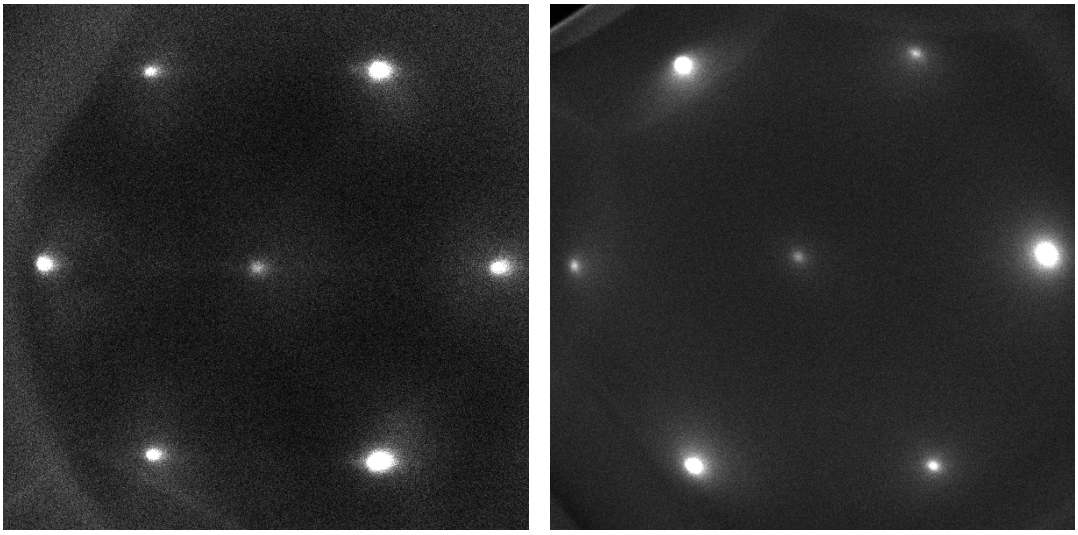

(a) (b)

Figure 5.14: LEED patterns of (a) hydrogen-terminated and (b) oxygen-terminated (111) diamond. The electron beam energy was 190 eV for (a) and 120 eV for (b).

5.6 Electronic Behaviour

The electronic structure for H- and O-terminated diamond was investigated using two techniques, energy-filtered photoemission electron microscopy (EF-PEEM) and ultraviolet photoemission spectroscopy (UPS) (see Chapters 3.5.5 and 3.5.6.2). As with the previous section the UV/ozone method was the chosen oxidation procedure to make O-terminated diamond.

5.6.1 Electronic Characteristics of the (100) Diamond Surface

Work function maps obtained from EF-PEEM are shown in Figure 5.15. On the micron-scale, both surfaces show homogeneous work functions. The work

function was determined to be 3.5 eV for the H-terminated surface and 6.0 eV for the O-terminated surface. The spots in the work function maps are believed to originate from surface abrasions caused by the polishing process. The local work function is affected by the topology because EF-PEEM applies a large bias to the sample.

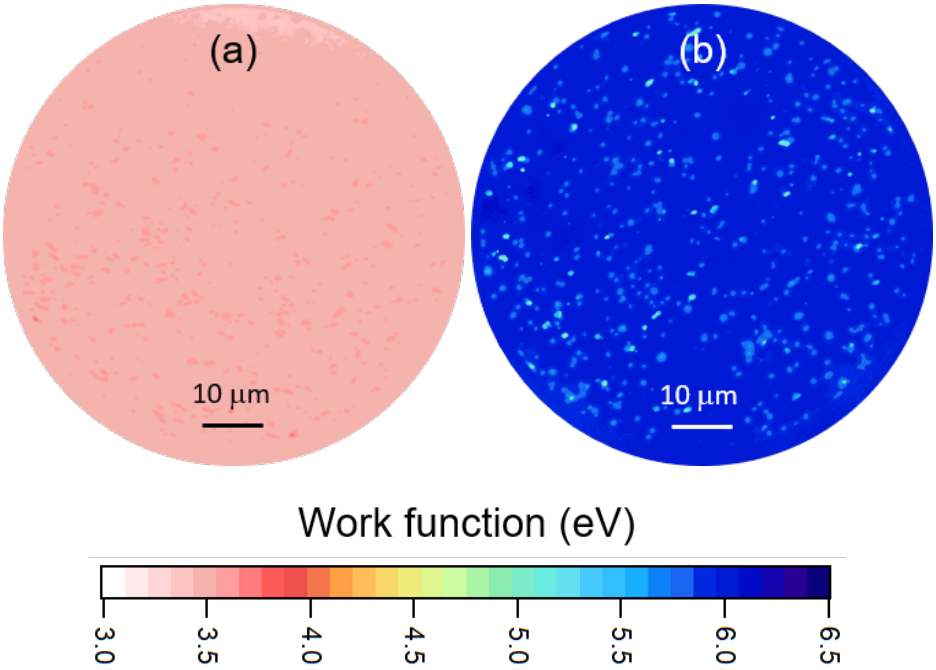

Figure 5.15: Colour-coded work function maps of (a) H- and (b) O-terminated (100) diamond.

UPS spectra for these samples are shown in Figure 5.16. Here and later, the spectra are normalised by the intensity of the valence band structure at ~8 eV. Inset in the figure is an expanded view of the position of the valence band maximum (VBM), E_{VBM}, relative to the Fermi energy, E_F. A fit has been applied to assist with determining $E_F - E_{VBM}$.

The main difference between the two spectra is the intensity and position of the secondary emission peak that appears at a high binding energy. The H-terminated sample has a much higher secondary electron emission as it has an NEA surface. There is an additional peak from the NEA, denoted with a * in Figure 5.16. Electron affinity values were calculated to be -1.2 eV for H-termination and 1.3 eV for O-termination.

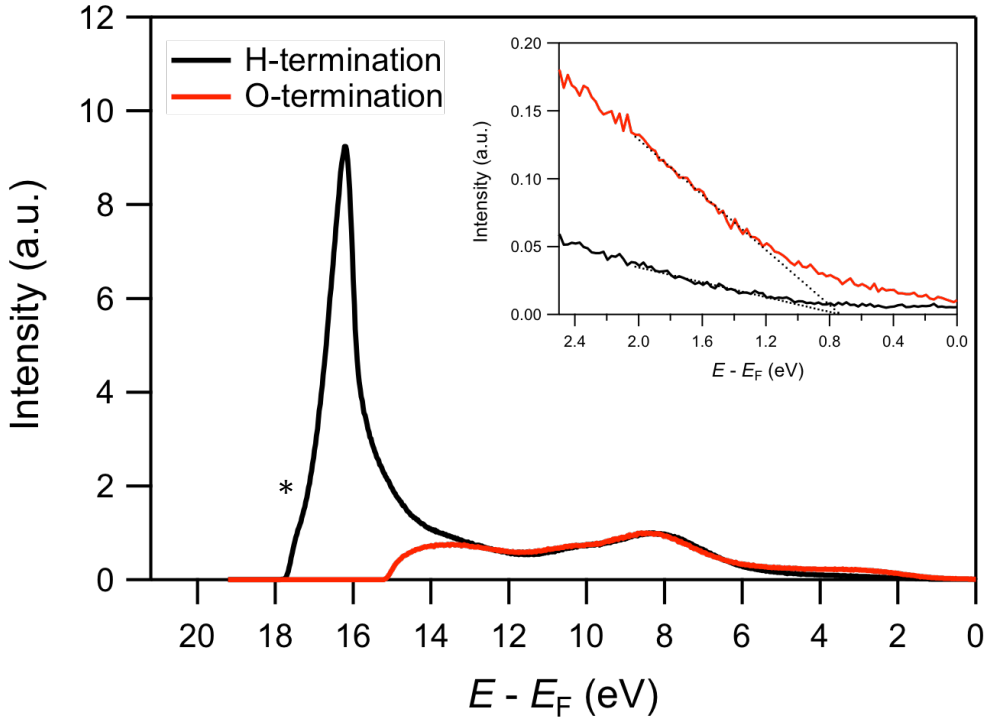

Figure 5.16: UPS spectra of H- and O-terminated (100) diamond. Inset shows a magnified view of the VBM energy relative to Fermi energy.

5.6.2 Electronic Characteristics of the (111) Diamond Surface

The same two techniques were performed to obtain electronic behaviour of the H- and O-terminated (111) surfaces. Work function maps, shown in Figure 5.17, indicate that the (111) surfaces also showed a relatively homogeneous work function across the surface. The work function of the H-terminated diamond was 3.5 eV, similar to that of the (100) surface. The O-termination showed a work function of between 5.0–5.4 eV. The lower work function of the oxidised (111) diamond compared to the respective (100) surface has been observed previously.[39]

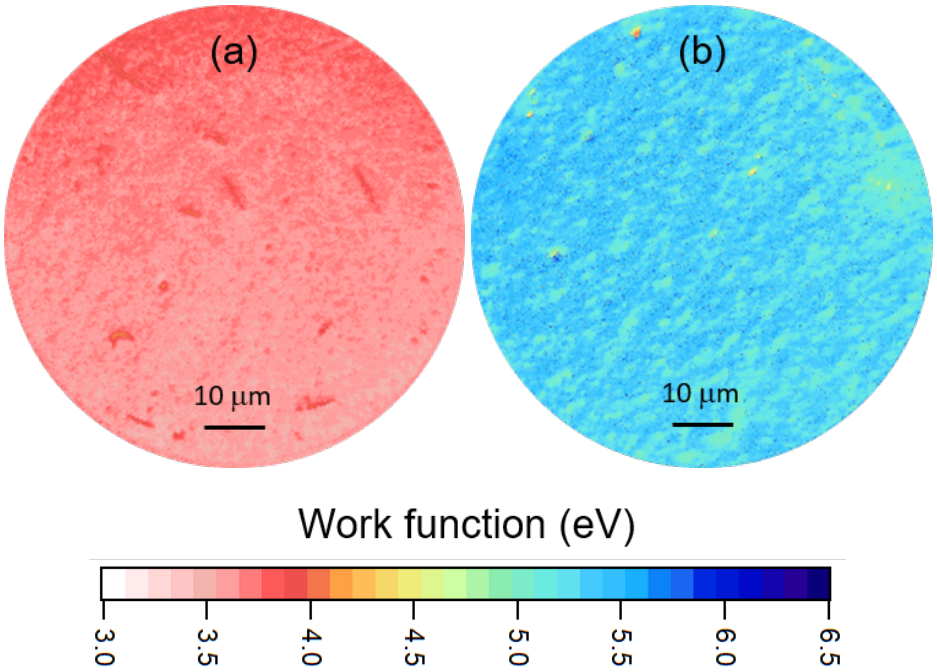

Figure 5.17: Colour-coded work function maps of (a) H- and (b) O-terminated (111) diamond.

UPS spectra for these samples are shown in Figure 5.18. The H- and O-terminated samples had similar UPS spectra to those from the (100) surface. The H-terminated diamond again showed an additional secondary electron peak component from NEA. Electron affinities were calculated to be -1.0 eV for the H-terminated diamond and between 0.5–0.9 eV for the O-terminated diamond.

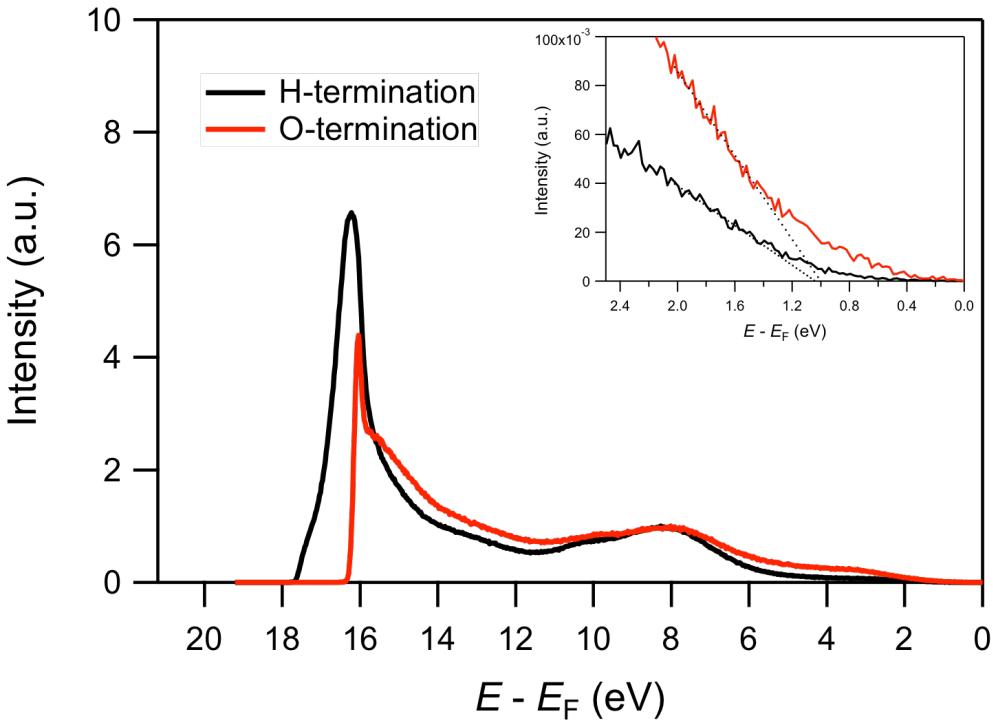

Figure 5.18: UPS spectra of H- and O-terminated (111) diamond. Inset shows a magnified view of the VBM energy relative to Fermi energy.

5.7 Conclusions

Three different oxidation methods – UV/ozone, oxygen plasma and acid treatment with H_2SO_4 and HNO_3 – were investigated on (100) and (111) diamond surfaces to determine the type of oxygen bonding they produce and the extent of surface coverage. The results indicate that all oxidation methods have some ether, ketone and hydroxyl bonds. There is slight variation of oxygen-bonding type depending on the oxidation method used, which is in agreement with other research into oxidation of diamond.

A good correlation between the C 1s and O 1s C-O/C=O ratios from XPS was obtained for the (100) surface when using a 3-component peak fit for the O 1s peak, and the relative amounts of the three oxygen bonding environments were in qualitative agreement with FTIR results. This indicates that a 3-component fit of the O 1s peak in XPS should be used in the future, as it gives detail of the ether and hydroxyl components. No such correlation was found between the C 1s and O 1s C-O/C=O ratio with either 2- or 3-component peak fitting for the (111) surface. This may be explained by a more complex surface structure due to

increased surface roughness of the single crystal, making XPS fitting more difficult.

It would therefore be worthwhile repeating the FTIR and XPS measurements for each oxidation method on the (111) surface after polishing to give a lower surface roughness. Future work could also use other techniques to probe the characteristics of O-terminated diamond in more detail. For instance, electron energy loss spectroscopy can give additional information on the different types of carbon-oxygen bonds. Techniques such as ellipsometry or atomic force microscopy could give an indication of any surface roughening caused by the different oxidation methods.

All experiments involving oxidation of diamond to date have focused on oxidising the bare or H-terminated surface. A novel route to controlling oxygen content could be to consider using reactions common in organic chemistry to convert between the existing oxygen bonds on an oxidised diamond surface. The diamond surface has been previously shown to undergo chemical reactions in a manner consistent with standard organic chemistry processes, and are described in Chapter 2. Three possible routes are suggested as examples for future experiments:

(i) *The Pinacol coupling reaction* (Scheme 1) is the reduction of two ketone groups to form a vicinal diol. The ketone groups would need to be adjacent for the reaction to proceed on the diamond surface. The (100) surface has the correct structure for this reaction, and would produce (2 × 1) reconstructed hydroxyl bonds from a (1 × 1) ketone surface. For the (111) surface, it is also possible to have adjacent ketone groups, and a (2 × 1) reconstructed ketone surface would give a (2 × 1) reconstructed hydroxyl-terminated surface, which is likely to be metastable with respect to the (1 × 1) surface.[38]

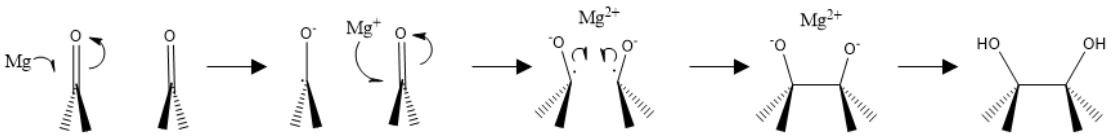

Scheme 1: The Pinacol coupling reaction, using Mg as a reducing agent.

(ii) *The diol oxidation reaction* (Scheme 2) is the reverse of the Pinacol coupling reaction, *i.e.* a vicinal diol is oxidised to form two ketone groups. This reaction is feasible on the (100) surface, assuming neighbouring hydroxyl groups are present. However, for the (111) surface, if the hydroxyl-bonded surface has no reconstruction, then the reaction is not expected to occur, since hydroxyl groups are no longer on adjacent carbons.

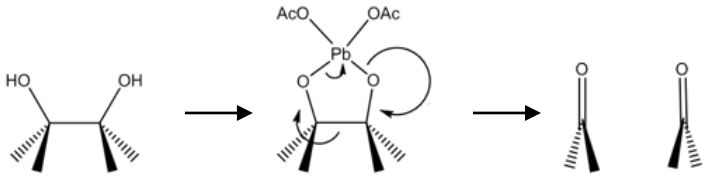

Scheme 2: The diol oxidation reaction, using $Pb(OAc)_4$ as an oxidising agent.

(iii) *The ether cleavage reaction* (Scheme 3) is a nuclear-substitution reaction, where an ether is converted into an alcohol plus a secondary functional group that depends on the nucleophile. In the liquid or gas phase, the ether cleavage reaction can proceed *via* S_N1 or S_N2 mechanisms depending on the reactants used. However, cleavage of ethers on a diamond surface would proceed only *via* the S_N1 mechanism due to the bulk diamond stabilising a carbocation intermediate and blocking the approach of nucleophiles from behind. Reaction of the diamond surface with dilute aqueous H_2SO_4 could result in an increase in hydroxyl content from cleavage of ether groups, forming two hydroxyl groups. In particular, the strained cyclic ether of the (111) surface would be susceptible to cleavage. This reaction is likely to be the most effective of the three as the reaction only involves one surface oxygen species.

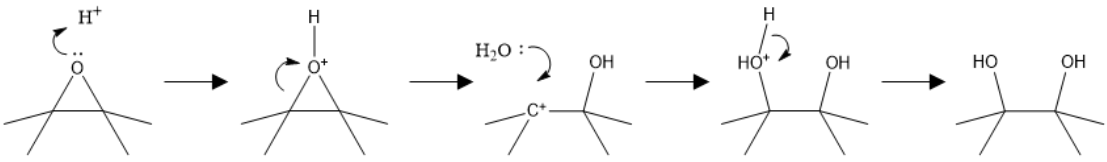

Scheme 3: The ether cleavage reaction, using H_2O as a nucleophile.

Alternatively, oxidation methods could be more selective in which bonds can form on the surface. The work of Yoshida *et al.*,[8] where (111) diamond was

heated in H_2O vapour to selectively obtain hydroxyl-terminated diamond, appears to be the closest approach to date for the formation of a singular type of oxygen bonding on (111) diamond, so perhaps a similar procedure could be used to hydroxyl-terminate the (100) surface.

References

1 T. Matsumoto, H. Kato, K. Oyama, T. Makino, M. Ogura, D. Takeuchi, T. Inokuma, N. Tokuda and S. Yamasaki, *Sci. Rep.*, 2016, **6**, 1–6.

2 A. Stacey, K. M. O'Donnell, J. P. Chou, A. Schenk, A. Tadich, N. Dontschuk, J. Cervenka, C. Pakes, A. Gali, A. Hoffman and S. Prawer, *Adv. Mater. Interfaces*, 2015, **2**, 1500079.

3 M. Wang, N. Simon, G. Charrier, M. Bouttemy, A. Etcheberry, M. Li, R. Boukherroub and S. Szunerits, *Electrochem. commun.*, 2010, **12**, 351–354.

4 H. Notsu, I. Yagi, T. Tatsuma, D. A. Tryk and A. Fujishima, *J. Electroanal. Chem.*, 2000, **492**, 31–37.

5 H. Notsu, T. Fukazawa, T. Tatsuma, D. A. Tryk and A. Fujishima, *Electrochem. Solid-State Lett.*, 2001, **4**, H1–H3.

6 F. Klauser, S. Ghodbane, R. Boukherroub, S. Szunerits, D. Steinmüller-Nethl, E. Bertel and N. Memmel, *Diam. Relat. Mater.*, 2010, **19**, 474–478.

7 S. Ghodbane, T. Haensel, Y. Coffinier, S. Szunerits, D. Steinmüller-Nethl, R. Boukherroub, S. I. U. Ahmed and J. A. Schaefer, *Langmuir*, 2010, **26**, 18798–18805.

8 R. Yoshida, D. Miyata, T. Makino, S. Yamasaki, T. Matsumoto, T. Inokuma and N. Tokuda, *Appl. Surf. Sci.*, 2018, **458**, 222–225.

9 H. Notsu, I. Yagi, T. Tatsuma, D. A. Tryk and A. Fujishima, *Electrochem. Solid-State Lett.*, 1999, **2**, 522–524.

10 H. Girard, N. Simon, D. Ballutaud, M. Herlem and A. Etcheberry, *Diam. Relat. Mater.*, 2007, **16**, 316–325.

11 M. Wang, N. Simon, C. Decorse-Pascanut, M. Bouttemy, A. Etcheberry, M. Li, R. Boukherroub and S. Szunerits, *Electrochim. Acta*, 2009, **54**, 5818–5824.

12 S. Torrengo, A. Miotello, L. Minati, I. Bernagozzi, M. Ferrari, M. Dipalo, E. Kohn and G. Speranza, *Diam. Relat. Mater.*, 2011, **20**, 990–994.

13 J. Navas, D. Araujo, J. C. Piñero, A. Sánchez-Coronilla, E. Blanco, P. Villar, R. Alcántara, J. Montserrat, M. Florentin, D. Eon and J. Pernot, *Appl. Surf. Sci.*, 2018, **433**, 408–418.

14 D. A. Shirley, *Phys. Rev. B*, 1972, **5**, 4709–4714.

15 M. Steenackers, S. Q. Lud, M. Niedermeier, P. Bruno, D. M. Gruen, P. Feulner, M. Stutzmann, J. A. Garrido and R. Jordan, *J. Am. Chem. Soc.*, 2007, **129**, 15655–15661.

16 A. Maréchal, M. Aoukar, C. Vallée, C. Rivière, D. Eon, J. Pernot and E. Gheeraert, *Appl. Phys. Lett.*, 2015, **107**, 141601.

17 S. Ghodbane, D. Ballutaud, A. Deneuville and C. Baron, *Phys. Status Solidi*, 2006, **203**, 3147–3151.

18 A. K. Schenk, K. J. Rietwyk, A. Tadich, A. Stacey, L. Ley and C. I. Pakes, *J. Phys. Condens. Matter*, 2016, **28**, 305001.

19 I. Yagi, H. Notsu, T. Kondo, D. A. Tryk and A. Fujishima, *J. Electroanal.*

Chem., 1999, **473**, 173–178.
20 A. Gaisinskaya, R. Akhvlediani, R. Edrei, E. Alagem, Z. Joselzon and A. Hoffman, *Diam. Relat. Mater.*, 2010, **19**, 305–313.
21 K. Huang, X. Hu, H. Xu, Y. Shen and A. Khomich, *Appl. Surf. Sci.*, 2014, **317**, 11–18.
22 T. Ando, K. Yamamoto, M. Ishii, M. Kamo and Y. Sato, *J. Chem. Soc. Faraday Trans.*, 1993, **89**, 3635–3640.
23 Y. Wang, H. Huang, J. Zang, F. Meng, L. Dong and J. Su, *Int. J. Electrochem. Sci.*, 2012, **7**, 6807–6815.
24 J. Bartoň, H. Krýsová, P. Janda, H. Tarábková, P. Ashcheulov, V. Mortet, A. Taylor, J. Vávra, P. Cígler and L. Kavan, *Appl. Mater. Today*, 2018, **12**, 153–162.
25 M. W. Geis, T. H. Fedynyshyn, M. E. Plaut, T. C. Wade, C. H. Wuorio, S. A. Vitale, J. O. Varghese, T. A. Grotjohn, R. J. Nemanich and M. A. Hollis, *Diam. Relat. Mater.*, 2018, **84**, 86–94.
26 H. H. Zhang, Y. T. Liu, R. Wang, X. Y. Yu, X. W. Qu and Q. X. Zhang, *Chinese Chem. Lett.*, 2011, **22**, 485–488.
27 K. Ushizawa, Y. Sato and T. Mitsumori, *Chem. Phys. Lett.*, 2002, **351**, 105–108.
28 P. Krysiński, Y. Show, J. Stotter and G. J. Blanchard, *J. Am. Chem. Soc.*, 2003, **125**, 12726–12728.
29 J. Raymakers, A. Artemenko, S. S. Nicley, P. Štenclová, A. Kromka, K. Haenen, W. Maes and B. Rezek, *J. Phys. Chem. C*, 2017, **121**, 23446–23454.
30 M. Hoeb, M. Auernhammer, S. J. Schoell, M. S. Brandt, J. A. Garrido, M. Stutzmann and I. D. Sharp, *Langmuir*, 2010, **26**, 18862–18867.
31 T. Wade, M. W. Geis, T. H. Fedynyshyn, S. A. Vitale, J. O. Varghese, D. M. Lennon, T. A. Grotjohn, R. J. Nemanich and M. A. Hollis, *Diam. Relat. Mater.*, 2017, **76**, 79–85.
32 W. Hongthani, N. A. Fox and D. J. Fermín, *Langmuir*, 2011, **27**, 5112–5118.
33 E. Fuente, J. A. Menéndez, M. A. Díez, D. Suárez and M. A. Montes-Morán, *J. Phys. Chem. B*, 2003, **107**, 6350–6359.
34 Y. M. Wang, K. W. Wong, S. T. Lee, M. Nishitani-Gamo, I. Sakaguchi, K. P. Loh and T. Ando, *Diam. Relat. Mater.*, 2000, **9**, 1582–1590.
35 P. E. Pehrsson and T. W. Mercer, *Surf. Sci.*, 2000, **460**, 49–66.
36 R. Klauser, J. M. Chen, T. J. Chuang, L. M. Chen, M. C. Shih and J. C. Lin, *Surf. Sci.*, 1996, **356**, L410–L416.
37 B. B. Pate, *Surf. Sci.*, 1986, **165**, 83–142.
38 K. P. Loh, X. N. Xie, S. W. Yang and J. C. Zheng, *J. Phys. Chem. B*, 2002, **106**, 5230–5240.
39 G. Wan, M. Cattelan and N. A. Fox, *J. Phys. Chem. C*, 2019, **123**, 4168–4177.

Chapter 6 – Experimental Determination of the Work Function and Negative Electron Affinity from Al on O-Terminated Diamond

6.1 Introduction

The computational work discussed in Chapter 4 suggests that a negative electron affinity (NEA) can readily occur from the addition of sub-monolayer (ML) coverage of aluminium onto oxygen-terminated diamond surfaces. Specifically, NEA values are determined to be most negative at 0.25 ML Al coverage, and calculated to be up to -1.36 eV and -2.17 eV for the (100) and (111) surfaces, respectively. The adsorption energies are large, up to -6.36 eV/atom for the (100) surface and -8.19 eV/atom for the (111) surface, compared to ~-4 eV/atom for H-terminated diamond.

This chapter now focuses on experimental addition of Al to O-terminated diamond. As shown by Figure 6.1, two different methods were attempted. Figure 6.1(a) shows the thick-film process, which involves the deposition of over 20 nm of metal in a high vacuum chamber, followed by a washing step to dissolve the excess metal. O'Donnell *et al.*[1] first used this method to produce an LiO-terminated (100) diamond sample, from Li deposition and washing in water. They observed a high secondary emission yield using scanning electron microscopy, but found that the emission was not uniform. This thick-film process has also been used in a preliminary study investigating NEA from Ti, Cr and Al deposition onto oxidised polycrystalline diamond, although these samples were each submerged in 1 M HCl at 100 °C for 2–4 hours in order to remove the excess metal, and each sample was additionally annealed at 650 °C after the acid wash.[2]

The second deposition method, shown in Figure 6.1(b), involves the ultrahigh vacuum (UHV) deposition of a thin (<3 Å) metal layer followed by an anneal at a temperature of at least 600 °C. Using ultraviolet photoelectron spectroscopy (UPS), this procedure has produced a large secondary electron emission intensity for 0.4 Å and 2.8 Å Li layers on O-terminated (100) diamond.[1] This thin-film process has similarly been used to prepare MgO-terminated diamond from

deposition of a 1.5 Å Mg layer onto oxidised (100) diamond, although in this case, the NEA was largest without any annealing step.[3] The formation of VO-terminated diamond has also used this method, by deposition of a 1 Å V layer on oxidised polycrystalline diamond and annealing at 650 °C.[4] Si- and Ge-terminated (100) diamond have similarly been prepared using the thin-film process, but from deposition onto bare diamond surfaces, with annealing above 900 °C.[5,6]

In this chapter, AlO-terminated diamond is fabricated using both thick- and thin-film deposition procedures. Two different approaches were used for deposition of sub-ML coverage of Al by the thin-film process. The first was Al deposition by atomic layer deposition (ALD), and the second was deposition by electron-beam evaporation.

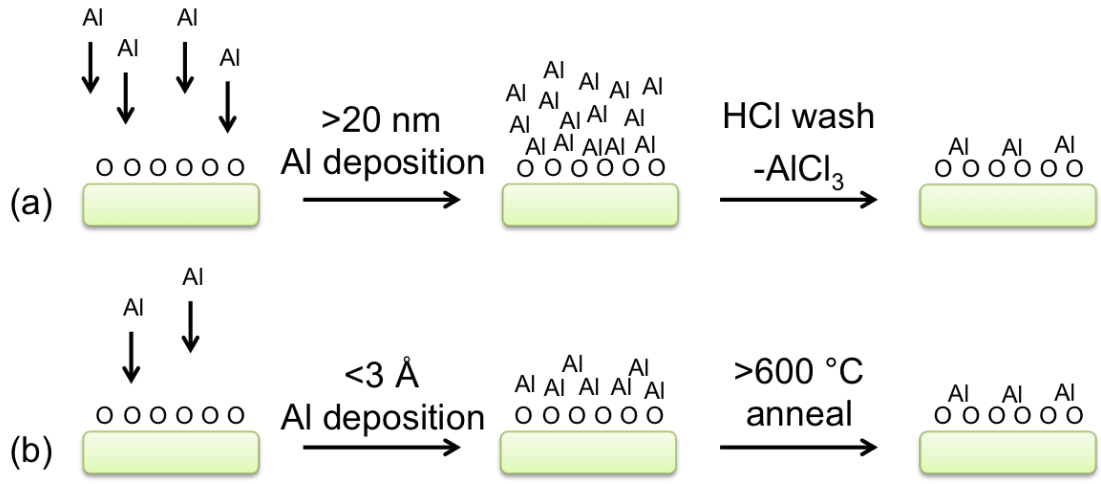

Figure 6.1: Two different experimental approaches have been used to fabricate aluminium-oxygen-terminated diamond. (a) The thick-film method deposits a thick metal layer onto O-terminated diamond, and excess metal (*i.e.* metal atoms that are not chemically bonded to the oxygenated surface) is selectively removed. (b) The thin-film method deposits a thin metal layer that can be 'activated' by thermal annealing. Adapted from O'Donnell *et al.*[1]

6.2 Experimental Details

Full details of materials and techniques are given in Chapter 3. Here, single-crystal diamond substrates were used to individually study the AlO-terminated (100) and (111) facets. The preparation procedure was identical to that described in Chapter 5.2. New or reused samples were acid cleaned, a boron-

doped diamond (BDD) epitaxial overlayer was grown to provide a conductive surface, and the samples were subjected to a hydrogen plasma to produce a pristine, H-terminated surface. The diamond surface was subsequently oxidised and then Al was deposited. All AlO-terminations prepared by the thick-film method or by electron-beam evaporation of Al were oxidised by UV/ozone treatment, as this method was established in Chapter 5.4 to be a reliable and reproducible way to oxidise diamond with a relatively high ketone component. The AlO-terminations prepared by ALD of Al were oxidised either with UV/ozone treatment or within the ALD chamber by heating the sample in H_2O vapour.

Polycrystalline BDD samples were used to explore the effectiveness of the thick-film Al deposition process. These were prepared by growing a BDD thin film by hot filament chemical vapour deposition (CVD) on silicon substrates for 3 h. A cross-section of the thin film was prepared using a laser cutter to cut the sample in half. As shown by Figure 6.2(a), scanning electron microscopy (SEM) determined that there was a ~1 μm-thick diamond layer.

Thermionic emission studies were performed using polycrystalline nitrogen-doped diamond (NDD). These were grown by microwave plasma CVD on molybdenum substrates for 15 min. Using SEM, a cross-section of NDD grown on silicon under the same conditions showed a ~2.5 μm-thick diamond layer (Figure 6.2(b)).

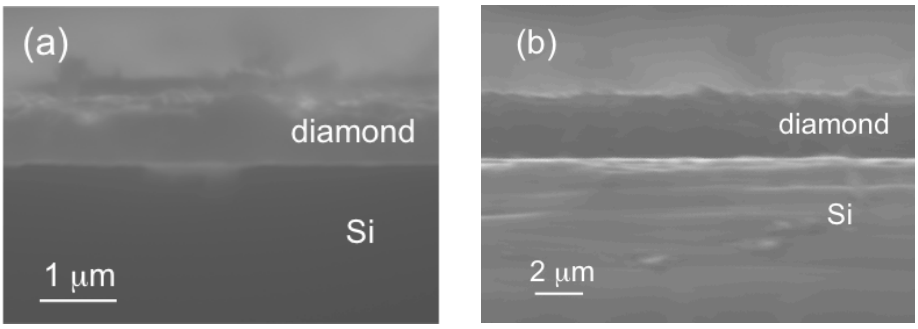

Figure 6.2: SEM images showing cross-sections of (a) BDD grown on Si by hot filament CVD, and (b) NDD grown on Si by microwave plasma CVD.

6.3 Thick-Film Deposition

6.3.1 Al Deposition on Polycrystalline Diamond

The thick-film deposition procedure was first tested using a polycrystalline BDD film grown on an Si substrate. Figure 6.3 shows the Raman spectrum of a typical BDD film after growth. The polycrystalline diamond has a large sp^3 carbon content, confirmed by the prominent peak at 1332 cm^{-1}. There was a small amount of graphitic sp^2 carbon content, observed as a broad G-band peak at ~1580 cm^{-1}. The broad peaks at ~970 cm^{-1} and ~1200 cm^{-1} are associated with the silicon substrate and boron impurities in diamond, respectively.[7,8]

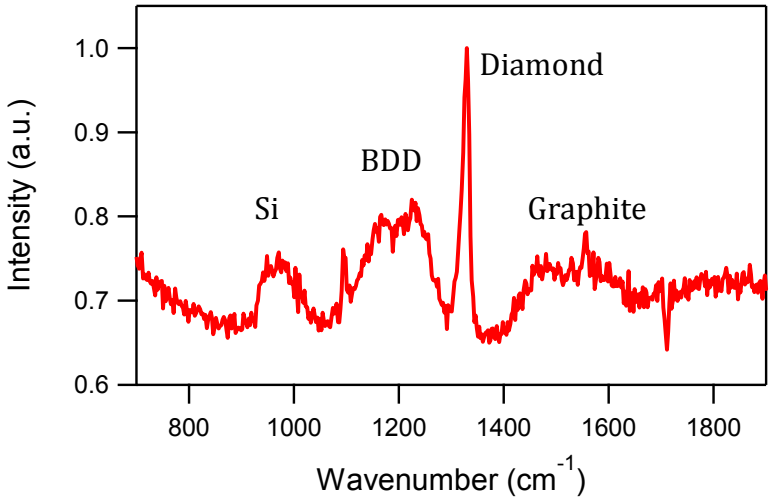

Figure 6.3: Raman spectrum (514 nm) of a BDD thin film on an Si substrate.

Al was deposited on two samples, one that was annealed at 300 °C for 1 h after Al deposition and before removing from vacuum, and one that was not annealed. Post-deposition, the presence of Al is clearly visible as a shiny metallic coating. For the HCl acid-wash step, the chosen reaction conditions were slightly modified from the previous preliminary study.[2] The acid concentration was changed from 1 M to 0.1 M, and the sample was kept at room-temperature. These conditions were chosen to give high uniformity of the surface termination by limiting the reactivity of the acid, thus ensuring only the removal of metallic Al. A longer reaction time of 20 h allowed the reaction to reach completion. For both samples, after one hour of acid etching the metallic surface looked less uniform, and after 20 h no trace of the metallic surface remained visible to the naked eye.

Figure 6.4(a)–(c) shows SEM images in turn after the diamond growth step, after the Al deposition step, and after the HCl treatment step, respectively. It appears that the excess metallic Al has been removed after the acid washing procedure, as the acid-treated sample is indistinguishable from the as-grown sample. This was the case regardless of whether an annealing step was performed after deposition.

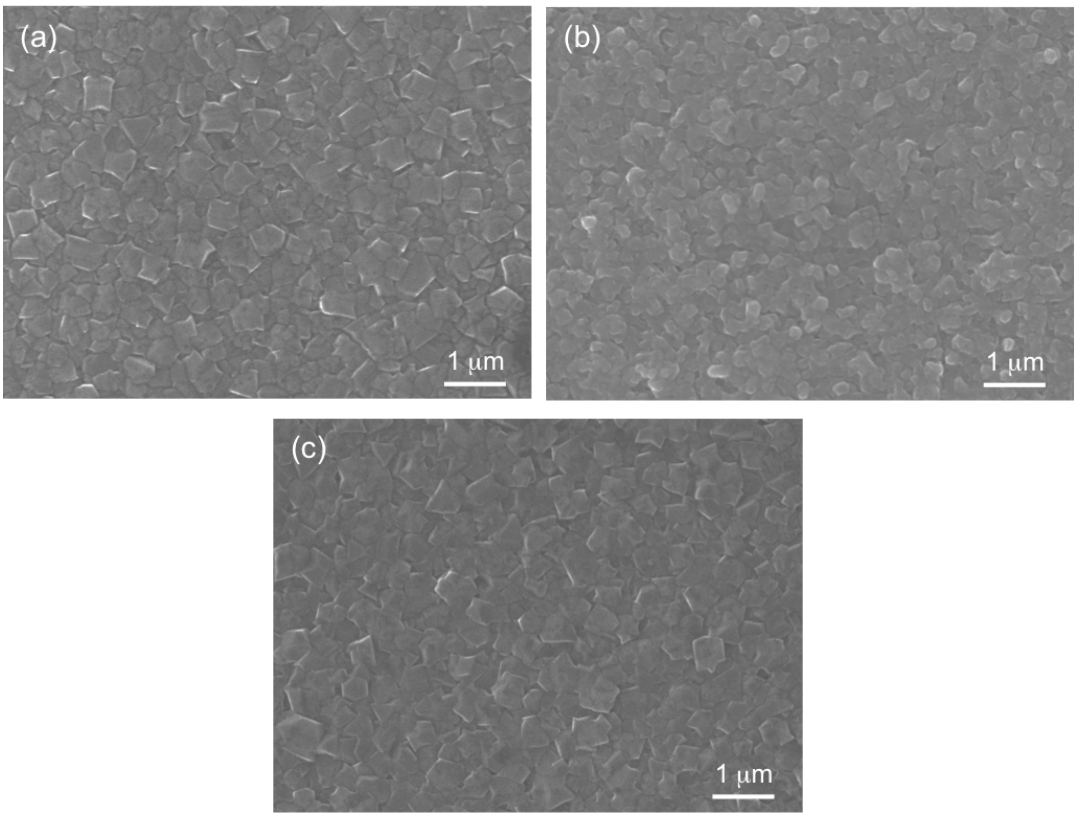

Figure 6.4: SEM images of (a) O-terminated diamond, (b) after 20 nm Al deposition, and (c) after HCl treatment.

X-ray photoelectron spectroscopy (XPS) was used to confirm the presence of Al. The Al 2p peak has a small spin-orbit splitting (<0.5 eV) and so appears as a singular peak. Table 6.1 gives the expected component peak positions of the Al 2p peak, while Figure 6.5 shows the Al 2p XPS spectra for the two AlO-terminated samples. The presence of the Al 2p peak in both instances indicates that the AlO-termination is both air- and water-stable, even with no annealing. For both spectra there are two Al environments; the lower binding energy peak is attributed to metallic Al and the higher binding energy peak to oxidised Al.

There is a slight decrease of the metallic component with annealing, from 16% to 13%, suggesting that annealing can increase the aluminium-oxygen bonding.

Table 6.1: Approximate Al 2p peak positions from XPS.[9]

Peak	Binding Energy (eV)	Assignment
Al1	72.0	Metallic Al
Al2	74.5	Oxidised Al

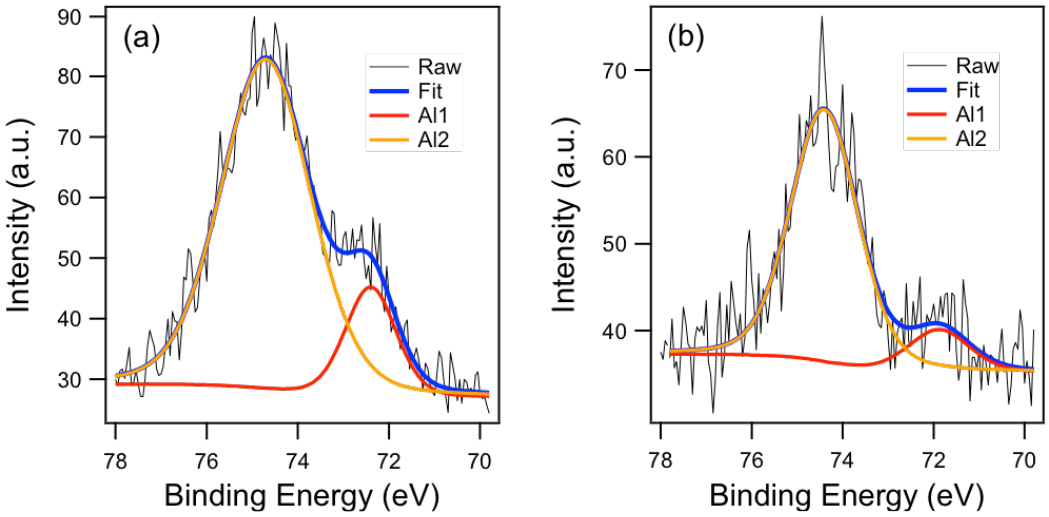

Key: Al1: metallic Al; Al2: oxidised Al

Figure 6.5: XPS spectra of the Al 2p peak for polycrystalline AlO-terminated BDD prepared by the thick-film process. (a) No annealing was performed and (b) a 300 °C anneal was performed for one hour after deposition.

A further sample was prepared using the same procedure, except a mask was used to cover half of the sample so that Al was deposited only on the other half. XPS spectra of the two sides of the surface showed that Al was only present on the side where deposition had occurred. This indicated that Al does not migrate during the acid-washing step.

6.3.2 Analysis of the (100) and (111) Surfaces

Following the successful creation of an AlO-termination by the thick-film process on polycrystalline diamond, next the properties of single-crystal (100) and (111) surfaces were studied. The AlO-terminations were prepared in the same manner, and were annealed at 300 °C for 1 h after Al deposition. The two samples were

fully characterised after annealing at three different temperatures. The lowest temperature, 300 °C, was the temperature used for sample degassing upon introduction to the UHV system. Higher annealing temperatures of 600 °C and 800 °C were selected as they can give an indication of the change in surface characteristics within the expected temperature range for thermionic emission. The annealing was performed for 10 min at 10^{-8} mbar using a resistive heater.

Figure 6.6 shows normalised XPS spectra of the C 1s, O 1s and Al 2p peaks for (100) and (111) single-crystal diamond surfaces at each annealing temperature. As described in Table 5.2 in Chapter 5, the oxidised C 1s peak comprises of bulk and surface C-C bonding component peaks, plus C-O and C=O component peaks at higher binding energies. The O 1s peak is expected to be a complex combination of the ether, ketone and hydroxyl peaks, as described in Table 5.4 of Chapter 5, in addition to an Al-O peak. An Al-O component peak would be expected at a similar binding energy to the hydroxyl peak (~531.0 eV).[9]

The C 1s peak did not notably change in shape for the (100) sample, but there was a decrease in the C-O and C=O components of the C 1s peak between the 300 °C and 600 °C anneals for the (111) sample (Figure 6.6(b)). None of the C 1s peaks here or later contained a carbide component, which would have been observed at a binding energy of ~282 eV.[9] The O 1s peak for the (100) sample showed a relatively large increase of a low binding energy component with temperature (Figure 6.6(c)); this is attributed to an increase in the Al-O component peak. For both the (100) and (111) samples, the Al 2p peak was centred at ~74.5 eV, indicating that Al was oxidised. There was a slight metallic Al component at lower binding energy for the (100) sample, ~20% of the total peak area at each temperature, similar to the polycrystalline samples. No metallic Al was observed for the (111) sample. With increasing annealing temperature, both samples showed a slight shift of all three peaks to higher binding energies. This could either be due to sample charging, or increasing downwards band bending at the surface, caused by a change in surface states.[10]

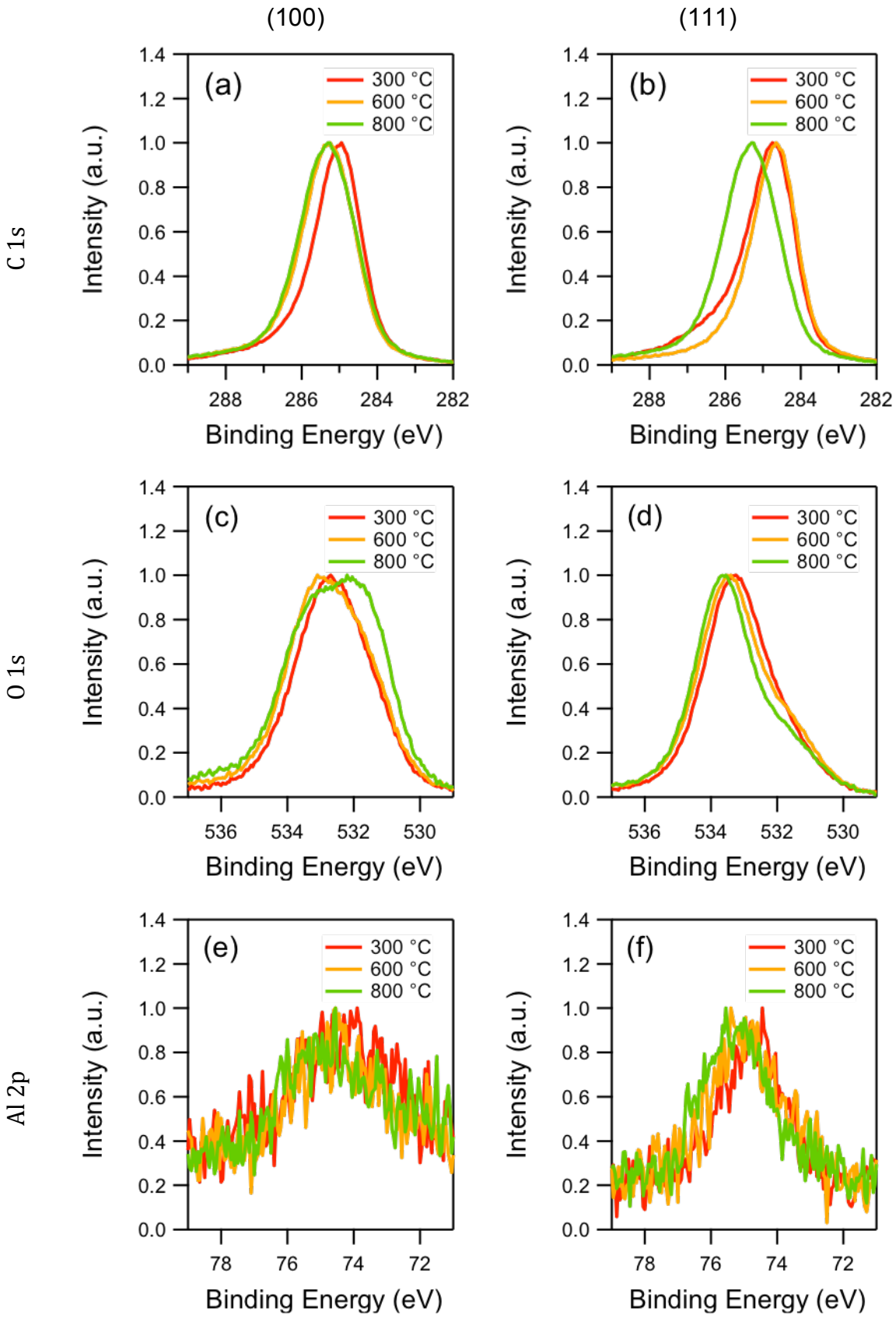

Figure 6.6: XPS spectra of (a)–(b) C 1s, (c)–(d) O 1s, and (e)–(f) Al 2p peaks at different annealing temperatures for thick-film-prepared AlO-terminated diamond. (a), (c), (e) are from the (100) surface, and (b), (d), (f) are from the (111) surface.

Figure 6.7 shows the O and Al atomic percentages at different annealing temperatures, calculated using Equation 3.3 in Chapter 3. There was no change in the amount of Al with annealing, suggesting it was strongly bound to the surface. The total amount of Al was similar between the two samples, just over 1%. The slight increase in the O atomic percentage with temperature was unexpected, but may be from spatial variation. From Chapter 5.4, it was determined that ~6–7% of O was equivalent to 1 ML coverage for O-terminated diamond, suggesting that Al is present at sub-ML coverage here. By contrast, the O atomic percentage was larger than expected, particularly for the (111) surface; this was attributed to additional O bonded to Al, possibly from air or water exposure. This C-O-Al-O bonding arrangement would be expected to have a detrimental effect by increasing the work function and electron affinity (EA), since it would form an additional dipole with negative charge outermost from the surface.

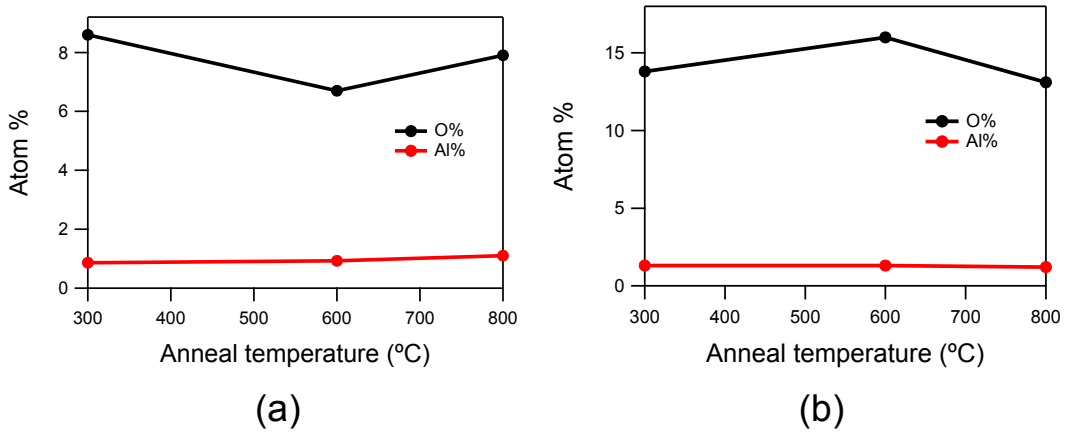

Figure 6.7: Atomic percentages of O and Al at different annealing temperatures for thick-film-prepared AlO-terminated (a) (100) and (b) (111) diamond surfaces.

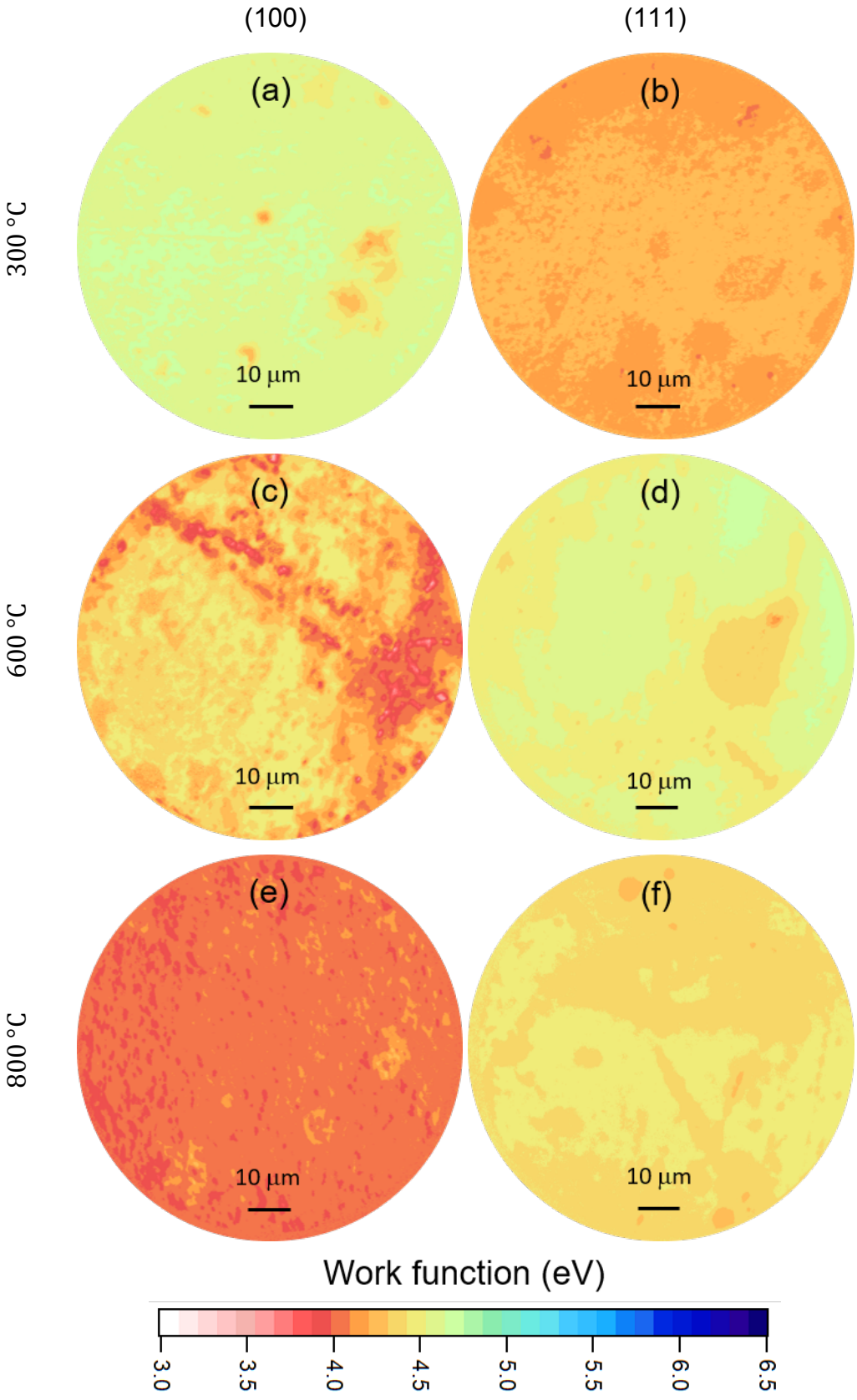

Figure 6.8: Colour-coded work function maps of AlO-terminated diamond prepared by the thick-film procedure, after annealing at (a)–(b) 300 °C, (c)–(d) 600 °C and (e)–(f) 800 °C. (a), (c) and (e) show the (100) surface and (b), (d) and (f) show the (111) surface.

The work function across the surface was measured after each of the annealing steps. Shown in Figure 6.8 are work function maps for both the (100) and (111) surfaces. Starting with the (100) surface, after the 300 °C anneal the work function was just under 4.7 eV and was relatively uniform across the surface, with exception of a few regions where it was just below 4.0 eV. After the 600 °C anneal, the work function had decreased, and ranged between 3.7–4.3 eV. After the 800 °C anneal, there was a relatively consistent work function between 4.0–4.2 eV across the surface.

The (111) surface, meanwhile, exhibited the lowest work function after the 300 °C anneal, with a relatively uniform value of ~4.1 eV. This increased to between 4.2–4.6 eV after the 600 °C anneal, with similar range of 4.2–4.5 eV observed after the 800 °C anneal.

Shown in Figure 6.9 are UPS spectra obtained after the 300 °C anneal. Here and later the spectra were acquired from the lowest work function regions, and are normalised by intensity of the valence band structure. Inset in the figure is a magnified plot showing the energy of the valence band maximum (VBM), E_{VBM}, relative to the Fermi energy, E_F. A fit has been applied to assist with determining $E_F - E_{VBM}$.

The secondary emission peak for the (100) sample was four times the height of the (111) sample, and the (100) sample had a slightly more negative EA, calculated (using Equation 3.4 in Chapter 3) to be -0.5 eV compared to -0.4 eV for the (111) sample. Acquiring UPS spectra in different regions of the surface showed that $E_F - E_{VBM}$ remained relatively constant. As such, most of the (100) surface (which showed a larger work function) exhibited a positive electron affinity (PEA) of 0.3 eV.

UPS spectra were not obtained after higher temperature anneals, but the EA values were still calculated from the work function maps and by using the change in C 1s peak position from XPS to determine $E_F - E_{VBM}$.[11] The EAs for the (100) sample varied between -0.4 eV and 0.2 eV after the 600 °C anneal, and between -0.1 eV and 0.1 eV after the 800 °C anneal. The EAs for the (111) sample varied between -0.4 eV and 0.0 eV after the 600 °C anneal and between -0.3 eV and 0.0 eV after the 800 °C anneal.

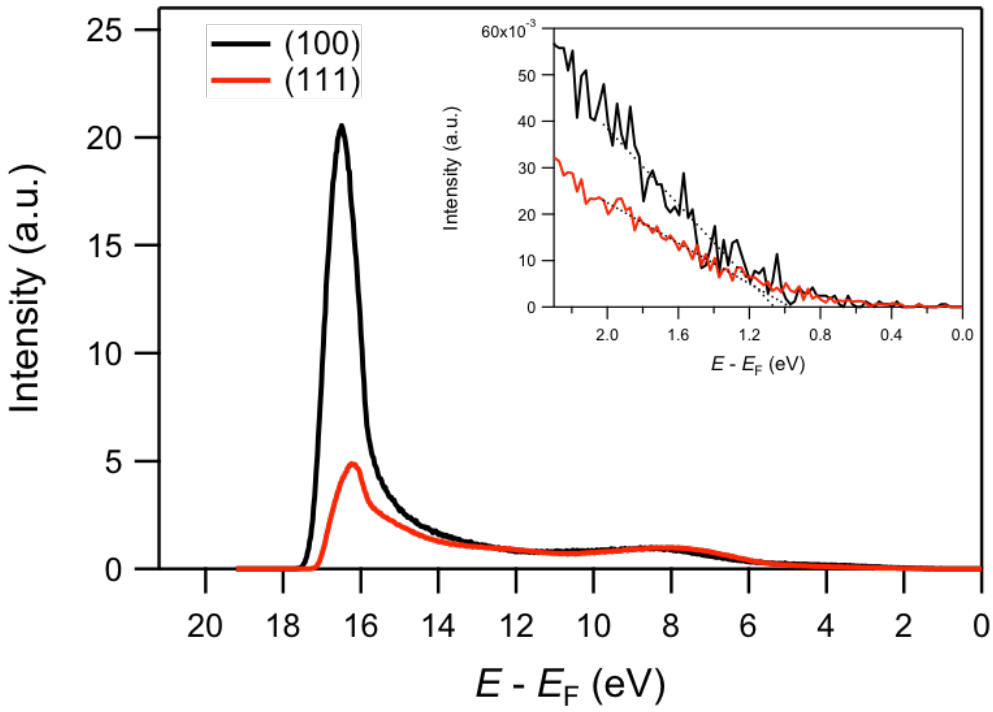

Figure 6.9: UPS spectra acquired after a 300 °C anneal for AlO-terminated (100) and (111) single-crystal diamond prepared by the thick-film procedure. Inset shows a magnified view of the VBM energy relative to Fermi energy.

6.4 Thin-Film Deposition by ALD

6.4.1 Effect of Oxidation Method

Initially, AlO-terminations were prepared on two (100) single-crystal diamond samples: one that had been oxidised by the UV/ozone method, and one that was oxidised *in situ* by the ALD technique by introducing one pulse of H_2O for one minute. Al was deposited on these samples by ALD, then the samples were annealed for 1 h at 300 °C.

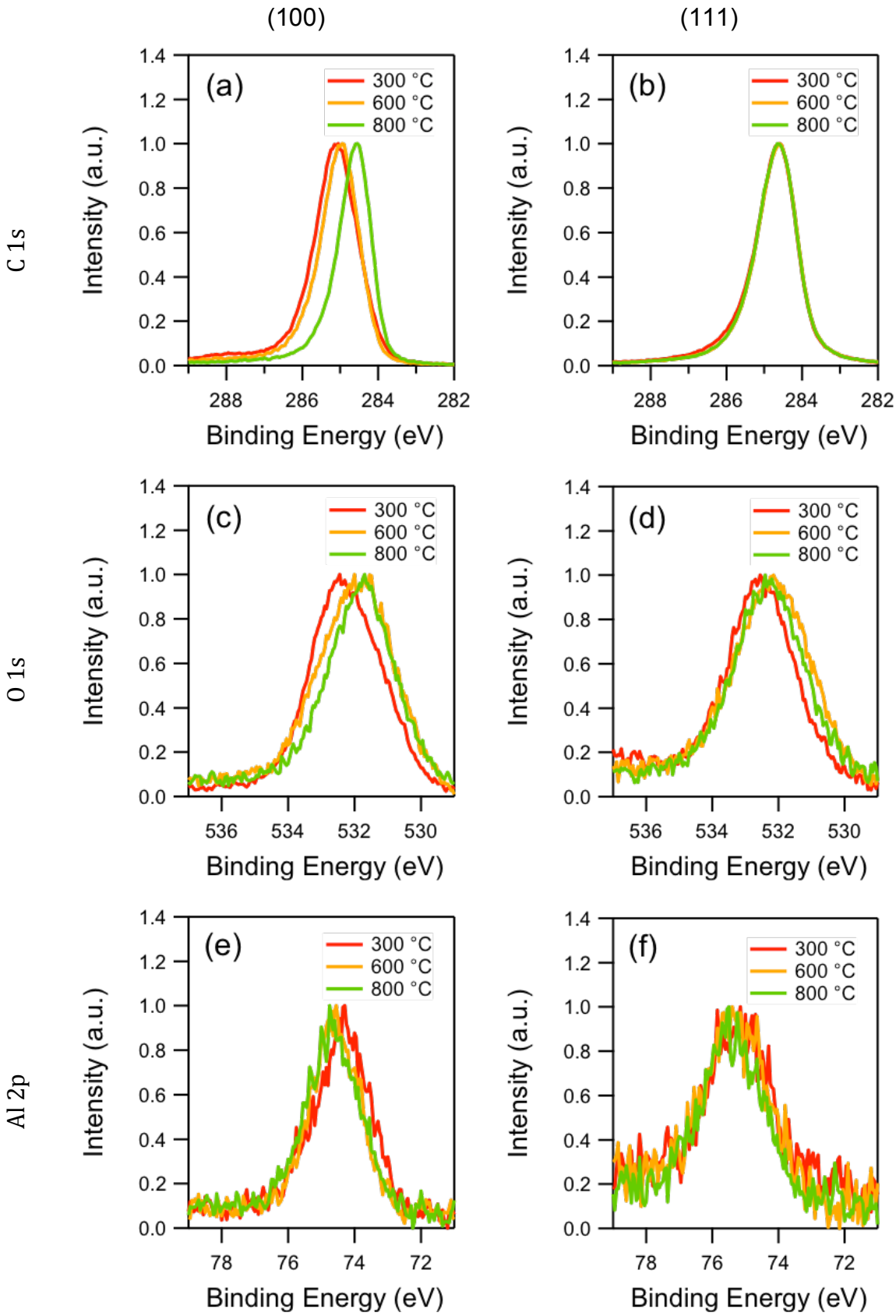

Figure 6.10: XPS spectra of (a)–(b) C 1s, (c)–(d) O 1s, and (e)–(f) Al 2p peaks at different annealing temperatures for ALD-prepared AlO-terminated diamond. (a), (c), (e) are from the UV/ozone-oxidised sample, and (b), (d), (f) are from the ALD-oxidised sample.

As with the thick-film deposition procedure, XPS was used to monitor the change in bonding at annealing temperatures of 300 °C, 600 °C and 800 °C. Normalised XPS spectra of the C 1s, O 1s and Al 2p peaks for these two samples at different annealing temperatures are shown in Figure 6.10. Neither of the C 1s peaks showed a change in peak shape with temperature, but the (100) sample showed a shift to lower binding energy after the 800 °C anneal. The O 1s peaks both showed an increase in a low binding energy component between 300 °C and 600 °C, similar to the thick-film method, but little change between 600 °C and 800 °C. Both Al 2p peaks had no metallic component, and showed relatively little change in the peak shape and position with annealing.

Figure 6.11 shows the O and Al atomic percentages at different annealing temperatures. The sample that had been oxidised by the UV/ozone method had a much higher oxygen content (9.1%) compared to that of the ALD-oxidised sample (1.9%). The UV/ozone sample had over 1 ML oxygen coverage, which, as with the thick-film method, is attributed to further oxidation of the surface after atmospheric exposure, giving a C-O-Al-O bonding arrangement. The ALD-oxidised sample appeared to be poorly oxidised and so the presence of H-termination (up to ~700 °C) in addition to AlO-termination could not be ruled out. The oxygen content decreased drastically for the UV/ozone-oxidised sample, especially in the relatively low-temperature range 300–600 °C. This was likely to be due to removal of the oxygen bonded only to Al, as there was no decrease of C-O or C=O components of the C 1s peak. The Al atomic percentage remained relatively stable in both cases; for the UV/ozone-oxidised sample it was similar to AlO-termination prepared by the thick-film deposition method, just over 1%, while <1% Al was observed for the ALD-oxidised sample. This was probably due to the poorly oxidised surface in the latter case.

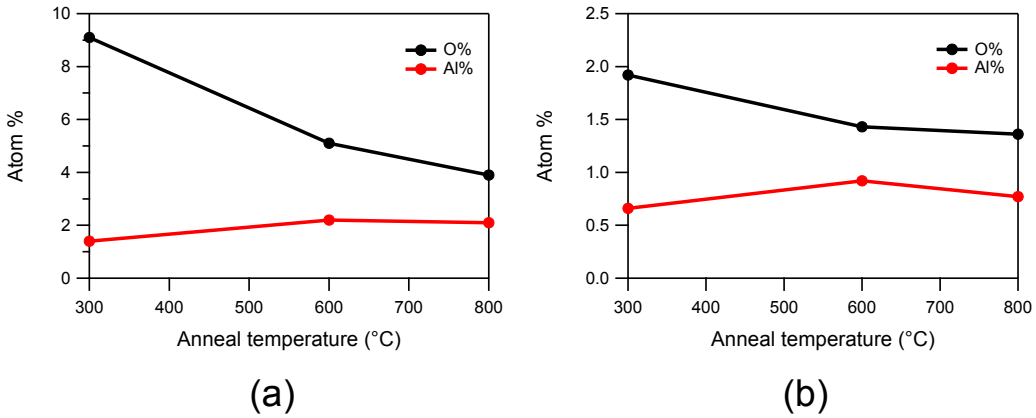

Figure 6.11: Atomic percentages of O and Al at different annealing temperatures for ALD-prepared AlO-terminated (100) diamond, using (a) UV/ozone and (b) ALD oxidation methods.

The work function after the 300 °C anneal was measured for both samples. Figure 6.12 shows that the UV/ozone-oxidised sample had a consistent work function of ~4.5 eV across the surface. The ALD-oxidised sample had a lower work function of ~4.0 eV with some striations across the surface where the work function was slightly lower at ~3.9 eV. The origin of these striations was unclear.

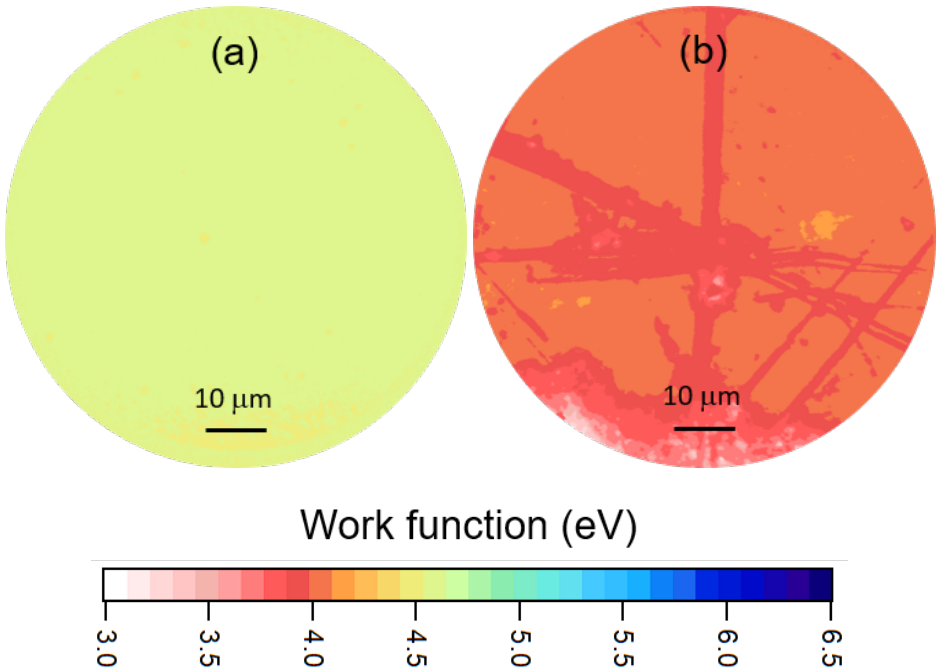

Figure 6.12: Colour-coded work function maps acquired after a 300 °C anneal for AlO-terminated (100) diamond prepared by the ALD procedure, using (a) UV/ozone and (b) ALD oxidation methods.

Figure 6.13 shows UPS spectra of these two samples after the 300 °C anneal. The UV/ozone-oxidised sample had a very small NEA of -0.1 eV. The ALD-oxidised sample had a much larger NEA of -0.9 eV. The secondary electron peak had a larger intensity for this sample and there was an additional secondary electron peak from the NEA, similar to that observed for H-termination (Chapter 5.6).

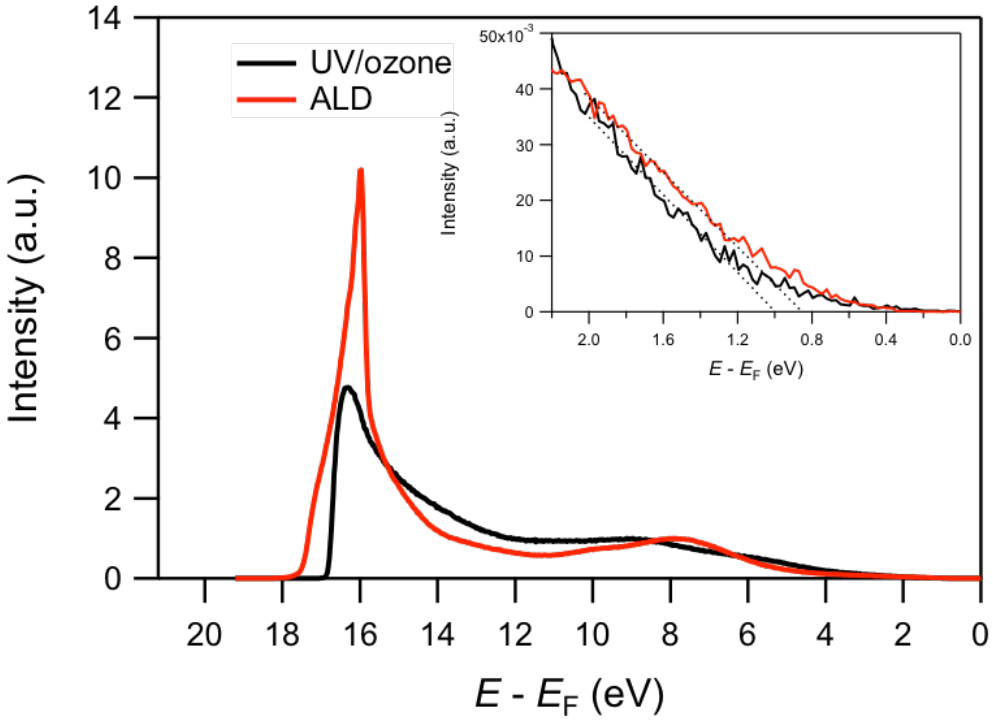

Figure 6.13: UPS spectra acquired after a 300 °C anneal for AlO-terminated (100) single-crystal diamond prepared by the ALD procedure, using UV/ozone or ALD as the oxidation method. Inset shows a magnified view of the VBM energy relative to Fermi energy.

6.4.2 Analysis of the (100) and (111) Surfaces

A (100) and a (111) single-crystal diamond sample were subsequently AlO-terminated by using ALD for oxidation and Al deposition, as this oxidation technique showed the more negative NEA. As the initial test indicated that the surface was poorly oxidised, the oxidation conditions were changed; for these samples two pulses of H_2O were introduced into the chamber for a total of 5 min.

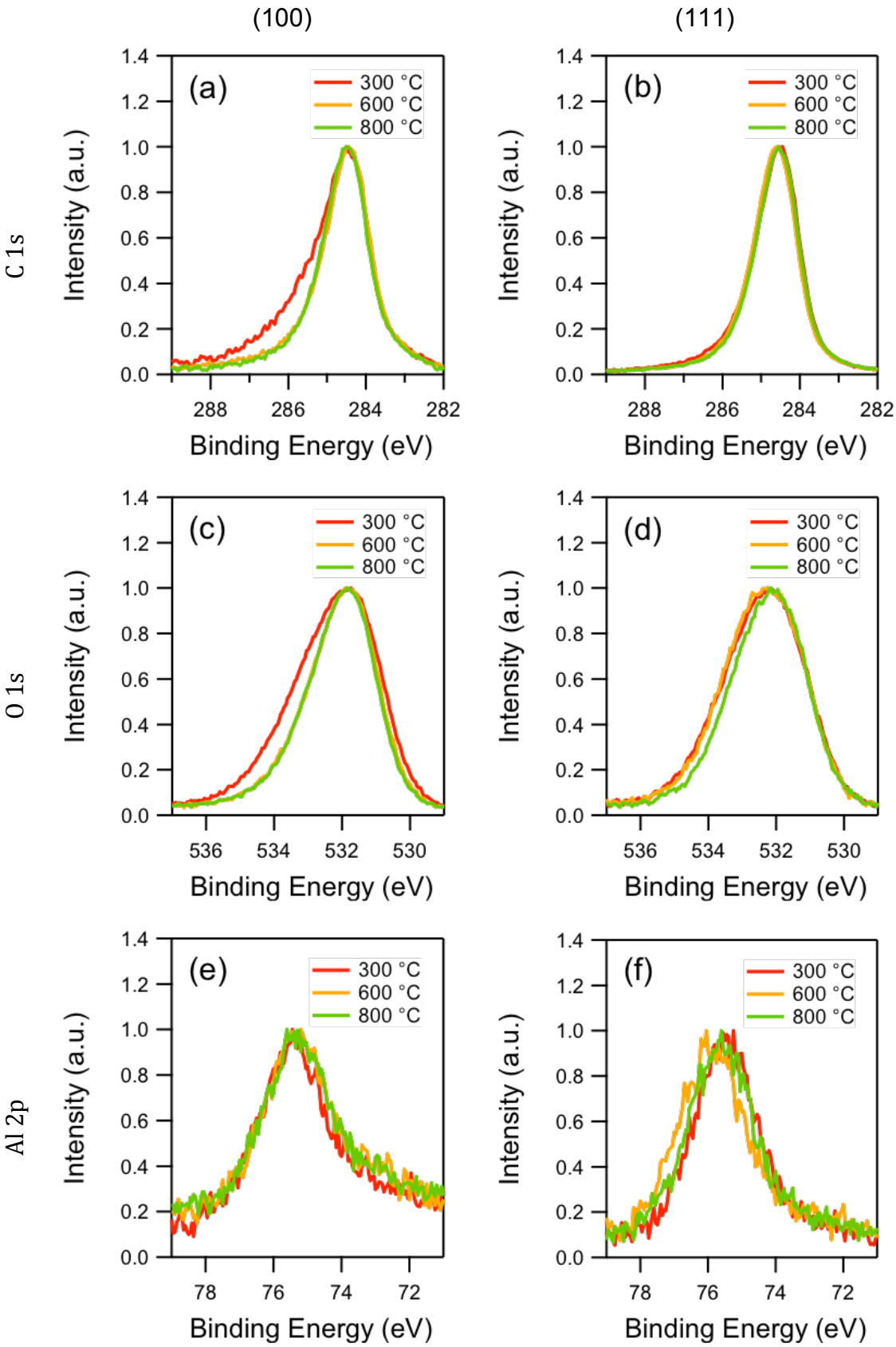

Figure 6.14: XPS spectra of (a)–(b) C 1s, (c)–(d) O 1s, and (e)–(f) Al 2p peaks at different annealing temperatures for ALD-prepared AlO-terminated diamond. (a), (c), (e) are from the (100) surface, and (b), (d), (f) are from the (111) surface.

Figure 6.14 shows the normalised XPS spectra for the C 1s, O 1s and Al 2p peaks at different annealing temperatures. The peak shapes and positions did not appear to change significantly with temperature, with the exception of a relative decrease in C-O and C=O components of the C 1s peak for the (100) sample between 300 °C and 600 °C, suggesting that some oxygen had either desorbed or moved into the Al layer. This was accompanied by an increase in the low binding energy component of the O 1s peak. The Al 2p peak was centred at a slightly higher binding energy than expected for both (100) and (111) samples (~75.5 eV), suggesting that it was more highly oxidised than in previous experiments.

Figure 6.15 shows the relative atomic percentages of O and Al for the two samples at different annealing temperatures. The (100) sample did not produce the same deposition behaviour as the initial sample prepared by ALD. Instead, the Al and O atomic percentages were much higher than previously, suggesting that aluminium oxide had been deposited onto the diamond surface, in a manner similar to that used for field effect transistor device fabrication.[12] The (111) sample, meanwhile, had a relatively high O content (15.0%) at 300 °C, decreasing to 7.8% by 600 °C. The corresponding Al coverage remained consistent across the temperature range at ~4%.

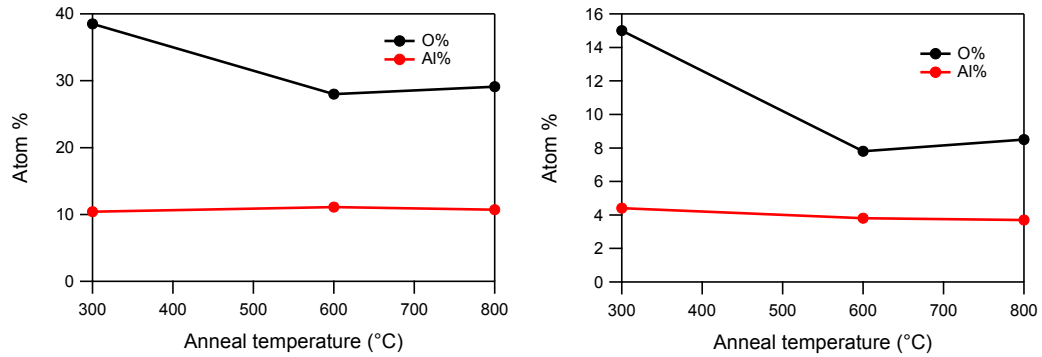

Figure 6.15: Atomic percentages of O and Al at different annealing temperatures for (a) (100) and (b) (111) surfaces.

The electronic structure for the (100) surface is not shown due to unfavourable surface termination determined from XPS. Work function maps acquired at each annealing temperature for the (111) sample are shown in

Figure 6.16. The work function was 3.8 eV after the 300 °C anneal, increasing to 4.1 eV after the 600 °C anneal. After the 800 °C anneal, the work function across most of the surface then increased to 4.6 eV, but small regions showed a work function as low as 4.0 eV.

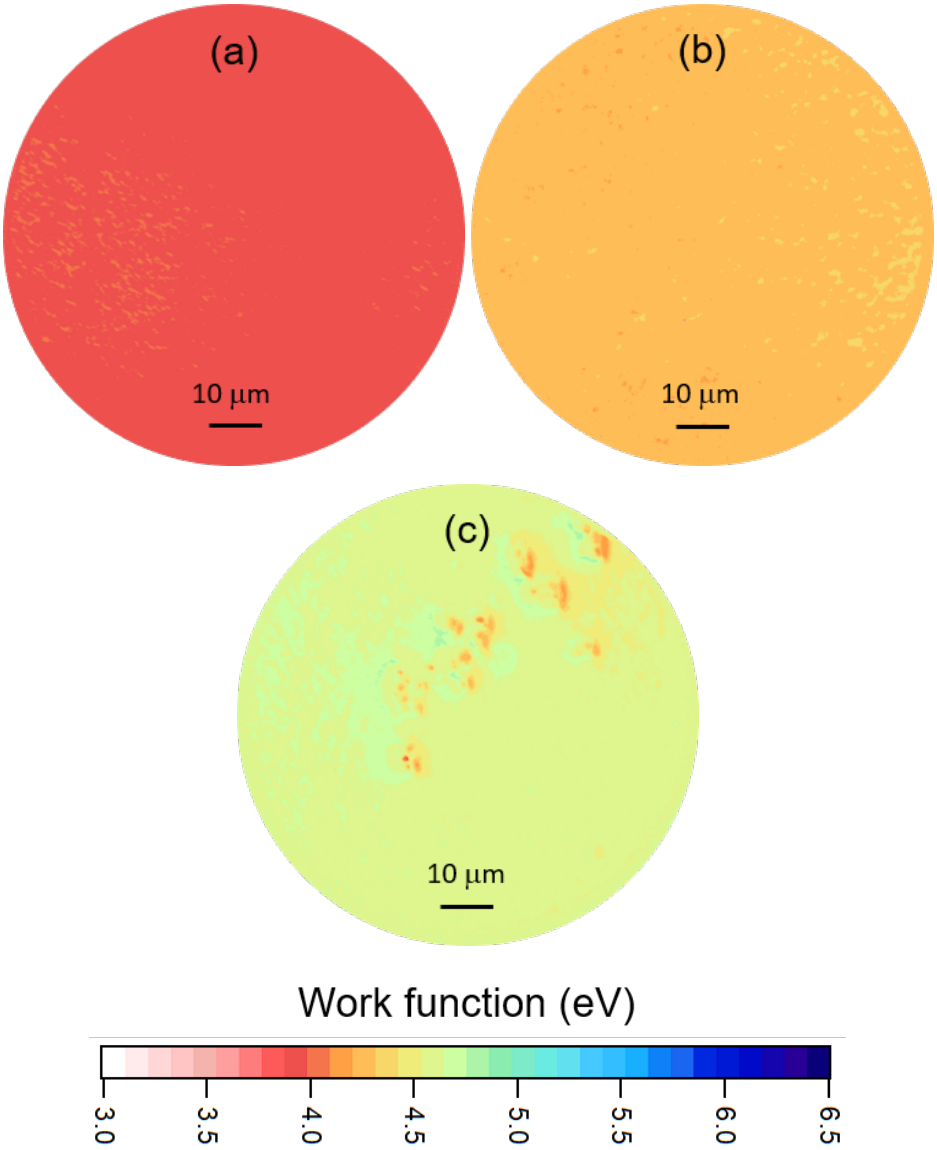

Figure 6.16: (a)–(c) Colour-coded work function maps of AlO-terminated (111) diamond prepared with the ALD procedure, after annealing at 300 °C, 600 °C and 800 °C, respectively.

Figure 6.17 shows UPS spectra for the (111) sample at each annealing temperature. The highest secondary emission peak was observed after the 300 °C anneal. The EAs were calculated to be -0.8 eV after the 300 °C

anneal, -0.7 eV after the 600 °C anneal, and between -0.5 eV and -0.1 eV after the 800 °C anneal.

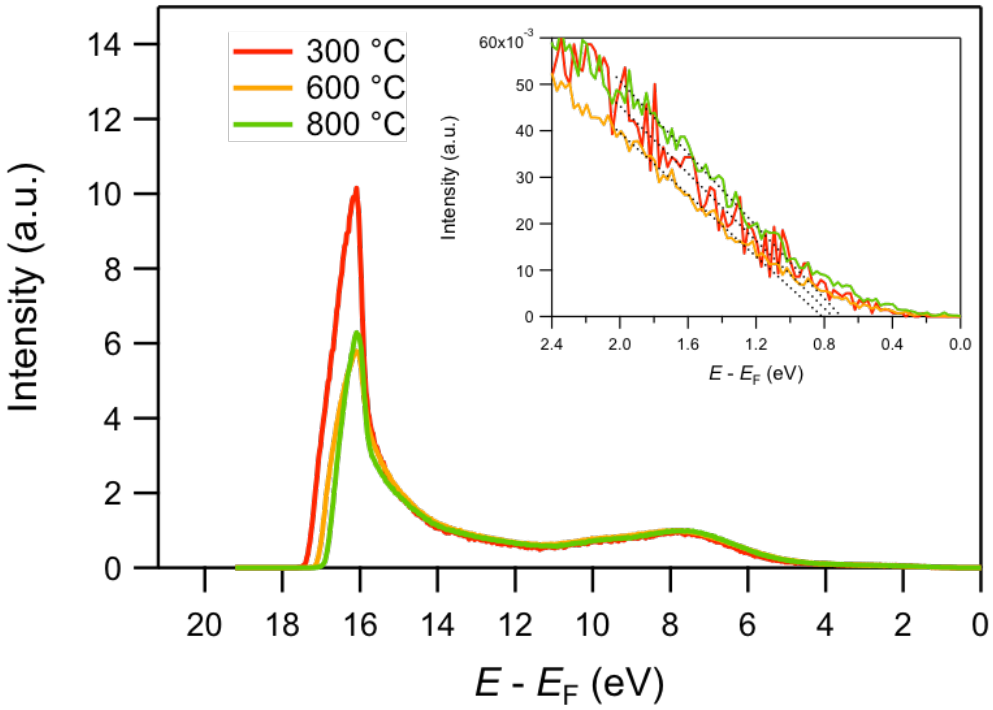

Figure 6.17: UPS spectra of AlO-terminated (111) diamond prepared with the ALD procedure. Inset shows a magnified view of the VBM energy relative to Fermi energy.

6.5 Thin-Film Deposition by Electron-Beam Evaporation

6.5.1 Calibration of Al Evaporation

While using ALD for the deposition of Al showed some promising results, there was no controllability or consistency in the amount of O or Al on the surface. This was not expected to be an issue for the electron-beam evaporation technique.

To calibrate 1 ML Al deposition onto diamond, it was assumed that the deposition of 2.34 Å Al would be equal to 1 ML as this is the distance between the (111) planes of bulk Al. This was checked against the Al atomic percentage using Al-terminated (100) and (111) single-crystal diamond samples. These samples were first heated to 950 °C for 10 min in UHV and XPS confirmed that after this procedure only carbon was present. Al was then deposited onto these samples, without breaking vacuum. After deposition of 1 ML of Al, the relative atomic percentages of Al were measured by XPS to be 6.3% and 6.5% for the (100) and

(111) surfaces, respectively. This was in excellent agreement with the expected value for 1 ML of oxygen on diamond (Chapter 5.4).

6.5.2 Analysis of the (100) and (111) Surfaces

AlO-terminations were prepared by deposition of 0.25 ML Al (0.59 Å) onto O-terminated (100) and (111) single-crystal diamond samples. This was followed by annealing at 300 °C for 1 h.

Normalised XPS spectra for the C 1s, O 1s and Al 2p peaks are shown in Figure 6.18. In both cases the Al 2p peak was centred at ~74.5 eV, indicating that Al was oxidised. For the (100) sample, as previously observed, there was a large increase of a low binding energy component peak in the O 1s spectrum (Figure 6.18(c)), attributed to Al-O bonding. In this case, there was not an associated decrease in the C-O and C=O components of the C 1s peak. There was, however, a shift of the Al 2p peak to slightly higher binding energy after the 600 °C anneal, suggesting that, here, oxygen remained bonded to carbon, and bonded more strongly with Al. Each peak for the (111) sample, meanwhile, showed little change with successive annealing steps.

Figure 6.19 shows the relative atomic percentages of O and Al immediately after Al deposition and after annealing at successive temperatures. There is a notable decrease in O atomic percentage for both (100) and (111) surfaces after each annealing step. It is unclear why the O desorbed so readily for these samples, but did not do so in previous instances. The Al atomic percentage, meanwhile, remained relatively constant in both cases, ~1.0–1.4% for the (100) surfaces, and ~2.0–2.2% for the (111) surface.

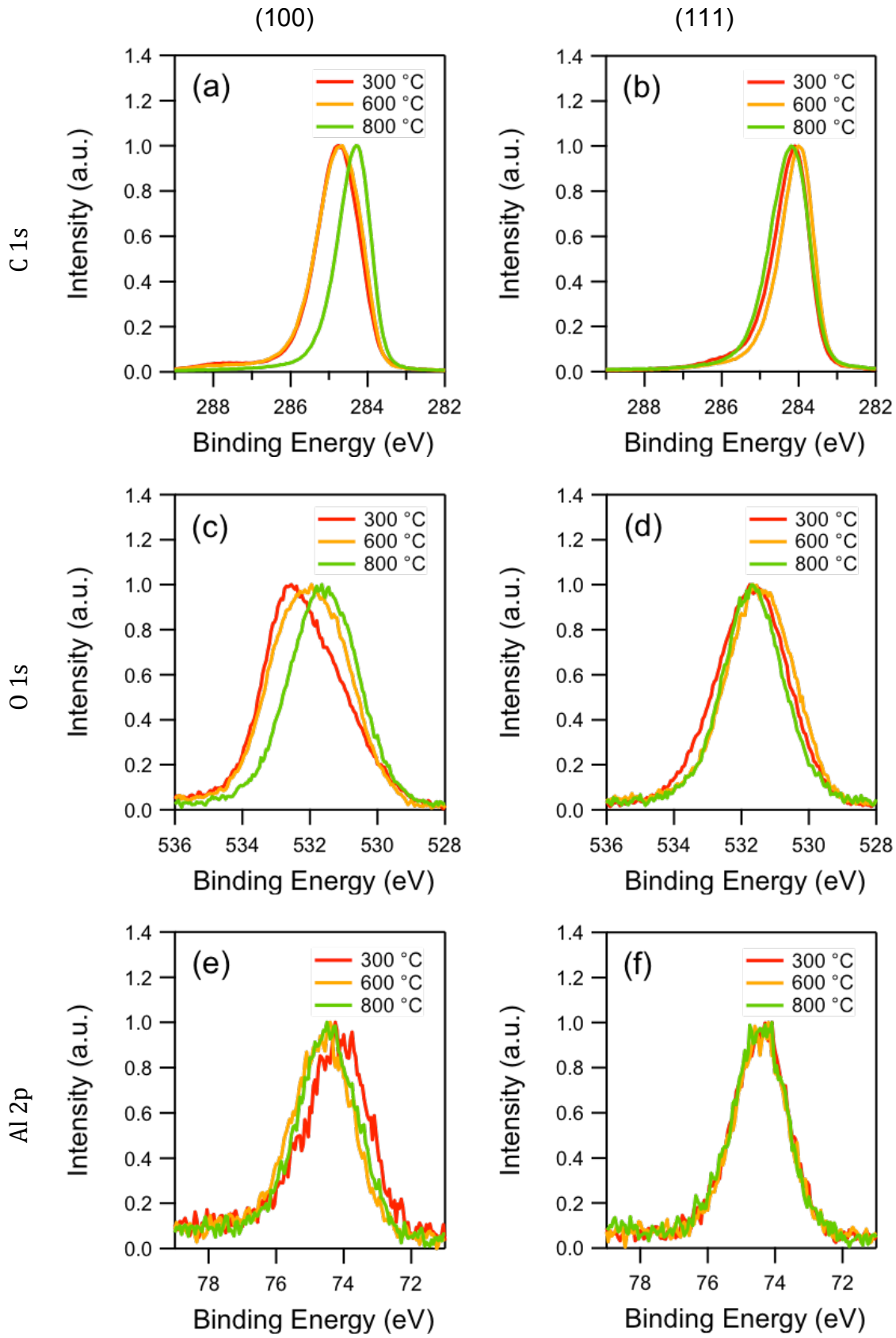

Figure 6.18: XPS spectra of (a)–(b) C 1s, (c)–(d) O 1s, and (e)–(f) Al 2p peaks at different annealing temperatures for AlO-terminated diamond prepared by electron-beam evaporation. (a), (c), (e) are from the (100) surface, and (b), (d), (f) are from the (111) surface.

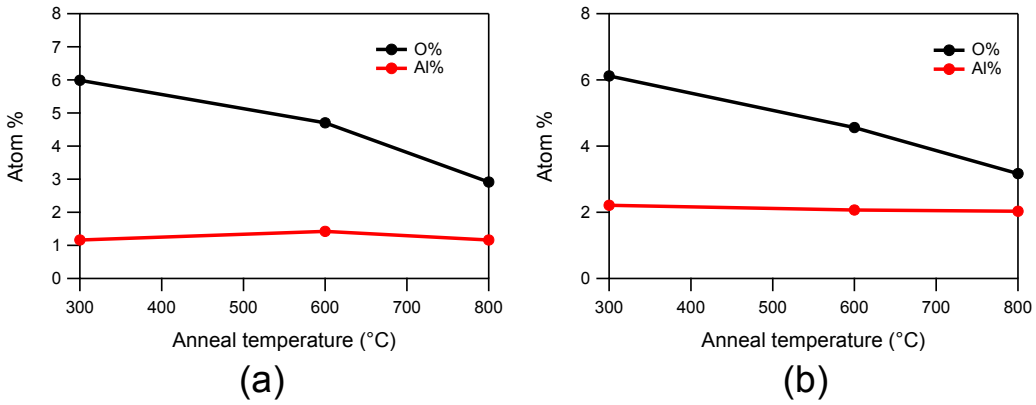

Figure 6.19: Atomic percentages of O and Al for AlO-terminated (a) (100) and (b) (111) diamond prepared by electron-beam evaporation.

Work function maps of these surfaces at different annealing temperatures are shown in Figure 6.20. Starting with the (100) surface, the work function varied between 4.0–4.8 eV after the 300 °C anneal, between 3.1–4.1 eV after the 600 °C anneal, and between 4.3–5.0 eV after the 800 °C anneal. The (111) surface varied between 4.1–5.2 eV after the 300 °C anneal, between 4.1–4.7 eV after the 600 °C anneal, and between 4.1–5.0 eV after the 800 °C anneal. In both cases, there was a gradual increase in work function around a central point. This suggested that the Al coverage was not uniform, and could have originated either from uneven deposition of Al during the electron-beam evaporation step, or from the deposited layers of Al being weakly-bound to the surface, causing agglomeration after annealing.

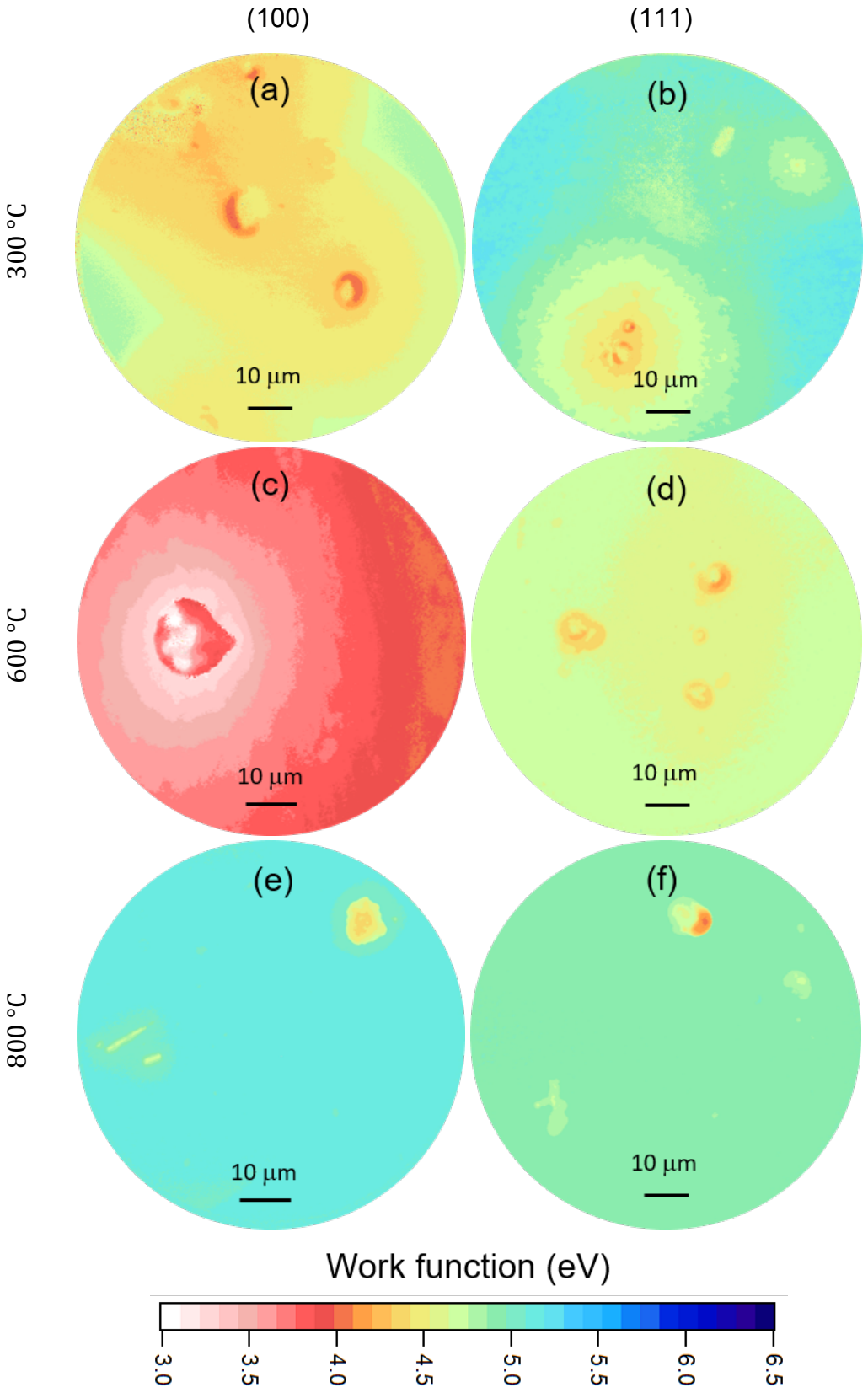

Figure 6.20: Colour-coded work function maps of AlO-terminated diamond prepared by electron-beam evaporation, at annealing temperatures of (a)–(b) 300 °C, (c)–(d) 600 °C and (e)–(f) 800 °C. (a), (c) and (e) are for the (100) surface and (b), (d) and (f) are for the (111) surface.

Figure 6.21 shows UPS spectra for the two surfaces at the different annealing temperatures. The (100) surface showed a relatively small secondary emission peak after the 300 °C anneal, increasing in height with successive annealing steps. After the 600 °C anneal the spectrum showed a broad multi-component secondary emission peak, and the Fermi level was close to the VBM position. The (111) surface showed no variation of secondary electron emission peak height. For the (100) surface EAs were calculated to be between -0.1 eV and 0.7 eV after the 300 °C anneal, between -2.3 eV and -1.3 eV after the 600 °C anneal, and between -0.3 eV and 0.4 eV after the 800 °C anneal. For the (111) surface EAs were calculated to be between -0.4 eV and 0.7 eV after the 300 °C anneal, between -0.7 eV and -0.1 eV after the 600 °C anneal, and between -0.8 eV and 0.1 eV after the 800 °C anneal.

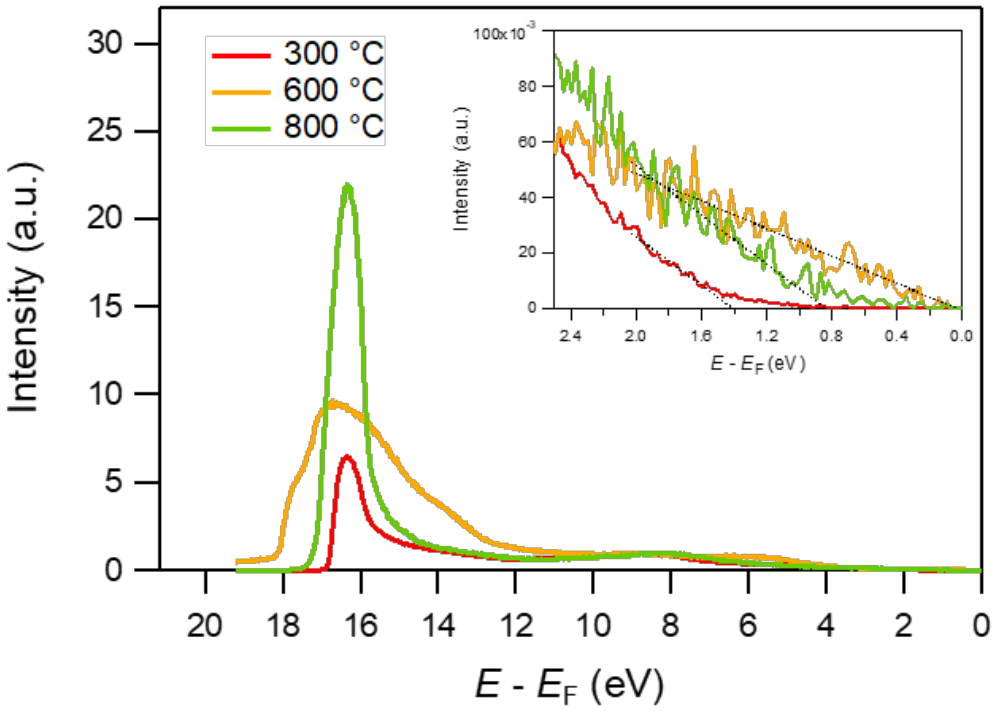

(a)

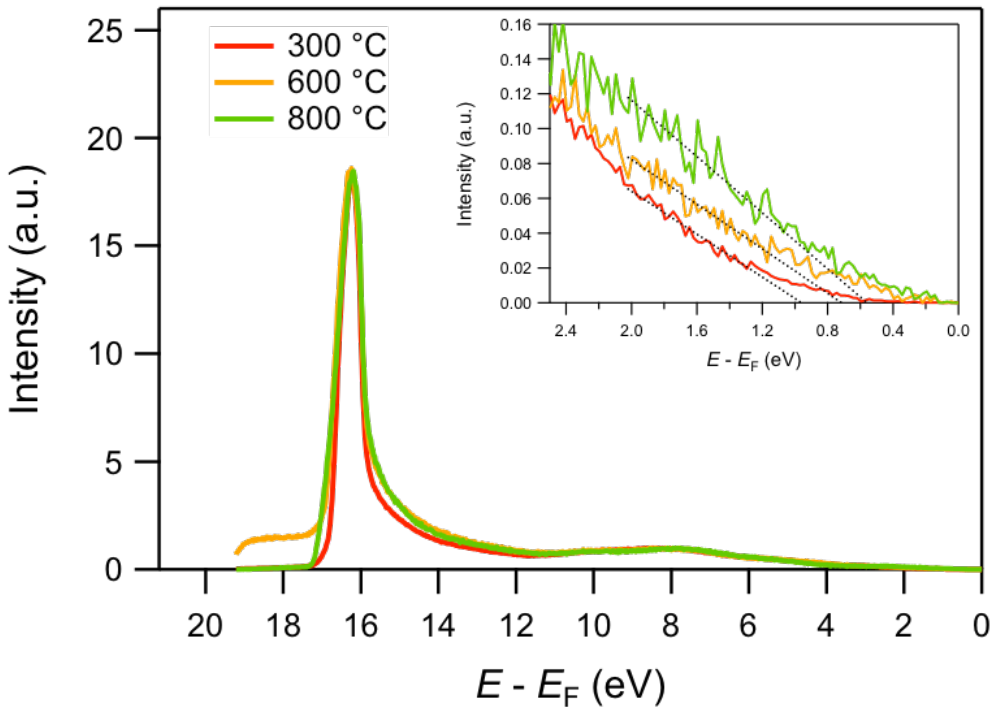

(b)

Figure 6.21: UPS spectra of AlO-terminated (a) (100) and (b) (111) diamond prepared by electron-beam evaporation. Inset shows a magnified view of the VBM energy relative to Fermi energy.

Low energy electron diffraction (LEED) was also performed on these samples to determine whether any surface ordering had occurred. Shown in Figure 6.22, these were acquired after the 800 °C anneal. The (100) surface showed a (2 × 1) LEED pattern, as predicted by computational experiments. The (111) surface showed a (1 × 1) LEED pattern. Either the surface had not changed from an O-terminated surface (suggesting a weak Al-O interaction), or the surface structure had changed to lose the Pandey-chain reconstruction. The latter case was anticipated from computational calculations, as it was the most stable predicted structure.

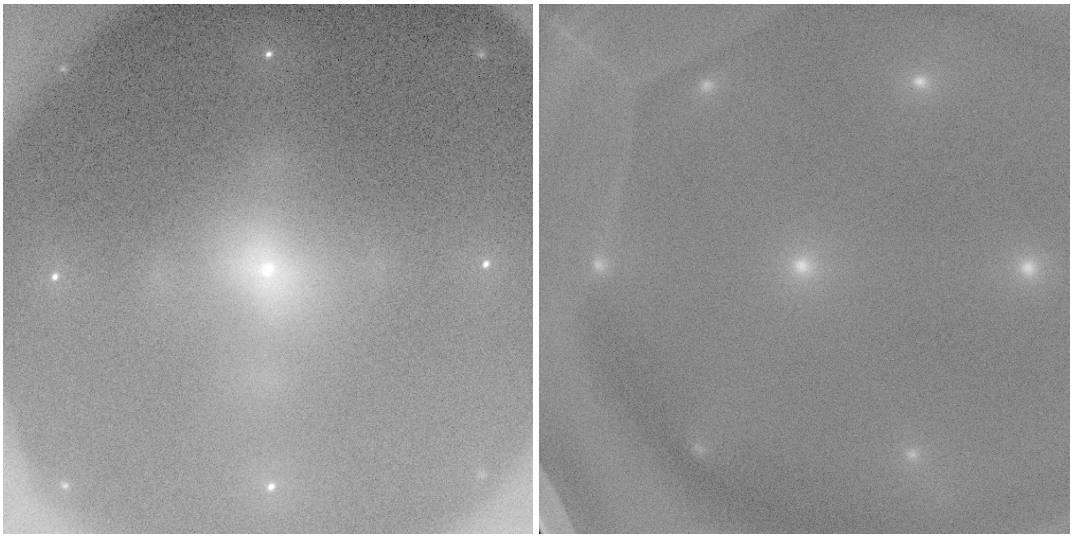

Figure 6.22: LEED patterns for AlO-terminated (a) (100) and (b) (111) diamond. The electron beam energy was 170 eV for both.

6.6 Thermionic Emission Tests

6.6.1 Diamond Characterisation

Figure 6.23 shows a typical Raman spectrum for an NDD film after growth. The diamond peak is centred at 1339 cm^{-1}, a result of strain from growth on the Mo substrate. For these samples there was significant graphitic sp^2 carbon content, observed as a broad G-band peak at ~1580 cm^{-1}. There was an additional peak at 1133 cm^{-1}, which is attributed to *trans*-polyacetylene, and is commonly observed in nanocrystalline diamond films.[13] From the SEM image in Figure 6.24, it can be seen that the NDD is nanocrystalline.

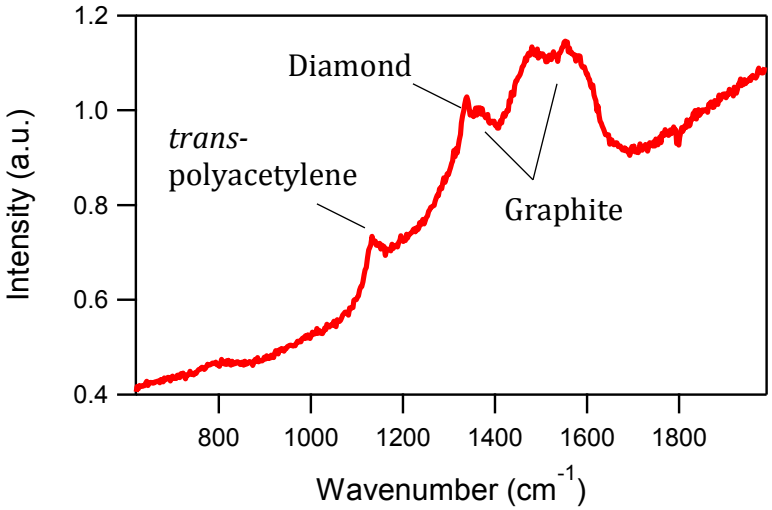

Figure 6.23: Raman spectrum of an NDD thin film on a Mo substrate.

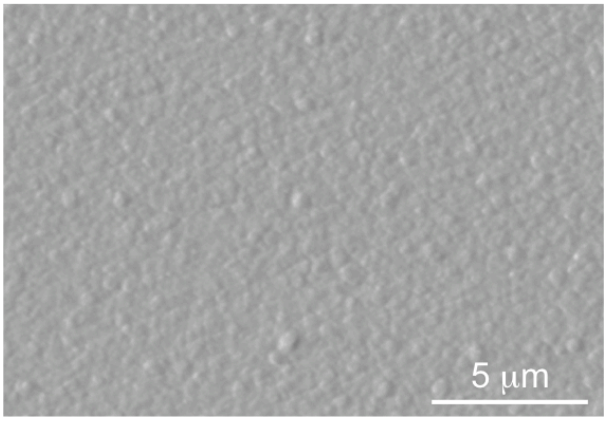

Figure 6.24: SEM image of an NDD thin film.

6.6.2 H-Termination

Figure 6.25 shows the change in emission current density with temperature for an H-terminated NDD thin film. Values of work function and Richardson constant were calculated using Equation 3.5 in Chapter 3 and a model containing these parameters was also plotted. A value of 1.59 eV was obtained for the work function, ϕ, and 0.02 A cm^{-2} K^{-2} for the Richardson constant, A. The work function is similar to previously reported values for thermionic emission from polycrystalline NDD.[14,15] The deviation of thermionic current density from the model at ~700 °C due to the hydrogen desorption is evident.

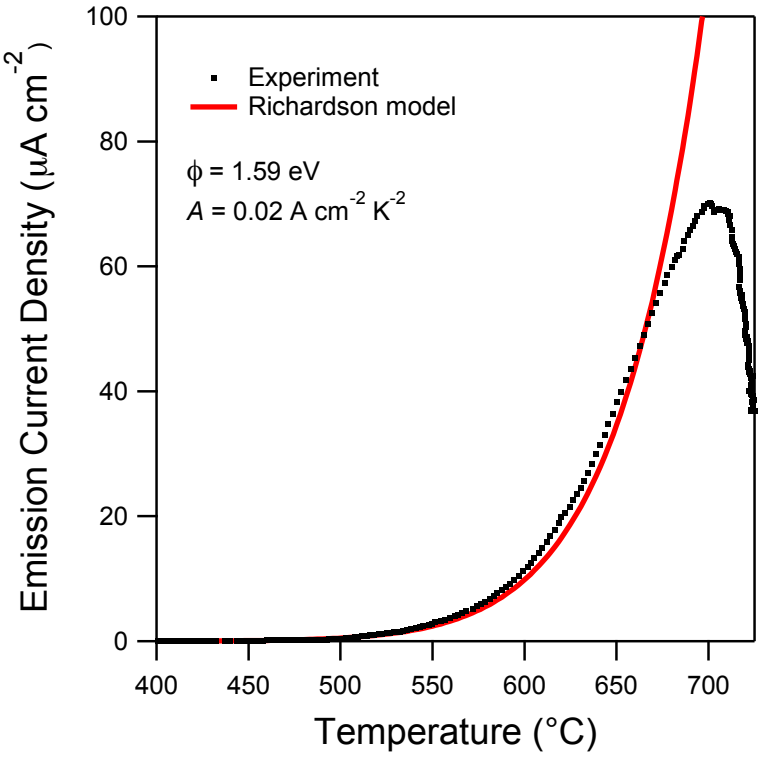

Figure 6.25: Change in thermionic emission current with temperature from an H-terminated NDD thin film.

6.6.3 AlO-Terminations

Thermionic experiments were performed on AlO-terminated NDD prepared using each of the three Al deposition methods. The sample prepared by ALD used ALD for oxidation (two pulses H_2O and residence of 5 min), and the sample prepared by electron-beam evaporation had 0.25 ML Al deposited. All samples were annealed at 300 °C for 1 h after Al deposition before removal from vacuum.

Figure 6.26 shows normalised XPS spectra of the C 1s, O 1s and Al 2p peaks for each sample. Due to the high resistivity of NDD there was a slight charging of ~1 eV that was corrected for by aligning the C 1s peak to 284.3 eV. The thick-film-prepared sample had a notably large C=O component of the C 1s peak. The O 1s and Al 2p peaks were largely similar in shape, and for all three, the Al 2p peak appeared to show entirely oxidised Al.

The atomic percentages for Al and O for each sample are given in Table 6.2. The larger surface area would be expected to increase the atomic percentage of surface species compared to the polished single-crystal samples. This is indeed observed, with exception of the Al atomic percentage for the thick-film-prepared

sample, which is similar to the amount found on single-crystal samples. There is a slight variation of O and Al between the different methods.

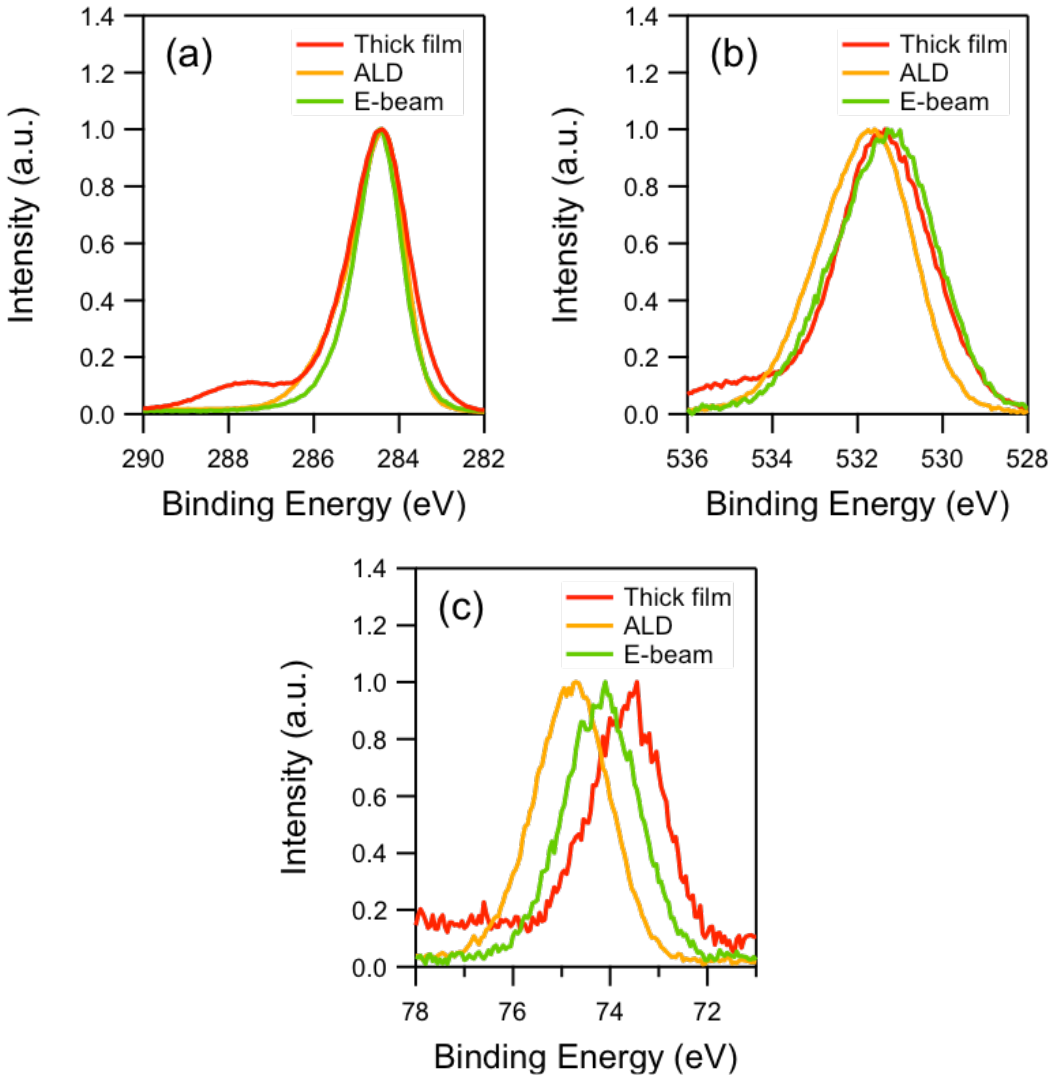

Figure 6.26: XPS spectra of the (a) C 1s, (b) O 1s, and (c) Al 2p peaks for AlO-terminated NDD thin films prepared using thick-film, ALD and electron-beam evaporation procedures.

Table 6.2: Atomic percentages of O and Al for AlO-terminated NDD prepared by different Al deposition methods.

Sample	O at. %	Al at. %
Thick film	15.3	1.3
ALD	8.6	3.8
Electron-beam evaporation	10.8	4.6

Figure 6.27 shows the change in thermionic emission current with temperature for each Al deposition procedure. No thermionic emission was detected for the ALD-prepared sample. A small emission current density of between ~0.3–0.5 μA cm^{-2} was observed between 800–900 °C for the thick-film sample and the sample prepared by electron-beam evaporation. Whilst this was at a higher temperature than for the H-terminated sample, the maximum emission current density observed was two orders of magnitude smaller. The thick-film prepared sample showed the expected exponential increase in emission current density with temperature, but the e-beam sample showed a steady emission current across the temperature range that emission was observed.

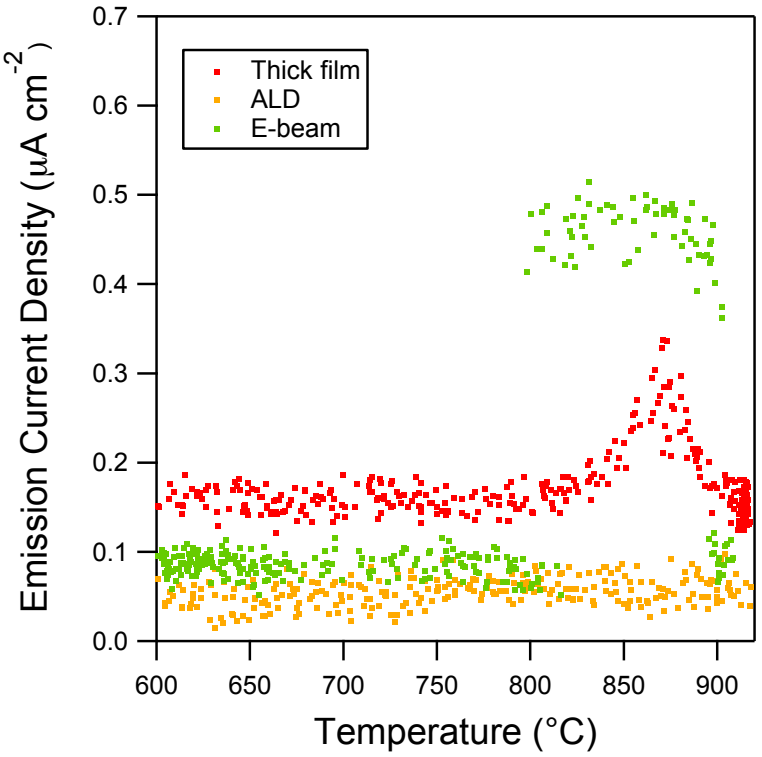

Figure 6.27: Change in thermionic emission current with temperature for AlO-terminated NDD thin films.

6.7 Conclusions

Three different methods were used to deposit Al onto O-terminated diamond, with the intention of producing a thermally-stable surface with low work function and NEA. The deposition of Al did reduce the work function and EA compared to O-terminated diamond, and NEA was observed. In some instances

the work function and EA were even lower than that observed for H-terminated diamond.

However, for each deposition method the work function and EA varied significantly with increasing annealing temperature. This is likely resulting from change of the atomic structure of the surface. XPS results showed that this was not simply due to Al desorption from the surface; in fact, for each deposition procedure a consistent amount of Al remained on the surface up to 800 °C. Instead, the biggest change was observed in the amount and the bonding environment of the oxygen. For the thin-film-prepared samples, at higher temperatures some of the oxygen (as much as half of the O atomic percentage) was lost. This was unexpected, since O-terminated diamond is usually stable to ~900 °C.[16,17] The thick-film-prepared samples did not suffer this issue. Additionally, in many cases, the oxygen-bonding environment changed, as shown by an increase of an Al-O component in the O 1s peak. There were two associated changes that occurred to varying degrees. The first was a shift of the Al 2p peak to a higher binding energy, suggesting stronger Al-O bonds had formed. The second was a decrease of C-O and C=O components in the C 1s peak. This was less desirable as it indicated that the Al atoms had broken both carbon-oxygen bonds and abstracted the O atoms into the Al layer. This behaviour was observed in the computational work for 1 ML Al adsorption to the ether O-terminated (111) surface, and is described in Chapter 4.4.3.

One notable distinction between different preparation methods was the variance of work function spatially, as shown by the work function maps. Both the thick-film and ALD deposition methods produced a relatively uniform work function in all instances. The electron-beam evaporation method showed a much higher spatial variation in work function, which was attributed to uneven distribution of Al on the surface, either from the deposition itself or from agglomeration upon annealing.

Thermionic emission experiments showed a lower emission current from the AlO-terminated surfaces compared to that from H-termination. Nevertheless, emission occurred at a temperature higher than that obtainable for H-terminated diamond. This is encouraging for future investigations using other metal-oxygen

NEA surface terminations. The lack of significant thermionic emission here may be caused by a few different reasons:

(i) The threshold for emission from the H-terminated sample was ~450 °C, but the corresponding value for AlO-terminated diamond would likely be even higher, since there was generally a larger work function and smaller NEA. This would prevent any emission at lower temperatures.

(ii) While low work functions and NEAs were obtained, these were not consistent across the entire surface, and often were restricted to small areas. As such, the surrounding PEA would not contribute to emission. This results in a small emission-current density.

(iii) There could be a significant recombination pathway that exists for electrons to lose energy before they can be thermionically emitted. Density-of-states calculations suggest that this is not the case for surface terminations consisting of 0.25 ML Al evenly spread on O-terminated diamond, however this may be the case for a non-ideal surface.

These issues can be overcome in the future; further optimisation of these surface termination could enable a more homogeneously terminated surface, giving a widespread NEA and eliminating potential loss mechanisms. Other metal-oxygen terminations of diamond using group I and II metals[1,3] have also shown large NEAs, and could be further optimised in future. These metals are arguably the most promising for thermionic applications since they benefit from being much more electropositive than Al, while also demonstrating stability at thermionic temperatures. They also have weak metal-metal bonds, thus favouring ionic bonding to the diamond surface. This would reduce recombination pathways for electrons, a potential factor for hindering electron emission here.

References

1 K. M. O'Donnell, T. L. Martin, M. T. Edmonds, A. Tadich, L. Thomsen, J. Ristein, C. I. Pakes, N. A. Fox and L. Ley, *Phys. Status Solidi*, 2014, **211**, 2209–2222.

2 M. Z. Othman, *Studies of n-type Doping and Surface Modification of CVD Diamond for use in Thermionic Applications*, PhD Thesis, University of Bristol, 2014.

3 K. M. O'Donnell, M. T. Edmonds, A. Tadich, L. Thomsen, A. Stacey, A.

Schenk, C. I. Pakes and L. Ley, *Phys. Rev. B*, 2015, **92**, 035303.
4 T. Sun, *Combined Photo- and Thermionic Electron Emission from Low Work Function Diamond Films*, PhD Thesis, Arizona State University, 2013.
5 A. Schenk, A. Tadich, M. Sear, K. M. O'Donnell, L. Ley, A. Stacey and C. Pakes, *Appl. Phys. Lett.*, 2015, **106**, 191603.
6 M. J. Sear, A. K. Schenk, A. Tadich, B. J. Spencer, C. A. Wright, A. Stacey and C. I. Pakes, *J. Phys. Condens. Matter*, 2017, **29**, 145002.
7 D. S. Knight, R. Weimer, L. Pilione and W. B. White, *Appl. Phys. Lett.*, 1990, **56**, 1320–1322.
8 M. Bernard, C. Baron and A. Deneuville, *Diam. Relat. Mater.*, 2004, **13**, 896–899.
9 J. F. Moulder, W. F. Stickle, P. E. Sobol and K. D. Bomben, *Handbook of X-ray Photoelectron Spectroscopy*, Perkin-Elmer, Eden Prairie, MN, USA, 1992.
10 G. Wan, M. Cattelan and N. A. Fox, *J. Phys. Chem. C*, 2019, **123**, 4168–4177.
11 F. Maier, J. Ristein and L. Ley, *Phys. Rev. B*, 2001, **64**, 165411.
12 Y. Yang, F. A. Koeck, M. Dutta, X. Wang, S. Chowdhury and R. J. Nemanich, *J. Appl. Phys.*, 2017, **122**, 155304.
13 H. Kuzmany, R. Pfeiffer, N. Salk and B. Günther, *Carbon*, 2004, **42**, 911–917.
14 F. A. M. Koeck and R. J. Nemanich, *J. Appl. Phys.*, 2012, **112**, 113707.
15 F. A. M. Koeck and R. J. Nemanich, *Diam. Relat. Mater.*, 2006, **15**, 217–220.
16 P. K. Baumann and R. J. Nemanich, *Surf. Sci.*, 1998, **409**, 320–335.
17 K. P. Loh, X. N. Xie, S. W. Yang and J. C. Zheng, *J. Phys. Chem. B*, 2002, **106**, 5230–5240.

Chapter 7 – Thesis Summary

7.1 Summary

This thesis has reported the theoretical modelling and experimental deposition of Al onto diamond for the purposes of creating a thermally stable surface with low work function and negative electron affinity (NEA), thus capable of high-temperature electron emission. The (100) and (111) diamond surfaces were examined throughout this thesis as these are the two most prevalent surfaces for diamond.

7.1.1 Computational Modelling

Initially, computational modelling was performed using the CASTEP density functional theory code on the University of Bristol's BlueCrystal supercomputer. The structures and energies from Al deposition onto the bare, oxygenated and nitrogenated diamond surfaces were investigated at 0.25, 0.5 and 1 monolayer (ML) coverages. The key computational results are summarised in Table 7.1, which lists the largest adsorption energies and associated electron affinities for the Al coverages that showed NEA for each surface termination.

Results for adsorption onto the bare (100) surface suggested that Al adsorption sites can be categorised as having more covalent or more ionic character. In covalent sites, Al was two-coordinate to surface C atoms and had a smaller Mulliken charge, and the corresponding Al-C bond was smaller and had a higher Mulliken bond population than for the four-coordinate ionic sites. Similar behaviour was observed for Al adsorption onto the bare (1 × 1) (111) surface. The Al adsorption energy for Al-terminations at 1 ML Al coverage were comparable to that of H-termination but the NEA was less negative.

Al adsorption onto the oxygenated diamond surface showed more promising properties. On both (100) and (111) diamond the adsorption energy of Al was greatest at 0.25 ML coverage, significantly higher than that of H-termination, and decreased with increasing coverage, which is desirable for avoiding island formation of Al on the surface. At these low coverages Al exhibited highly ionic behaviour with the surface: Al had a high coordination number to O (4 for the

(100) surface and 3 for the (111) surface), a high Mulliken charge, and a large density-of-states (DOS) above the Fermi energy (indicating charge transfer had occurred). At higher coverages of Al (0.5 and 1 ML) the AlO-terminated surface was calculated to have a positive electron affinity (PEA) in many Al sites; this correlated with lower Mulliken charge, appearance of an Al-Al Mulliken bond population, and a lowering in energy of the Al DOS, thus suggesting that Al exhibited more metallic behaviour. A larger supercell for the (100) O-terminated surface indicated that there was a PEA at 0.125 ML Al coverage and, generally, an NEA at 0.375 ML Al coverage.

For Al adsorption to the (100) O-terminated surface, at all coverages Al adsorbed well to the ketone surface but poorly to the ether surface, indicating that Al could break the π-bond of the ketone with greater ease than the σ-bond of the ether. For the (111) surface, Al adsorbed to both ether and ketone surfaces, but 1 ML Al coverage on the ether surface caused both C-O bonds to break and O was abstracted into the Al layer.

Al addition to the nitrogenated diamond surfaces was not as promising. Al adsorption to the (100) surface gave a lower adsorption energy than to the oxygenated surface, and the electron affinity was generally positive. Al did not bond with the nitrogenated (111) surface.

Table 7.1: Summary of key computational results from this thesis.

Termination	Surface	Coverage (ML)	Adsorption Energy (eV/atom)	Electron Affinity (eV)
Al	(100)	1	-4.11	-1.47
Al	(111)	1	-4.19	-1.01
AlO	(100)	0.25	-6.36	-0.37
AlO	(111)	0.25	-8.19	-1.19
AlN	(100)	0.25	-4.32	-0.47

7.1.2 Oxygenation Studies

As the computational study of Al addition to O-terminated diamond exhibited the most promising characteristics for forming a thermally stable NEA surface termination, an experimental investigation was conducted into different O-termination methods. For NEA studies, maximising ketone coverage was most

desirable. Three oxidation methods were investigated: UV/ozone treatment, oxygen plasma, and acid washing in H_2SO_4 and HNO_3. The effect of oxidation time was first investigated, and the time to form 1 ML coverage was determined by observing the change in contact angle of a water droplet on the surface.

Subsequently, X-ray photoelectron spectroscopy (XPS) was used to analyse the different types of oxygen bonding. This was done by analysis of the C 1s peak in XPS, which contains component peaks corresponding to C-O and C=O bonds. A C-O/C=O ratio was thus obtained. In this study, the O 1s peak was also considered, in order to gain more insight into the surface bonding. In the literature, there is disagreement about assignment of the O 1s peak, and it has been fitted with two or three components. The (100) surface showed good agreement in the C-O/C=O ratio between the C 1s and O 1s peaks for a three-component fit of the O 1s peak, corresponding to ether, ketone and hydroxyl bonding environments. There was also a good qualitative agreement with Fourier transform infrared (FTIR) spectroscopy results. The (111) surface showed poorer agreement between C 1s and O 1s peaks, and no peaks observed in FTIR, which is perhaps due to the relatively high surface roughness. The UV/ozone oxidation procedure was determined to produce the largest proportion of ketone component for experimental NEA studies, although ether and hydroxyl components were still present.

Additionally, the surface structure and electronic properties of the hydrogen and oxygen terminations were examined using low energy electron diffraction (LEED), energy-filtered photoemission electron microscopy (EF-PEEM) and ultraviolet photoelectron spectroscopy (UPS). The work function and electron affinity were determined for the (100) and (111) surfaces for comparison with experimentally fabricated AlO-terminated diamond, and the results are displayed in Table 7.2.

Table 7.2: Summary of experimental results from different surface terminations in Chapter 5.

Termination	Surface	Work Function (eV)	Electron Affinity (eV)
H	(100)	3.5	-1.2
	(111)	3.5	-1.0
O	(100)	6.0	1.3
	(111)	5.0 – 5.4	0.5 – 0.9

7.1.3 Experimental NEA Studies

Three methods were used to deposit Al onto diamond: (i) thick-film (>20 nm) deposition of Al, followed by HCl acid wash to remove excess metallic Al, (ii) thin-film deposition of Al by atomic layer deposition (ALD), and (iii) thin-film deposition of Al by electron-beam evaporation. Each technique deposited Al onto O-terminated (100) and (111) diamond, and the surface structure, work function and electron affinity were investigated after annealing at temperatures of 300 °C, 600 °C and 800 °C. The results for each method are displayed in Table 7.3.

Work function maps indicated that the thick-film method gave a relatively uniform work function across the surface. This has been a problem for other metal-oxygen terminations prepared by this method and the uniformity here is attributed to the mild conditions and long reaction time employed during the acid wash step. NEAs were observed up to 800 °C, and there was little change in the O and Al amounts and peak shapes in XPS with increasing annealing temperatures. Using this method, a small thermionic emission current was observed between 800–900 °C for a nitrogen-doped diamond (NDD) sample.

The ALD-prepared samples showed particularly low work function values after the 300 °C anneal, and work function maps from this procedure exhibited the highest degree of uniformity. However, for the (100) surface the low work function was not reproducible, and for the (111) surface the work function increased significantly with temperature. In some cases, there was significant O and Al coverage on the surface, suspected to be from aluminium oxide deposition onto the surface rather than termination of the surface. No thermionic emission from an NDD sample was detected using this method.

The electron-beam evaporation method showed a much larger spatial variance of work function compared to the other two methods, suggesting that deposition was not uniform or there was agglomeration of Al upon annealing. Annealing resulted in a loss of oxygen from the surface and a significant change in work function. Nevertheless, low work functions and NEA were observed, including after high temperature anneals, and an NDD sample terminated with this procedure showed a small thermionic emission current between 800–900 °C.

For each deposition procedure, the main issue with the AlO-termination was determined to be the change in oxygen behaviour rather than desorption of Al. The C-O and C=O component peaks of the C 1s spectra in XPS were often observed to decrease slightly relative to the bulk sp^3 carbon peak, and this was accompanied by an increase of a low binding energy component of the O 1s peak, attributed to increasing Al-O bonding. This indicated that Al could break both C-O bonds and abstract O atoms from the surface. The O content was also often higher than expected for 1 ML coverage, suggesting that Al has been partly oxidised in air. This would be detrimental, since it would form a C-O-Al-O bonding arrangement with an additional dipole at the surface with negative charge outermost. As such, it appears that the propensity for Al to bond with O is, in fact, slightly detrimental for thermionic applications.

Table 7.3: Summary of experimental results from different surface terminations in Chapter 6. *This was the initial sample that was oxidised by ALD.

Al Deposition Method	Surface	Temperature (°C)	Work Function (eV)	Electron Affinity (eV)
Thick-film	(100)	300	4.0 – 4.7	-0.5 – 0.3
		600	3.7 – 4.3	-0.4 – 0.2
		800	4.0 – 4.2	-0.1 – 0.1
Thick-film	(111)	300	4.1	-0.4
		600	4.2 – 4.6	-0.4 – 0.0
		800	4.2 – 4.5	-0.3 – 0.0
ALD*	(100)	300	3.9 – 4.0	-0.9
ALD	(111)	300	3.8	-0.8
		600	4.1	-0.7
		800	4.0 – 4.6	-0.5 – -0.1
E-beam	(100)	300	4.0 – 4.8	-0.1 – 0.7
		600	3.1 – 4.1	-2.3 – -1.3
		800	4.3 – 5.0	-0.3 – 0.4
E-beam	(111)	300	4.1 – 5.2	-0.4 – 0.7
		600	4.1 – 4.7	-0.7 – -0.1
		800	4.1 – 5.0	-0.8 – 0.1

7.2 Future Work

There are a number of different avenues that can be explored for future work. Computational calculations of Al on diamond were limited to ≤1 ML Al, but for addition to the bare diamond surface NEA became more negative with increasing Al coverage. It would be useful to understand how much Al can be deposited before the bulk properties of the metal dominate. Alternatively, further work could be completed on AlO-terminated diamond. Different Al coverages could be explored computationally using a larger supercell for the (111) surface, for instance. DOS calculations could use an N-doped slab or hybrid functionals to better model electronic behaviour within the band gap region.

The study of the different oxidation methods showed that UV/ozone treatment gave a large coverage of ketone, but since ether and hydroxyl groups were still present there is great scope for improving the oxygen surface termination such that it contains a higher proportion of one of the three types of

bonds. Reactions routine to organic chemistry were suggested in Chapter 5 to modify the type of bonding at the O-terminated surface, such as a Pinacol coupling, diol oxidation or ether cleavage reaction. This has benefits beyond NEA studies, for instance specific O-terminations are desirable for the development of novel biosensors or field effect transistors.

Regarding the experimental formation of AlO-terminated diamond, each Al deposition process could be further optimised in the future. For the thick-film deposition, it would be of interest to quantify how different acid-washing conditions affect the amount of Al that remains on the surface. A lot of the issues with the ALD method arose from the *in situ* oxidation, and so Al deposition on pre-oxidised samples could be further explored. For the electron-beam evaporation method, it would be of interest to understand and minimise spatial variance of work function.

Finally, while this study focused on Al, other metal-oxygen terminations could be studied in the future, and make use of trends observed in this work. There are a number of elements such as light group I and II metals and first-row transition metals that are more electropositive than Al and could continue to be optimised or have yet to be explored at all.

Appendix – Publications and Presentations

List of Publications

1. M. C. James, F. Fogarty, N. A. Fox and P. W. May, 'A Review of Surface Functionalisation of Diamond for Thermionic Emission Applications' *in preparation*.
2. M. C. James, P. W. May and N. L. Allan, '*Ab Initio* Study of Negative Electron Affinity from Light Metals on the Oxygen-Terminated (111) Diamond Surface' *J. Phys. Condens. Matter*, 2019, **31**, 295002.
3. M. C. James, A. Croot, P. W. May and N. L. Allan, 'Negative Electron Affinity from Aluminium on the Diamond (100) Surface: A Theoretical Study' *J. Phys. Condens. Matter*, 2018, **30**, 235002.

List of Oral Presentations

1. Hasselt Diamond Workshop – SBDD XXIII, Hasselt, Belgium. March 2018.
2. Materials Research Society Fall Meeting and Exhibit, Boston, MA, USA. November 2018.
3. 13th New Diamond and Nano Carbons Conference, Hualien, Taiwan. May 2019.

List of Poster Presentations

1. Hasselt Diamond Workshop – SBDD XXII, Hasselt, Belgium. March 2017.
2. 69th De Beers Diamond Conference, Warwick, UK. July 2017.
3. 11th International Nanoscience Student Conference, Bristol, UK. August 2017.
4. 12th New Diamond and Nano Carbons Conference, Flagstaff, AZ, USA. May 2018.